UNIVERSITÉ DE GENÈVE

Archive ouverte UNIGE
https://archive-ouverte.unige.ch

Thèse 2015

Open Access

This version of the publication is provided by the author(s) and made available in accordance with the copyright holder(s).

Numerical and experimental investigation of particle terminal velocity and aggregation in volcanic plumes

Bagheri, Gholamhossein

How to cite

BAGHERI, Gholamhossein. Numerical and experimental investigation of particle terminal velocity and aggregation in volcanic plumes. Doctoral Thesis, 2015. doi: 10.13097/archive-ouverte/unige:77593

This publication URL: https://archive-ouverte.unige.ch/unige:77593
Publication DOI: 10.13097/archive-ouverte/unige:77593

© This document is protected by copyright. Please refer to copyright holder(s) for terms of use.

Université de Genève
Département des Sciences de la Terre

Faculté des sciences
Professeur Costanza Bonadonna

Numerical and Experimental Investigation of Particle Terminal Velocity and Aggregation in Volcanic Plumes

THÈSE

présentée à la Faculté des sciences de l'Université de Genève
pour obtenir le grade de Docteur ès sciences, mention Sciences de la Terre

par

Gholamhossein Bagheri

de Shiraz (Iran)

Thèse N^o 4844

Genève
Atelier de reprographie Repromail
2015

UNIVERSITÉ
DE GENÈVE

FACULTÉ DES SCIENCES

Doctorat ès sciences
Mention sciences de la Terre

Thèse de *Monsieur Gholamhossein BAGHERI*

intitulée :

"Numerical and Experimental Investigation of Particle Terminal Velocity and Aggregation in Volcanic Plumes"

La Faculté des sciences, sur le préavis de Madame C. BONADONNA, professeure associée et directrice de thèse (Département des sciences de la Terre), Madame I. MANZELLA, docteure (Département des sciences de la Terre), Monsieur B. CHOPARD, professeur ordinaire (Département d'informatique) et Monsieur A. DURANT, docteur (Department of Geosciences, University of Oslo, Norway), autorise l'impression de la présente thèse, sans exprimer d'opinion sur les propositions qui y sont énoncées.

Genève, le 9 novembre 2015

Thèse - 4844 -

Le Doyen

N.B. - La thèse doit porter la déclaration précédente et remplir les conditions énumérées dans les "Informations relatives aux thèses de doctorat à l'Université de Genève".

Acknowledgements

I would like to thank my thesis director, Costanza Bonadonna, for her precious guidance, encouragement and immense support. It was a great honor for me to do a PhD in such an inserting field under her supervision. I have learned many exciting things from her, in particular in the field of earth sciences, which opened new horizons to me. I cannot imagine how could I have done a PhD in a field completely new to me, without having an open-minded supervisor like Costanza.

I would also like to thank Irene Manzella who helped me with many aspects of my PhD study from the design of the vertical wind tunnel to particle shape and aerodynamic characterization. I had many insightful discussions with her and she always gave me great advises and suggestions.

I would like to acknowledge members of the jury committee, Adam Durant, Irene Manzella and Bastien Choprad for their time and insightful comments that helped me to improve the final version of the thesis.

I thank my great officemates Sébastien Biass, Eduardo Rossi, Federico Brogi, Lucia Dominguez, Stefano Polastri, Fabrizio Alfano, Caroline Bouvet and Kae Tsunematsu. I would never forget nice memories and worldwide adventures we had together from Geneva to Sakurajima! Your companionship made my PhD an unforgettable experience. I would also like to thank and express my appreciation to Corine Frischknecht, Laura Pioli and Christine Lovis for their kind helps in many occasions.

I would like to thank Piero Pontelandolfo, Patrick Haas, Christophe Cerutti and Roberto Putzu from the CMEFE group who helped and guided me with the design and construction of the vertical wind tunnel. In particular, Piero spent countless hours to help me with the transportation of instruments, testing numerous experimental set-ups and calibration of the wind tunnel. In regards to settling columns and various experimental set-ups, I thank Frederic Arlaud for building precision instruments, some times in very short notice, which significantly helped me performing experiments.

I would like to thank the Swiss National Science Foundation (SNSF, Grant No. 200020-125024), the Faculty of Science and the Department of Earth Sciences of the University of Geneva (in particular Rossana Martini), the PASC project (Optimal deployment of multiscale applications on a HPC infrastructure) and Fondation Ernst et Lucie Schmidheiny that made my PhD possible by providing financial support at various stages.

Last but not least, I thank my wife, Pari, who stood by me with love, encouragement and support. I owe a great part of my achievements to her. Special thanks go to my mother, father, sisters and brothers. I would never forget their supports long before starting my PhD, which gave me the encouragement to continue my study and do a PhD abroad.

Gholamhossein Bagheri
November 2015, Geneva

Table of Contents

List of Figures

List of Tables

Summary

Recent eruptions of Eyjafjallajökull 2010, Grimsvotn 2011 (Iceland) and Puyehue-Cordon Caulle 2011 (Chile) have strikingly underlined the vulnerability of our highly globalized society to the atmospheric dispersal of volcanic clouds from even moderate-size explosions and highlighted significant shortcomings in schemes currently used to forecast the dispersal of volcanic ash. A significant impact associated with volcanic explosive eruptions is due to the dispersion of large amounts of ash, which can sediment on the ground or be transported in the atmosphere up to 100s of kilometers away from the volcano. As an example, dispersal of volcanic ash produced by the 2010 eruption of Eyjafjallajökull (Iceland) caused widespread flight cancellations over Europe and a global economic loss of U.S. $5.0 billion. During that crisis operative models overestimated the concentration of distal airborne ash that led to the closure of large parts of European airspace to air traffic. The main uncertainty in the forecasting models was due to lack of a robust understanding of dispersal and transportation of volcanic particles. In particular, the models were associated with unknown uncertainties on evaluating terminal velocity of individually falling particles and accounting for processes of particle aggregation. Thus, for the development of appropriate preparedness and mitigation strategies it is important to have a better assessment and understanding of particle sedimentation (e.g. particle terminal velocity) and aggregation. The main objectives of this thesis are i) to investigate methods of characterizing size, shape and terminal velocity of irregular volcanic particles separately, ii) assess the relationship between all these parameters, iii) provide reliable and robust models for quantifying terminal velocity of volcanic particles based on easy-to-measure shape descriptors and iv) better understand the characteristics of volcanic aggregates and their effect on tephra sedimentation.

In order to achieve these objectives, first a 4-meter high vertical wind tunnel is introduced, which has been designed and constructed at the University of Geneva in collaboration with the Groupe de comptence en mcanique des fluides et procds

nergtiques. With its diverging test section, the tunnel is designed to study the aerodynamical behavior of non-spherical particles with terminal velocities between 5 and 27 $\mathrm{m\,s^{-1}}$. A Particle Tracking Velocimetry (PTV) code was developed to calculate drag coefficient of particles in *standard* conditions (e.g. low accelerations, no wall effects).

In the next step, existing protocols were assessed and new strategies for the study of size and shape of irregular particles were introduced by performing a comprehensive characterization of 127 volcanic clasts with diameters between 155 µm and 37 mm. Methods include caliper measurements, image analysis, laser scanning and scanning electron microscope micro-computed tomography. Volume, surface area and various shape descriptors including form factors (e.g. flatness, elongation), circularity measures and sphericity were analyzed.

By using the vertical wind tunnel, settling columns and a sample of fully characterized irregular particles, the terminal velocity and drag coefficient of non-spherical particles were investigated in a wide range of Reynolds numbers. A new general model for the prediction of the drag coefficient of non-spherical solid particles of regular and irregular shapes falling in gas or liquid is presented that is valid for sub-critical particle Reynolds numbers (i.e. $Re < 3 \times 10^5$). In addition, effect of particle orientation and surface roughness on the drag coefficient are discussed in detail.

Finally, the aggregation of volcanic particles were investigated by applying a state-of-the-art combination of field and numerical strategies. The outcomes show the importance of coated particles on fine ash sedimentation, which until now has been neglected. This is demonstrated by the thick shell of small particles (< 90 µm) covering larger particles (200-500 µm) that typically fall off on the impact with ground. In addition, dedicated numerical inversions show how coated particles can rapidly form within 175 seconds from eruption onset. Lastly, our observations represent the first field-based evidence of the so-called *rafting* effect, in which the sedimentation of coarse ash as coated particles is delayed due to the increase of the drag coefficient.

Résumé en Français

Les éruptions récentes des volcans islandais Eyjafjallajökull (2010) et Grimsvotn (2011) ainsi que l'éruption du volcan chilien Puyehue Cordon Caulle (2011) ont remarquablement souligné l'impact que les éruptions de taille moyenne peuvent occasionner sur notre société hautement mondialisée. Cela a également mis en évidence les lacunes existantes dans les procédures actuelles de prévision de la dispersion des cendres volcaniques. Un des impacts les plus significatifs associés aux éruptions volcaniques explosives est lié à la dispersion de grandes quantités de cendres transportées dans l'atmosphère jusqu'à des centaines de kilomètres autour du volcan. à titre d'exemple, la dispersion des cendres volcaniques produites par l'éruption de l'Eyjafjallajökull en 2010 a causé une annulation des vols aériens sur l'ensemble de l'Europe causant une perte économique mondiale de l'ordre de 5 milliards de dollars US. Au moment de cette crise volcanique, les modèles opérationnels ont surestimé la concentration de cendres dans l'atmosphère distale du volcan, ce qui a généré la fermeture inutile d'une grande partie de l'espace aérien européen. La principale faiblesse de ces modèles de prévision provient d'une compréhension insuffisante des processus de dispersion et de transport des particules volcaniques dans l'atmosphère. Ces modèles n'ont pas pris pas en compte l'incertitude liée à l'évaluation de la vitesse terminale de particules individuelles qui tombent du panache volcanique, influenant ainsi les processus d'agrégation des particules. Par conséquent, une meilleure caractérisation de la sédimentation des particules en termes de vitesse terminale et de l'agrégation est indispensable pour le développement de plans de préparation et de mitigation des impacts induits par les panaches volcaniques. Les objectifs principaux de cette thèse sont i) développer des méthodes de caractérisation de la taille, forme et de la vitesse terminale des particules volcaniques individuelles, ii) évaluer la relation entre tous les paramètres, iii) fournir des modèles fiables et robustes pour la quantification de la vitesse terminale des particules volcaniques basés sur des descripteurs de forme faciles à mesurer, et, iv) mieux comprendre les caractéristiques

des agrégats volcaniques et leurs effets sur la sédimentation de tephra.

Pour atteindre ces objectifs, une soufflerie verticale de 4 mètres de haut a été conue et construite pour la première fois à l'Université de Genève, en collaboration avec le groupe de compétence en mécanique des fluides et procédés énergétiques. En raison de sa section de test divergente, la soufflerie permet d'étudier le comportement aérodynamique de particules non-sphériques avec des vitesses terminales entre 5 et 27 $\mathrm{m\,s^{-1}}$. Un code numérique (Particle Tracking Velocimetry PTV) a été développé pour calculer le coefficient de traînée de particules dans les conditions standards, à savoir, accélérations faibles et pas d'effets de paroi.

Dans une seconde étape, les protocoles existants ont été évalués et de nouvelles stratégies pour l'étude de la taille et de la forme des particules irrégulières ont été introduites en effectuant une caractérisation approfondie de 127 particules volcaniques avec des diamètres compris entre 155 µm et 37 mm. Les méthodes utilisées incluent des mesures avec pieds à coulisse, l'analyse d'images, le balayage laser et la microtomographie par microscope électronique à balayage. Différents paramètres ont été analysés, tels que le volume, la surface, et plusieurs descripteurs de forme, par exemple l'applatissement ou l'allongement, ainsi que la circularité et la sphéricité.

D'autre part, en utilisant à la fois la soufflerie verticale, des colonnes de sédimentation et un échantillonnage de particules irrégulières bien décrites, la vitesse terminale ainsi que le coefficient de traînée des particules ont été analysés pour un large intervalle de valeurs du nombre de Reynolds. Cela permet de présenter dans ce travail de recherche un nouveau modèle général pour la prédiction du coefficient de traînée de particules solides non-sphériques, de formes régulières et irrégulières, tombant dans des fluides gazeux et liquides, valide pour des nombres de Reynolds des particules sous-critiques ($Re < 3 \times 10^5$). De plus, les effets d'orientation des particules et de la rugosité de la surface sur le coefficient de traînée sont largement discutés.

En conclusion, l'agrégation des particules volcaniques a été étudiée en appliquant une stratégie novatrice combinant à la fois les données de terrain et l'analyse numérique. Nos résultats montrent l'importance des particules enrobées dans la sédimentation des cendres fines, un effet qui a été négligé jusqu'à présent. Cela est démontré par l'épaisse carapace de petites particules ($< 90\,\mu\mathrm{m}$) recouvrant de plus

grandes particules (200-500 µm) qui tombent généralement au moment de l'impact avec la surface. En outre, les inversions numériques démontrent comment les particules enrobées peuvent se former rapidement, en moins de 175 secondes après le début de l'éruption. Finalement, nos observations représentent les premières évidences de terrain de l'effet *rafting* dans lequel la sédimentation de cendres grossières, sous forme de particules enrobées, est retardée en raison de l'augmentation du coefficient de traînée.

Chapter 1

Introduction

Explosive volcanic eruptions can inject into the atmosphere a large amount of volcanic particles (*tephra*) of a wide range of sizes and shapes. Based on the classification proposed by Fisher (1961), size of volcanic particles spans from bombs and blocks ($> 64\,\text{mm}$), which deposit within a few kilometres from the vent, to lapilli (2 mm-64 mm), coarse ash (63 µm-2 mm) and fine ash ($< 63\,\mu\text{m}$) that can be transported hundreds of kilometres from the vent depending on their terminal velocity. Tephra particles can sediment individually or within aggregates and are associated with different hazards depending on their size. In particular, blocks and bombs can significantly damage infrastructures close to the vent. Accumulation of ash- and lapilli-sized particles can lead to collapse of roofs, damage to vegetation, contamination of water supplies, disruption of electricity and telecommunication networks and perturbation of ground transportation. Finally, due to their small size, fine volcanic ash can be transported hundreds of kilometers away from the vent and poses a significant threat to aviation safety and human health. Since volcanic ashes are not detectable with common radars aboard aircraft, they can be sucked into the jet engines and due to the melting/solidification, reduce the performance of the jet engine up to complete failure (Casadevall, 1994; Marzano et al., 2013). Fine ash $< 10\,\mu\text{m}$ can provoke asthma or bronchitis symptoms and $< 4\,\mu\text{m}$ can cause inflammatory responses in human lungs and respiratory system (Horwell and Baxter, 2006). As a result, the study and modeling of tephra dispersal is crucial both to our understanding of volcanic eruptions and to the hazard assessment of active volcanoes that have the potentials of disrupting societies and ecosystems at both local and global scales.

The main parameter controlling dispersal and sedimentation of volcanic particles is their *terminal velocity*. When a particle starts to fall in still air with zero initial velocity, it accelerates under the gravitational acceleration until the sum of the forces acting on the particle becomes zero and the particle reaches a constant falling velocity, called the terminal velocity. Since volcanic plumes can reach heights of several kilometres, it is typically assumed that particles fall at their terminal velocity as soon as they are released in the atmosphere (e.g. see Bonadonna et al., 1998). Terminal velocity of volcanic particles is an important parameter for the determination of their residence time in the atmosphere. For example, individual large volcanic particles (e.g. bombs, lapilli) have terminal velocity of the order of $10\,\mathrm{m\,s^{-1}}$, whereas terminal velocity of individually falling fine ash is of the order of $< 10^{-1}\,\mathrm{m\,s^{-1}}$. Thus, the residence time of bombs and lapiilies are of the order of minutes, while fine ash can stay suspended in the atmosphere for days or weeks. Main variables affecting terminal velocity are size and shape of particles (e.g. see Clift et al., 2005; Loth, 2008). As a result, in order to have a proper assessment of particle terminal velocity, it is necessary to quantify their size and shape. Volcanic clasts are known to have highly non-spherical and irregular shapes, with physical, chemical and optical characteristics significantly different from those of spherical particles. Numerous studies show the importance of particle shape on various particle properties, such as their scattering and aerodynamical behaviour (Mishchenko et al., 2000; Riley, 2003; Clift et al., 2005; Loth, 2008; Folch, 2012; Kylling et al., 2014). Nevertheless, volcanic particles have often been approximated as spheres in numerical descriptions and observation strategies.

Another important parameter affecting sedimentation of volcanic particles is particle aggregation (Brown et al., 2012) (Fig. 1.1). It is also a primary source of uncertainty in forecast models since fundamental questions, such as timing and deposition dynamics of volcanic aggregates, still remain unanswered. Particle aggregation can also significantly affect the sedimentation pattern of tephra deposit by generating secondary maxima of accumulation (e.g. 1980 eruption of Mount St. Helens, see Fig. 1 in Durant et al., 2009)

Particles mainly collide and aggregate because of complex interactions of surface

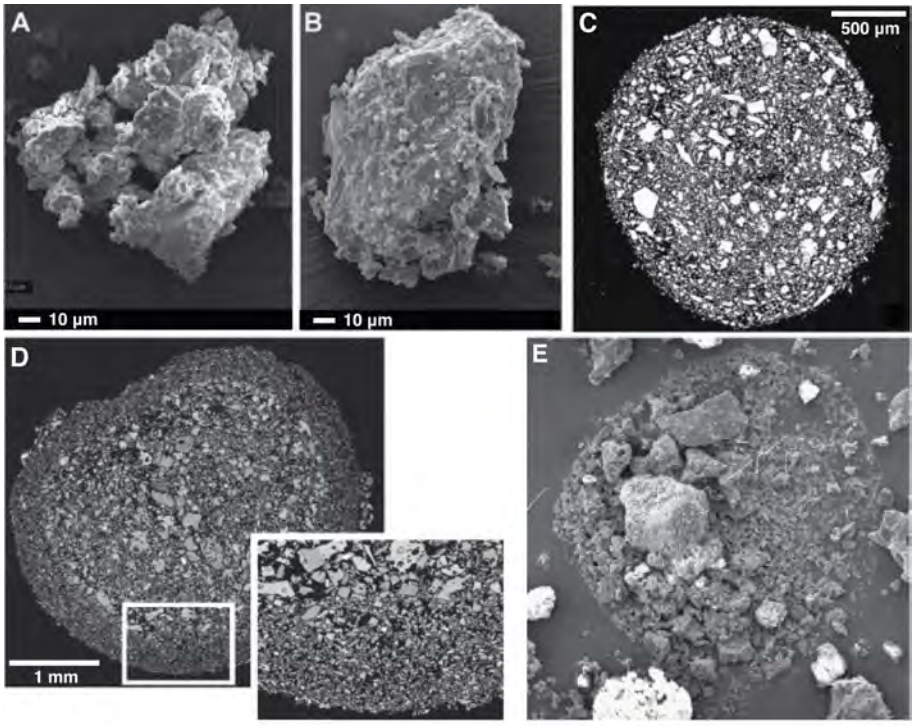

Figure 1.1: Various types of volcanic aggregates. (A) Ash cluster, PC1; (B) coated particle, PC2; (C) poorly-structured pellets, AP1; (D) pellets with concentric structure, AP2; (E) Evaporated mud rain droplet, AP3. (A), (B) and (E) are from the 2010 eruption of Eyjafjallajokull volcano, Iceland (Bonadonna et al., 2011); (C) is from Soufriere Hills volcano, Montserrat (Bonadonna et al., 2002b); (D) is from Upper Scoria deposits, Santorini, Italy. Figure adjusted from Brown et al. (2012).

liquid layers, electrostatic forces, turbulence and/or differences in settling velocities. Aggregation processes significantly affect sedimentation of fine ash ($< 63\,\mu m$) by increasing its terminal velocity and, hence, reducing its residence time in the atmosphere. Although residence time of individually falling fine ash in the atmosphere is of the order of days and weeks (Rose and Durant, 2009), fine ash mostly deposits on the ground in < 1 day as a result of aggregation (Rose and Durant, 2011). Understanding aggregation processes is crucial since fine ash represents a large part of the tephra produced during explosive volcanic eruptions (Brown et al., 2012) and it poses a significant threat to aviation safety and human health. If particle aggregation is not considered, volcanic ash transport and dispersal models fail to accurately describe both particle deposition in proximal area and atmospheric concentrations in the far field, with important implications for both long-term hazard assessment and real-time ash forecasting (Costa et al., 2010; Rose and Durant, 2011; Brown et al., 2012).

1.1 Terminal Velocity and Drag Coefficient of Volcanic Particles

Various forces (and momentums) in different directions can act on a falling particle, such as buoyancy, drag, lift, added mass and Basset forces (Clift et al., 2005). The most important, however, are the gravitational, buoyancy and drag forces. By taking into account only these forces, particle terminal velocity v_t can be derived as:

$$v_t = \sqrt{\frac{4\,g\,d_{eq}(\rho_p - \rho_f)}{3\,\rho_f\,C_D}} \tag{1.1}$$

where g is the gravitational acceleration, d_{eq} is the *spherical equivalent diameter* (i.e. diameter of a sphere with the same volume as the particle), ρ_p and ρ_f are particle and fluid density, respectively, and C_D is the drag coefficient of the particle. The drag coefficient is the most challenging parameter to determine since for a freely falling particle it depends on many parameters, including particle Reynolds number, shape, orientation and particle-to-fluid density ratio (e.g. see Clift et al., 2005). Particle Reynolds number is defined as:

$$Re = \frac{\rho_f d_{eq} |v_r|}{\mu_f} \tag{1.2}$$

where v_r is the relative velocity between the particle and air and μ_f is the fluid dynamic viscosity.

Except for $Re \ll 1$, where an analytical solution exists for spheres based on Stokes (1851) solution and for ellipsoids based on Oberbeck (1876) solution, no general solution can be found for calculating the drag coefficient of particles of any shape (Happel and Brenner, 1983; Clift et al., 2005; Loth, 2008). At higher Reynolds numbers, the interaction between fluid and particle is highly non-linear and complex, and no analytical solution is available for estimating the drag coefficient, even for spherical particles for which shape quantification is not an issue. Thus, experimental measurements are the main source of information while numerical solutions and boundary layer theory can provide additional information (Clift et al., 2005). In the absence of a general solution, a large number of empirical correlations for predicting

the drag coefficient of spherical and non-spherical particles are introduced that are associated with different ranges of validity and accuracy (Walker, 1971; Wilson and Huang, 1979; Suzuki, 1983; Happel and Brenner, 1983; Haider and Levenspiel, 1989; Ganser, 1993; Clift et al., 2005; Dellino et al., 2005; Pfeiffer et al., 2005; Loth, 2008; Hölzer and Sommerfeld, 2008).

Non-spherical models typically incorporate effects of the particle shape on the drag coefficient through a parameter called *shape descriptor*. Shape descriptors are mathematical functions that require previous determination of dimensional variables, such as values of length, diameter, projection perimeter, projection area, surface area or volume. In studies related to transport and sedimentation of non-spherical particles, the most common shape descriptors are *sphericity* and *form factors* (e.g. flatness, elongation and their combinations) (Pettyjohn and Christiansen, 1948; McNown and Malaika, 1950; Sneed and Folk, 1958; Christiansen and Barker, 1965; Isaacs and Thodos, 1967; Wilson and Huang, 1979; Baba and Komar, 1981; Leith, 1987; McKay et al., 1988; Haider and Levenspiel, 1989; Ganser, 1993; Gögüs et al., 2001; Loth, 2008; Chow and Adams, 2011). Sphericity is defined as the ratio of the surface area of a volume equivalent sphere to the surface area of the particle. Thus, for irregular and porous volcanic particles, sphericity is challenging to measure since surface area of an irregular particle can only be measured with sophisticated instruments, such as a 3D laser scanner. In addition, surface area of an irregular particle is not an absolute value and it depends on the resolution of measuring instruments (e.g. Taylor et al., 2006; Alfano et al., 2011). Form factors (e.g. flatness, elongation), which are functions of particle length in three dimensions, represent the other type of important shape descriptors. As an example, the model of Wilson and Huang (1979) that is widely used for estimating drag coefficient of on sub-millimeteric volcanic particles is based on a form factor. However, given that form factors and sphericity are not correlated with each other for an irregular particle, it is not clear which aspect of the particle shape controls aerodynamic of irregular particles.

1.2 Experimental Methods for the Measurement of Particle Drag Coefficient

Settling columns represent the most used technique for experimental determination of particle terminal velocity and drag coefficient (e.g. Marchildon et al., 1964; Willmarth et al., 1964; Christiansen and Barker, 1965; Isaacs and Thodos, 1967; Stringham et al., 1969; List and Schemenauer, 1971; McKay et al., 1988; Gögüs et al., 2001; Tran-Cong et al., 2004; Chow and Adams, 2011). In this technique, particles are released from the top of a vertical column, usually filled with a liquid (e.g. water-based mixtures), and its terminal velocity is measured (e.g. by stopwatch timing, video imaging) after it traveled for a *sufficiently* long distance, where particle acceleration becomes negligible. The required falling distance is dependent on several parameters including the particle size and shape and properties of the fluid (i.e. density and viscosity). For example, a spherical particle with diameter of 1 cm and density of $2700\,\mathrm{kg\,m^3}$ needs an air-filled column of at least 130 m in order to reach 99% of its terminal velocity ($Re \approx 1.6 \times 10^4$), whereas in the water it would only need 16 cm ($Re \approx 8.2 \times 10^3$). This explains why most falling column experiments are performed in liquids.

Although measuring particle terminal velocity and drag coefficient in settling columns is more feasible with liquids, they limit the experiments at very low values of particle-to-fluid density ratios. As mentioned earlier density can influence the drag coefficient of freely falling particles in particular at high Reynolds numbers ($Re >\sim 1000$). The alternative technique is to use a wind tunnel. There are two types of wind tunnels, namely horizontal and vertical wind tunnel. In horizontal wind tunnels particles are typically fixed on a balance that can measures forces and momentum (in one or several directions) exerted on the particle from the fluid. Thus, for non-spherical particles measurements should be carried out at various orientations. In any case, most of available balances are suitable for large bodies (e.g. airplane models) and, thus, cannot be used for centimeter and sub-centimeter particles. A more suitable option for the study of aerodynamics of freely falling particles is a vertical wind tunnel. In vertical wind tunnels, the particle terminal

velocity is measured while it is suspended within a well-calibrated section (i.e. the *test section*), where flow-related quantities (e.g. velocity, pressure) are known. As the particle floats in the test section its weight is counterbalanced by the drag force exerted from the wind. Given that the drag force is related to the particle relative velocity (which is equal to the wind speed if the particle is in *still-suspension*) and size of the particle, the drag coefficient can be measured. This technique is mostly used to measure terminal velocity of water droplets and to study their internal circulation and freezing behavior in meteorology, since their shape symmetry allow them to have a still-suspension in the test section (Beard and Pruppacher, 1969; Pruppacher and Beard, 1970; Spengler and Gokhale, 1972; Pitter and Pruppacher, 1973; Stow and Woodward, 1974; Kamra et al., 1985; von Blohn et al., 2005).

Still-suspension, however, is difficult to achieve for non-spherical particles since they experience forces and momentum in various direction during suspension. There is a technique called *velocity profile shaping* to improve still-suspension of particles in vertical wind tunnels, in which the air velocity profile in the test section is shaped to be lower at the center (Spengler and Gokhale, 1972; Stow and Woodward, 1974; Kamra et al., 1991). Nevertheless, for some non-spherical particles, the stability cannot be improved even with velocity profile shaping (Knight, 2001; Ellis, 2000).

1.3 Particle Size Characterization

Particle size in physical volcanology is typically characterized based on mechanical sieving, laser diffraction analysis and/or dynamic image analysis (DIA) that provide a rapid description of one form dimension equivalent to the medium length of the particle, to the diameter of the equivalent Mie sphere and to various parameters (e.g. diameter of the equivalent circle, particle width and length of particle projection), respectively (also see Mishchenko et al., 2000; Riley, 2003; Kylling et al., 2014). In particular, mechanical sieving is commonly performed down to 63 µm, while laser diffraction (e.g. CILAS and Mastersizer of Malvern Instrument) and DIA analysis (e.g. CAMSIZER®) can provide measurements at various size ranges between 0.1 µm and 30 mm. Instruments based on laser diffraction measure the light scat-

tered by particles in order to calculate particle size based on Mie theory and assuming spherical shape. In DIA analysis, two-dimensional projections of particles are captured with camera(s) as they fall through the backlighted measurement volume. Then projections are analysed with image analysis software and various size/shape characteristics of particles are measured. As a result, DIA analysis is more suitable for the characterization of non-spherical particles. It also provides robust statistics of the measured quantities since particles are characterized in a dynamic process and in different orientations. However, the measurements are two-dimensional in nature.

Other less common techniques used to characterize particle size include sedimentation (e.g. SediGraph®) and electrical zone sensing (EZS) methods (Beckman Coulter®). The sedimentation technique is designed based on the Stokes law, which can correlate the settling velocity of an individually falling sphere in a fluid with its diameter. However, this technique is valid for measuring volume of very small particles (e.g. $\sim 2 - 50\,\mu m$), time consuming and biased by irregularity of volcanic particles (IVHHN Guidelines for grain-size distribution analysis, www.ivhhn.org). The EZS techniques is developed based on the Coulter principle, in which low volume fractions of particles are suspended in an electrolyte solution and the impedance between two electrodes are measured as particles pass between them. The impedance is correlated with the particle volume (based on the Coulter principle) and can be measured as a voltage or current pulse. This technique has been used in volcanology to measure volume of volcanic ash with diameters between $\sim 1 - 100s\,\mu m$ (e.g. Murrow et al., 1980; Sulpizio et al., 2008).

As mentioned earlier, most tephra deposits are characterized by a wide size range and, therefore, a combination of two techniques is often necessary to provide a comprehensive size characterization, one for the coarser fraction (i.e. sieving) and one for the finer fraction (e.g. laser diffraction or DIA). Given that these strategies are based on different shape assumptions, their combination is not always straightforward, especially when particles are very irregular. In any case, simple grainsize analysis has allowed making fundamental advances in the characterization and classification of explosive volcanic eruptions by providing first-hand estimations

of grainsize distribution of various volcanic deposits (e.g. Walker, 1973; Rust and Cashman, 2011).

Above-mentioned techniques are powerful tools for rapid assessment of bulk grain size distribution. However, they cannot be used to accurately derive important characteristics of individual particles, such as volume and surface area. Volume and surface area are the two aspects of particle size that are of most importance for the determination of particle physical, optical and chemical behaviour, such as terminal velocity and reflectivity. Although for a spherical particle these parameters can be quantified simply by knowing its diameter, for irregular volcanic particles it is not that simple. Except for large volcanic particles (of order of cm), where simple methods can be used to determine particle volume (e.g. methods based on Archimedes principle), volume and surface area can only be measured directly with sophisticated instruments, such as 3D scanners and Computed-Tomography (CT) scanners. In many studies, simpler and more rapid indirect methods, such as image analysis, are used since direct methods are time consuming and not available to all.

1.4 Particle Shape Characterization

Shape and texture of volcanic particles range from non-porous sub-spherical to highly porous and irregular. Particle size and shape are both influencing factors for determining their aerodynamic behaviour, e.g. terminal velocity, and their residence time in the atmosphere(e.g. Folch et al., 2009). They are also important parameters in remote sensing applications. As an example, many remote sensing retrieval algorithms are based on the conventional Lorenz-Mie theory or its modifications, in which the particle shape is assumed to be spherical. However, scattering properties of non-spherical particles can differ dramatically from those of equivalent Mie spheres, which affect estimations of sizes and mass concentrations within an eruption cloud (Mishchenko et al., 2000; Riley, 2003; Kylling et al., 2014). In fact, the assumption of spherical shapes for volcanic particles can overestimate mass concentration and optical depth of the ash cloud, and underestimate particle effective diameter (Riley, 2003, and references therein).

In order to characterize particle shape, several shape descriptors have been introduced over the last few decades. Unlike spherical and regular particles, whose shape can be simply quantified based on one or two parameters (e.g. diameter and height for a cylindrical shape particle), quantification of shapes for irregular particles has been subject of many studies during past decades (Cox, 1927; Wadell, 1933; Riley, 1941; Barrett, 1980; Riley, 2003; Taylor et al., 2006; Blott and Pye, 2007; Asahina and Taylor, 2011; Garboczi et al., 2012; Vonlanthen et al., 2015). This is mainly due to the fact that various aspects of shapes can be defined for irregular particles and a single shape descriptor cannot provide a complete description. For an irregular particle, four major aspects of shape can be defined, namely form (e.g. flatness, elongation), *roundness* (i.e. angularity of particle edges), *irregularity* (i.e. concavity of particle projections) and sphericity (i.e. *circularity* in 2D) (Blott and Pye, 2007). However, the most influential aspects of particle shape for aerodynamic behaviour and scattering properties of volcanic particles are form and sphericity (Wilson and Huang, 1979; Mishchenko et al., 1997; Riley, 2003; Clift et al., 2005; Dellino et al., 2005; Nousiainen et al., 2006; Blott and Pye, 2007; Loth, 2008; Nousiainen et al., 2011).

For irregular particles, there are various methods of measuring or estimating particle form and sphericity. However, different measurements techniques and estimation can give very different results. Gas adsorption has been used widely in various fields of science (e.g. material science), but it has been recently applied also in volcanology (Riley, 2003; Alfano et al., 2011, and references therein). Through gas-adsorption methods, the amount of gas adsorbed by a sample at different pressure conditions is measured, which is related to the total exposed surface and allows an estimation of the sample specific surface area (Delmelle et al., 2005; Alfano et al., 2011). Specific surface area is defined as the surface area of the particle(s) per unit mass (or volume). The total surface area of the sample can be found by using the so-called Brunauer, Emmett and Teller (BET) method (Brunauer et al., 1938). Through this method, the weight of the absorbed gas is plotted against the relative pressure, and the slope and intercept of the liner fit is found. Finally, the slope and intercept are used to find the total surface area by the BET equation, which can be

divided by the sample mass in order to obtain the specific surface area.

More recently, surface area of volcanic particles has been measured directly with 3D laser scanning and SEM micro-CT (Ersoy et al., 2010; Alfano et al., 2011; Vonlanthen et al., 2015). SEM micro-CT enables non-destructive 3D reconstruction and characterization of small objects within the chamber of an SEM (Pauwels et al., 2010). The technique uses the X-rays generated in the SEM chamber when the electron beam is focused on a metal target. The object to be analyzed is placed in front of the X-ray beam and step-wise rotated over an incremental range of angular orientations. Shadow projections of the sample are then collected by an X-ray sensitive camera and used to reconstruct 2D CT slices and 3D models of the object with a resolution in the order of 1 µm to 3 µm.

SEM stereo-imaging is another direct method that can be used to measure surface area of particles with diameters of very fine ash (e.g. Mills and Rose, 2010). The main drawback of SEM stereo-imaging, however, is that it generates a digital elevation model only for the upper surface of the particle, while the lower surface is inaccessible to the electron beam and has to be interpolated (Vonlanthen et al., 2015).

Besides requiring sophisticated instruments, another complexity associated with the measurement of surface area of irregular particles is its dependence on the resolution at which the measurements are carried out. As an example, the surface area of a particle measured by the gas-adsorption method can be orders of magnitude higher than that measured by 3D laser scanning (Riley, 2003; Lin and Miller, 2005; Ersoy et al., 2010; Mills and Rose, 2010; Alfano et al., 2011). In addition, some of characterization methods are not standardized yet and measured quantities are operator dependent (e.g. flatness and elongation measured by caliper Blott and Pye, 2007, ; as it will be better explained in Chapter 3).

1.5 Volcanic Aggregates

Observations of various types of volcanic aggregates in the field have been reported and documented since 1962 (Moore and Peck, 1962) (see Brown et al., 2012, and references therein). This led to a comprehensive classification of volcanic aggregates

and their characteristics, Fig. 1.1 (Brown et al., 2012). Depending on the water content, particle aggregation results in the formation of particle clusters (typically considered dry) and accretionary pellets (typically considered wet) (Sparks et al., 1997; Brown et al., 2012, and references therein).

Based on the classification proposed by Brown et al. (2012), accretionary pellets can be of three sub-categories, namely AP1 (poorly structured pellets), AP2 (pellets with concentric structure) and AP3 (liquid pellets). AP1 are poorly structured aggregates consisting of particles $< 1-400\,\mu m$ with a median of $\sim 30-90\,\mu m$ particles and rarely particles $> 1\,mm$. AP2 aggregates have typically poorly structured cores similar to AP1 with median grain size distribution of $\sim 25-50\,\mu m$. The core of AP2 particles is surrounded by rim (cross-section width $0.6-1.5mm$) of one or more multiple very fine-grained ash laminae (cross-section thickness $\sim 200-500\,\mu m$). The median size of particles in the rim is $\sim 10-15\,\mu m$. AP3 aggregates are liquid water drops containing poorly sorted ash particles $< 1\,mm$. Unlike AP1 and AP2, AP3 aggregates break up on impact and, therefore, have poor preservation in the geological record (Brown et al., 2012).

In any case, although there are debates about the source and origin of AP1 and AP2 aggregates, their characteristics (e.g. size distribution of constituent particles, porosity) are well characterized. Particle clusters are another type of volcanic aggregates, which is divided in two sub-categories of ash clusters and coated particles. Ash clusters are characterized by irregular and fragile aggregates with density of 60-200 $kg\,m^3$ mainly composed of particles $< 40\,\mu m$. Their size (measured after impact) spans from 10s µm to a few centimeters. Coated particles are defined as typically coarse ash particles partially covered with fine ash particles $< 40\,\mu m$.

During the last two decades several experimental, numerical and field investigations have attempted to describe aggregation processes in terms of grain-size distribution, terminal velocity, density and porosity (Lane et al., 1993; Gilbert and Lane, 1994; Schumacher and Schmincke, 1995; James et al., 2002; Bonadonna et al., 2011; Taddeucci et al., 2011; Telling and Dufek, 2012; Van Eaton et al., 2012; Van Eaton and Wilson, 2013). Nonetheless, the low preservation potential of aggregates in the deposits and the difficulties to recreate the appropriate environmental and

eruptive conditions in the laboratories make the understanding of particle aggregation difficult. The most noticeable experiments on volcanic aggregates is the work of (Gilbert and Lane, 1994; Schumacher, 1994; James et al., 2002; Telling and Dufek, 2012).

Gilbert and Lane (1994) used a vertical wind tunnel to inject ash from a narrow pipe on the surface a sphere fixed in the tunnel test section. The water vapour was also introduced to the ash flow, which created a liquid layer around the sphere by condensation. They suggested that accretionary pellets can be created by collision of particles coated with a film of water and build up of concentric grain-size rims is resulted from differences in the supply of particular grain sizes during aggregate growth. In a second set of experiments, they also showed that accretionary pellets cannot be formed by the scavenging of particles in rain droplets. The first laboratory experiment on the clustering of volcanic particles was conducted by Schumacher (1994), who found that electrically charged volcanic ash from the 1980 eruption of Mount St. Helens could cluster when transported within an electrostatic field. Results also show how the first particle clusters to sediment were coated particles that included a large particle $> 63\,\mu m$ and some accreted fines, whereas the last to sediment were ash clusters composed of particles $< 45\,\mu m$ and some incorporated larger particles up to 125-180 µm. The comparison with grain-size data from other volcanic eruptions suggested that the change in structures of proximal to distal particle clusters is not unique to Mount St. Helens.

Almost a decade later, James et al. (2002) conducted a similar experiment to study the role of electrostatic charge on the aggregation of volcanic particles freely falling in dry conditions (relative humidity $\sim 25 - 30\%$). By charging pumices from the 1980 eruption of Mount St. Helens through fragmentation, they found that ash particles $< 70\,\mu m$ can cluster together to create particle clusters up to $800\,\mu m$ with density of $\sim 100 - 200\,kg\,m^{-3}$ and settling velocity of $< 1\,m\,s^{-1}$. Recently, Telling and Dufek (2012) conducted experiments on ash aggregation with diameters between 106-250 µm in an enclosed tank, in which relative humidity could be adjusted and monitored. Experimental samples were accelerated into the tank through a vertical nozzle and particle positions (and velocities) were determined with a high-

speed camera and Particle Image Velocimetry (PIV) technique. They found that, *aggregation efficiency* (i.e. the fraction of colliding particles that stick together) is significantly affected by the collision kinetic energy, while it was not affected by the humidity. Finally, they proposed that electrostatic aggregation is the most plausible mechanism for aggregation.

In general, there are field visual evidence for AP1 and AP2 aggregates since they are less fragile compared to particle clusters. Particle clusters have very poor preservation potential in tephra deposits. As a result, most of our knowledge about is based on after impact interpretation of deposits (Bonadonna et al., 2011, e.g.), theoretical studies (Lane et al., 1993, e.g.) and experimental investigations (James et al., 2002, e.g.). Only recently, field investigations by Taddeucci et al. (2011) during 2010 eruption of Eyjafjallajökull, showed that terminal velocity of particle clusters (before impact) falling in proximal regions ($\sim 7\,\mathrm{km}$) was mostly between $1 - 4\,\mathrm{m\,s^{-1}}$. However, the type (i.e. ash cluster vs. coated particle) and internal structure (e.g. grain size distribution) of particle clusters before impact were not investigated.

In addition to the structure of particle clusters, their effect on the sedimentation of tephra is not fully understood. As an example, Sorem (1982) observed large ash particles ($40\,\mu\mathrm{m}$ to $60\,\mu\mathrm{m}$) deposited within ash clusters far beyond the distance at which they would have settled if traveling independently. He called this effect *rafting*, in which large particles inside aggregates fall with lower settling velocity than if they fall individually. However, later Lane et al. (1993) and James et al. (2002) ruled out the possibility of rafting based on theoretical analysis, since they found out rafting of particles $< 80\,\mu\mathrm{m}$ within aggregates is very unlikely.

1.6 Objectives of this work

Previous sections show that there are still important open questions on the subject of tephra dispersal and sedimentation, which need to be addressed, in particular:

- What are the most accurate and rapid methods for characterizing size and shape of irregular volcanic particles, in particle volcanic ash?

- Which aspect of shape (e.g. form, sphericity) controls aerodynamic behavior of non-spherical particles?
- What are the aerodynamical and structural properties of particle clusters?
- When and where do particle clusters form, and how they affect tephra sedimentation?

This thesis consists of four main chapters. **Chapter 2** describes the design of a unique four-meter high vertical wind tunnel and the experimental setup developed for the study of the terminal velocity of volcanic particles (published as Bagheri G., Bonadonna C., Manzella I., Pontelandolfo P. and Haas P. (2013): Dedicated vertical wind tunnel for the study of sedimentation of non-spherical particles, *Review of Scientific Instruments*, 84(5), 054501.).

Chapter 3 presents the state-of-the-art methods for characterization of irregular particles (published as Bagheri G., Bonadonna C., Manzella I. and Vonlanthen P. (2015): On the characterization of size and shape of irregular particles, *Powder Technology*, 270, 141-153.). In particular, we describe methods of measuring volume, surface area and sphericity of irregular particles with *direct* (i.e. 3D laser scanning, scanning electron microscope micro-computed tomography) and *indirect* method (i.e. image analysis, caliper measurements). In addition, protocols for measuring particle *form dimensions* are revised and a new protocol is introduced. Furthermore, various aspects of particle shape are measured and their correlation with each other are discussed.

In **Chapter 4** terminal velocity and drag coefficient of particles characterized in Chapter 3 are measured in air-filled settling columns of various heights ($9 < Re < 1000$) and the vertical wind tunnel ($8 \times 10^3 < Re < 6 \times 10^4$) (submitted to *Powder Technology*, Bagheri G., Bonadonna C. (2015):On the Drag of Freely Falling Non-Spherical Particles.). Besides irregular volcanic particles, aerodynamics of various regular particles (e.g. ellipsoids, cylinders) are also measured and presented. In addition, drag coefficient of 10^4 ellipsoids of various forms at very low Reynolds numbers ($Re << 1$) are also calculated analytically. Thus, aerodynamics of non-spherical particles of regular and irregular shape particles (e.g. drag coefficient,

orientation effects) are investigated in a wide range of Reynolds numbers.

Finally, **Chapter 5** is focused on field investigation carried out on aggregates produced by the Vulcanian explosions of Skaurajima volcano in Japan (to be submitted). In particular, we present our findings on characteristics of coated particles based on High-Speed-High-Resolution (HS-HR) imaging combined with in-situ sample collection and numerical modeling to characterize volcanic aggregates. This multi-technique approach allowed us to provide a complete characterization of aggregates in terms of terminal velocity, structure and grain size distribution of constituent particles. Lastly, numerical inversions of the field observations are used to shed light on the location and timing of particle cluster formation.

Chapter 2

Dedicated vertical wind tunnel for the study of sedimentation of non-spherical particles[1]

2.1 Introduction

Transportation of solid particles within a continuum fluid is common in a wide range of phenomena. Dispersal of volcanic particles (Bonadonna and Costa, 2013), sedimentation and erosion in river channels (Stringham et al., 1969), deposition of solid carbon dioxide hydrate in ocean (Chow and Adams, 2011), particle transport in fluidized beds (Hilton et al., 2010) and deposition of airborne particles in indoor environmrents (Bagheri et al., 2012) are just a few examples. These phenomena are associated with various types of fluids, process speed and particle shape, size and density. Forces and torques, which fluids exert on the particles, represent some of the most important aspects that characterize the interaction between fluids and particles. Many natural and industrial processes involve transportation of particles either in high particle to fluid density ratios or high particle Reynolds numbers, which include many processes where solid particles are transported in gases. Drag coefficient has typically been measured of large fixed particles in horizontal wind tunnels (Wieselsberger, 1922; Achenbach, 1972; Zdravkovich et al., 1989) or of par-

[1] Published as: Bagheri G., Bonadonna C., Manzella I., Pontelandolfo P. and Haas P. (2013): Dedicated vertical wind tunnel for the study of sedimentation of non-spherical particles, *Review of Scientific Instruments*, 84(5), 054501.

ticles freely falling in liquids (Marchildon et al., 1964; Willmarth et al., 1964; Christiansen and Barker, 1965; Isaacs and Thodos, 1967; Stringham et al., 1969; List and Schemenauer, 1971; McKay et al., 1988; Gögüs et al., 2001; Tran-Cong et al., 2004; Chow and Adams, 2011). However the measurements of the drag coefficient strongly depend on the nature of particle secondary motions, which are different for different density ratios (Marchildon et al., 1964; Christiansen and Barker, 1965; Jayaweera and Mason, 1965; Isaacs and Thodos, 1967; Stringham et al., 1969; List and Schemenauer, 1971; Komar and Reimers, 1978; Wilson and Huang, 1979; Baba and Komar, 1981; McKay et al., 1988; Gögüs et al., 2001; Tran-Cong et al., 2004; Namkoong et al., 2008; Chow and Adams, 2011; Ern et al., 2012). Besides, it is found that the drag coefficient of particles of any shape at intermediate Reynolds numbers ($1 < Re < 10^4$) is related to values of their drag coefficient at very low ($Re << 1$) and at very high Reynolds numbers ($10^4 < Re < 10^5$) (Ganser, 1993; Loth, 2008). Therefore characterization of drag coefficient of particles at both high Reynolds number and high density ratios can be used either directly or to be used for estimating particle drag coefficient at intermediate Reynolds numbers.

A dedicated vertical wind tunnel has been built at the University of Geneva in collaboration with the Groupe de comptence en mcanique des fluides et procds nergtiques (CMEFE) from the University of Applied Sciences Western Switzerland in Geneva (HES-SO//hepia) (Fig. 2.1) in order to characterize drag coefficient of volcanic particle (i.e. highly irregular particles of various shapes, sizes, densities and porosities). In the following section we first discuss fundamental aspects of forces exerted on the particle when it is freely transported in a fluid and the relationship with the particle orientation. This is followed by the methods available in the literature for the measurements of drag coefficient of particles. Advantages and disadvantages of these methods are discussed along with our motivation of building a vertical wind tunnel. Design parameters of our wind tunnel components are then presented and discussed. Our particle tracking code (PTV) developed to extract the results from the experiments with the wind tunnel is described. Finally, error estimation on our measuring method and the validation of our measurements of some spherical and cylindrical particles is presented.

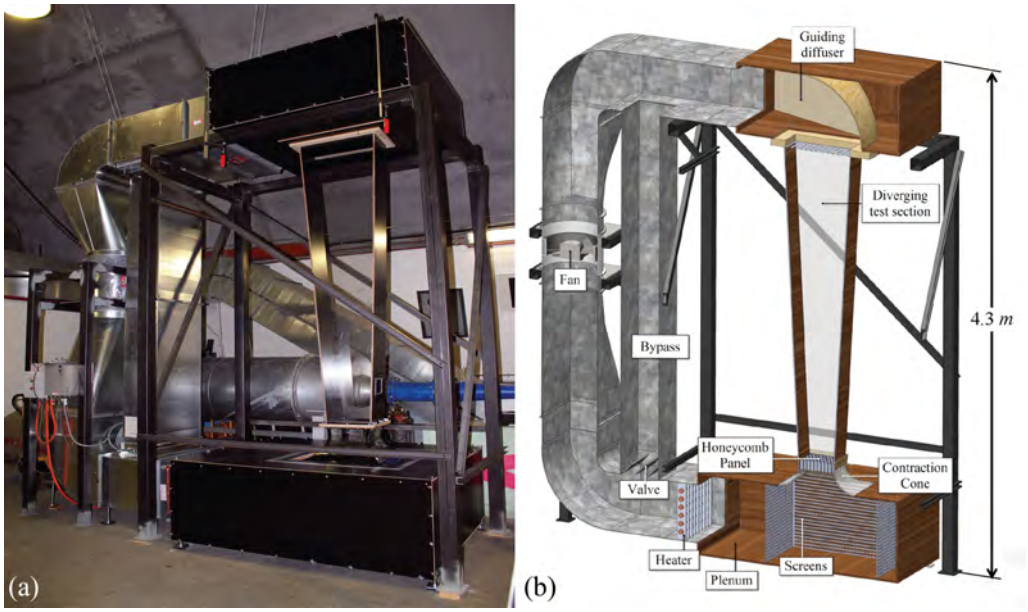

Figure 2.1: (a) Wind tunnel built at the University of Geneva; (b) Schematic of the wind circuit.

2.2 Drag Coefficient

Particle transportation, in most cases, is associated with a fluid flow, with a fall due to gravity, with rising due to buoyancy or with various combinations of these processes. Particles of arbitrary shapes when transported in a fluid experience forces and momentum on all three coordinate axes (White, 1998, p.452). Magnitude of these forces is related to the shape and size of the particle, particle rotation, relative density and velocity of the particle with respect to the fluid, and fluid viscosity. As an example, when a spherical particle translates, without rotation, in a fluid with constant relative velocity the only forces acting on the sphere are buoyancy and drag. Buoyancy is a constant force which acts on the particle in opposite direction to gravity and its magnitude is equal to the weight of the fluid that is displaced by the particle volume. The drag force acts on the opposite direction to the particle motion and its magnitude is much more complex to determine. The drag force is defined as:

$$F_D = \frac{1}{2}\,\rho_f\,C_D\,A\,v_r^2 \tag{2.1}$$

where ρ_f is the fluid density, A is a reference area which is usually chosen to be the particle projected area normal to the direction of particle motion, v_r is the relative

velocity of the particle and C_D is the drag coefficient. The drag coefficient itself is a function of particle Reynolds number, shape and ratio of particle to fluid density. Particle Reynolds number is defined as:

$$Re = \frac{\rho_f \left| v_r \right| d}{\mu_f} \tag{2.2}$$

where μ_f is fluid viscosity and d is a reference length of the particle. In case of smooth spherical particles moving with constant relative velocity in an undistributed and unbounded flow, the drag coefficient is a function of Reynolds number only. Plot of drag coefficient measured in such conditions versus Reynolds number identifies the standard drag coefficient curve (Clift and Gauvin, 1971). For spherical particles numerous experiments are performed in a wide range of Reynolds number(Clift and Gauvin, 1971; Loth, 2008) and various correlations are derived for them with a good level of accuracy, such as the model of Clift and Gauvin (1971) which fits the experimental data with less than 6% error (Clift et al., 2005, p. 111). Unlike spherical particles, determination of drag coefficient of non-spherical particles is very complex and considerable amount of researches are dedicated to this category (Wieselsberger, 1922; Marchildon et al., 1964; Willmarth et al., 1964; Christiansen and Barker, 1965; Jayaweera and Mason, 1965; Isaacs and Thodos, 1967; Stringham et al., 1969; List and Schemenauer, 1971; Komar and Reimers, 1978; Wilson and Huang, 1979; Baba and Komar, 1981; McKay et al., 1988; Haider and Levenspiel, 1989; Ganser, 1993; Cheng, 1997; Gögüs et al., 2001; Tran-Cong et al., 2004; Dellino et al., 2005; Hölzer and Sommerfeld, 2008; Chow and Adams, 2011; Ren et al., 2011).

Non-spherical particles can have either regular or irregular shapes. Regular particles are characterized by known geometrical shapes, such as circular cylinders, square cylinders, disks and prisms. Irregular particles exist in many natural and industrial processes such as tephra transport in volcanic eruptions (Alfano et al., 2011), sedimentation in riverbeds (Briggs, 1962), mineral processing and chemical blending (Tran-Cong et al., 2004). There are several issues in the determination of the drag force of non-spherical particles. The first issue is the lack of a shape descriptor which can relate the drag coefficient of the particle to its shape. Many studies use sphericity (Wadell, 1933) as a shape descriptor to correlate shape of non-

spherical particles to their drag coefficients (Haider and Levenspiel, 1989; Ganser, 1993; Hölzer and Sommerfeld, 2008; Chhabra et al., 1999). However, beside issues of measuring and constraining sphericity of irregular particles (Alfano et al., 2011), McKay et al. (1988) found that although elongated cylinders have same value of sphericity as disks, their values of drag coefficients are very different. Another issue on the measurement of drag coefficient of irregular particles is due to their secondary motion when they are freely transported in a fluid (Marchildon et al., 1964; Willmarth et al., 1964; Christiansen and Barker, 1965; Jayaweera and Mason, 1965; Isaacs and Thodos, 1967; Stringham et al., 1969; List and Schemenauer, 1971; Komar and Reimers, 1978; Wilson and Huang, 1979; Baba and Komar, 1981; McKay et al., 1988; Gögüs et al., 2001; Tran-Cong et al., 2004; Namkoong et al., 2008; Chow and Adams, 2011; Ern et al., 2012). Secondary motions have significant effect on the drag coefficient of the particles in the direction of their primary motion (Marchildon et al., 1964; Christiansen and Barker, 1965; Isaacs and Thodos, 1967; Stringham et al., 1969; List and Schemenauer, 1971; Namkoong et al., 2008; Chow and Adams, 2011).

2.2.1 Secondary motions of particles

Different types of particle secondary motion are reported for different particle shapes, ranging from small oscillation and rotation to tumbling and chaotic motions (Marchildon et al., 1964; Willmarth et al., 1964; Christiansen and Barker, 1965; Jayaweera and Mason, 1965; Isaacs and Thodos, 1967; Stringham et al., 1969; List and Schemenauer, 1971; Komar and Reimers, 1978; Wilson and Huang, 1979; Baba and Komar, 1981; McKay et al., 1988; Gögüs et al., 2001; Tran-Cong et al., 2004; Namkoong et al., 2008; Chow and Adams, 2011; Ern et al., 2012). Two main sources are known to be responsible for secondary motions of particles. The first source is the way that hydrodynamical forces and torques evolve when particle degrees of freedom change. Variation in particle state of equilibrium results in the variation of pressure and velocity fields around the particle which may help the particle to roll back to its previous state of equilibrium or may force the particle into a new equilibrium or unsteady conditions. The second source is the wake instability which occurs behind

the body beyond a critical Reynolds number even if the body moves with a constant velocity and orientation. Wake instability changes the exerted vortical force and torque on the body which changes the body motion and eventually leads to a new equilibrium state in the body/fluid system. Even in case of axisymmetric bodies, when the wake behind the body loses its symmetry due to instability, an asymmetric load is produced which makes the body rotate and move sideways (Ern et al., 2012).

Secondary motions are related to particle shape, Reynolds number and the ratio of particle to fluid density, $S = \rho_p/\rho_f$. Recently it is found that secondary motion not only exists in case of freely moving non-spherical particles, but also in case of spheres (Veldhuis and Biesheuvel, 2007; Ern et al., 2012). Secondary motions received more attention in case of non-spherical particles because they can affect the drag coefficient considerably. Reynolds number is also an important factor on the secondary motion of particles. Studies on non-spherical particles show that for most shapes when the Reynolds number exceeds value of $\sim 100 - 300$, secondary motions start (Marchildon et al., 1964; Willmarth et al., 1964; Christiansen and Barker, 1965; Isaacs and Thodos, 1967; Stringham et al., 1969; List and Schemenauer, 1971; Tran-Cong et al., 2004). Increasing Reynolds number changes the type of secondary motions from small oscillations and rotation to tumbling and chaotic motion. Finally, the last parameter affecting secondary motion of the particle is the density ratio, S. It is found that for non-spherical particles increasing density ratio increases secondary motions of particles which leads to a lower value of drag coefficient (Marchildon et al., 1964; Christiansen and Barker, 1965; Isaacs and Thodos, 1967; Chow and Adams, 2011; Clift et al., 2005).

2.2.2 Strategies for the measurement of particle drag coefficient

Experimental strategies represent the most accessible way to investigate the drag force of non-spherical particles freely moving in fluids. Numerical methods, on the other hand, can be performed on very basic cases, such as two-dimensional simulation of a falling cylinder (Namkoong et al., 2008). Experimental studies available in the literature mostly focus on the measurement of drag coefficient of freely falling

particles of regular shapes and, in particular, of circular cylinders of various aspect ratios, $E = L/d$ (Marchildon et al., 1964; Willmarth et al., 1964; Christiansen and Barker, 1965; Isaacs and Thodos, 1967; Stringham et al., 1969; List and Schemenauer, 1971; McKay et al., 1988; Gögüs et al., 2001; Tran-Cong et al., 2004; Chow and Adams, 2011). In these experiments the velocity of a particle released from the top of a vertical column filled with a fluid, mostly water-based mixtures, is measured at the bottom of the column by means of optical methods when the particle reaches to a non-accelerating state. Velocity of the particle in this state is called terminal velocity, which is a constant value since the relative acceleration of particle is zero. Relative acceleration is the acceleration calculated from relative velocity of the particle and differs from particle absolute acceleration when the fluid acceleration is not zero. Zero relative acceleration is one of the conditions mentioned earlier necessary for producing standard drag coefficient curves. Previous studies (Clift and Gauvin, 1971; Marchildon et al., 1964; Clift et al., 2005) (Wang, 1970) 1970) indicate that measured drag coefficient of accelerating or decelerating particles are different than those measured in standard conditions. Since methods of free-fall column need a column of a certain height in order for particles to reach the state of zero relative acceleration, most researchers used liquids (e.g. water and mixtures of water-glycerin) so that a particle reaches zero relative acceleration in much lower heights compared to gas filled columns. For example, a spherical particle with diameter of 1 cm and density of $2700\,\mathrm{kg\,m^3}$ needs an air-filled column of at least 130 m in order to reach 99% of its terminal velocity ($Re \approx 1.6 \times 10^4$). The same particle would reach the terminal velocity in water after 16 cm ($Re \approx 8.2 \times 10^3$).

Although liquids provide the possibility to measure drag coefficient of particles in a wide range of Reynolds number, they limit the experiments at very low values of density ratios. Effect of density ratio, as mentioned previously has a significant effect on the secondary motion of particle and on the drag coefficient. In previous studies which used falling columns filled with liquids to measure the drag coefficient of solid particles, density ratio ranged from 0.74 to 11.7 (Marchildon et al., 1964; Isaacs and Thodos, 1967; Chow and Adams, 2011). Some studies measured drag coefficient of particles in the air but in very low Reynolds numbers (< 100) due to small height of

falling columns, e.g. Wilson and Huang (1979). The exception is the experiments of Christiansen and Barker (1965) who used a 140 m high smokestack to measure terminal velocity of spherical and cylindrical particles in the air at high Reynolds numbers ($Re \approx 8 \times 10^4$). Although Christiansen and Barker (1965) extended the range of drag coefficient measurement to both high Reynolds numbers and high density ratios ($S \approx 2880$), only drag coefficient of cylinders with aspect ratio of 1.75 and of one disk with aspect ratio of 0.225 were measured.

Falling column method is really limited to measuring drag coefficient of particles with high density ratios and high Reynolds numbers since it requires very tall columns. The other method is to use vertical wind tunnels which can suspend particles in their calibrated vertical test section. Vertical wind tunnels with open or closed circuits were mostly used to measure terminal velocity of water droplets and to study their internal circulation and freezing behavior in meteorology (Beard and Pruppacher, 1969; Pruppacher and Beard, 1970; Spengler and Gokhale, 1972; Pitter and Pruppacher, 1973; Stow and Woodward, 1974; Kamra et al., 1985; von Blohn et al., 2005). In this method water droplets are released in the center of tunnel test section where the drag flow exerted by the upward air flow counterbalance droplet weight and result in free suspension of water droplets. By pre-calibration of the air flow, value of air velocity is known at the droplet stabilization point which is equal to terminal velocity of the droplet. In some wind tunnels air velocity profile in the test section is shaped to be lower at the center (Spengler and Gokhale, 1972; Stow and Woodward, 1974; Kamra et al., 1991). Shaping of velocity profile is done by using different combination of honeycombs and screens, and minimizes secondary motion of droplets which helps stabilize them in the center of test section. In addition to water droplets there are some studies which used vertical wind tunnels to suspend solid particles, such as agricultural seeds (Tabak and Wolf, 1998; Jongejans and Schippers, 1999) and firebrands.(Knight, 2001; Ellis, 2000). However a systematic way of measuring drag coefficient has not yet been achieved.

A vertical wind tunnel represents the only solution for the measurements of drag coefficient of highly irregular volcanic particles in air at high particle Reynolds numbers. Therefore a dedicated vertical wind tunnel was built at the University of

Geneva in collaboration with the fluid mechanics group Groupe de comptence en mcanique des fluides et procds nergtiques (CMEFE) from the University of Applied Sciences Western Switzerland in Geneva (HES-SO//hepia) (2.1). The wind tunnel was designed and calibrated to measure drag coefficient of freely suspended non-spherical solid particles.

2.3 Wind Tunnel Design and Components

A maximal wind tunnel height of 4 m was allowed due to logistic reasons. Two plenums made of 15 mm thick wood are used to decrease the turbulence intensity in the tunnel circuit, one before the contraction cone and the second at the top of the diverging test section. The diverging test section is bi-dimensional and opens with a total angle of 6° (3° on each side) with two 10 mm thick plexiglass walls at back and front, and two side walls made of wood. Height of the test section is 2.7 m with minimum cross-section area of 0.31 m × 0.30 m at the bottom which increases to 0.59 m × 0.30 m at the top. A few doors at different heights on one of the test section walls have been built for inserting and removing particles. Based on the suggestion of Barlow et al. (1999) the divergence angle is small enough to avoid separation at the walls. However, to explore possibility of having separation points, tufts were taped to both side walls of the test section and no sign of separation was observed. Velocity of air flow decreases along the test section due to the increase in the cross-section area. The velocity decrease is essential for the investigation of suspension of particles at high Reynolds numbers and particle to fluid density ratios, for which due to particle secondary motion, the suspension velocity is not constant. The relation between the wind tunnel circuit head loss and the flow volume has been calculated using the head loss tables reported by I.E. Idel'cik (1986). The head loss given by all circuit components, including honeycombs and grids, was added together to determine the total head loss of the wind tunnel circuit. This result leads to the selection of a high-pressure axial blower able to give 1625 Pa pressure difference for a flow volume of 15 000 $m^3\,h^{-1}$, which is powered by a 15 kW asynchronous electrical motor controlled by a variable frequency drive. A heat exchanger and a chiller are also

installed at the upstream plenum ducts so to be able to control the air temperature. The radiator fins have positive effects on the laminarization of the flow before the test section. Plenum and screens installed at the bottom provide a homogeneous environment to distribute uniformly and equally the air flow between different sides of the contraction cone. A contraction cone (Fig. 2.2) is used to increase flow speed by decreasing area and to produce a uniform velocity profile and decreasing turbulence intensity. Ratio of the area at the cone inlet to its area at the outlet (contraction ratio) is 6.25. A wooden guiding diffuser at the top plenum channels the air flow from outlet of the test section to the fan inlet and reduces the flow turbulence. The wind tunnel at its current set up (high-velocity set-up) can reach velocities between 5 and 27 $\mathrm{m\,s^{-1}}$ and, therefore, we can suspend volcanic particles between 10 and 40 mm ($5 \times 10^3 < Re < 8 \times 10^4$, $500\,\mathrm{kg\,m^{-3}} < \rho_P < 2700\,\mathrm{kg\,m^{-3}}$). Velocities lower than $5\,\mathrm{m\,s^{-1}}$ can be obtained when tissue filters are added at the entrance of the diverging test section in addition to using the bypass channel.

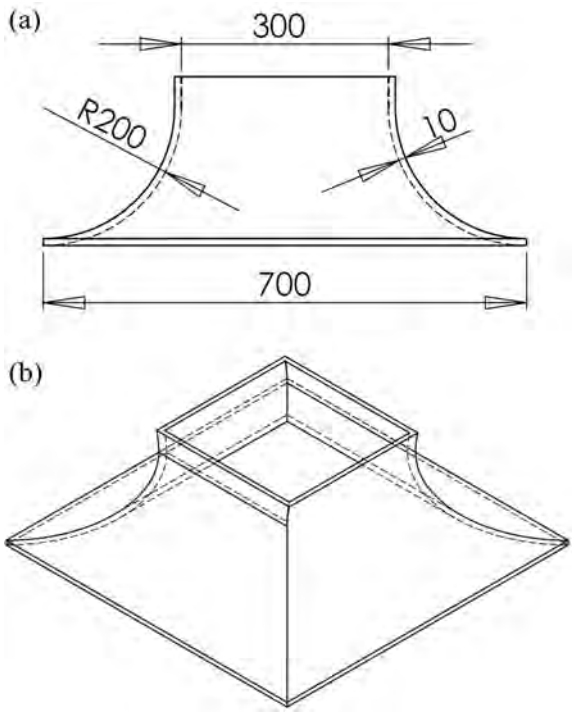

Figure 2.2: Circular contraction cone with square section; (a) front view, dimensions are in mm; (b) perspective view.

2.3.1 Airflow in the Diverging Test Section

Previous works show that a curved velocity profile with the minimum at the center helps the stabilization of droplets (Spengler and Gokhale, 1972; Stow and Wood-

ward, 1974; Kamra et al., 1991). However, Knight (2001) reported that these velocity profiles do not stabilize non-spherical particles, which, due to secondary motions, frequently collide with test section walls. The effects of velocity profiles on particle suspension in our wind tunnel were investigated. A combination of honeycomb, screens and drinking straws were used to shape the velocity profile to be lower at the center of test section. It was found that the collision of spherical particles with test section walls was significantly reduced. However in case of non-spherical particles no improvement was achieved except for light polyfoam pyramids, which suspended stably at the center of test section with their apex downward. Therefore, we decided not to use velocity-profile shapers and to create a flat velocity profile in the test section. Air velocity in the test section is calibrated with a Prandtl pitot tube and two micromanometers. One of the micromanometers measured the static pressure difference between the bottom of plenum and the outlet of contraction cone as a reference pressure, δP_{ref}, while the other micromanometer measured the dynamic pressure of airflow, $\rho_f \, v_f^2/2$, from a pitot tube installed in the test section. Since the experiment setup was limited to height of the light source (see Fig. 2.3) the test section has been calibrated up to the height of 1 m in three horizontal planes of 0.1 m, 0.5 m and 1.0 m. A linear correlation with $R^2 = 0.999$ has been found between the reference pressure and dynamic pressure in each calibration planes, which is used to calculate air velocity in the cropped area (see Fig. 2.3):

$$v_f = \sqrt{2\,\delta P_{ref}\,(0.1041\,y^2 - 0.3584\,y + 0.7816)\,/\rho_f} \tag{2.3}$$

This correlation allows us to calculate the expected air velocity within the calibrated area only by measuring the reference pressure. Boundary layer thickness, measured with Pitot tube, varies from 1 cm at bottom of test section to 4 cm at height of 1.5 m.

2.3.2 Experimental Setup

Fig. 2.3 shows a schematic representation of the experimental setup. In each experiment an individual particle was suspended inside the test section while being filmed with a monochrome Phantom v10 high speed camera. The camera is placed 3 m

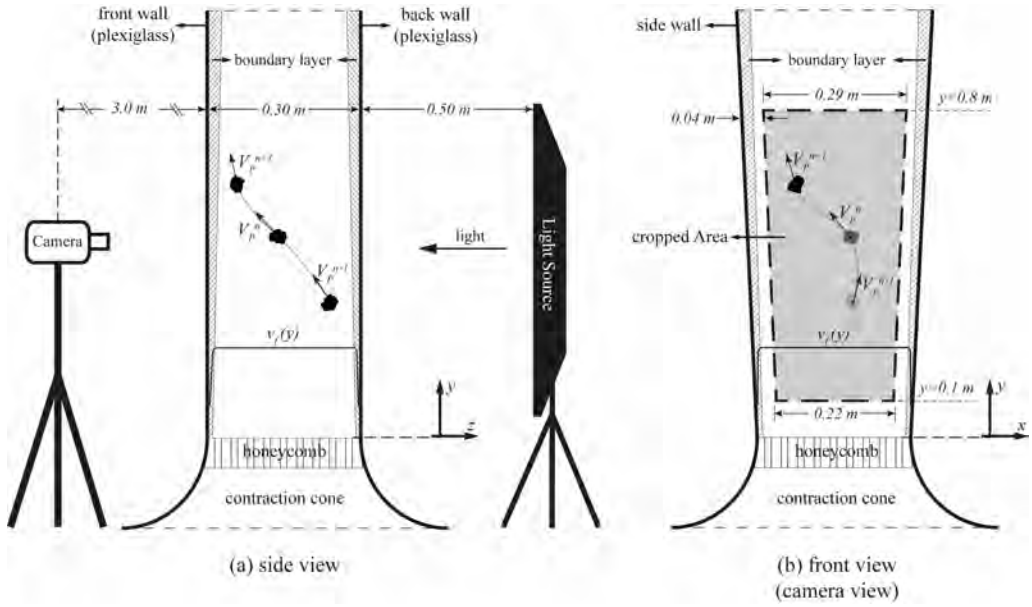

Figure 2.3: Schematic of experimental setup. The shadow image of one irregular particle inside the test section is sketched in three successive recording frames. The particle projected area and shape vary in different views and frames since the particle is irregular; (a) side view (yz plane); (b) front view (xy plane) which is the camera view with z being perspective direction of the camera.

away from the wind tunnel and the lens is focused at the center of the test section. The camera lens is AF Micro-Nikkor 60 mm $f/2.8D$ which produces low distortion images. Camera depth of field is wide enough to cover the whole regions of the divergence in the z direction. The particle is backlit with a high frequency light source with 8 fluorescent tubes and the camera records shadow image of the particle for time periods between two and three minutes with the frequency of 25 fps. A paper diffuser is attached to the back wall of test section to create a homogeneous backlight. In Fig. 2.3, a particle is shown in different time frames denoted by superscript n. The particle moves with velocity equal to at time t, while at time $t-dt$ its velocity is and in time $t+dt$ is where dt ($= 0.04$ s) is the time difference between successive frames. Note that particle projected area and shape change in different views and frames since the particle shape is irregular. Proper positioning of the light source leads to having different mean gray values (MGV) on the shadow image of the particle based on their position in the z direction (see Fig. 2.3b). The closer the particle to the front wall the lower the MGV of the particle (darker shadow) and vice versa. Variation of particle MGV allows us to determine the approximate

position of the particle in the z direction which will be disused later on the filters used in the PTV code. IV. Particle tracking velocimetry (PTV) code The equation of particle motion in a fluid at very low Reynolds numbers (< 1) is presented by Maxey and Riley (1983) and proved by Mordant and Pinton (2000) to be valid also for particles moving at high Reynolds numbers (up to $\sim 10^4$). Based on the fact that the flow is incompressible in our test section ($M < 0.1$) and assuming the fluid velocity is steady and its components in x and z direction are zero, the equation of particle motion in the y direction reduces to:

$$m_P\, a_P = -\left(m_P - m_f\right) g + m_f\, v_f \frac{dv_f}{dy} + \frac{1}{2}\,\rho_f\, A\, C_D\, |v_r|\, v_r + F_{added\,mass} + F_{Basset} \quad (2.4)$$

where m_P is the particle mass, a_P is the absolute acceleration of the particle in the y direction, m_f is the fluid mass displaced by the particle ($\rho_f\, m_P/\rho_P$) and v_r ($= v_f - v_P$) is the relative speed of fluid with respect to the particle in the y direction. $F_{added\,mass}$ and F_{Basset} are functions of the particle relative acceleration, a_r. These forces are negligible for high density ratios and high Reynolds numbers (Clift et al., 2005), so we neglect them in our calculations. In order to produce standard drag coefficient curves, variables in Eq. 2.4 need to be measured accurately. The air density and viscosity can be calculated with classic thermodynamic correlations from values logged by installed sensors in the test section measuring pressure, temperature and relative humidity. By knowing air density, air velocity can be simply calculated at the particle position using Eq. 2.3.

To measure particle absolute velocity, v_P, absolute acceleration, a_P, and relative acceleration, a_r, a particle tracking velocimetry (PTV) code is developed. The PTV code, written in FORTRAN language, analyzes the data file extracted from an image analysis program, the data logged by sensors during the experiment and the particle physical and geometrical properties (e.g. mass, density and shape parameters) in order to calculate drag coefficient of the particle from Eq. 2.4. In order to provide the input data for the code, movies recorded during experiments are converted frame by frame to 8-bit TIFF format. Images are then cropped as shown in Fig. 2.3b, so only the area which is outside of side walls boundary layer is used by the PTV code. A filter based on particle image MGV is developed to assure that analysis are only

made on particle outside of the flow boundary layers that form near both the front and back walls. Software ImageJ (Schneider et al., 2012) is then used to analyze the cropped images and to extract a table of the particle centroid coordinates in each frame in addition to some other factors, such as the particle area, perimeter, size of bounding box and MGV. Images where the particle was on the border of cropped area are excluded by ImageJ automatically.

The PTV code calculates particle absolute velocity, v_P, absolute acceleration, a_P, and relative acceleration, a_r, using three-frame polynomial fit of second order (Joe D. Hoffman and Steven Frankel, 2001). Polynomial and spline fitting is especially important to reduce errors on velocity measurements when the tracked particle moves with acceleration (LÜTHI et al., 2005; Feng et al., 2011). A test on the movement of a pendulum in air is set up to examine possible effects of camera recording speed on the amplification of numerical noise resulted from using fitting formulas. Maximum velocity of the pendulum was $1\,\mathrm{m\,s^{-1}}$, which is in the same order of particle absolute velocity in the wind tunnel. Ratio of pendulum area to camera field of view was also in the same order to that of particles in wind tunnel experiments (1.14 pixel/mm). The pendulum test is captured and analyzed in various camera speed frequencies including 25, 50, 100, 200 fps. It is found that recording speed higher than 25 fps can result in significant amplification of numerical noise especially in the calculation of acceleration value (Fig. 2.4). Therefore all movies are recorded with speed of 25 fps.

Two sets of filters are defined in the particle tracking code: acceleration filter and shadow filter. Acceleration filter is used to exclude the frames where the magnitude of relative and absolute acceleration of the particle is greater than $0.05 \times g$. This filter assures that the results have the required conditions of standard drag coefficient curves. The shadow filter is used to exclude the frames where the particle is near the front and back walls of the test section. In near wall regions the air velocity is not known due to formation of flow boundary layers, and, therefore, the drag coefficient cannot be calculated.

To calibrate the shadow filter, MGV of some selected particles of different shapes and sizes in different places of the cropped area and different perspective positions

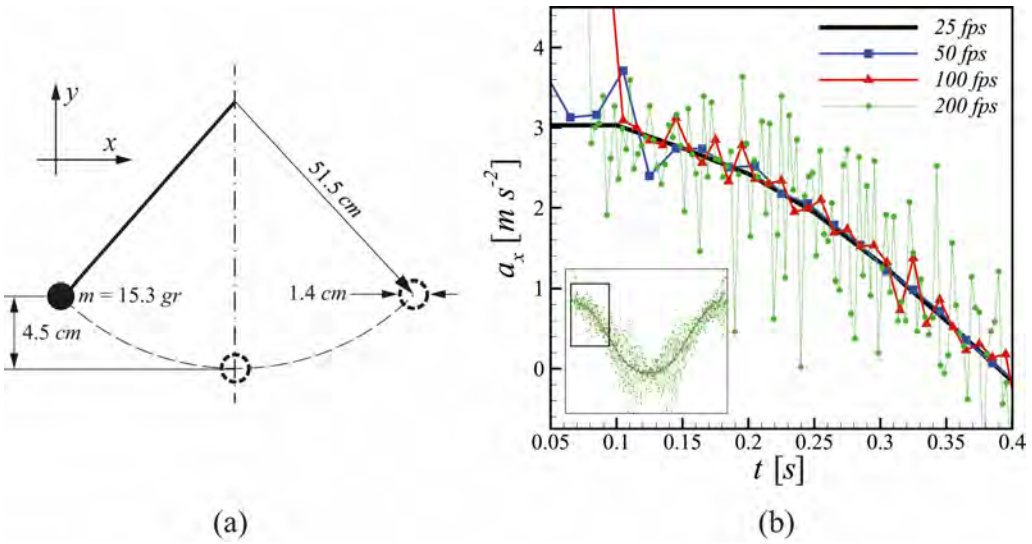

Figure 2.4: (a) Schematic of the pendulum experiment setup; (b) Acceleration of pendulum in x direction calculated with the PTV code from movies recorded with recording speeds between 25 and 200 fps. The results show that increasing recording speed leads to the amplification of numerical noise in the calculation of the pendulum acceleration especially when the pendulum speed is small ($t < 0.15s$).

are measured. The cropped area is divided into three vertical and three horizontal intervals which leads to having 9 grid zones. Then each selected particle is kept fixed in the middle of grid zones in the xy plane and in three positions in perspective direction, i.e. attached to the front wall, center and attached to the back wall. It is found that the minimum gray value, MGV_{min}, occurred when the particle was attached to the front wall, and the maximum gray value, MGV_{max}, are measured when the particle is attached to the back wall. The calibration experiments suggested that if the MGV of the particle in zone i is greater than $1.4 \times MGV_{min}|_i$ and is less than $0.85 \times MGV_{max}|_i$, the particle is in the center of the test section in perspective direction. In the experiments, however, it is not possible to pre-calibrate MGV_{min} and MGV_{max} of each single particle in all grid zones. Therefore, MGV_{min} and MGV_{max} are approximated after the experiment by analyzing distribution of particle MGV during its suspension in the wind tunnel and assuming that MGV_{min} and MGV_{max} of the particle in each grid zone occurred when the particle was near back and front walls of the test section in that grid zone. In Eq. 2.1 and 2.4, A can be any reference area of the particle. However, drag coefficient of bluff bodies in high Reynolds number is mainly pressure drag which is affected by the cross-sectional or projected area, $A_{projected}$, of the particle. In addition to drag coefficient,

knowing the projected area helps us to understand better the secondary motion of particles and the existence of preferred orientations and their effects on the particle drag coefficient. Installing a second camera and another backlight source in the test section could be a solution. However, some drawbacks are identified: 1) extra cost associated with acquisition of a second camera, 2) increase of data preparation time associated with synchronization of all devices, 3) generation of high level turbulence and unsteadiness of airflow related to the fact that either the camera or the light source should be positioned upstream.

A more convenient solution for measuring particle projected area, $A_{projected}$, is to use computer vision algorithms. In this method, a database of particle image in two perpendicular views, e.g. front and top, is needed for each particle. 3D-model of particles scanned by a 3D-Scanner are used to create a database of particle image in 500 random orientations and in two front and top views (result in total 1000 images). The 3D-models were originally created for measuring shape parameters of the particle and correlating them to their measured drag coefficients. The random-orientation database then is analyzed by ImageJ to extract various factors of particle image, such as area, perimeter, Ferets diameter and angle of major axis in each orientation. Finally, the PTV code uses the results of database analysis to find the closest match between particle image in the wind tunnel experiments and the database by comparing different factors such as area, angle of major axis, circularity and aspect ratio (e.g. Fig. 2.5).

Besides calculating the particle drag coefficient experimentally, the PTV code uses random-orientation database and particle 3D-model to calculate various shape descriptors introduced by previous researchers (e.g. circularity, Corey shape factor, sphericity) and calculates the particle drag coefficient in a condition similar to that of the wind tunnel (e.g. similar air density and viscosity) with both known spherical and non-spherical models (e.g. models of Clift and Gauvin (1971) , Wilson and Huang (1979) and Ganser (1993)). This leads to having a database of the particle shape descriptors and estimation of various models for each single particle that can be used for future investigations.

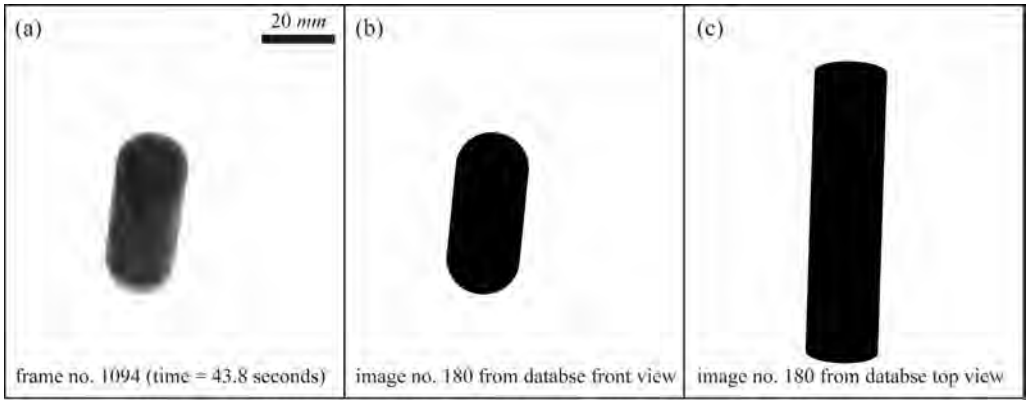

Figure 2.5: Computer vision algorithms are used to calculate particle projection area from a random-orientation database of the particle; (a) shadow image of the particle C3 (see Table 2.1) recorded by the camera during its suspension in the wind tunnel test section; (b) the closest image to particle shadow image (a) found by the PTV code from 500 images in the random-orientation database of particle C3; (c) top view of image (b) in the database of particle C3 whose area is used as the projected area, Aprojected, of particle C3 of image (a).

2.4 Estimation of Errors

In order to estimate the errors in the calculation of drag coefficients, the standard deviation of variables used in Eq. 2.4 should be known. Air velocity is calculated by Eq. 2.3 with maximum standard deviation of 2% including fitting and repeatability errors. Validity of air velocity measurements are verified by using various flow measurement units, such as micromanometer, precision pitot tubes and fan anemometers.

Centroid position of a particle is measured with ImageJ by pre-setting particle shadow threshold in order to segment particle boundaries from background. Due to the light scattering, particle shadow has soft edges and it may result into measuring lower projection area in some frames. The area reduction is almost uniform with mean of 15% and standard deviation of 5%. However, the area reduction is uniform around the perimeter of a particle shadow and should not affect the measured position of the particle centroid. The error associated with the polynomial fit in the calculation of particle acceleration and velocity cannot be estimated explicitly but they are likely negligible since their accuracies are in the order of dt or dt^2. Due to the lens perspective effects, an uncertainty on the particle position in the y direction exists. To measure this uncertainty some guidelines are inserted in the test

section at various heights and their height deviations at their ends are measured. The measurements showed that this uncertainty can result into a maximum error of 0.3% when calculating v_f at the particle position. The error on the particle absolute velocity and acceleration resulted from lens perspective effects are investigated statistically by assuming that the distribution of particle velocity in the z direction is similar to the distribution of u_p. The average error is 3% for velocity and 7% for acceleration calculations.

Effects of wall on the particle suspension velocity, on the other hand, should be investigated more in detail. Previous studies showed that measured suspension velocity of particles in bounded mediums is lower than those measured in unbounded mediums (Latto et al., 1973; Achenbach, 1972; Okuda, 1975; Awbi and Tan, 1981; Bougas and Stamatoudis, 1993; Chhabra, 1996; Arsenijević et al., 2010). This reduction in high Reynolds numbers is a function of particle cross-section area to cross section area of the suspension column, $\lambda = A_P/A_c$. Awbi and Tan (1981) measured drag coefficients of spheres in the range of λ greater than 0.06 in a square cross section wind tunnel and Reynolds number between 10^4 and 2×10^5. Comparisons of standard drag coefficient of spheres and those measured by Awbi and Tan (1981) show that the wall effect is negligible for λ of 0.06 and it becomes more considerable as λ increases. In the case of our experiments, however, λ is less than 0.03 ($80\,mm^2 < A_P < 3000\,mm^2, 0.09\,m^2 < A_c < 0.11\,m^2$) and wall effects on the suspension velocity and drag coefficient is completely negligible.

Our method of calculating particle projected area is benchmarked by creating images of a particle from a random-orientation database with same scaling ratio as the real experiments and estimating the particle projected area using another random-orientation database of the same particle. A Gaussian distributed random noise with mean of 15% and standard deviation of 5% is added to the scaled database in order to synthetically create inhomogeneity in the projected image of the particles. This allows us to investigate on the effects of lens distortion and area reduction resulted from particle shadow thresholding. The benchmarks showed that our computer vision algorithm can estimate projected area of regular particles with the average error of 3% (median error of 0.7%) and 8% for irregular particles (median error of

7%). This shows that our method is reliable and precise in case of regular particles while in case of irregular particles it has an acceptable accuracy, i.e. the results are accurate enough for studying secondary motions of particles and their preferred orientations but uncertainties may exist on the value of projected area. However, it is common to calculate drag coefficients of irregular particles based on the projected area of volume-equivalent sphere of the particle as the reference area. As a result, in case of irregular particles, we will statistically investigate the preferred orientations of the particle to assess the most likely projected area.

2.5 Validation

To check the validity of wind tunnel calibration and PTV code, drag coefficient of some spherical and cylindrical particles are measured. Physical properties of the particles and wind tunnel conditions are listed in Table 2.1. Spherical and cylindrical particles are chosen for the validation of our experimental set up since several studies exist on drag coefficient of particles of these shapes.

Table 2.1: Properties of the particles used in our experiments and air in the wind tunnel.

ID	Shape	d [cm]	L [cm]	ρ_P [kg m^{-3}]	ρ_f [kg m^{-3}]	$\mu \times 10^5$ [Pa s]
S1	sphere	3.1	–	766	1.12	1.88
S2	sphere	3.9	–	403	1.14	1.86
S3	sphere	3.9	–	82	1.15	1.84
S4	sphere	6.0	–	25	1.15	1.85
S5	sphere	6.2	–	148	1.15	1.85
C1	cylinder	2.0	2.1	636	1.13	1.87
C2	cylinder	2.0	4.7	650	1.13	1.87
C3	cylinder	2.0	8.0	643	1.12	1.88

Fig. 2.6 shows measured values of relative velocity of particle S5 and particle C2 resulted from the PTV code. Standard deviation of measured relative velocity before applying filters for Particle S5 is $0.34\,\mathrm{m\,s^{-1}}$, which reduces to $0.26\,\mathrm{m\,s^{-1}}$ after applying filters. For particle C2 these values are $0.57\,\mathrm{m\,s^{-1}}$ and $0.53\,\mathrm{m\,s^{-1}}$ respectively. By applying the filters, data range is reduced from $2.0\,\mathrm{m\,s^{-1}}$ to $1.1\,\mathrm{m\,s^{-1}}$ and from $3.5\,\mathrm{m\,s^{-1}}$ to $2.4\,\mathrm{m\,s^{-1}}$ for particle S5 and particle C2, respectively. Experiments

on each particle are repeated at least three times to check repeatability of measurements. Two of the experiments are performed in a same reference pressure and the third one in a different reference pressure. Average of relative standard deviation of the measured drag coefficient between repeated experiments of all particles is 1.7% with the maximum of 2.0%.

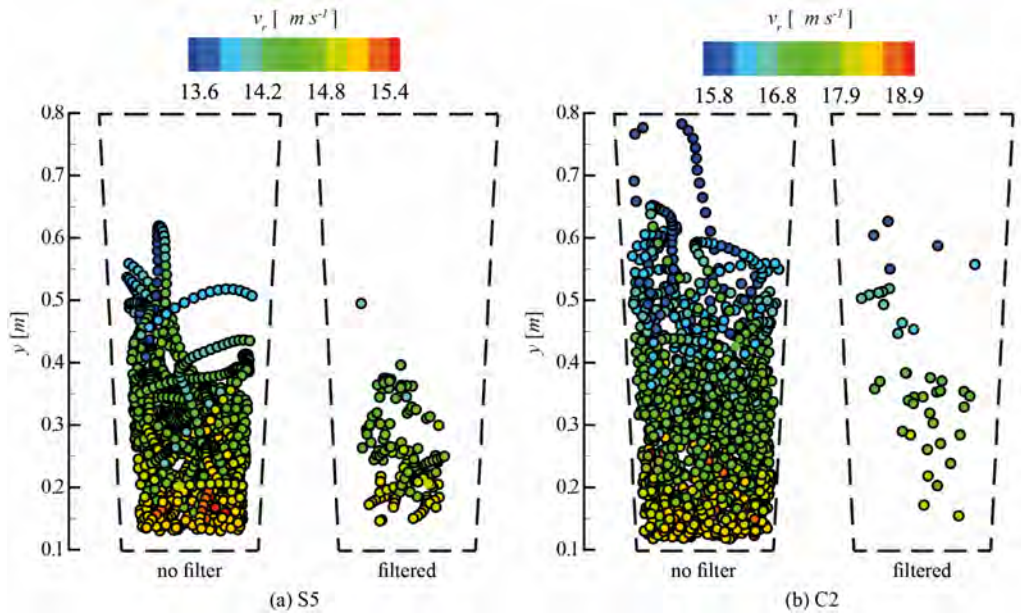

Figure 2.6: Relative velocity, v_r, of particles calculated by the PTV code before and after applying shadow and acceleration filters. (a) Relative velocity of particle S5 (standard deviation and range are 0.34 m s^{-1} and 2.0 m s^{-1} before applying filters, and 0.26 m s^{-1} and 1.1 m s^{-1}, after applying filters); (b) relative velocity of particle C2 (standard deviation and range are 0.57 m s^{-1} and 3.5 m s^{-1} before applying filters, and 0.53 m s^{-1} and 2.4 m s^{-1}, after applying filters).

A comparison of measured drag coefficient of spherical particles in the wind tunnel with those reported in the literature (Clift and Gauvin, 1971; Christiansen and Barker, 1965; Schlighting, 1968; Achenbach, 1972) is presented in Fig. 2.7. Average deviation of mean of measured velocity and drag coefficient in our wind tunnel with respect to model of Clift and Gauvin (1971) is 1.8% and 3.6%, respectively, which shows the accuracy of wind tunnel calibration and reliability of the measurements.

Drag coefficients of cylindrical particles measured in the wind tunnel is also compared with previous studies (Fig. 2.8), i.e. data of Wieselsberger (1922) based on experiments on fixed cylinders with two free ends in a wind tunnel, data of freely falling cylinders in water by Isaacs and Thodos (1967) and cylinders freely falling in air by Christiansen and Barker (1965). It can be seen from Fig. 8 that the drag

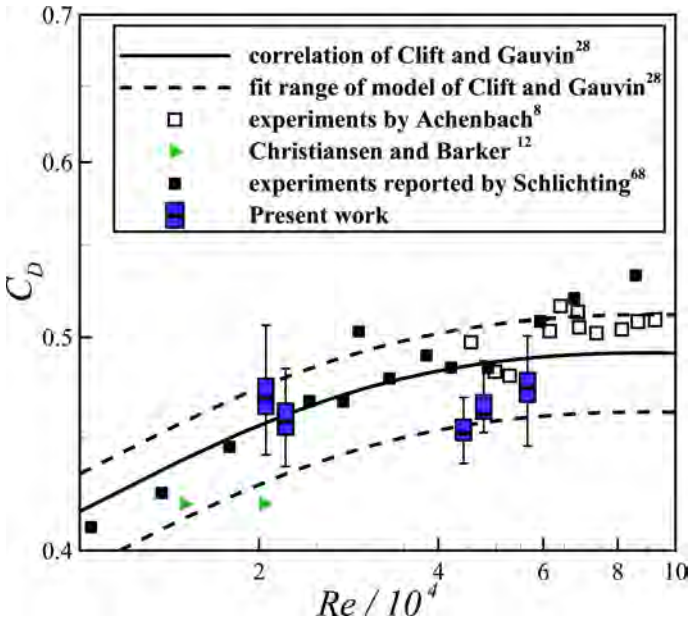

Figure 2.7: Comparison of drag coefficient of spherical particles measured in the present study with those reported in literature. The measurements of the present work are shown by boxplots: the ends of the bars represent the smallest and the largest measurements, the box thickness indicates the first and the third quartiles and the horizontal line is the median (second quartile) of the measurement.

coefficient of long cylinders (two-dimensional) is considerably higher than for short cylinders (three-dimensional), which shows that the flow around cylinders with finite aspect ratio is completely three dimensional and cannot be approximated by measurements on two dimensional (long) cylinders. In addition to that, drag coefficients of cylinders with finite aspect ratio fixed in a wind tunnel and freely falling cylinders in water are higher than those measured by Christiansen and Barker (1965) and our wind tunnel. This shows, first, that the secondary motions of particles during their suspension in a fluid decrease their drag coefficient compared with when they are fixed in a wind tunnel. Second, the effect of density ratio is very important on the measured drag coefficient. Drag coefficients measured in air (high S) are lower ($\sim 30\%$) than those measured in water (low S). This is similar to findings of previous studies which indicated that higher density ratios result into having lower drag coefficients for freely suspended particles (Marchildon et al., 1964; Christiansen and Barker, 1965; Isaacs and Thodos, 1967; Chow and Adams, 2011; Clift et al., 2005).

Chow and Adams (2011) investigated the effect of cylinder density ratio and aspect ratio on its drag coefficient and provided an approximate analytic solution for estimating drag coefficient of cylindrical particles in high $\sqrt{S/E}$ values. They approximated that the distribution of pressure force exerted on cylinders in free fall is similar to that measured by Fage and Johansen (1927) on a fixed inclined flat plate. Then by approximating oscillation angle of a cylinder during its fall,

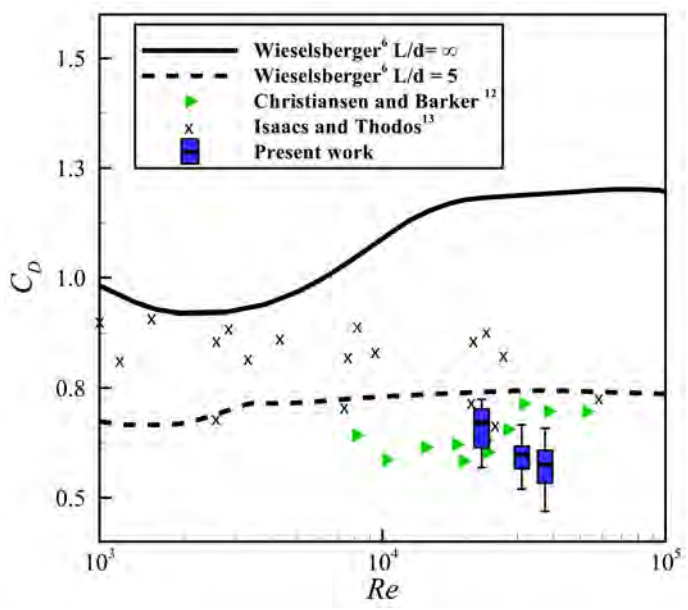

Figure 2.8: Comparison of drag coefficient of cylindrical particles measured in the present study with those reported in literature using $L\,d$ as A in the calculation of drag coefficient; Wieselsberger (1922) results are from wind tunnel measurements on fixed cylinders with two free ends; Christiansen and Barker (1965) data is from measurements on cylinders ($E = 1.75$) falling freely in the air ($1000 < S < 2800$); Isaacs and Thodos (1967) data is from measurements on cylinders ($E = 2.0$) falling freely in the water ($1.05 < S < 11.27$).

Chow and Adams (2011) estimated actual particle projected area of freely falling cylinders. Based on their approximate solution, the drag coefficient of cylindrical particles with $\sqrt{S/E} > 1.5$ should converge to value of $2/\pi$. Fig. 2.9 shows that our measurements of cylindrical particles are in close agreement with the approximate solution of Chow and Adams (2011). In addition we can see how for low values of $\sqrt{S/E}$ drag coefficient of cylindrical particles decreases as $\sqrt{S/E}$ increases, while, for high values of $\sqrt{S/E}$ drag coefficient is almost independent on this parameter.

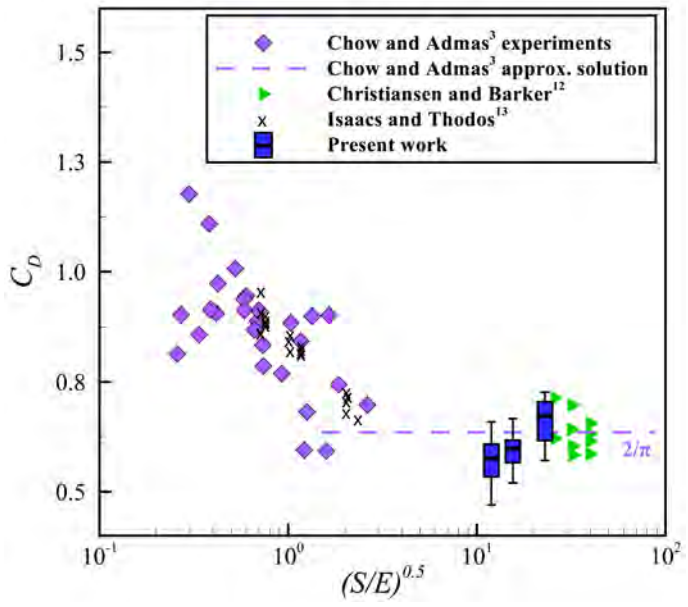

Figure 2.9: Variation of drag coefficient of cylindrical particles with respect to $\sqrt{S/E}$ measured in the present study with those reported in literature using Ld as A in the calculation of drag coefficient; values of $\sqrt{S/E}$ for particles C1, C2 and C3 are 23, 16 and 12, respectively; Chow and Adams (2011) experimental data is from measurements on cylinders ($2 < E < 100$) falling freely in the water ($1.1 < S < 8.5$).

To investigate the effect of the cylinder aspect ratio, E, on secondary motions

and projected area, histograms of area ratio, A^*, for each particle after applying the filters is presented in Fig. 2.10. A^* is defined as:

$$A^* \equiv \frac{A_{projected} - A_{min}}{A_{max} - A_{min}} \tag{2.5}$$

where A_{min} and A_{max} are minimum and maximum projected area of the particles respectively and $A_{projected}$ is the actual projected area of the cylinder calculated by the PTV code with the method described earlier. In case of cylindrical particles, $A_{min} = \pi\, d^2/4$ and A_{max} is a function of E and is equal to $L\, d$ for a cylinder with $E = \infty$.

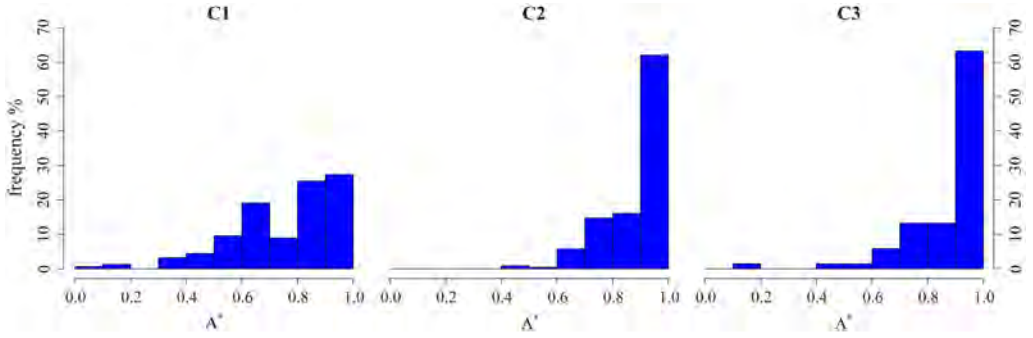

Figure 2.10: Histograms of area ratio of cylindrical particles after applying filters. No preferred orientation can be found for particle C1, while particles C2 and C3 in more than 60% of the cases are suspended with $A^* > 0.9$.

As it can be seen in Fig. 2.10, for particle C1 no preferred orientation exists while particles C2 and C3 tend to be suspended with their maximum projected area in more than 60% of the frames. This was expected as previous studies mentioned that oscillation frequency of cylinders decreases with the increase of the aspect ratio (Jayaweera and Mason, 1965; Isaacs and Thodos, 1967; McKay et al., 1988; Tran-Cong et al., 2004; Chow and Adams, 2011). Using results of the PTV code, secondary motions of cylindrical and non-spherical particles in general can be quantified and used in future models to provide better estimations of particle drag coefficients. High values of $A*$ do not imply that cylinder axis is horizontal (normal to air flow direction) since A_{max} occurs in different axis angle for cylinders with different aspect ratios. To clarify this, variations of a projected area of the cylindrical particles versus their axis angle is presented in Fig. 2.11. This figure shows that the cylinder aspect ratio increases for maximum projected area associated with low

angles. Comparing Figs. 2.10 and 2.11 it can be seen that in more than 60% of the cases particles C2 and C3 fall with $A^* > 0.9$, which corresponds to axis angles lower than 40°. In contrast particle C1 falls with $A^* > 0.6$, which corresponds to axis angles between 5° and 70°. Based on the investigation of Chow and Adams (2011) cylinders with $\sqrt{S/E} > 2.5$ undergo tumbling motion when they freely fall. They mentioned that particles with oscillation angles greater than 60° will begin to transition to tumbling. This is similar to the result of our experiments since for all our cylindrical particles ($\sqrt{S/E} \geq 12$), existence of A^* lower than 0.6 ($\alpha > 6°$) indicates that the particles are going under tumbling motion.

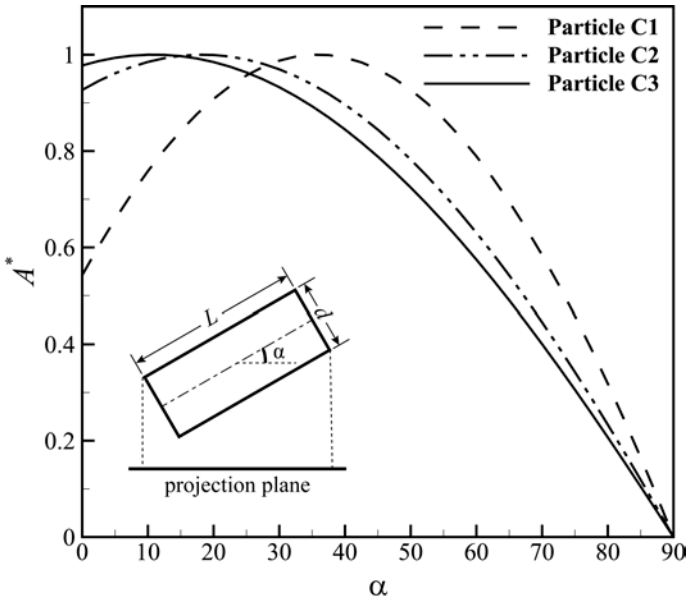

Figure 2.11: Variation of A^* versus cylinder axis angle. A^* is calculated from Eq. 2.5 and $A_{projected}$ ($= L\,d\cos(\alpha) + \pi\,(d/2)^2\sin(\alpha)$) is the area of the particle projected on the projection plane.

2.6 Discussion and Conclusions

Particle transport in either high particle to fluid density ratios or high particle Reynolds number is very common in a wide range of applications. Almost all the processes which involve transportation of solid particles in a gas continuum have very high values of density ratios. Existing literature on the drag coefficient of particles is mostly based on horizontal wind tunnel measurements on fixed bodies or freely falling particles in liquids. Data obtained with such methods cannot be used to estimate drag coefficient of freely moving solid particles in gases. In order to provide models on the drag coefficient of freely moving particles in high density ratios and

high Reynolds numbers, a 4 m high vertical wind tunnel was built at the University of Geneva in collaboration with the fluid mechanics group (CMEFE) from the University of Applied Sciences Western Switzerland in Geneva (HES-SO//hepia). The wind tunnel is primarily designed to study drag coefficient of non-spherical particles especially highly irregular volcanic particles and can reach velocities between $5\,\mathrm{m\,s^{-1}}$ and $27\,\mathrm{m\,s^{-1}}$ (i.e. it can suspend volcanic particles between 4 mm and 40 mm, which correspond to $5 \times 10^3 < Re < 8 \times 10^4$, $500\,\mathrm{kg\,m^3} < \rho_P < 2700\,\mathrm{kg\,m^3}$). Due to high level of particle secondary motions inside the test section, a PTV code is developed to calculate drag coefficient of particles from particle equation of motion (Eq. 2.4). The input data to the PTV code include: i) data provided by ImageJ on the particle centroid position in each frame, ii) geometrical and physical properties of the particles resulted from 3D-scanning and laboratory measurements, iii) database created from projected image of particle 3D-model in random orientations, iv) equation of air velocity resulted from airflow calibration (Eq. 2.3), v) data logged by temperature, pressure and humidity sensors installed in the test section. The PTV code calculates absolute and relative velocity and acceleration of the particle, thermodynamic properties of air during the experiment. Particle shape descriptors based on random-orientation database, drag coefficient of the particle using existing models in the literature for benchmarking and drag coefficient of the particle measured in standard conditions using its real projected area as the reference area. By measuring real projected area of the suspended particles, the PTV code can provide very useful information on the secondary motions of particles and their preferred orientations which can affect particle drag coefficient.

The experiments are repeatable with the average relative standard deviation of 1.7%. Our measurements on the drag coefficient of spherical particles are in close agreement with previous studies. In case of cylindrical particles our results closely agree with results of Christiansen and Barker (1965) who measured drag coefficient of freely falling cylindrical particles in the air. On the other hand, significant difference between drag coefficient measured in our wind tunnel with those measured in horizontal wind tunnel and free fall in water is observed. This shows that the effects of density ratio and secondary motion of particles are very important on its drag

coefficient. The PTV code performance on the calculation of real projected area of the particle is compared qualitatively with the descriptive reports available on the secondary motion of cylindrical particles and good agreements are found. Results show that the tunnel design parameters and its calibration along with the PTV code can be used to produce reliable and accurate measurements of the drag coefficient of particles of various shapes. The wind tunnel is designed originally for the study of settling velocity and aggregation of volcanic particles, but it could also be used in various fields of multiphase flows that include fluid-particle or particle-particle interactions.

2.7 Acknowledgments

This research is funded by the Swiss National Science Foundation (SNSF, Grant No. 200020-125024). The authors would like to thank Anthony Haroutunian, Jeremy Phillips, and Flavio Noca for their early contribution on the initial design of the wind tunnel.

2.8 Author's contributions

G. Bagheri and P. Pontelandolfo performed the calibration and validation experiments. G. Bagheri developed the PTV code. All authors were involved in the design process of the wind tunnel, drafting and reviewing of this chapter.

Chapter 3

On the characterization of size and shape of irregular particles[1]

3.1 Introduction

Size and shape characterization of particles is of key interest in various fields of science and engineering, including soil and atmospheric sciences, pharmaceutical and food processing, and advanced materials development (Sneed and Folk, 1958; Garboczi, 2002; Kalashnikova and Sokolik, 2002; Taylor, 2002; Dubovik et al., 2002; Banta et al., 2003; Riley, 2003; Vallebuona et al., 2003; Taylor et al., 2006; Ersoy et al., 2008; Matzl and Schneebeli, 2010; Alfano et al., 2011; Bagheri et al., 2013). In volcanology, size and shape of particles play an important role in various processes with large implications for the assessment of hazards, such as dispersion and sedimentation of volcanic particles (Wilson and Huang, 1979; Bonadonna et al., 1998; Dellino et al., 2005; Scollo, 2005; Coltelli et al., 2008; Alfano et al., 2011), reaction of air-borne particles with gases and water vapor in the eruption plume (Delmelle et al., 2005), threats to aviation and public health (Horwell et al., 2003; Horwell and Baxter, 2006; Rose and Durant, 2008, 2009; Durant et al., 2010; Alfano et al., 2011) and geophysical monitoring such as satellite retrievals (Krotkov et al., 1999; Lindqvist et al., 2011).

In order to characterize particle shape several shape descriptors have been introduced over the last few decades. Shape descriptors are mathematical functions that

[1] Published as: Bagheri G., Bonadonna C., Manzella I. and Vonlanthen P. (2015): On the characterization of size and shape of irregular particles, *Powder Technology*, 270, 141-153.

require previous determination of dimensional variables, such as values of length, diameter, perimeter, area or volume. They are here categorized in 1D, 2D and 3D shape descriptors based on the associated methods and variables. A well-known class of 1D shape descriptors called *form factors* that are defined based on the particle lengths in three dimensions (i.e. *form dimensions*), which can be measured rapidly using a ruler or a caliper. A common example of form factors are flatness and elongation. *2D shape descriptors* are based on *2D variables*, which are determined through image analysis of particle projections (also called shadowgraphs or silhouettes) (Riley, 2003; Lin and Miller, 2005; Ersoy et al., 2010; Mills and Rose, 2010; Asahina and Taylor, 2011; Garboczi et al., 2012; Ersoy, 2010; Taylor et al., 2006; Alfano et al., 2011). Examples of 2D variables typically determined by image analysis are the projection perimeter, area, and diameters of inscribing and circumscribing circles. Traditionally, projections are standard images taken by light microscopes and binoculars. Nowadays modern techniques, such as laser scanning (LS) and computed tomography (CT) can reconstruct external geometry of particles into 3D models that can be used to generate a large number of virtual 2D projections. *Sphericity* is the only *3D shape descriptor* considered in this study, which is defined as the ratio between surface area of a sphere with the same volume as the particle and the surface area of the particle (Wadell, 1933). Sphericity is a measure of the degree to which the shape of a particle approximates that of a true sphere (Wadell, 1933; Blott and Pye, 2007). In order to calculate sphericity particle volume and surface area need to be measured using a 3D method, such as 3D Laser Scanning (LS) and Scanning Slectron Microscope micro-Computed Tomography (SEM micro-CT).

Form dimensions used for calculation of form factors (e.g. flatness, elongation) consist of three length values, L, I and S, measured along different, usually perpendicular, directions. Several protocols have been established to determine L, I and S. According to the *Standard* (STD) protocol proposed by Krumbein (1941), L corresponds to the longest dimension of the particle, I to the longest dimension perpendicular to L, and S to the longest dimension perpendicular to both I and L. In contrast, Blott and Pye (2007) defined L, I and S with respect to the longest,

intermediate and shortest edge dimensions of the *Minimum Bounding Box* (MBB) enclosing the particle. The accuracy of these procedures is, however, highly dependent on the ability of the operator to identify the directions along which form dimensions are to be measured. In particular, errors mostly arise from the difficulty to evaluate the perpendicularity relationship between L, I and S (Blott and Pye, 2007; Bonadonna et al., 2013) (STD protocol) and the proportions of the MBB (MBB protocol).

Similar to caliper measurements, image analysis is subject to operator-dependent errors. In particular, results vary as a function of the orientation and number of selected projections. The analysis of a single randomly-selected projection clearly leads to incomplete results. However, it is not yet clear how many projections of an irregular particle are needed in order to guarantee reliable characterization of size and shape. Cauchy (1832) showed that accurate calculations of the surface area, SA, of a convex body (i.e. every line segment between two vertices remains inside or on the boundary of the body) from the area of its projections require an infinite number of projections. Laurentini (1997) reported that the volume, V, of any polyhedron of n faces can only be reconstructed provided that n^5 random projections are available. In practice, however, the number of projections is often adapted to the quantities to be measured. As an example, calculations of the terminal fall velocity of volcanic ash particles are generally based on one (Riley, 2003; Scollo, 2005; Coltelli et al., 2008; Alfano et al., 2011) or two (Dellino et al., 2005) projections. Blott and Pye (2007) suggested the use of three perpendicular projections to estimate particle sphericity from circularity measures, and Asahina and Taylor (2011) and Taylor et al. (2006) used 31 and 65 projections, respectively, to calculate the surface area of gravel-sized rock pieces.

1D and 2D variables can be easily obtained from caliper measurements and image analysis. On the other hand, the determination of volume, surface area and sphericity, which are hereafter indicated as 3D parameters, needs more sophisticated instruments (e.g. LS) that are more time consuming and in most cases cannot be applied to a large number of particles. Many studies can be found in the literature that explore the possibility of obtaining 3D parameters from 1D and 2D variables

(Cauchy, 1832; Aschenbrenner, 1956; Kunii and Levenspiel, 1968; Zhang et al., 2012; Blott and Pye, 2007; Garboczi et al., 2012; Asahina and Taylor, 2011; Biass and Bonadonna, 2011; Riley, 2003; Taylor et al., 2006; Mills and Rose, 2010). However, a comprehensive investigation on this subject is still needed since most of previous studies did not measure 3D parameters directly and/or their relationships with 1D and 2D were not analyzed in detail.

Shortcomings of existing strategies include i) the difficulty in identifying the perpendicularity amongst L, I and S, which can generate large operator-dependent errors and ii) the lack of quantification of the dependence of image analysis on the number of irregular-particle projection, which can also generate large errors. Finally, in order to better characterize critical particle parameters (e.g. sphericity), which can help describe important physical processes, such as particle transport and sedimentation, a comprehensive study of shape of highly irregular particles is required. This should include simple (e.g. caliper) to complex (e.g. LS and SEM micro-CT) measurement strategies. The evaluation of 3D parameters (e.g. volume, surface area, sphericity) based on 1D and 2D variables also needs to be investigated in more detail. In order to address the issues and shortcomings mentioned above, we have carried out a systematic study on 127 volcanic clasts between 155 µm – 36 mm, which are good general case studies of irregular particles. Several methods for the characterization of our particles are used, including caliper measurements, image analysis, LS and SEM micro-CT. First, existing procedures commonly applied to determine the variables of shape descriptors are revised (i.e. 1D and 2D variables). In particular, a new protocol, called *projection area-based protocol* (PA), is proposed for the measurement of form dimensions with low operator-dependent errors. Second, 1D and 2D variables are used to calculate shape descriptors (i.e. form factors, circularity, sphericity). Third, both new and existing empirical correlations are benchmarked for applications where 3D parameters are obtained indirectly from shape descriptors and both 1D and 2D variables.

3.2 Samples

Selected particles are divided in two sample sets (Table 3.1) based on the common size classification used in volcanology: lapilli ($2\,\text{mm} < d_{eq} < 64\,\text{mm}$) and ash particles ($d_{eq} < 2\,\text{mm}$), where d_{eq}, obtained from LS and SEM micro-CT measurements, is the equivalent spherical diameter defined as the diameter of the sphere with the same volume V as the particle ($d_{eq} = \sqrt[3]{6\,V/\pi}$).

Table 3.1: Samples and methods used in this study.

Sample Set	Type	No	d_{eq}	Surface	Measurement method
1	Lapilli	65	11 – 35 mm	vesicular	Caliper, image analysis and LS
	Lapilli	13	15 – 21 mm	non-vesicular	
	Lapilli Parafilm®-wrapped	37	11 – 37 mm	non-vesicular	
2	Ash	3	205 – 266 µm	vesicular	Image analysis and SEM micro-CT
	Ash	9	155 – 930 µm	non-vesicular	

Sample Set 1 consists of 115 lapilli-sized particles with collected from various tephra deposits, including those of Chaitn (Chile, 2008), Llaima (Chile, 1957), Villarrica (Chile, Chaimilla unit, 3500 BP), Cotopaxi (Ecuador, Layer 2, 290 years BP and Layer 5, 1180 years BP Barberi et al., 1995), Masaya (Nicaragua, Fontana Lapilli, 60 ka Costantini et al., 2010). and Stromboli (Italy, 2007). 65 particles of Sample Set 1 are vesicular (opening diameter of the vesicles corresponding to 5 – 40% of , with a mode around 10 – 25%) and 13 particles have non-vesicular surfaces. The term *vesicle* here refers to surface vesicles only and internal vesicles have not been considered. In addition, 37 particles are also wrapped in Parafilm® (a self-sealing, moldable and flexible wax film) to cover the surface vesicles and increase the population of *non-vesicular* samples without changing their macroscopic shape characteristics. LS 3D models of selected lapilli-sized particles are shown in Fig. 3.1.

Sample Set 2 consists of 12 ash particles with $155\,\mu\text{m} < d_{eq} < 930\,\mu\text{m}$ that includes 3 vesicular and 9 non-vesicular. Because of their small size, these particles were investigated through SEM micro-CT (Fig. 3.2) instead of LS and image anal-

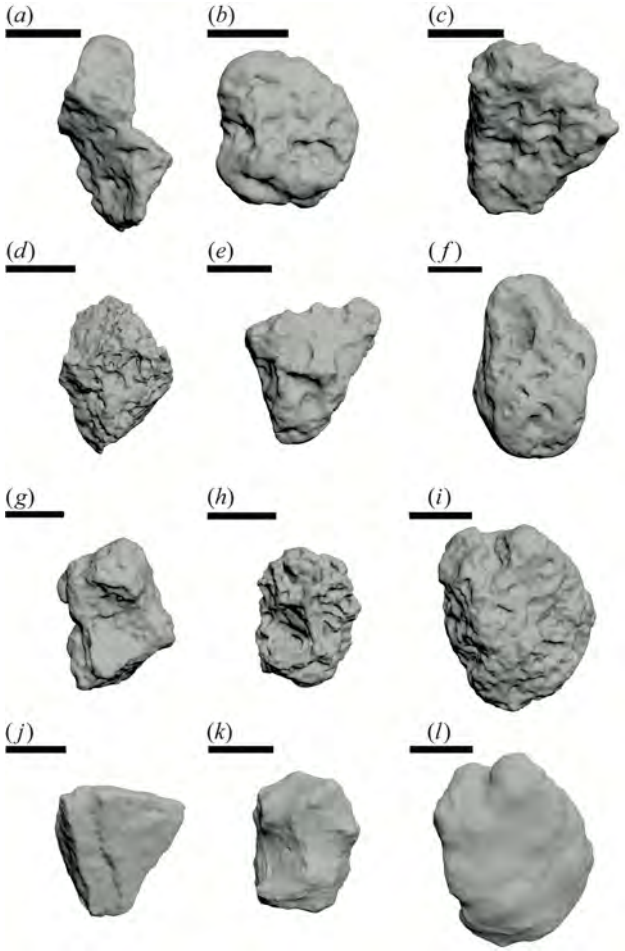

Figure 3.1: LS 3D models of selected particles of Sample Set 1 (scale bar: 10 mm). Particles k and l are Parafilm® -wrapped models of particles h and i, respectively. Particles a to i are considered as vesicular and particles j to l are considered as non-vesicular. Source of particles are as follows: a and c from Cotopaxi Layer 5, b from Cotopaxi Layer 2, d from Villarrica Chaimilla unit, h from Llaima 1957, f and l from Chaitn 2008, e, i and g from Masaya Fontana Lapilli.

ysis. The small population of ash particles is due to the fact that SEM micro-CT is a time-consuming technique, which cannot be applied to a large number of particles (Vonlanthen et al., 2015). Ash particles were collected from the tephra deposits of Klauea (Hawaii, Mystery Unit of Keanakakoi formation, 1790 AD), Chaitn (Chile, 2008) and Masaya (Nicaragua, Fontana Lapilli, 60 ka Costantini et al., 2010).

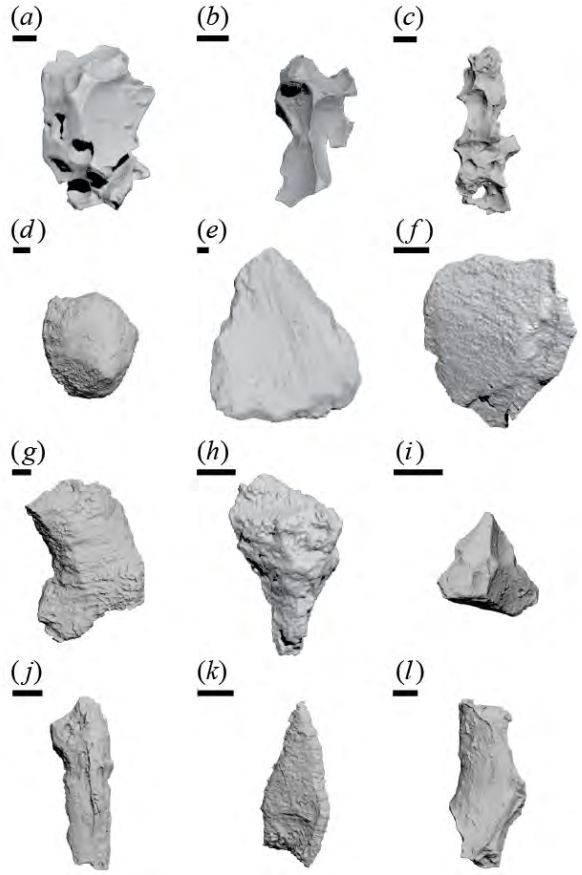

Figure 3.2: SEM micro-CT models of the volcanic ash particles of Sample Set 2 (scale bar:100 µm). Particles a to c are considered as vesicular and particles d to l are considered as non-vesicular. Source of particles area as follow: b, d, f, g, h, i and k from Klauea Mystery Unit of Keanakakoi formation; a, c, j and l from Masaya Fontana Lapilli; and e from Chaitn 2008.

3.3 Measurements Methods

3.3.1 Laser Scanner (LS)

LS enables the external envelope of a particle to be reconstructed in 3D (Fig. 3.1). The lapilli-sized particles (Sample Set 1) were scanned using the NextEngine Inc. desktop laser scanner with accuracy of 100 µm and particle volume and surface area were calculated using the ScanStudio HD Pro software (v.1.3.2) delivered with the apparatus. Samples were glued onto a needle-shaped screw, fixed to a self-rotating and tiltable stage, and rotated over 360°. Digital scans of the samples were taken using increments of 45° to 60° depending on the irregularity of the particle shape. This preliminary scan was then inspected visually and completed by additional scans to improve the orientation coverage. The successive scans were later aligned digitally

and a mesh of the particle surface was created. In most cases further cleaning and patching of the mesh is necessary to reduce noise and remove artifacts. Acquisition and post-processing took about 2 hours on average for each particle. Our preliminary test showed that particles with d_{eq} of 5 mm are the smallest particle size that can be reconstructed by our LS. In order to validate LS measurements, an official table tennis ball (40 mm in diameter) approved by the ITTF (International Table Tennis Federation) was scanned and its surface area and volume calculated from its 3D model. The errors were within 0.5% with respect to the analytical calculations.

3.3.2 Scanning Electron Microscope (SEM) micro-CT

SEM micro-CT enables non-destructive 3D reconstruction and characterization of small objects within the chamber of an SEM (Pauwels et al., 2010). The technique uses the X-rays generated in the SEM chamber when the electron beam is focused on a metal target. The object to be analyzed is placed in front of the X-ray beam and step-wise rotated over an incremental range of angular orientations. Shadow projections of the sample are then collected by an X-ray sensitive camera and used to reconstruct 2D CT slices and 3D models of the object with a resolution in the order of 1 µm to 3 µm (see Fig. 3.2).

SEM micro-CT analyses were carried out at the University of Lausanne (Switzerland) using a CamScan MV2300 SEM equipped with a Bruker SEM micro-CT attachment. This device consists of a Princeton Instruments PIXIS XO X-ray camera and a computer-controlled motorized stage. The SEM was operated at 30 kV and 300 nangstrom to maximize the penetration power of X-rays and to increase the signal-to-noise ratio in the shadow projections. Depending on the density, particles with diameters between 0.1 mm and 1.0 mm can be reconstructed by using our SEM micro-CT. In order to check the accuracy of the method, the form dimensions obtained from SEM micro-CT were compared to the dimensions measured using an optical microscope. Results showed a maximum of 3% deviation. For a detailed description of the SEM micro-CT technique and its applicability to volcanic ash, the reader is referred to Vonlanthen et al. (2015).

3.3.3 Caliper

A digital caliper with accuracy of 0.01 mm was used to measure form dimensions of particles in Sample Set 1. Because of the impracticality of manipulating small objects, caliper measurements could not be performed on particles of Sample Set 2.

3.3.4 Image Analysis

For each particle, image analyses were performed on 1000 random projections that were extracted from the 3D models obtained from LS and SEM micro-CT. The size of each projection is $1000\,pixel \times 1000\,pixel$, which corresponds to spatial resolution of 11 µm/pixel to 36 µm/pixel for the particles of Sample Set 1 and nominal spatial resolution of 0.2 µm/pixel to 1.0 µm/pixel for those of Sample Set 2. Random projections were analyzed using the ImageJ software (Schneider et al., 2012) to extract 2D variables that include the perimeter, P, circle equivalent diameter, d_{2D}, area, A, diameter of the largest inscribed circle, D_i, and diameter of the smallest circumscribed circle, D_c (see Fig. 3.3). Other than these variables, there are other variables that can be obtained from image analysis, such as minimum and maximum caliper lengths of the projection (i.e. l_{min} and l_{max}). l_{min} and l_{max} can be considered as equivalent to L, I or S depending on the particle orientation in the projection. Therefore, they can be used as alternatives for measuring form dimensions since they are associated with less operator-dependent errors compared to those obtained by caliper. A dedicated FORTRAN code was developed to merge the data obtained from caliper measurement, image analysis, LS and SEM micro-CT and to calculate all shape descriptors. The statistical analysis on the output data from the code was done by the R statistical package (RCT, 2014).

3.4 Measurement of particle volume and surface area

Depending on the instrument used for measuring volume and surface area of an irregular particle different values might be obtained. In particular, surface area

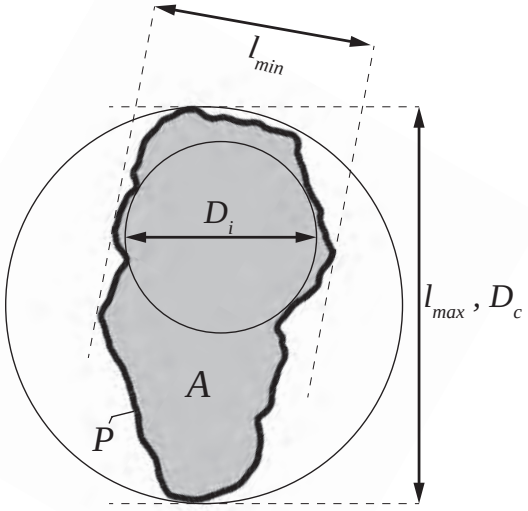

Figure 3.3: Variables determined for a particle projection using ImageJ. The projection shown in this figure is the maximum projection area of particle a in Fig. 3.1. For each particle in Sample Sets 1 and 2, up to 1000 projections in random orientations of the particle are created from the particle 3D model and analyzed by ImageJ. $A \equiv$ projection area, $P \equiv$ projection perimeter, $d_{2D} \equiv$ circle equivalent diameter, $l_{min} \equiv$ minimum caliper length, l_{max} maximum caliper length, $D_i \equiv$ diameter of the largest inscribed circle and $D_c \equiv$ diameter of the smallest circumscribed circle.

of an irregular porous object is a function of scale and depends on the considered measurement strategy (Taylor et al., 2006). For example, gas-adsorption methods measure particle surface area down to molecule level while LS and SEM micro-CT work at much higher scales (0.1 – 1.0% of d_{eq}) (Riley, 2003; Lin and Miller, 2005; Alfano et al., 2011). As a result, surface area and related parameters, such as sphericity, obtained with LS and SEM micro-CT cannot be compared with those obtained from gas-adsorption methods. In this study, in order to have a reference value for 3D parameters, i.e. particle volume (and eventually d_{eq}), surface area (SA) and sphericity (ψ), values obtained from LS and SEM micro-CT are used.

3.5 Results

3.5.1 Measuring strategies

Form dimensions: the new Projection Area (PA) protocol

In order to reduce the operator-dependent errors associated with both the STD and MBB protocols, a new approach based on Projection Area (PA) is introduced for the measurement of form dimensions (i.e. L, I, S). Unlike the STD and MBB protocols, the PA protocol does not require L, I and S to be measured perpendicularly to each other. Instead, they are measured on two specific projections of the particle, namely the projections with maximum and minimum areas. L and I are defined as the largest and smallest dimensions measured on the maximum-area projection, and S corresponds to the smallest dimension measured in the minimum-area projection. A sketch illustrating the dimensions associated with the STD, MBB and PA protocols is shown in Fig. 3.4.

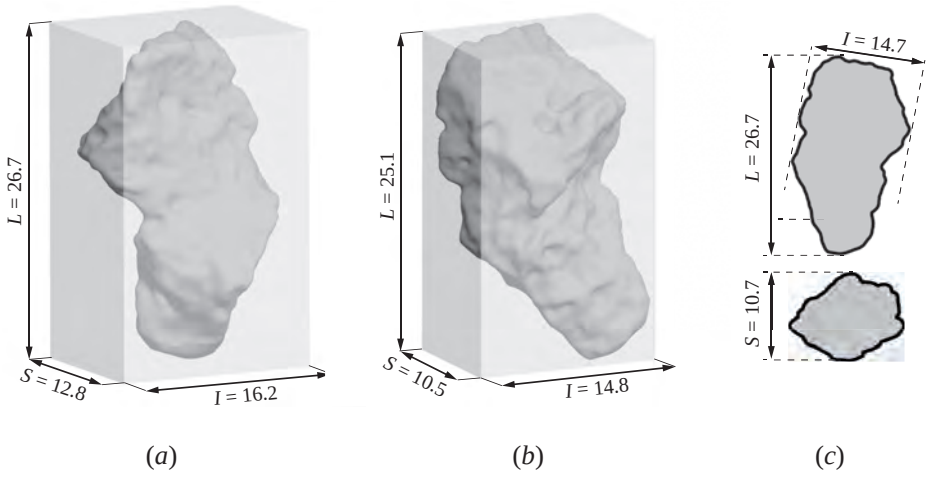

Figure 3.4: Schematic illustration of different protocols used to measure form dimensions (L, I and S) of particle a in Fig. 3.1 (dimensions are in mm). (a) The Standard (STD) protocol proposed by Krumbein and Pettijohn (1938); (b) The Minimum Bounding Box (MBB) of Blott and Pye (2007) determined using the MATLAB toolbox of Korsawe (2008); (c) Form dimensions inferred from the Projection Area (PA) protocol. Top and bottom projections are the maximum and minimum area projections, respectively.

In order to test the operator-dependency of the PA protocol, three different operators measured form dimensions of particles shown in Fig. 1 through both the MBB and PA methods by using a digital caliper (Table 3.2). The application of

the MBB protocol with caliper is described by Blott and Pye (2007) and shown in Fig. 3.4b. In contrast, the application of the PA protocol is based on the maximum and minimum projections visually identified by different operators (Fig. 3.4c). Maximum and minimum dimensions were then measured with a digital caliper. We did not consider the STD method since it is already proven to be highly operator dependent (Blott and Pye, 2007; Bonadonna et al., 2013). Results show that the PA method is associated with lower operator-dependent errors (1.3 – 2%) than the MBB method (2.4 – 5.3%).

Table 3.2: Comparisons of the MBB (Blott and Pye, 2007) and PA protocols for measuring form dimensions of particles shown in Fig. 3.1 (Dimensions are in mm). Three different operators (oprs.) made caliper measurements and values in table are mean of their readings. Deviations shown at bottom of caliper readings are the deviation between readings of different operators. Errors presented in the last row are relative errors between average of caliper readings and MATLAB toolbox (Korsawe, 2008) for the MBB (Blott and Pye, 2007); and caliper readings and image analysis for the PA.

ID	MBB						PA					
	Mean Caliper			Matlab			Mean Caliper			Matlab		
	L	*I*	*S*	*L*	*I*	*S*	*L*	*I*	*S*	*L*	*I*	*S*
a	25.9	15.0	11.0	25.1	14.8	10.5	25.9	15.0	10.6	26.7	14.7	10.7
b	19.6	16.7	13.3	19.5	15.8	13.8	20.1	16.8	13.3	20.4	17.6	13.6
c	25.2	21.2	9.2	25.1	20.8	9.4	26.0	20.8	9.3	26.1	21.1	9.5
d	21.9	16.8	14.9	19.0	16.1	14.5	22.5	15.4	14.5	22.6	16.0	15.1
e	24.7	19.0	12.2	21.7	20.9	12.6	26.1	19.0	12.5	26.2	18.9	12.7
f	34.5	22.0	15.4	33.0	22.9	16.0	34.5	22.6	15.4	34.8	22.5	16.1
g	26.2	18.8	13.5	26.3	18.6	13.6	27.3	19.1	13.6	27.3	18.8	13.7
h, k	19.7	16.2	11.2	20.2	16.5	11.0	20.5	16.5	11.0	21.2	16.5	11.1
i, l	30.2	24.2	16.6	30.6	24.2	18.2	30.9	24.2	17.8	31.1	23.8	17.6
j	32.2	26.1	13.0	32.7	25.4	13.5	32.9	25.4	13.4	32.8	25.7	13.6
Max. dev oprs. %	6.5	7.4	4.6				5.0	4.4	3.9			
Avg. dev. oprs. %	**2.4**	**5.3**	**2.7**				**1.5**	**1.3**	**2.0**			
Max. error %				15.1	5.8	4.7				3.4	4.9	4.5
Avg. error %				**4.6**	**2.9**	**2.8**				**1.2**	**2.4**	**2.0**

In addition, the accuracy of both protocols has been evaluated based on comparison between the caliper measurements and reference form dimensions (Table 3.2). For the MBB protocol, references consist of the edge dimensions of the Minimum Bounding Box calculated using the MATLAB toolbox (Korsawe, 2008). For the PA protocol, references are calculated from the maximum and minimum area projections among 1000 random projections created from 3D models. In order to do so, l_{min} and l_{max} of the maximum projection area of the particle are assigned

as L and I, respectively, and l_{min} of the minimum projection area is assigned as S. The average error between measurements and references ranges between 2.8% and 4.6%, with a maximum of 15.1% (for L) for the MBB protocol, and between 1.2% and 2.4%, with a maximum of 4.9% (for I) for the PA protocol.

The ability of the PA protocol to account for common morphological quantities has been tested in two ways. First, the particle spherical equivalent diameter, d_{eq}, obtained from LS and SEM micro-CT was compared to the averaged geometrical diameter of the equivalent ellipsoid, $d_G = \sqrt[3]{L\,I\,S}$, (i.e. an ellipsoid with same tri-axial dimensions as the particle form dimensions). Second, the particle surface area, SA, obtained from LS (Sample Set 1) and SEM micro-CT (Sample Set 2) was compared to the surface area of the equivalent ellipsoids, $SA_{ellip.}$. Taylor et al. (2006) used the following approximate solution for calculating $SA_{ellip.}$ that is associated with relative error of 0.1% compared to exact results:

$$SA_{ellip.} = 4\,\pi \left[\frac{(L\,I/4)^{\lambda} + (L\,S/4)^{\lambda} + (I\,S/4)^{\lambda}}{3 - k(1 - 27\,L\,I\,S\,(L + I + S)^{-3})} \right]^{1/\lambda} \tag{3.1}$$

where $\lambda = 1.5349$ and $k = 0.0942$. Fig. 3.5 shows the ratios of $SA_{ellip.}$ to SA, and of d_G to d_{eq} as boxplots. In each boxplot the ends of the bars represent the smallest and the largest measurements. The box height indicates the first and the third quartiles and the horizontal in the box line is the median (second quartile) of the measurement. The outliers (outside 1.5 times the interquartile range above the upper quartile and bellow the lower quartile) are shown by circles, however, they are not considered for discussion. The number at the bottom of each boxplot is the mean of the distribution. Fig. 3.5 shows that ratios obtained from the PA protocol are closer to unity and have narrower maximum deviations than those obtained from the MBB protocol. This trend is confirmed by the Pearson correlation coefficient, r, between $SA_{ellip.}$ and SA, and between d_G and d_{eq}. Using the MBB protocol, r values are 0.981 between $SA_{ellip.}$ and SA, and 0.987 between d_G and d_{eq}, while they are 0.994 and 0.989, respectively, using the PA protocol.

The use of the new PA protocol can reduce operator-dependent errors for measuring form dimensions of irregular particles (Table 3.2) and can also provide better estimation of particle volume and surface area (Fig. 3.5). The PA protocol is also

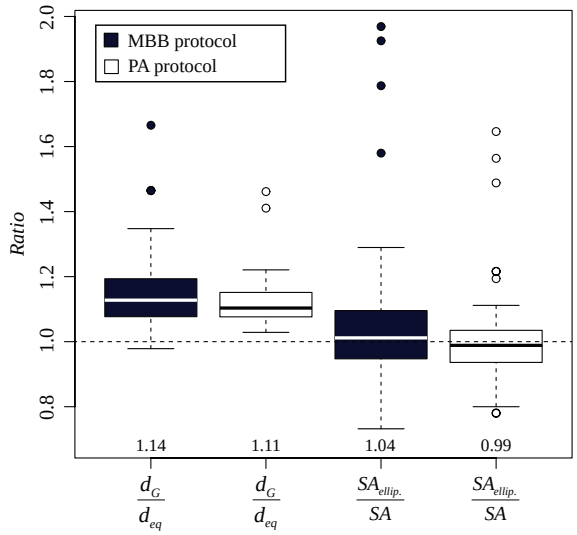

Figure 3.5: Box plot showing the variability of ratios of d_G and $SA_{ellip.}$ calculated from the form dimensions (L, I and S) to d_{eq} and SA obtained from LS and SEM micro-CT measurements. Each boxplot shows the distribution of the corresponding ratio within all particles of Sample Sets 1 and 2. Form dimensions were measured using a digital caliper following either the MBB (Blott and Pye, 2007) (black boxes) or the PA protocol (white boxes).

much easier to apply since it is not necessary to maintain the perpendicularity between projections or measured dimensions. The only subjectivity associated with the PA protocol is the choice of maximum and minimum particle projections. In the following sections form dimension of particles are obtained by applying the PA protocol on 1000 random orientation projections. Through this procedure, we make sure that the presented results are not biased by possible operator-dependent errors that might arise from using the caliper.

Image analysis: effect of particle orientation and number of projections

The particle 3D model (obtained from LS or SEM micro-CT) enables the generation of several hundreds of randomly oriented projections. This allows us to determine easily the influence of the number of projections, N, on widely-used 2D variables and shape descriptors: the circle equivalent diameter, , the Riley circularity (Riley, 1941), ϕ_{Riley}, and the Cox circularity (Cox, 1927), ϕ_{Cox} (Fig. 3.6). The definitions of circularity measures are presented in Table 3.3. The average values of d_{2D}, ϕ_{Riley} and ϕ_{Cox} were calculated for each particle for $N = 1, 2, 3, 10, 20, 50, 100 and 1000$. Values that averaged over 1000 projections, shown by overscores (i.e. $\overline{d_{2D}}$, $\overline{\phi}_{Riley}$,

$\overline{\phi}_{Cox}$), were used as references for the values averaged over $N < 1000$. For $N = 1$ the projection with maximum area was selected since it is the most possible orientation of the particle when its image is taken by microscopes (due to higher stability in such orientations) among other possible orientations. The minimum and maximum area projections were used for $N = 2$, and three perpendicular projections were selected for $N = 3$ (the first being the maximum area projection). For $N > 3$, the three perpendicular projections were completed by randomly selected projections.

Fig. 3.6 shows that the average of deviations decreases as the number of projections increases. For $N = 1$ the deviation of the median is +12% for d_{2D}, +4% for ϕ^*_{Riley}, and +1% for ϕ^*_{Cox} (compared to the value averaged over 1000 projections $N = 1000$, dotted horizontal line). For $N = 2$ the deviation of the median remains constant for ϕ^*_{Cox}, while it significantly decreases for ϕ^*_{Riley} (+2%) and d_{2D} (-1%). Whiskers shrink significantly with increasing N (20% for $N = 1$, $5 - 8\%$ for $N = 3$, and 2.5% for $N = 50$).

In summary, a single projection ($N = 1$) is not sufficient to estimate $\overline{d_{2D}}$, but it can estimate $\overline{\phi}_{Riley}$ and $\overline{\phi}_{Cox}$ with error distributions centered around zero. Using a large amount of projections ($N > 10$) significantly improves the results. However, acquisition and post-processing time increases when a large number of projections is considered. Using two projections that include minimum and maximum projections ($N = 2$) or three perpendicular projections ($N = 3$) can be considered as the best compromise between time and accuracy.

3.5.2 Shape descriptors of Sample Set 1 and 2

In the previous section, 1D variables (i.e. form dimensions) of sample particles were obtained through PA protocol and 2D variables by image analysis. In this section various shape descriptors are calculated and the shape characteristics of our sample particles are investigated. In particular, shape descriptors considered in this study are those that are most used in transport and sedimentation studies (Loth, 2008) and are divided in 1D, 2D and 3D descriptors (Table 3.3). 1D shape descriptors are typically called form factors since they are defined based on form dimensions (i.e. L, I, S). Form factors considered here include: (i) elongation and flatness (Zingg,

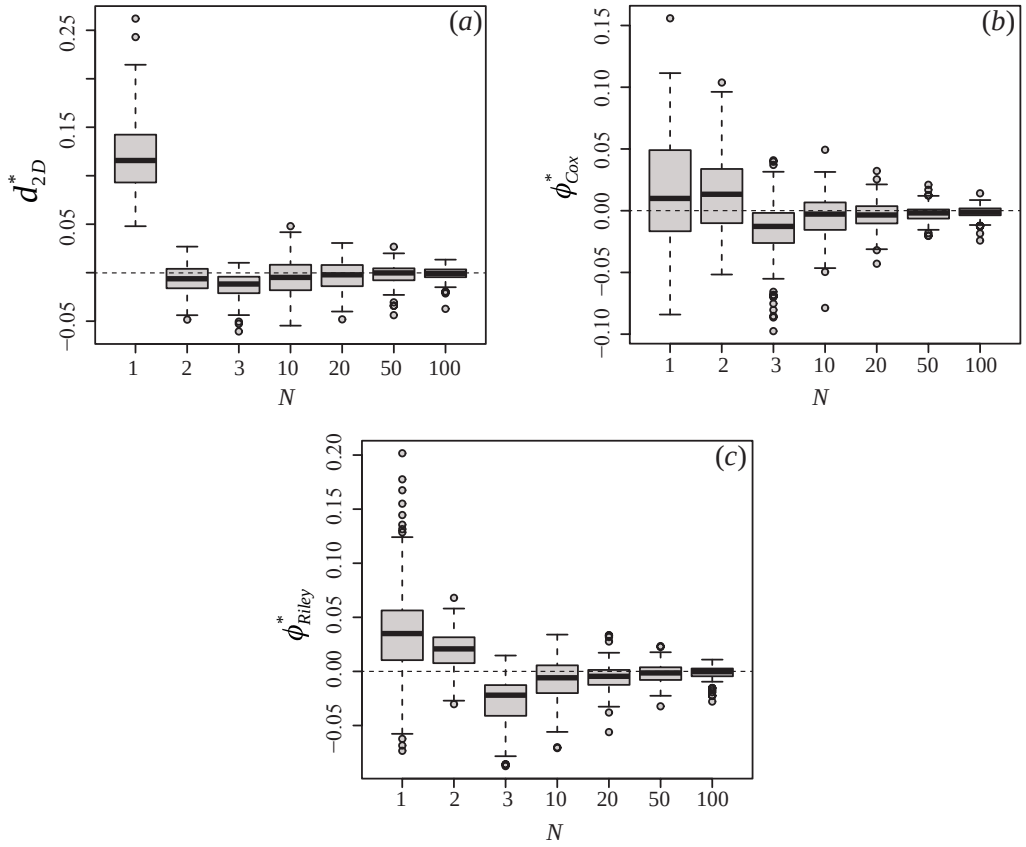

Figure 3.6: Influence of number of projections N on the deviation of on the average of (a) circle equivalent diameter d_{2D}, (b) the Cox (1927) circularity ϕ_{Cox}, and (c) the Riley (1941) circularity ϕ_{Riley}. For each parameter x (i.e. d_{2D}, ϕ_{Cox}, ϕ_{Riley}) the deviation x^* is calculated as $x^* = (\left[\sum_{i=1}^{N} x_i/N)\right] - \overline{x})/\overline{x})$ where $\overline{x}$ is the average over 1000 projections. Each boxplot shows the distribution of the deviation x^* for all particles in Sample Sets 1 and 2.

1935), (ii) Krumbein intercept sphericity (Krumbein, 1941), (iii) Corey shape factor (Corey, 1963), (iv) Sneed and Folk maximum projection sphericity (Sneed and Folk, 1958), (v) Aschenbrenner working sphericity (Aschenbrenner, 1956), (vi) Wilson and Huang shape factor (Wilson and Huang, 1979). 2D shape descriptors include circularity measures (i.e. Cox circularity (Cox, 1927) and Riley circularity (Riley, 1941) that are based on 2D variables obtained through image analysis. Finally, the sphericity (Wadell, 1933) that is related to the particle volume and surface area (obtained from LS and SEM micro-CT) is considered as a 3D shape descriptor. There are other types of shape descriptors, such as roundness, irregularity, convexity indexes and surface texture descriptors that are not considered in this study since we are mainly interested in shape descriptors related to transport and sedimentation

behavior of particles.

Table 3.3: Shape descriptors measured for each particle. Shape descriptors are categorized based on the classification proposed by Blott and Pye (2007) and, therefore, might differ from that of original papers (for more details please refer to Blott and Pye, 2007).

Formula	Notes
Form Factors (1D)	
$e = I/L$	Elongation (Zingg, 1935)
$f = S/I$	Flatness (Zingg, 1935)
$F_{Kr} = \sqrt[3]{I\,S/L^2}$	Krumbein intercept sphericity (Krumbein, 1941)
$F_{Cr} = S/\sqrt{L\,I}$	Corey shape factor (Corey, 1963)
$F_{SF} = \sqrt[3]{S^2/L\,I}$	Sneed and Folk (1958) maximum projection sphericity
$F_{Ac} = \frac{12.8\,\sqrt[3]{f^2\,e}}{1+f\,(1+e)+6\,\sqrt{1+f^2\,1+e^2)}}$	Aschenbrenner (1956) working sphericity, is sphericity of a tetrakaidekahedron derived from its flatness and elongation
$F_{WH} = (I+S)/2\,L$	Wilson and Huang (1979) shape factor for estimating drag coefficient of irregular volcanic particles
Circularity measures (2D)	
$\phi_{Cox} = 4\,\pi\,A/P^2$	Cox (1927) circularity (originally called roundness)
$\phi_{Riley} = \sqrt{D_i/D_c}$	Riley (1941) circularity (originally called inscribed circle sphericity)
Sphericity (3D)	
$\psi = \pi\,d_{eq}^2/SA$	Sphericity (Wadell, 1933)

In this section, first variability range of shape descriptors of our sample particles is presented. This gives insights both into shape characteristics of volcanic particles and into the influence of surface vesicularity on the variability of shape descriptors. Second, through a correlation matrix, we investigate how the shape descriptors are related together and explore the possibility of estimating one shape descriptor from another.

Variability

Variability of all the shape descriptors listed in Table 3.3 is shown in Fig. 3.7 for both vesicular and non-vesicular particles. 1D shape descriptors cannot be used to

distinguish between vesicular and non-vesicular particles since they are formulated based on form dimensions, which are not sensitive to vesicularity. Fig. 3.7a shows that particles of Sample Set 1 have elongation between 0.51 and 0.91 and flatness between 0.40 and 1.00.

According to the classification terminology suggested by Blott and Pye (2007), the particles of Sample Set 1 can be classified as *moderately elongate* to *not elongate* and *moderately flat* to *not flat*. Out of all 1D shape descriptors, the working sphericity of citeAschenbrenner1956, F_{Ac}, has the lowest variability and the highest mean value, whereas Corey (1963), F_{Cr}, and Wilson and Huang (1979), F_{WH}, shape descriptors have the lowest mean values. The Riley circularity, $\overline{\phi}_{Riley}$, shows the same range of values for both non-vesicular and vesicular particles. On the other hand, both sphericity, ψ, and Cox circularity, $\overline{\phi}_{Cox}$, show different values for vesicular and non-vesicular particles with a very narrow overlapping. Sphericity of non-vesicular particles varies between 0.77 and 0.90 while for vesicular particles sphericity is on average 18% less than non-vesicular particles and varies between 0.53 and 0.80. This is due to the fact that vesicular particles have higher surface area compared to non-vesicular particles of the same volume and, as a result, their sphericity is lower (according to sphericity definition in Table 3.3). Fig. 3.7b shows the variability of shape descriptors for Sample Set 2. Form factors have a wide range of variability between 0.25 and 0.90. Particles of Sample Set 2 have elongation between 0.33 and 0.86 and flatness between 0.34 and 0.88. They can be classified as *very elongate* to *not elongate* and *very flat* to *not flat*. Similarly to Sample Set 1, values of ψ and $\overline{\phi}_{Riley}$ are different for non-vesicular and vesicular particles. Sphericity of non-vesicular particles in Sample Set 2 varies between 0.50 and 0.86 while for vesicular particles sphericity is in average 33% less than non-vesicular particles and varies between 0.43 and 0.46. In general, all the shape descriptors of Sample Set 2 have lower average values than those of Sample Set 1.

Correlation between shape descriptors

Correlation matrix between various shape descriptors of Table 3.3 is shown in Fig. 3.8. The diagonal elements are symbols of the shape descriptor listed in Table 3.3.

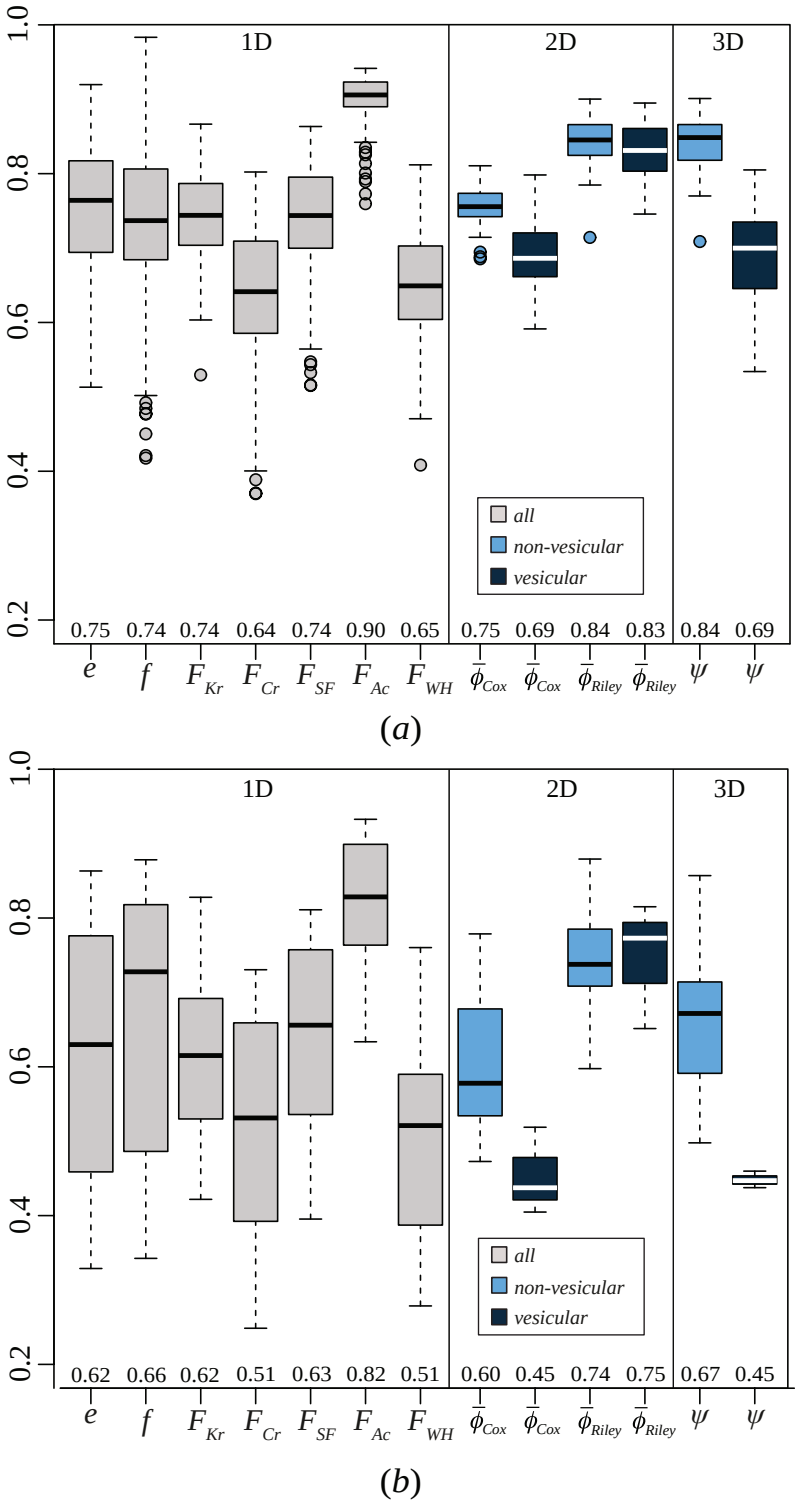

Figure 3.7: Distributions of the shape descriptors listed in Table 3.3 for the particles of (a) Sample Set 1 and (b) Sample Set 2. $\overline{\phi}_{Riley}$ and $\overline{\phi}_{Cox}$ are obtained by averaging ϕ_{Riley} and ϕ_{Cox} over 1000 projections. The number at the bottom of each boxplot is the mean of the distribution. Regarding 1D shape descriptors, no distinction could be made between particles with vesicular and non-vesicular surface texture since they are formulated based on form dimensions (L, I and S) that are not sensitive to vesicularity.

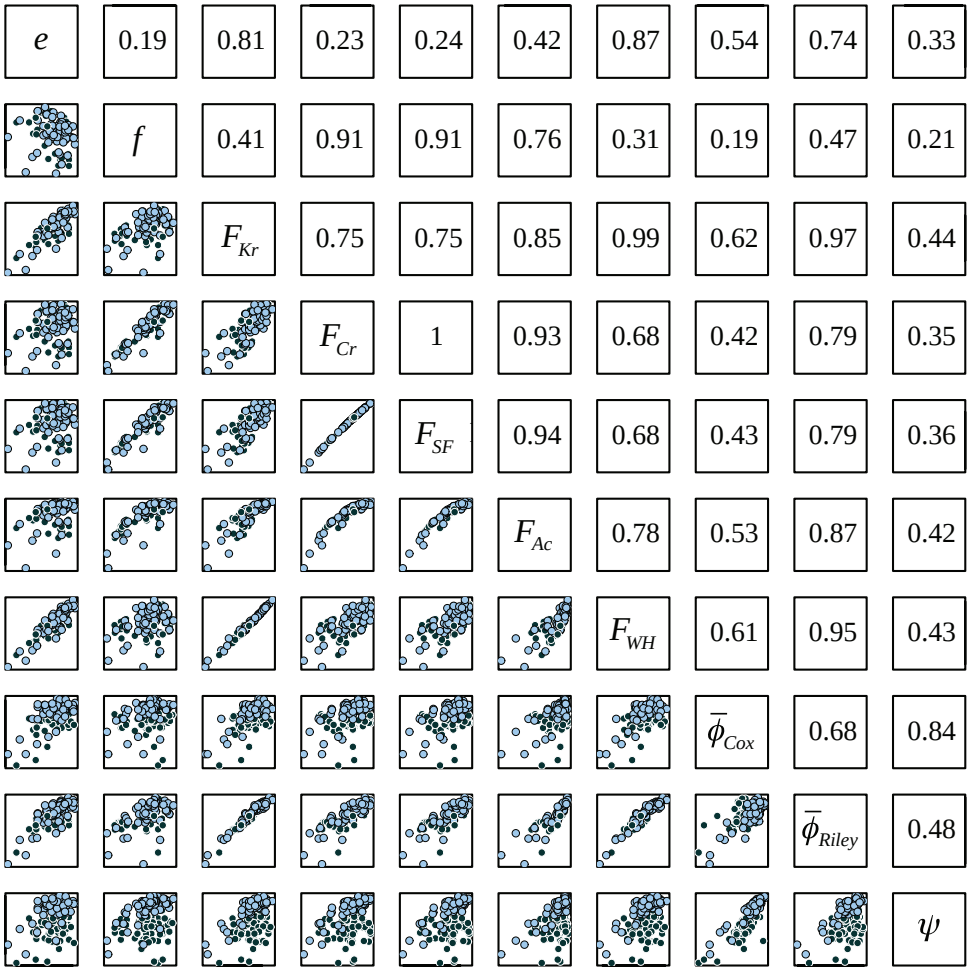

Figure 3.8: Correlation matrix of shape descriptors listed in Table 3.3 for both sample sets. $\overline{\phi}_{Riley}$ and $\overline{\phi}_{Cox}$ are obtained by averaging ϕ_{Riley} and ϕ_{Cox} over 1000 projections. Data corresponding to particles with vesicular and non-vesicular surface are shown by dark and light colors, respectively.

The scatter plots between shape descriptors are shown under the main diagonal and the corresponding Pearson's correlation coefficients, r, are shown above the main diagonal. As an example, a strong linear correlation in the scatter plot between F_{Kr} and F_{WH} can be seen, which is also reflected in the correlation coefficient of 0.99 between these variables.

1D shape descriptors are either affected by the particle elongation or by their flatness. F_{Cr}, F_{SF} and F_{Ac} are highly correlated with each other ($r = 0.93 - 1.00$) and all of them have high correlation coefficients with the particle flatness ($r = 0.76 - 0.91$). A similar situation exists between F_{Kr}, F_{WH} and particle elongation. The correlation matrix shows that, as we go from 1D shape descriptors to 2D and then to 3D shape descriptors, the relation between shape descriptors of different

dimensions weakens so that there is almost no correlation between 1D descriptors and sphericity. Amongst 1D descriptors, F_{Kr} has the highest correlation coefficient with the sphericity and, as shown in Fig. 3.7, its range of variability is also very close to that of sphericity. But in any case, the correlation between F_{Kr} and sphericity is not significant as it can be seen from their scatterplot. Strong correlations between $\overline{\phi}_{Riley}$ and most of 1D descriptors, in particular F_{Kr} and F_{WH}, exist. This can be explained by looking at the formulation of $\overline{\phi}_{Riley}$ ($= \sqrt{D_i/D_c}$) that is defined based on 2D variables that are constrained by 1D variables. In fact, D_c and D_i are constrained by L and S, respectively, and as a result $\overline{\phi}_{Riley}$ can be roughly approximated by $\sqrt{S/I}$. Interestingly, the correlation between $\overline{\phi}_{Riley}$ and $\overline{\phi}_{Cox}$ is not very strong ($r = 0.68$) although both of them are introduced as measures of circularity. Finally, the sphericity, ψ, has very strong correlation with $\overline{\phi}_{Cox}$, whereas there is almost no correlation between the particle sphericity and $\overline{\phi}_{Riley}$. In the next section we discuss in more detail the relationship between sphericity and circularity measures.

Various shape descriptors are measured for both sample sets. All shape descriptors (Fig. 3.7), imply that the ash particles of Sample Set 2 are more irregular compared to particles of Sample Set 1. This indicates that, at least for the sample sets characterized in this study, shape of volcanic particles is a function of size and irregularity increases with decreasing size. A more definite conclusion could be made if a larger number of ash-size particles were characterized. The decrease for the shape descriptors shown in Fig. 3.7 between ash and lapilli-size particles is around 5 – 42%.

3.5.3 Indirect evaluation of 3D parameters based on 1D and 2D variables

In this section we investigate how results obtained in previous sections can be used for indirect evaluation of 3D parameters (i.e. volume, surface area and sphericity). First, we benchmark existing strategies and then we introduce new strategies that are associated with smaller relative errors and uncertainties. Volume, surface area and sphericity of 3D models (obtained from LS or SEM micro-CT) are considered as

the reference values for benchmarking estimations of 1D- and 2D-based strategies.

Existing strategies

Volume

In order to estimate particle volume indirectly from 1D or 2D variables, the equivalent spherical diameter of the particle, d_{eq}, should first be estimated. The most used techniques for estimating from 1D variables is to average the particle form dimensions either arithmetically, $d_A = (L + I + S)/3$, or geometrically, $d_G = \sqrt[3]{L\,I\,S}$. As mentioned earlier, estimating d_{eq} by d_G is equivalent to estimating particle volume by volume of the equivalent ellipsoid. For estimating d_{eq} from 2D variables, a common method is to use the circle equivalent diameter that is averaged over multiple projections, $\overline{d_{2D}}$ (Garboczi et al., 2012; Asahina and Taylor, 2011; Taylor et al., 2006; Mills and Rose, 2010; Biass and Bonadonna, 2011). However, in some applications only a single projection of the particle obtained from microscope is used to estimate $\overline{d_{2D}}$ (Riley, 2003; Scollo, 2005; Coltelli et al., 2008). Therefore, in addition to $\overline{d_{2D}}$, we also consider the circle equivalent diameter of particles obtained from their maximum area projection, $max(d_{2D})$, as another common estimator for d_{eq}.

In Fig. 3.9 ratios of d_A, d_G, $max(d_{2D})$ and $\overline{d_{2D}}$ to the reference d_{eq} versus particle sphericity for both sets of particles are shown. Interestingly, all ratios are greater than one, which indicates that in all cases d_{eq} is overestimated (up to 80%) by parameters based on 1D or 2D variables. On average the overestimation of d_A is 16%, of $max(d_{2D})$ is 26% and values of both d_G and $\overline{d_{2D}}$ are on average 12% higher than d_{eq}. However, if more particles with sphericity lower than 0.5 existed in our sample, the average of overestimation could be higher. The general trend in Fig. 3.9 shows that the overestimation is strongly dependent on the particle sphericity so that, as the particle sphericity increases, the overestimation decreases. For each parameter a non-linear curve is fitted and their coefficients of determination, R^2, are shown on the plot. Slope of fitted curves indicate that ratios of d_A and $max(d_{2D})$ to d_{eq} are more affected by the particle sphericity than those of d_G and $\overline{d_{2D}}$.

Surface area (SA)

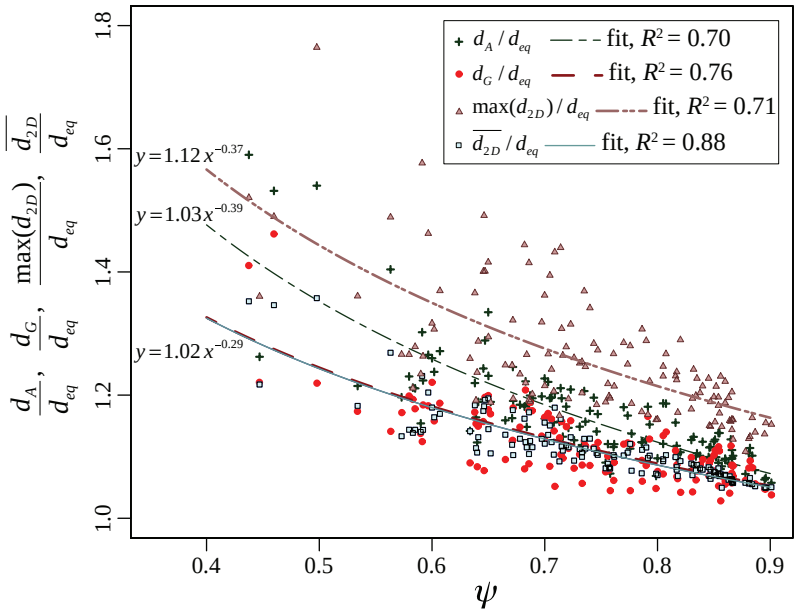

Figure 3.9: d_{eq} and ψ are obtained from LS and SEM micro-CT measurements. For each parameter, a power-law curve is fitted and the associated coefficient of determination, R^2, is shown.

The common method for estimating SA from 1D variables is the surface area of an ellipsoid with the same form dimensions as the particle, as shown in Eq. (3.1) (Kunii and Levenspiel, 1968; Dellino et al., 2005; Taylor et al., 2006). Taylor et al. (2006) found that the SA of crushed granite rocks obtained from X-ray CT are on average 10% higher than $SA_{ellip.}$. In the case of volcanic particles, Dellino et al. (2005) directly used $SA_{ellip.}$ for estimating surface area of lapilli-sized particles (2 mm to 64 mm), whereas Ersoy et al. (2010) found $SA_{ellip.}$ to be inadequate for estimating surface area of volcanic ash ($d_{eq} < 125\,\mu m$).

Among approaches based on 2D variables, Cauchys theorem (Cauchy, 1832) is the most used method for estimating particle surface area (Taylor et al., 2006). Cauchy (1832) proved that the actual surface area of a convex body is equal to four times the average of projected areas:

$$SA_{Cauchy} = \pi\,\overline{d_{2D}}^2 \tag{3.2}$$

A particle is convex if every line segment between two vertices remains inside or on the boundary of the particle. Later, Underwood (1970) proved that for non-convex bodies Cauchys method is the minimum bound. Therefore, any deviation

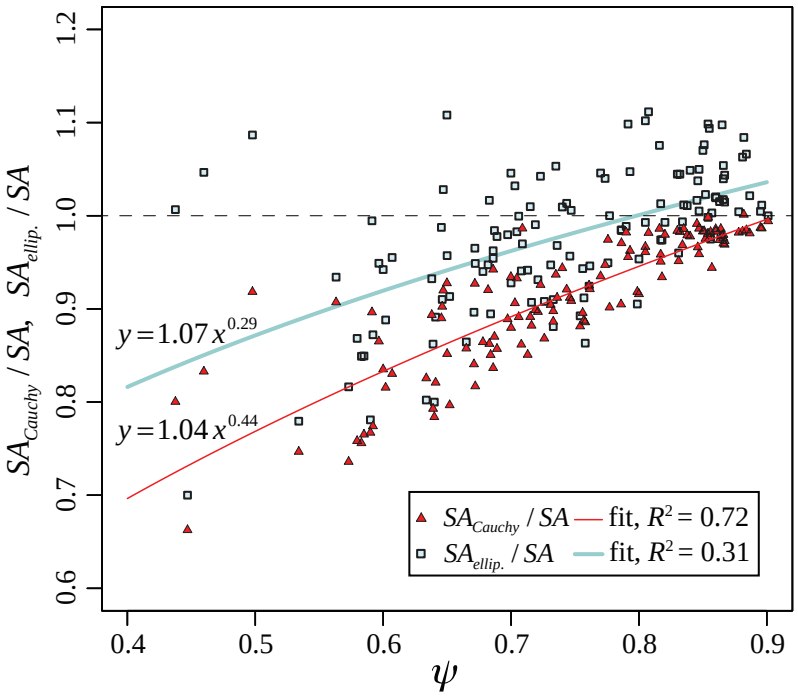

Figure 3.10: Ratios of $SA_{ellip.}$ (Eq. 3.1) and $SA_{Cauchy.}$ (Eq. 3.2) to SA versus sphericity, ψ. SA and ψ are obtained from LS and SEM micro-CT measurements. For each parameter, a power-law curve is fitted and the associated coefficient of determination, R^2, is shown.

between results obtained by Cauchys method and actual surface area of particles can be interpreted as a non-convexity measure.

In this study, both $SA_{ellip.}$ and SA_{Cauchy} are calculated for particles of Sample Set 1 and 2 and compared against reference SA (Fig 3.10). Data points of $SA_{ellip.}/SA$ are scattered around 1.0 with a weak correlation with the particle sphericity. The fitted curve for $SA_{ellip.}/SA$ indicates that in most cases when the particle sphericity is less than 0.8, $SA_{ellip.}$ underestimates surface area and when sphericity is greater than 0.8, it overestimates surface area. On the other hand, the ratio of SA_{Cauchy}/SA is always less than 1.0, which is a sign of non-convexity of volcanic particles (Underwood, 1970).

Sphericity

Results presented in Figs. 3.7 and 3.8 show that the particle sphericity is sensitive to surface vesicularity and, therefore, 1D shape descriptors are not good candidates for estimating particle sphericity. 2D shape descriptors, on the other hand, are sensitive

to the particle vesicularity and therefore are better candidates for the estimation of sphericity. In particular, the Cox circularity (Cox, 1927), $\overline{\phi}_{Cox}$, has a strong correlation with the particle sphericity (Fig. 3.8). Using circularity measures for estimating the sphericity is also suggested by Blott and Pye (2007). They proposed that the Riley circularity (Riley, 1941), $\overline{\phi}_{Riley}$, is the best to be used for estimating the particle sphericity since it is simple to calculate and its estimation is in agreement with another circularity index proposed by citeWadell1935.

Fig. 3.11 shows the variation of sphericity obtained from LS and SEM micro-CT with respect to $\overline{\phi}_{Riley}$ and $\overline{\phi}_{Cox}$ obtained by image analysis. In Fig. 3.11, $\overline{\phi}_{Riley}$ points are scattered and have a weaker correlation with the particle sphericity. Compare to $\overline{\phi}_{Riley}$, $\overline{\phi}_{Cox}$ is less scattered and has strong positive correlation with the particle sphericity. However, in general, none of circularity measures is good for estimating sphericity of both vesicular and non-vesicular particles, since $\overline{\phi}_{Riley}$ overestimates sphericity of vesicular particles and $\overline{\phi}_{Cox}$ underestimates sphericity of non-vesicular particles. The best estimations for sphericity are $\overline{\phi}_{Riley}$ for non-vesicular particles and $\overline{\phi}_{Cox}$ for vesicular particles.

3.5.4 New strategies

In previous section it was shown that existing strategies for estimating particle volume and surface area could be improved if particle sphericity is taken into account. Sphericity can be best constrained when the characteristics of the particle surface are considered, e.g. vesicularity. As a result, new strategies are separately introduced for each category of vesicular and non-vesicular particles (Table 3.4 and Fig. 3.12). First, we provide correlations based on only 1D variables, as they are the simplest to obtain. Then we investigate how accurate 3D parameters can be estimated by using various combinations of 1D and 2D variables.

Evaluation of 3D parameters based on 1D variables only

Sphericity cannot be well constrained only based on 1D variables as vesicularity requires a 2D or 3D shape descriptors (Fig. 3.8). Therefore simple linear curve fitting is the most straightforward solution for estimating d_{eq} from d_G, and SA from $SA_{ellip.}$:

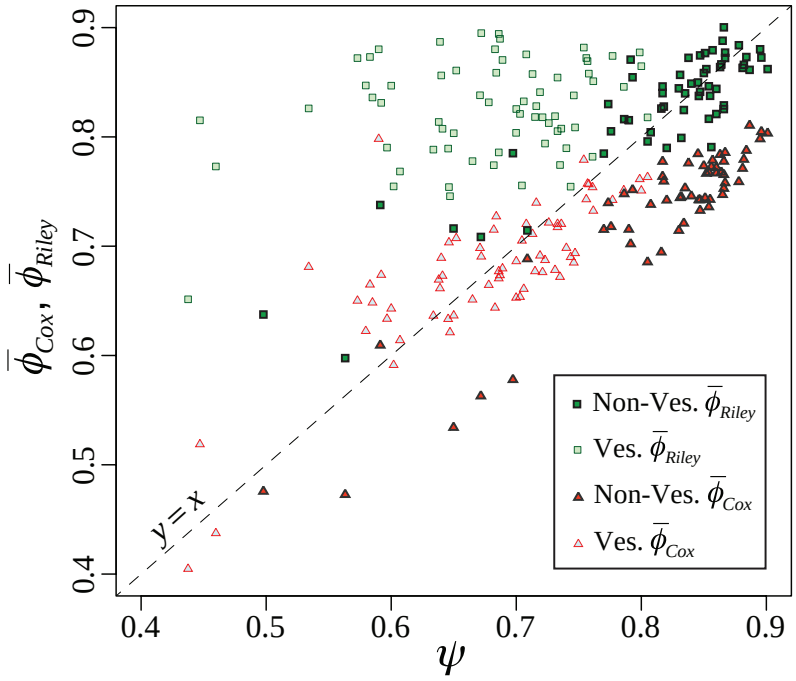

Figure 3.11: The variation of Cox circularity (Cox, 1927), $\overline{\phi}_{Cox}$, and Riley circularity (Riley, 1941), $\overline{\phi}_{Riley}$, obtained by image analysis versus sphericity, ψ, obtained from LS and SEM micro-CT measurements. $\overline{\phi}_{Cox}$ and $\overline{\phi}_{Riley}$ are obtained by averaging ψ_{Cox} and ψ_{Riley} over 1000 projections.

$$d_{eq} = \begin{cases} 0.928\, d_G & \text{non-vesicular particles} \\ 0.887\, d_G & \text{vesicular particles} \end{cases} \tag{3.3}$$

$$SA = \begin{cases} 0.995\, SA_{ellip.} & \text{non-vesicular particles} \\ 1.094\, SA_{ellip.} & \text{vesicular particles} \end{cases} \tag{3.4}$$

The best estimation of sphericity based on 1D variables is derived from the sphericity definition summarized by Eqs. (3.3) and (3.4):

$$\psi = \begin{cases} \pi(0.928\, d_g)^2/(0.995\, SA_{ellip.}) & \text{non-vesicular particles} \\ \pi(0.887\, d_g)^2/(1.094\, SA_{ellip.}) & \text{vesicular particles} \end{cases} \tag{3.5}$$

The relative error associated with Eqs. (3.3) to (3.5) are shown with boxplots in Fig. 3.12. The lowest average error is for d_{eq} and the highest is for sphericity. In summary, maximum error by neglecting outliers is less than 10% for estimating d_{eq} and less than 20% for estimating SA and ψ. It is important to mention that most

outliers in the corresponding boxplot of Eq. (3.5) are related to vesicular particles.

Evaluation of 3D parameters based on 1D and/or 2D variables

Figs. 3.9 and 3.10 showed that estimating d_{eq} and SA from 1D and 2D variables is highly correlated with sphericity. Therefore, if we want to estimate 3D parameters from 1D and\or 2D variables we should start with the sphericity. In the previous section, Eq. (3.5) is presented for estimating particle sphericity only based on 1D variables that is associated with maximum error of less than 20% and outliers with errors up to 50%. However, in Figs. 3.8 and 3.11 it was shown that sphericity could be estimated better from 2D circularity measures than from 1D shape descriptors. In particular, $\overline{\phi}_{Riley}$ gives the best results for sphericity of non-vesicular particles, while $\overline{\phi}_{Cox}$ is best for estimating sphericity of vesicular particles (Fig. 3.11), which is:

$$\psi = \begin{cases} \overline{\phi}_{Riley} & \text{non-vesicular particles} \\ \overline{\phi}_{Cox} & \text{vesicular particles} \end{cases} \tag{3.6}$$

Where vesicular particles are those covered with vesicles with opening diameter of the corresponding to 5 – 40% of d_{eq}, with a mode at around 10 – 25%, otherwise they are considered as non-vesicular. For error analysis of the correlations presented in this section two scenarios are considered: when 1000 projections are used, $N = 1000$, and when only the maximum area projection of the particle is used, $N = 1$, for calculating 2D variables (in latter case the boxplot label is marked by *). For Eq. (3.6), sphericity estimations have an average error of 4.6% while the average error of Eq. (3.6*) (see the definition in Table 3.4) is 7.6% (see Fig. 3.12). In any case, the maximum errors associated with Eqs. (3.6) and (3.6*) are lower than that of Eq. (3.5).

For estimating the following equations can be written based on curve fits found in Fig. 3.9:

$$d_{eq} = \frac{d_G}{1.022\,\psi^{-0.29}} \tag{3.7}$$

$$d_{eq} = \frac{\overline{d_{2D}}}{1.022\,\psi^{-0.29}} \tag{3.8}$$

$$d_{eq} = \frac{max(d_{2D})}{1.119\,\psi^{-0.37}} \tag{3.9}$$

In Eqs. (3.7) and (3.8) ψ is estimated from Eq. (3.6) and in the case of Eqs. (3.7*) and (3.9), where only a single projection is considered to be available for calculating 2D variables, ψ is estimated from Eq. (3.6*). Fig. 3.12 shows that the lowest average error of 1.9% for estimating d_{eq} of particles of Sample Sets 1 and 2 is obtained by using Eq. (3.8). The associated average error of Eq. (3.7) is 2.6% that is not significantly higher than that of Eq. (3.8). In the case of Eq. (3.7*) (see the definition in Table 3.4), where just a single projection of the particle is used for estimating ψ, an average error of 2.8% is obtained that is comparable to that of Eq. (3.7). The highest estimation error is associated with Eq. (3.9) that is on average 5.5%. This can be explained by the fact that in Eq. (3.9) both $max(d_{2D})$ and sphericity are calculated from a single projection. However, an average error of 5.5% is a significant improvement compared to the average error of 26% found when d_{eq} is directly estimated by $max(d_{2D})$ (see Fig. 3.9).

Particle surface area is estimated from several methods. The first method is to use the sphericity definition (Table 3.3) to calculate surface area based on sphericity and d_{eq}:

$$SA = \frac{\pi\, d_{eq}^2}{\psi} \tag{3.10}$$

The second option is to use curve fits shown in Fig. 3.10 for improving the estimations of $SA_{ellip.}$ and SA_{Cauchy}. However, $SA_{ellip.}$ estimations cannot be improved by sphericity since the correlation between $SA_{ellip.}/SA$ and sphericity is very weak. On the other hand, SA_{Cauchy}/SA has a strong correlation with sphericity and using sphericity as the second parameter can significantly improve estimations of Cauchys method:

$$SA = \frac{SA_{Cauchy}}{1.044\,\psi^{-0.44}} \tag{3.11}$$

Table 3.4: Summary of new correlations obtained in the present study for estimating 3D parameters from 1D and 2D variables. Presented notes in this table indicate how the equations are combined together in order to perform the error analysis shown in Fig. 3.12. All 2D-related parameters (e.g. d_{2D}, SA_{Cauchy}, ϕ_{Riley}, ϕ_{Cox} needed for error analysis of Eqs. (3.6*), (3.7*), (3.9), (3.10*) and (3.11*) are obtained from a single projection (i.e. the maximum projection area).

Eq.	Formula	Type	Notes
Spherical equivalent diameter (d_{eq})			
(3.3)	$d_{eq} = \begin{cases} 0.928\, d_G & \text{non-ves.} \\ 0.887\, d_G & \text{ves.} \end{cases}$	1D	
(3.7)	$d_G/1.022\,\psi^{-0.29}$	1D	ψ from Eq. (3.6)
(3.7*)	$d_G/1.022\,\psi^{-0.29}$	1\2D	ψ from Eq. (3.6*)
(3.8)	$\overline{d_{2D}}/1.022\,\psi^{-0.29}$	2D	ψ from Eq. (3.6)
(3.8*)	$max(d_{2D})/1.119\,\psi^{-0.37}$	2D	ψ from Eq. (3.6*)
Surface area (SA)			
(3.4)	$SA = \begin{cases} 0.995\, SA_{ellip.} & \text{non-ves.} \\ 1.094\, SA_{ellip.} & \text{ves.} \end{cases}$	1D	
(3.10)	$\pi\, d_{eq}^2/\psi$	2D	ψ from Eq. (3.6) and d_{eq} from Eq. (3.8)
(3.10*)	$\pi\, d_{eq}^2/\psi$	2D	ψ from Eq. (3.6*) and d_{eq} from Eq. (3.9)
(3.11)	$SA_{Cauchy}/1.044\psi^{-0.44}$	2D	ψ from Eq. (3.6)
(3.11*)	$SA_{Cauchy}/1.044\psi^{-0.44}$	2D	ψ from Eq. (3.6*)
Sphericity (ψ)			
(3.5)	$\psi = \begin{cases} \pi\, d_{eq}^2/SA & \text{non-ves.} \\ \pi\, d_{eq}^2/SA & \text{ves.} \end{cases}$	1D	d_{eq} from Eq. (3.3) and SA from Eq. (3.4)
(3.6)	$\psi = \begin{cases} \overline{\phi}_{Riley} & \text{non-ves.} \\ \overline{\phi}_{Cox} & \text{ves.} \end{cases}$	2D	$\overline{\phi}_{Riley}$ and $\overline{\phi}_{Cox}$ are obtained by averaging ϕ_{Riley} and ϕ_{Riley} over 1000 projections
(3.6*)	$\psi = \begin{cases} \phi_{Riley} & \text{non-ves.} \\ \phi_{Cox} & \text{ves.} \end{cases}$	2D	ϕ_{Riley} and ϕ_{Riley} are obtained from a single projection (i.e. the maximum area projection)

In Eqs. (3.10) and (3.11), is estimated from Eq. (3.6) and from Eq. (3.8). For Eqs. (3.10*) and (3.11*) (see the definitions in Table 3.4), i.e. where a single projection is considered, is estimated from Eq. (3.6*) and is calculated from Eq. (3.9) since it is originally derived based on a single projection. Fig. 3.12 shows that results obtained from Eq. (3.11) have the lowest average error, i.e. 2.7%. On the other hand, Eq. (3.11*) is associated with an average error of 25% and maximum error of 60%. After Eq. (3.11), Eq. (3.10) is associated with the lowest value of average error (3.8%). If only a single projection is used for calculating 2D variables, Eq. (3.10*) with an average error of 8.3% performs significantly better than Eq. (3.11*).

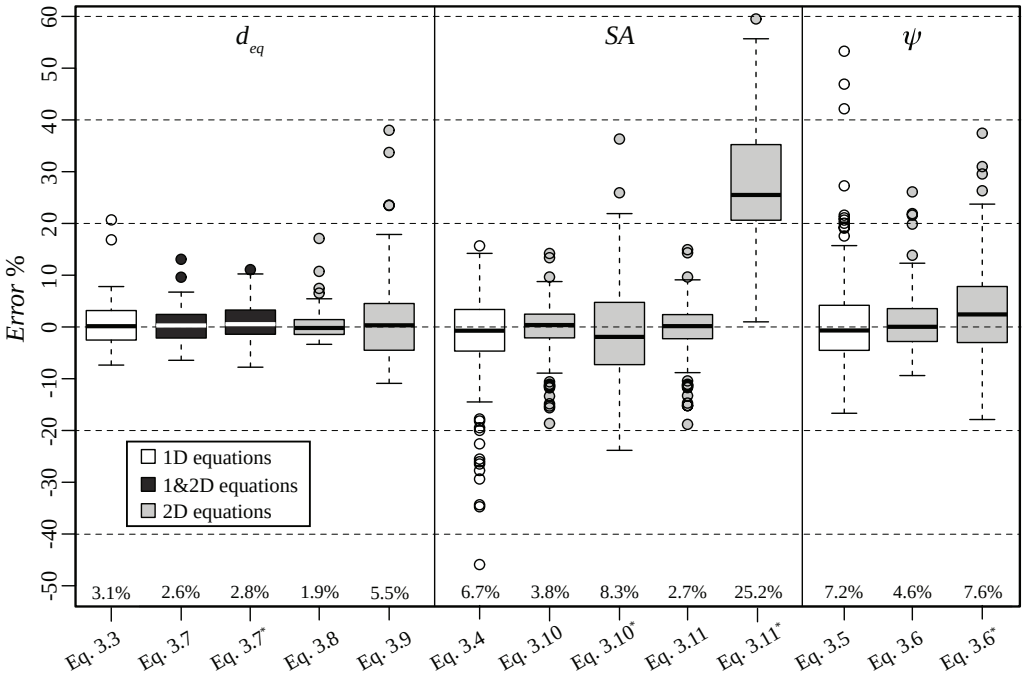

Figure 3.12: Distribution of relative errors for estimating spherical equivalent diameter, d_{eq}, surface area, SA, and sphericity, ψ, of particles by using Eqs. (3.3) – (3.11) (See Table 3.4 for details). Relative error, $Error\%$, is defined as $(estimation - reference) \times 100/reference$, where reference values for d_{eq}, SA and ψ are obtained from LS and SEM micro-CT measurements. Numbers at the bottom of boxplots are the absolute mean of $Error\%$ ($|\overline{Error\%}|$).

All equations shown in Fig. 3.12 and the way they are implemented for error analysis are summarized in Table 3.4. The objective of presenting various correlations in this study is not just to evaluate which is the most reliable model, but also to provide useful information for applications where particle characterization is limited to a few number of inputs, such as 2D variables obtained only from a single projection. In such applications, the error analysis presented in Fig. 3.12 clarifies the uncertainty associated with different methods. It is important to note that the obtained correlations (especially correlations based on 1D\2D and 2D variables) might be also used for characterization or firsthand estimations of size and shape of irregular and non-volcanic particles especially if they are non-convex particles.

3.6 Discussion and conclusions

Size and shape of 127 irregular volcanic particles of various origins and textural properties were characterized using caliper, LS, SEM micro-CT and image analysis.

This is the first study that characterizes size and shape of volcanic particles in a wide range of size (155 µm to 36 mm) and based on a wide range of measurement strategies. Particles characterized in this study are also good general case studies of irregular particles and, therefore, all results have fundamental implications for the description of particle transport and sedimentation in various environments, e.g. particle fallout and dispersal during volcanic eruptions, river sedimentations and aerosol dispersal. Based on our results the following conclusions can be drawn for the characterization of irregular particles:

- The PA (Projection Area) protocol introduced in this study for measuring form dimensions (i.e. L, I, S) is associated with the lowest operator-related errors with respect to existing protocols and associated form dimensions perform better for both the correlation and estimation of particle volume and surface area. In addition, the PA protocol is much easier to apply since it is not necessary to maintain the perpendicularity between projections or measured dimensions.

- The use of two (i.e. minimum and maximum area) or three perpendicular particle projections for measuring 2D variables was found to be the best compromise between analysis time and accuracy (maximum error compared to when 1000 projections are used is $< 10\%$).

- Particle sphericity ψ represents an important parameter for indirect evaluation of particle volume and surface area based on 1D and 2D variables (Figs. 3.9 and 3.10). As a result, if indirect and reliable evaluations of particle volume and surface area are needed, particle sphericity should be evaluated first. However, none of existing 1D shape descriptors (e.g. Aschenbrenner working sphericity (Aschenbrenner, 1956), Sneed and Folk maximum projection sphericity (Sneed and Folk, 1958)) have strong correlations with the sphericity (Fig. 3.8). If only 1D variables are available, Eq. (3.5) can be used for estimating sphericity that is associated with average error of 7.2% and maximum errors up to 20% (Fig. 3.12). More accurate sphericity estimations can be achieved by using 2D circularity measures (i.e. $\overline{\phi}_{Riley}$ and $\overline{\phi}_{Cox}$) since they are highly correlated

with sphericity (Figs. 3.8 and 3.11). A new correlation based on circularity measures and vesicularity of particles, Eq. (3.6), was found that could estimate sphericity of particles with an average error of 4.6% (Fig. 3.12).

- The best strategies to evaluate 3D parameters indirectly (i.e. volume, surface area, sphericity), are those based on 2D variables with average errors of 2.4 – 4.6% (Fig. 3.12). Estimations of 3D parameters based on 1D variables only are associated with higher average errors (between 3.1 – 7.2%) and, if used, maximum errors up to 50% have to be considered. Out of all correlations found for estimating 3D parameters from 1D and 2D variables, those related to sphericity have highest average errors. We can conclude that sphericity is the most challenging parameter to be estimated from 1D and 2D variables. Correlations summarized in Table 3.4 and associated uncertainties shown in Fig. 3.12 provide various solutions and fundamental insights for applications when 3D parameters need to be evaluated indirectly.

- Based on a correlation matrix (Fig. 3.8), it was found that all the form factors (i.e. 1D shape descriptors) are strongly correlated with either elongation or flatness. Therefore, they can be replaced with each other in order to reduce number of shape descriptors for characterizing particle shape.

3.7 Appendices

The dataset used to obtain outcomes of this chapter is available on the accompanied CD-ROM.

3.8 Acknowledgments

This research is funded by the Swiss National Science Foundation (SNSF, Grant No. 200020-125024).

3.9 Author's contributions

G. Bagheri performed the 3D laser scanning and P. Vonlanthen performed the SEM micro-CT. The statistical and image analyses are conducted by G. Bagheri. All authors were involved in the drafting and reviewing of this chapter.

Chapter 4

On the Drag of Freely Falling Non-Spherical Particles[1]

4.1 Introduction

Non-spherical particles are encountered in numerous fields of science and engineering, such as chemical engineering, civil engineering, mining engineering, physical sciences, biology and earth sciences (Happel and Brenner, 1983; Blott and Pye, 2007). The category of non-spherical particles, in general, includes both regular (e.g. ellipsoid, cube, cylinder) and irregular shapes (e.g. pharmaceutical powders, spore, pollen, coal particles, cosmic and atmospheric dust, sand, pebble, volcanic particles). Nonetheless, in many studies that deal with particulate flows, particles are assumed to be perfect spheres. This is mainly due to the fact that the shape characterization of irregular particles is a complex process and numerous shape descriptors have been developed in the past few decades to quantify various aspects, such as form, roundness, irregularity and sphericity (Blott and Pye, 2007; Bagheri et al., 2015). More importantly, the most accurate models for predicting the behavior of non-spherical particles in fluids are based on studies on regular particles (Haider and Levenspiel, 1989; Ganser, 1993; Chhabra et al., 1999), for which the characterization of the particle shape is not complex and can be obtained analytically.

Particles of arbitrary shapes when transported in a fluid experience forces and mo-

[1] Submitted to: *Powder Technology*; Bagheri G., Bonadonna C. (submitted): On the Drag of Freely Falling Non-Spherical Particles.

mentum on all three coordinate axes (White, 1998). In many applications the most important force acting on a particle is the one that is exerted in the opposite direction of particle motion, which is called the drag force F_D and defined as:

$$F_D = \frac{1}{2}\rho_f C_D A v_r^2 \tag{4.1}$$

where ρ_f is the fluid density, C_D is the drag coefficient of the particle, A is a reference area related to the particle size (e.g. $\pi d^2/4$ for a sphere with diameter of d), v_r is the relative velocity between the particle and fluid, and the factor $1/2$ is the traditional tribute to Euler and Bernoulli (White, 1998). The most challenging parameter to be determined in Eq. (4.1) is the drag coefficient C_D, which is dependent on many parameters including particle Reynolds number Re, shape, orientation, secondary motions, particle to fluid density ratio, fluid turbulence intensity and particle/fluid acceleration (Isaacs and Thodos, 1967; Stringham et al., 1969; Clift and Gauvin, 1971; Marchildon and Gauvin, 1979; Haider and Levenspiel, 1989; Ganser, 1993; Clift et al., 2005; Loth, 2008; Hölzer and Sommerfeld, 2008; Bagheri et al., 2013; Brosse and Ern, 2013). However, the main parameters that have a first order influence on C_D are particle Reynolds number Re, shape, particle to fluid density ratio and orientation (Loth, 2008; Hölzer and Sommerfeld, 2008; Brosse and Ern, 2013). Here, particle Reynolds number, Re , for both spherical and non-spherical particles is defined as:

$$Re = \frac{\rho_f d_{eq} |v_r|}{\mu_f} \tag{4.2}$$

where d_{eq} is the diameter of a sphere with the same volume as the particle and μ_f is the fluid dynamic viscosity. Except at very low values of Re ($\ll 1$), where an analytical solution exists for spheres based on Stokes solution (Stokes, 1851) and for ellipsoids based on Oberbeck solution (Oberbeck, 1876), no general solution can be found for calculating the drag coefficient of particles of any shape (Happel and Brenner, 1983; Clift et al., 2005; Loth, 2008). At higher Re, even for spherical particles, where quantification of particle shape is not an issue, experimental measurements are the main source of information while numerical solutions and boundary layer

theory can provide additional information (Clift et al., 2005).

In the absence of a general solution, a large number of empirical correlations for predicting the drag coefficient of spherical and non-spherical particles are introduced that are associated with different ranges of validity and accuracy (Wieselsberger, 1922; Albertson, 1953; Willmarth et al., 1964; Marchildon et al., 1964; Christiansen and Barker, 1965; Jayaweera and Mason, 1965; Isaacs and Thodos, 1967; Stringham et al., 1969; Komar and Reimers, 1978; Marchildon and Gauvin, 1979; Wilson and Huang, 1979; Baba and Komar, 1981; Leith, 1987; McKay et al., 1988; Haider and Levenspiel, 1989; Ganser, 1993; Cheng, 1997; Gögüs et al., 2001; Clift et al., 2005; Loth, 2008; Mandøand Rosendahl, 2010; Chow and Adams, 2011; Alfano et al., 2011). However, available correlations in the literature are associated with some drawbacks. First, data used in previous studies are mostly based on experiments on particles of regular shapes (e.g. cube, cylinder, disk). Available data for irregular particles lack of an accurate characterization of particle shape and size, or they do not cover a wide range of Reynolds numbers (Albertson, 1953; Komar and Reimers, 1978; Wilson and Huang, 1979; Baba and Komar, 1981; Cheng, 1997; Dellino et al., 2005). Second, most formulations are based on sphericity that is a function of particle surface area, which, in the case of irregular particles, is one of the most challenging parameters to be determined and requires sophisticated instruments (Bagheri et al., 2015). Third, almost all the available data are based on experiments in liquids for which the particle to fluid density ratio, $\rho' = \rho_p/\rho_f$, is in the order of $1 - 11$, whereas ρ' for solid particles moving in gases can be up to the order of 10^3. ρ' is an important parameter that can influence particle drag coefficient, especially at high Reynolds numbers. Finally, the effect of surface roughness and vesicularity on the drag coefficient of irregular particles is not yet well understood.

In the present study, a comprehensive analytical and experimental investigation on the drag coefficient of non-spherical particles including regular and irregular shapes with $Re < 3 \times 10^5$ is carried out. At $Re < 0.1$ (i.e. Stokes regime) the analytical solution of Oberbeck (Oberbeck, 1876) is solved numerically for ellipsoids with various elongation and flatness ratios. At $0.1 \leq Re < 1000$ (i.e. intermediate regime), the drag coefficient of 100 highly irregular volcanic particles and 17 regular

shape particles (i.e. cylinders and cubes) are measured in air-filled settling columns of various heights ($0.45 - 3.6m$). Finally, a vertical wind tunnel (Bagheri et al., 2013) is used to measure the drag coefficient of 116 irregular volcanic particles and 61 regular shape particles (i.e. ellipsoids, circular cylinder, disks, other geometrical shapes) at $1000 \leq Re < 3 \times 10^5$ (i.e. Newton's regime). A total of 10^4 analytical and 1285 experimental data points measured in the air are obtained. In addition, 881 experimental data points compiled from the literature for spherical and regular particles, most of which measured in liquids, are also considered (Pettyjohn and Christiansen, 1948; Willmarth et al., 1964; Christiansen and Barker, 1965; Isaacs and Thodos, 1967; McKay et al., 1988).

The main objective of this study is to find the simplest and the best correlated shape descriptors that could be used to estimate the drag coefficient of both regular and irregular particles moving in liquids (based on published data) or gases (based on new results). In addition, types of particle secondary motion, the effect of particle orientation, the effect of particle to fluid density ratio ρ' and surface roughness on the drag coefficient are discussed. Finally, a general drag coefficient model is presented that is valid for predicting the average and end members of drag coefficient of non-spherical particles freely moving in gases or liquids.

In the following sections, first we present a introduction on the aerodynamics of particles and associated effective parameters followed by a thorough review of the existing models for predicting the drag coefficient of spherical and non-spherical particles. Then methods and materials used in this study are described. Finally, results are presented and the impact of effective parameters on the drag coefficient of non-spherical particles is discussed in detail.

4.2 Aerodynamics studies: state-of-the-art

4.2.1 Aerodynamics of spherical particles

Drag of non-spherical particles can be framed easier if first we analyze aerodynamics of spherical particles. A great number of analytical, numerical and experimental studies can be found that are focused on the aerodynamics and, in particular, on

the drag of spheres (Clift et al., 2005). In addition, the dependency of the drag of non-spherical particles on Reynolds number is, in general, very similar to that of spherical particles.

Flow development as a function of Re

As it is shown in Fig. 4.1, the fluid flow around spherical particles is strongly dependent on the particle Reynolds number. The flow at $Re \ll 1$ is called the *Stokes regime* (or *creeping flow*), where the flow inertial terms are negligible with respect to viscous terms and flow remains attached to sphere with no wake behind (White, 1998). The flow remains attached up to $Re \approx 20$, which is the onset of flow separation. At $20 < Re < 130$ circular wakes behind a sphere grow but they remain steady and attached to the particle. As Re increases beyond 130 and up to 1000, vortex shedding begins and wakes behind the sphere gradually become instable and unsteady. At $1000 < Re < 3 \times 10^5$ wakes behind the sphere become fully turbulent while the boundary layer at the front of the sphere is laminar. This range of Reynolds number is called the *Newton's regime* (Clift et al., 2005). $Re > 3 \times 10^5$ corresponds to critical transition and supercritical regime where boundary layer and wake behind sphere are both turbulent. $Re = 3 \times 10^5$ is called the *critical Reynolds number*, at which the *drag crisis* occurs and reduces the drag coefficient markedly (Clift and Gauvin, 1971; Achenbach, 1972; Clift et al., 2005; Loth, 2008).

Dependency of C_D **on** Re

The variation of the sphere drag coefficient at subcritical Re can be studied in three different Reynolds regimes, namely the Stokes, intermediate and the Newton's regimes (Fig. 4.1). In 1851 Stokes (Stokes, 1851) showed that at $Re \ll 1$, where inertial terms in the Navier-Stokes equations are negligible, Navier-Stokes equations can be simplified to a linear differential equation, which can be solved analytically. Stokes solution showed that the drag coefficient of a smooth solid spherical particle in standard conditions (i.e. moving with constant relative velocity in an undistributed,

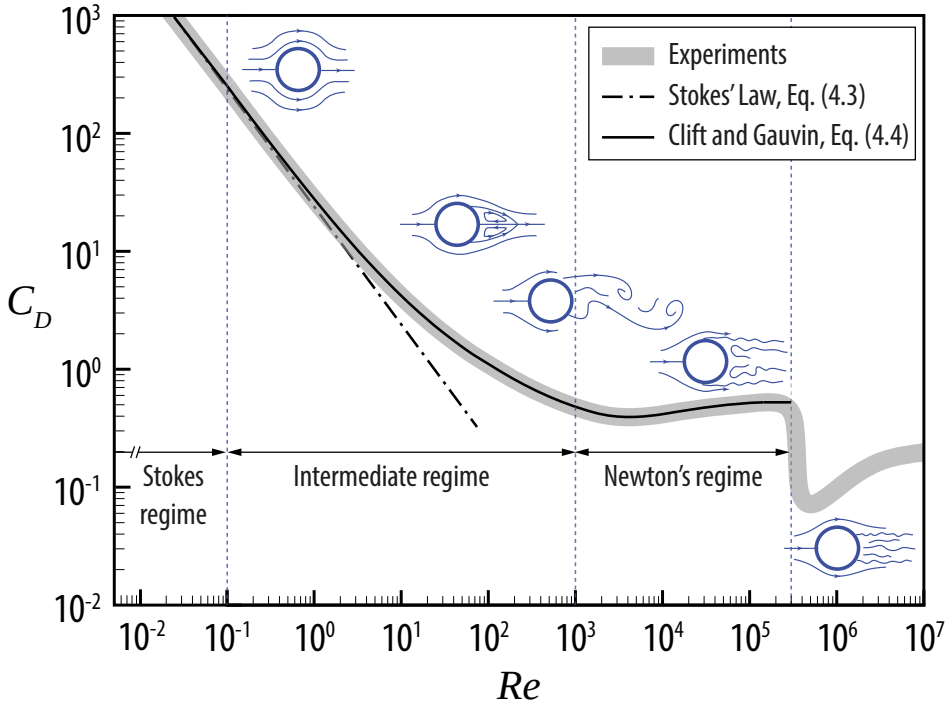

Figure 4.1: Dependency of C_D on Re for sphere. Streamlines around sphere at various Re are also shown in the plot.

unbounded and incompressible flow) at $Re \ll 1$ is (Stokes, 1851; Clift et al., 2005):

$$C_D = \frac{24}{Re} \tag{4.3}$$

Two thirds of this drag is due to viscous stresses (i.e. *friction drag*) and one third to the pressure gradients (i.e. *form drag* or *pressure drag*). Sphere drag predicted by the Stokes' law at $Re = 0.1$ is 2% less than those obtained from more accurate solutions in which inertial terms are taken into account (Happel and Brenner, 1983). Thus, in this study $Re < 0.1$ is assigned as the range for the Stokes' regime, where the Stokes solution is associated with an error of $< 2\%$ for spherical particles.

In the intermediate regime ($0.1 \leq Re < 1000$), the sphere drag coefficient continues to decrease as Re increases although the rate of decrease is lower than that at the Stokes' regime. Finally, the drag coefficient becomes almost constant in the Newton's regime ($1000 \leq Re < 3 \times 10^5$) with a minimum of 0.38 at 5×10^3 and a maximum of 0.50 at 7×10^4 (Clift and Gauvin, 1971). Average of the drag coefficient for sphere in the Newton's regime is about 0.46. One of the most accurate

correlations for predicting the drag coefficient of spherical particles at subcritical Re is the model of Clift and Gauvin (1971):

$$C_D = \frac{24}{Re}\left(1 + 0.15Re^{0.687}\right) + \frac{0.42}{1 + \frac{42500}{Re^{1.16}}} \quad \text{for } Re < 3 \times 10^5 \tag{4.4}$$

Eq. (4.4) is valid for subcritical Re and is within 6% of experimental measurements (Fig. 4.1) (Clift et al., 2005).

4.2.2 Drag of non-spherical particles

The dependency of the drag coefficient of non-spherical particles on the particle Reynolds number is very similar to that of spheres. In fact, for non-spherical particles, parameters other than the particle Reynolds number, such as particle shape, surface roughness, orientation and particle to fluid density ratio are the source of complexities in the determination of the drag coefficient. The impact of these parameters on the drag coefficient is dependent on the particle Reynolds number. To provide a clear background, the effect of these parameters on the drag coefficient is presented separately in the following sections.

Shape

In general, at a given particle Reynolds number, the average of the drag coefficient of a falling non-spherical particle is higher than that of a sphere as a consequence of its non-spherical shape. As a result, the main challenge is to quantify the shape of particles through a shape descriptor that is well correlated with the drag coefficient. Shape descriptors are mathematical functions that require previous determination of dimensional variables of the particle, such as lengths, diameter, projection perimeter, surface area or volume (Bagheri et al., 2015). Ideally, the shape descriptor should be easy-to-measure for particles of both regular and irregular shapes. In studies related to transport and sedimentation of particles the most common shape descriptors are sphericity and *form factors* (e.g. flatness, elongation and their combinations) (Pettyjohn and Christiansen, 1948; McNown and Malaika, 1950; Sneed and Folk, 1958; Christiansen and Barker, 1965; Isaacs and Thodos, 1967; Wilson and

Huang, 1979; Baba and Komar, 1981; Leith, 1987; McKay et al., 1988; Haider and Levenspiel, 1989; Ganser, 1993; Gögüs et al., 2001; Loth, 2008; Chow and Adams, 2011). Sphericity ψ is defined as the ratio of surface area of a sphere with the same volume as the particle to the actual surface area of the particle $SA_{particle}$ (Wadell, 1933):

$$\psi = \pi d_{eq}^2 / SA_{particle} \tag{4.5}$$

Sphericity is equal to 1 for spheres and decreases as particles become less spherical. As a result, for a fixed particle volume, the drag coefficient has an inverse correlation with the sphericity. The main disadvantage of sphericity is its dependency on the particle surface area. Although the surface area of a regular particle with smooth surface can be measured analytically, for irregular particles surface area can only be measured with sophisticated instruments, such as 3D scanners. In addition, the measured surface area is a function of measurement accuracy and, in particular, it increases as the measurement resolution and accuracy increase (Bagheri et al., 2015). As a result, sphericity is not an absolute shape descriptor for irregular particles and should be reported with the measurement accuracy in order to be reproducible. Additionally, particles with different shapes can have the same sphericity. As an example, sphericity of a very elongated cylinder with height to diameter ratio of 20 ($h = 20\,d$) is equal to the sphericity of an extremely flat disk with height to diameter ratio of 0.1 ($h = 0.1\,d$) (Table 4.1).

Particle form factors are simpler to measure than sphericity, are less dependent on the measurement resolution and can better discriminate particles with different forms. In order to calculate form factors for a particle, its *form dimensions* should be measured, which are defined and noted as L: longest, I: intermediate and S: shortest length of the particle (Bagheri et al., 2015). The most common form factors are flatness f (S/I) and elongation e (I/L). It should be noted that form factors, similar to sphericity, are a sub-category of shape descriptors and they are called form factors because they can provide information on the tri-dimensional characteristic of the particles (e.g. can quantify how flat or elongate a particle form is). Fig. 4.2 shows how shapes of ellipsoids vary by changing their elongation and flatness ratios. The most common form factor related to drag of non-spherical particles

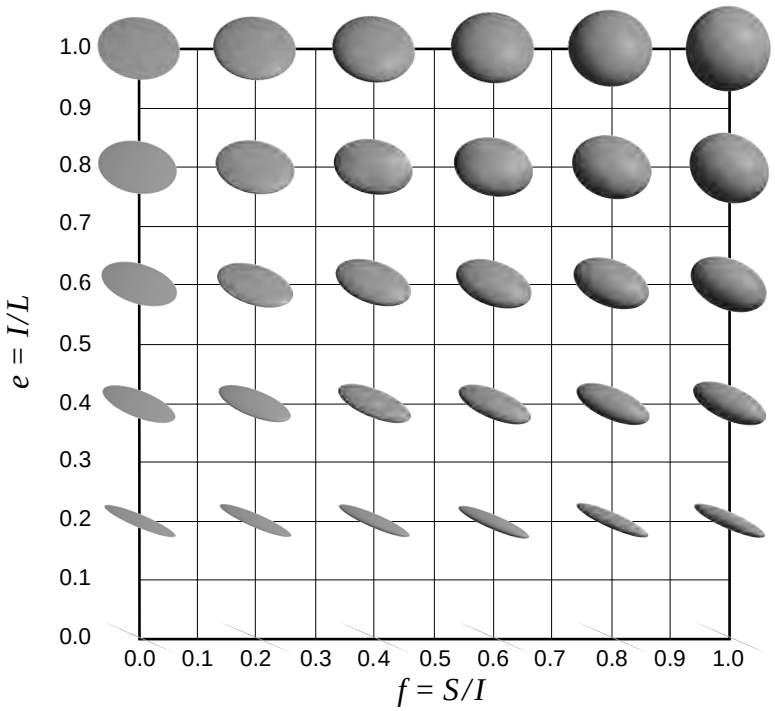

Figure 4.2: Effect of variation of flatness f and elongation e on the shape of ellipsoids. L, I and S are called from dimensions and defined as the longest, intermediate and shortest lengths of the particle, receptively.

is the Corey shape descriptor defined as $S/\sqrt{LI}$ (Albertson, 1953; Corey, 1963; Komar and Reimers, 1978; Loth, 2008), which is found to be highly correlated with the particle flatness (Bagheri et al., 2015). Interestingly, sphericity and Corey shape descriptor measured for irregular particles have a very weak correlation with each other (Bagheri et al., 2015), although they were both found to be correlated with the drag coefficient of non-spherical particles.

The main shortcoming of form dimensions is their dependency on the operator judgments (see Chapter 3). Several methods exist for measuring particle form dimensions that are associated with different levels of simplicity and operator-dependent errors. In Chapter 3 some of these methods are reviewed and a new method called the *projection area protocol* is presented. The projection area protocol is associated with the lowest operator-dependent errors and the measured form dimensions are better correlated with particle volume and surface area compared to other methods. Through the projection area protocol form dimensions are measured on two specific projections of the particle, namely the projections with maximum and minimum areas. L and I are defined as the largest and smallest dimensions mea-

sured on the maximum-area projection, and S corresponds to the smallest dimension measured in the minimum-area projection. Note that through this procedure form dimensions do not need to be perpendicular with each other. In this way, L and S correspond to the largest and smallest lengths of the particle, respectively, and therefore, are less affected by operator-dependent errors (Table 3.2). As an example, form dimensions of a cube with edge length of a are $\sqrt{3\,a}$, $\sqrt{2\,a}$ and a. Sphericity and form dimensions of some selected geometrical shapes measured through projection area protocol are shown in Table 4.1.

Table 4.1: Sphericity and form dimensions of some geometrical shapes. Semi-axes lengths of the ellipsoid are a, b and c, the edge length of cuboctahedron, octahedron, cube and tetrahedron is a, and the diameter and height of cylinders and disks are d and h, respectively.

Shape	d_{eq}	ψ	L	I	S
Ellipsoid ($a = 2\,b = 2\,c$)	$2\sqrt[3]{a\,b\,c}$	0.791	$2\,a$	$2\,b$	$2\,c$
Cuboctahedron	$\sim 1.65\,a$	0.905	$2\,a$	$\sqrt{2}\,a$	$\sqrt{2}\,a$
Octahedron	$\sim 0.97\,a$	0.846	$\sqrt{2}\,a$	a	a
Cube	$\sim 1.24\,a$	0.806	$\sqrt{3}\,a$	$\sqrt{2}\,a$	a
Tetrahedron	$\sim 0.61\,a$	0.670	a	$\sqrt{3/4}\,a$	$\sqrt{2/3}\,a$
Cylinder ($h = 20\,d$)	$\sqrt[3]{3\,d^2\,h/2}$	0.471	$\sqrt{h^2 + d^2}$	d	d
Disk ($h = 0.1\,d$)	$\sqrt[3]{3\,d^2\,h/2}$	0.471	$\sqrt{h^2 + d^2}$	d	d

Surface roughness

The drag coefficient in the Stokes' regime is relatively insensitive to surface roughness (Loth, 2008). This seems logical based on theorem of Hill and Power (Hill and Power, 1956), which shows that in the Stokes' regime the drag exerted on a particle is bounded by the drag exerted on bodies that inscribe and circumscribe the particle. As a result, the surface roughness should not alter the drag coefficient significantly, since the drag coefficient of the rough particle can be narrowly constrained by the drag coefficient of two smooth bodies. On the other hand, in the Newton's regime surface roughness and small-scale vesicularity can significantly decrease the drag coefficient. This is due to the downwind shift of the boundary layer separation point, which results in the occurrence of the drag crisis (see above) at Re lower

than the critical Reynolds number. Experiments on spheres (Achenbach, 1974) and cylinders (Nakamura and Tomonari, 1982) clearly show how by increasing the surface roughness, the critical Reynolds number shift to lower values and trigger a premature transition to the drag crisis. Loth (2008) mentioned that irregular particles exhibit little or no drag crisis since such particles have a consistent bluff-body separation point throughout a wide range of Re.

Particle orientation and particle to fluid density ratio

Particle orientation is another parameter that can affect the drag coefficient of non-spherical particles. As a result, repeated experiments performed on a non-spherical particle of a given shape will show a spread in the measured drag coefficient due to the change in the particle orientation (Happel and Brenner, 1983). In the Stokes' regime, Cox (Cox, 1965) showed that a freely falling spheroid with small eccentricity orients itself with the largest projection area normal to the direction of motion. Nevertheless, most particles with a certain well-defined symmetry properties (e.g. spheroidal, orthotropic, isometric, needle and plate particles) have no preferred orientations and fall without rotation in the Stokes' regime (Pettyjohn and Christiansen, 1948; Albertson, 1953; Marchildon et al., 1964; Happel and Brenner, 1983; Clift et al., 2005; Loth, 2008). If particles undergo Brownian motion, however, the particle orientation is changing randomly during descent. In such cases the most favorable estimation of the particle drag is an average value obtained from many random orientations (Happel and Brenner, 1983; Clift et al., 2005). Nonetheless, even when particles are not subjected to Brownian motion, an average of random orientations should be considered as the most relevant orientation for obtaining the average of the drag coefficient since in the Stokes' regime most particles do not have any preferred orientation and for a statistically representative run of experiments they can adopt any random orientation.

As Re increases up to ≈ 100, particles tend to fall with the largest projection area normal to the direction of motion (Marchildon et al., 1964; Komar and Reimers, 1978; Clift et al., 2005). Isometric particles show signs of oscillations and instability in the range $70 < Re < 300$ (Pettyjohn and Christiansen, 1948). Early studies on

falling cylinders showed that the wake instability starts at $Re > 50$ and angular oscillations and lateral deviations are observed at $Re > 80 - 300$(Marchildon et al., 1964; Jayaweera and Mason, 1965). Disks exhibit a steady-falling regime with maximum projection normal to the falling direction at $Re < 100$, and at $Re > 100$ the falling pattern changes from oscillations to chaotic and tumbling (Willmarth et al., 1964).

Finally, secondary motions become fully developed in the Newton's regime ($1000 \leq Re < 3 \times 10^5$). In addition, in the Newton's regime particle to fluid density ratio ρ' can significantly affect orientation and secondary motions of particles, and therefore, the drag coefficient (Willmarth et al., 1964; Marchildon et al., 1964; Christiansen and Barker, 1965; Isaacs and Thodos, 1967; List and Schemenauer, 1971; Tran-Cong et al., 2004; Chow and Adams, 2011; Bagheri et al., 2013). Studies on regular-shape particles show that as ρ' increases, the secondary motion of particles increases too (Marchildon et al., 1964; Christiansen and Barker, 1965; Isaacs and Thodos, 1967; Chow and Adams, 2011). This leads to the reduction of the average projected area of the particle during falling and, hence, the drag coefficient reduces. However, most studies on falling particles are performed in the range $1 < \rho' < 15$, which is significantly lower than ρ' for particles falling in the air that is $\mathcal{O}(10^3)$. Thus, it is not yet well understood how ρ' can influence the particle orientation at high ρ'.

Existing non-spherical drag coefficient models

Table 4.2 shows the most common models for estimating drag coefficient of non-spherical particles. Here, models of Ganser (1993) and Haider and Levenspiel (1989) are chosen since they were found to be the most accurate correlations for predicting the drag coefficient of non-spherical particles with average errors of 16.3% and 23.5%, respectively (Chhabra et al., 1999). Model of Haider and Levenspiel (1989), Eq. (4.6), is the first generalized correlations for drag coefficient of regular shape particles, which is based on Re and sphericity ψ. Haider and Levenspiel (1989) introduced Eq. (4.6) based on experimental data on the drag coefficient of isometric particles and disks at $1 < \rho' < 15$.

Later, Ganser (1993) proposed a simpler formulation, Eq. (4.7), by using simi-

Table 4.2: Most used correlations for estimating drag coefficient of non-spherical particles.

Ref.	Formula	Eq.
Haider and Levenspiel (1989)	$C_D = (24/Re)\,\left(1 + C_1\,Re^{C_2}\right) + C_3/\left(1 + C_4/Re\right)$	(4.6)
	$C_1 = \exp\left(2.33 - 6.46\,\psi + 2.45\,\psi^2\right)$	
	$C_2 = 0.096 + 0.556\,\psi$	
	$C_3 = \exp\left(4.90 - 13.89\,\psi + 18.42\,\psi^2 - 10.26\,\psi^3\right)$	
	$C_4 = \exp\left(1.47 + 12.26\,\psi - 20.73\,\psi^2 - 15.89\,\psi^3\right)$	
Ganser (1993)	$C_D = (24k_S/Re)\,\left(1 + 0.1118\,\left(Re\,k_N/k_S\right)^{0.6567}\right)$	(4.7)
	$+0.4305\,k_N/\left(1 + 3305/\left(Re\,k_N/k_S\right)\right)$	
Leith (1987)	$k_S = 1/3\sqrt{\psi_\perp} + 2/3\sqrt{\psi}$	(4.8)
Ganser (1993)	$k_S = 1/3 + 2/3\sqrt{\psi}$	(4.9)
Loth (2008)	$k_S = \left(L\,I\,/S^2\right)^{0.09}$	(4.10)
Ganser (1993)	$k_N = 10^{1.8148\,(-\log\psi)^{0.5743}}$	(4.11)
Hölzer and Sommerfeld (2008)	$C_D = 8/Re\sqrt{\psi_\parallel} + 16/Re\sqrt{\psi} + 3/\sqrt{Re}\,\psi^{3/4}$	(4.12)
	$+0.42 \times 10^{0.4(-\log\psi)^{0.2}}\,(1/\psi_\perp)$	

larity and dimensional analyses. He showed that the drag coefficient of non-spherical particles can be predicted by Re and two other shape-dependent parameters called Stokes' k_S and Newton's k_N drag corrections (Ganser (1993) noted them as shape factors):

$$k_S \equiv \frac{C_D}{C_{D,\,sphere}} = \frac{C_D}{24/Re} \tag{4.13}$$

$$k_N \equiv \frac{C_D}{C_{D,\,sphere}} = \frac{C_D}{0.463} \tag{4.14}$$

where

$$C_D = \frac{F_D}{\frac{1}{2}\rho_f\,(d_{eq}/2)^2\,v_r^2} \tag{4.15}$$

and $C_{D,\,sphere}$ is the drag coefficient of a sphere with same volume and Reynolds number as the particle. As the particle shape tends to a sphere, both k_s and k_N approach unity. Based on formulation of Ganser (1993), for a particle of a given shape the drag coefficient at any subcritical Reynolds number ($\approx Re < 3 \times 10^5$) can be predicted if k_S and k_N are known. Various correlations, Eqs. (4.8 – 4.11), exist in the literature that estimate k_s and k_N as functions of sphericity ψ, the so called crosswise sphericity $\psi_\perp$ and particle form dimensions. Eq. (4.8), i.e. $k_S = 1/3\sqrt{\psi_\perp} + 2/3\sqrt{\psi}$, suggested by Leith (1987) and used in the models of Ganser

(1993) and Hölzer and Sommerfeld (2008), is one of the most accepted model for estimating k_S in the Stokes' regime that considers both shape and orientation. The crosswise sphericity $\psi_\perp$ is an orientation dependent parameter and is defined as

$$\psi_\perp = \frac{\text{projected area of the volume equivalent sphere}}{\text{projected area of the particle normal to the falling direction}} \tag{4.16}$$

Ganser (1993) suggested to approximate $\psi_\perp$ to unity for isometric particles, Eq. (4.9), but it is not clear how it would change for non-isometric particles. Models of Ganser (1993) and Haider and Levenspiel (1989) are general models that can predict average drag coefficient of particles falling at $1 < \rho' < 15$. As a result, they cannot be used to predict the drag coefficient of non-spherical particles in a specific orientation. In order to do so, more complex models similar to the one introduced by Hölzer and Sommerfeld (2008), Eq. (4.12), is needed, in which the particle orientation is also taken into account. In fact, Hölzer and Sommerfeld (2008) used three different shape/orientation descriptors, namely particle sphericity ψ, crosswise sphericity $\psi_\perp$ and lengthwise sphericity $\psi_\parallel$. Amongst these parameters, the lengthwise sphericity $\psi_\parallel$ is the most complicated parameter to be obtained, which is defined as the ratio between the cross-sectional area of the volume equivalent sphere and the difference between half the surface area and the mean projected longitudinal cross-sectional area of the considered particle (Hölzer and Sommerfeld, 2008). Given that the evaluation of $\psi_\parallel$ is very complex, Hölzer and Sommerfeld (2008) suggested to replace it with $\psi_\perp$ with the cost of slight reduction in accuracy. In any case, calculation of both $\psi_\perp$ and $\psi_\parallel$ needs orientation of the particle to be known, and therefore, Eq. (4.12) is more suitable for Lagrangian computations where the particle orientation along the trajectory is also computed.

4.3 Materials

Particles used in our experiments were separated in different sample sets based on their size: Sample Set I and Sample Set II. Sample Set I includes 100 irregular volcanic particles, 13 cylinders, 4 parallelepiped and one spherical particle with $155\,\mu m \leq d_{eq} \leq 1.8\,mm$. Size and shape of 12 selected irregular vol-

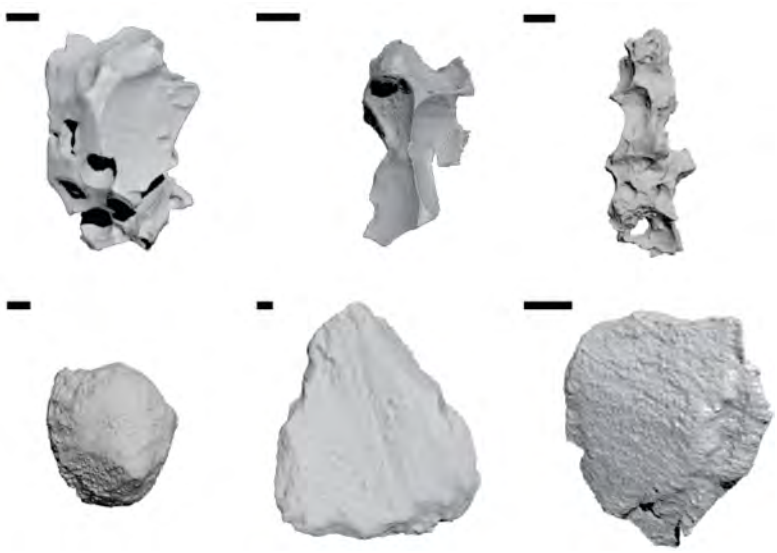

Figure 4.3: A selection of volcanic particles of Sample Set I tested in the settling columns adjusted from Bagheri et al. (Bagheri et al., 2015) (length of the scale bar is $100\,\mu m$).

canic particles are fully characterized using the Scanning Electron Microscope micro Computed-Tomography (SEM micro-CT) (Bagheri et al., 2015; Vonlanthen et al., 2015), whereas the rest of sub-millimetric irregular particles are characterized using multiple-projection image analysis techniques (see Chapter 3 for more details). Selected irregular particles in the Sample Set I are shown in Fig. 4.3. Volcanic particles are from Masaya (Nicaragua, Fontana Lapilli, 60 Ka), Kīlauea (Hawaii, Mystery Unit of Keanakakoi formation, 1790 AD), Villarrica (Chile, Chaimilla unit, 3500 BP), Cotopaxi (Ecuador, layer 2, 290 years BP and layer 5, 1180 years BP), Llaima (Chile, 1957), Chaitén (Chile, 2008) and Stromboli (Italy, 2007) (Bagheri et al., 2015) volcanoes.

Sample Set II includes 78 irregular volcanic particles, 21 ellipsoids, 12 cylinders, 8 disks and 21 regular shape particles with $10.9\,mm \leq d_{eq} \leq 61.2\,mm$ (Fig. 4.4a). In addition, 38 irregular volcanic particles were wrapped in Parafilm® (a self-sealing, moldable and flexible wax film) in order to make their surface smooth without significantly changing their macroscopic shape characteristics (Fig. 4.4b). This provides insights into the influence of surface roughness on the drag coefficient. Volume and surface area of particles are measured with a NextEngine Inc. desktop 3D laser scanner with accuracy of $\approx 100\,\mu m$ (Bagheri et al., 2013, 2015) and their mass were measured by a digital balance with accuracy of $0.001\,gr$.

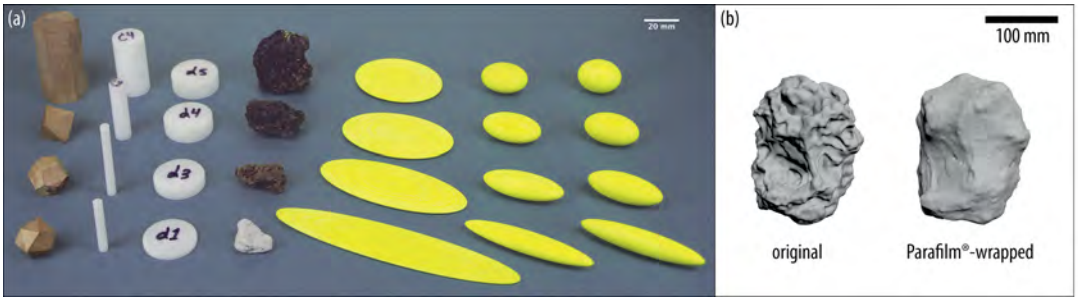

Figure 4.4: (a) A selection of non-spherical particles of Sample Set II tested in the wind tunnel experiments, (b) an irregular particle without and with Parafilm® wrap.

A list of all experimental data points used in this study, including those compiled from the literature, are summarized in Table 4.3. Form dimensions of all particles complied from the literature are recalculated based on the projection area protocol described in section 4.2.2 and shown in Table 4.1.

4.4 Methods

4.4.1 Stokes' regime: analytical solutions

The analytical solution of Oberbeck (1876) is solved numerically to obtain the drag coefficient of ellipsoids with both elongation e and flatness f between 0.01 and 1 (at 0.01 intervals), leading to 10^4 data points. Oberbeck (Oberbeck, 1876) showed that the ratio of the drag coefficient of an ellipsoid with the surface equation of $x^2/a^2 + y^2/b^2 + z^2/c^2 = 1$ moving in the direction of x axis (parallel to a), $C_{D,\,x}$, to the drag coefficient of a sphere with the same volume as the ellipsoid, $C_{D,\,sphere}$, at $Re \ll 1$ is equal to:

$$k_{S,\,x} \equiv \frac{C_{D,\,x}}{C_{D,\,sphere}} = \frac{8}{3}\,\frac{\sqrt[2/3]{a\,b\,c}}{\chi_0 + \alpha_0\,a^3} \tag{4.17}$$

where a, b, c are semi-axes of the ellipsoid and

$$\chi_0 = a\,b\,c \int_0^\infty \frac{\mathrm{d}\lambda}{\Delta} \tag{4.18}$$

$$\alpha_0 = a\,b\,c \int_0^\infty \frac{\mathrm{d}\lambda}{(a^2+\lambda)\,\Delta} \tag{4.19}$$

Table 4.3: Analytical and experimental databases used in this study. *No* indicates number of experiments/datapoints considered in each category, d_{eq} is the diameter of the volume-equivalent sphere, ψ is the sphericity, e is the elongation and f is the flatness of the particle, and ρ' is the particle-to-fluid density ratio. Literature data includes spheres from Pettyjohn and Christiansen (1948), Christiansen and Barker (1965), Schlighting (1968), Roos and Willmarth (1971) and Achenbach (1972); isometric particles (i.e. cube, cuboctahedron, octahedron, tetrahedron) from Pettyjohn and Christiansen (1948), disks and cylinders from Willmarth et al. (1964), Christiansen and Barker (1965), McKay et al. (1988), Isaacs and Thodos (1967) and Clift et al. (2005).

shape	No	$d_{eq}\,[mm]$	ψ	e	f	ρ'
Stokes' regime: $Re < 0.1$						
this work (analytical)						
ellipsoid	10^4	–	0.02 – 1	0.01 –1	0.01 – 1	–
literature (analytical and experimental)						
isometric	22	1.7 – 15.8	0.7 – 0.9	0.7 – 0.9	0.7 – 1	1 – 8
disk	16	–	0.5 – 0.9	0.7 – 1	0.1 – 1	–
cylinder	27	–	0.3 – 0.9	0.02 – 1	1	–
Intermediate regime: $0.1 \leq Re < 1000$						
this work (settling columns: Sample Set I)						
sphere	5	1.45	1	1	1	2270
cylinder	24	0.63 – 1.53	0.4 – 0.8	0.03 – 0.4	1	1400
prism	4	0.47 – 0.58	0.7 – 0.8	0.7 – 0.8	0.4 – 0.6	1400
irregular	196	0.15 – 1.80	0.3 – 0.9	0.3 – 0.8	0.2 – 1	2300
literature (experimental)						
sphere	148	–	1	1	1	1 – 15
isometric	323	1.4 – 15.8	0.7 – 0.9	0.7 – 0.9	0.7 – 1	1 – 11
disk	49	0.8 – 18.7	0.03 – 0.8	0.9 – 1	0.001 – 0.5	1 – 8
cylinder	7	4.5 – 18.3	0.8	0.4	1	1 – 3
Newton's regime: $1000 \leq Re < 3 \times 10^5$						
this work (vertical wind tunnel: Sample Set II)						
ellipsoid	120	22.6 – 23.2	0.2 – 1	0.2 – 0.8	0.1 – 1	870
isometric	72	17.7 – 61.2	0.8 – 0.9	0.7 – 1	0.7 – 1	150 – 1000
disk	48	16.2 – 24.3	0.5 – 0.9	0.7 – 1	0.1 – 0.9	1280
cylinder	72	11.2 – 35.9	0.6 – 0.9	0.1 – 0.7	1	560 – 1300
Other reg.	48	23.0 – 39.0	0.8 – 0.9	0.4 – 0.7	0.7 – 1	530 – 750
Irr. rough	468	10.9 – 36.2	0.5 – 0.9	0.5 – 0.9	0.4 – 1	175 – 2130
Irr. smooth	228	11.7 – 37.8	0.8 – 0.9	0.6 – 0.9	0.6 – 1	390 – 910
literature (experimental)						
sphere	136	–	1	1	1	–
isometric	54	2.9 – 15.8	0.7 – 0.9	0.7 – 0.9	0.7 – 1	2 – 11
disk	40	0.8 – 21.3	0.03 – 0.9	0.7 – 1	0.001 – 8	1 – 10
cylinder	59	4.5 – 73.3	0.7 – 0.9	0.2 – 0.7	1	1 – 2800

and

$$\Delta = \sqrt{(a^2+\lambda)\,(b^2+\lambda)\,(c^2+\lambda)} \tag{4.20}$$

$k_{S,y}$ and $k_{S,z}$ can be obtained similarly for ellipsoids moving in parallel to y and z axes. Eqs. (4.17 – 4.20) were solved numerically for each ellipsoid falling in x, y and z directions. Finally, average of k_S for an ellipsoid moving in random orientations

is calculated as (Happel and Brenner, 1983; Clift et al., 2005):

$$k_S = 3\left(\frac{1}{k_{S,x}} + \frac{1}{k_{S,y}} + \frac{1}{k_{S,z}}\right)^{-1} \tag{4.21}$$

4.4.2 Intermediate regime: experiments in settling columns

Settling columns of heights between 0.45 and 3.6 m are used for measuring the drag coefficient of particles of Sample Set I at the intermediate Re $(0.1-1000)$ (Fig. 4.5). However, experiments could only cover the range $9 \leq Re \leq 900$ due to particle size and set-up characteristics. In each experiment run, a particle was released with zero initial velocity at the top of the settling column and it was filmed at $1600-2000\,fps$ when it passed in front of a high-speed camera at the bottom of the column. A thin and short tube (guiding tube) is placed at the top of the settling column to keep the particle in the center after releasing. A high intensity 6x4 LED array and a holographic diffuser with transmission efficiency of $> 85\%$ was used to backlight the camera field of view. The temperature difference between glass doors in the front and back of settling column was monitored to be $< 1\,^{\circ}C$ during the experiments in order to prevent occurrence of natural convection inside the settling column. Effects of settling column walls on the measured velocity of falling particles are negligible since the ratio of particle cross-sectional area of the Sample Set I to that of settling columns (with diameter of 10 cm) is very small.

The high-speed camera was automatically triggered when the particle was in the field of view. By using a AF Micro-Nikkor $60\,mm$ $f/2.8D$ lens it was possible to record high-speed movies with pixel size of $20\,\mu m/px$ and maximum field of view of $25.6\,mm \times 16.0\,mm$ (1200×800 pixels). Depending on the particle velocity and field of view, between 7 and 30 frames of falling particles were captured in each run. The resulting videos were then converted to 8 bit Tiff format images and analyzed by ImageJ software (Schneider et al., 2012). A Particle Tracking Velocimetry (PTV) code (Chapter 2) was used to obtain particle velocity.

The main error in measuring velocity of falling particles is due to the uncertainty in the particle centroid position. Considering the exposure time of videos (50 µs) and falling velocity of particles (0.8 – 7.6 $\mathrm{m\,s^{-1}}$), the uncertainty in the particle

position δy is between 41 – 379 µm (i.e. exposure time multiplied by the falling velocity). Thus, given that the vertical displacement of particles in the image H is $800 \times 20\,\mu m$, the error on the measured velocity is between 0.3 – 2.5% ($= 100 \times \delta y/H$). Finally, to validate measurements, velocities of three glass spheres were measured and compared to previously published experimental data to validate the measurements. Comparisons showed that measurements have an acceptable average deviation of 5%.

In the settling column experiments the particle acceleration could not be calculated accurately since the field of view of the camera was relatively small. In order to make sure that particles reached their terminal velocity, they were tested at least in two column heights and the change in the measured velocity was monitored. The drag coefficient could be measured only for the 41 particles that reached their terminal velocity. Measurements for remaining particles, however, were used to benchmark the ability of the final drag coefficient model to predict particle velocity within a given falling distance. For benchmarking accuracy of models, we compare their relative errors with respect to reference values (i.e. analytical solutions or experimental measurements) as follows:

$$error(x) = \frac{|x_{ref.} - x_{model}| \times 100}{x_{ref.}} \tag{4.22}$$

4.4.3 Newton's regime: experiments in a vertical wind tunnel

A $4\,m$ high vertical wind tunnel (see Chapter 2) was used to measure the drag coefficient of Sample Set II particles. The vertical wind tunnel was built at the University of Geneva in collaboration with the fluid mechanics group (CMEFE) of the University of Applied Sciences Western Switzerland in Geneva (HES-SO//hepia). Particles were suspended in the upward airflow in the test section with an adjustable velocity of $5 - 27\,\mathrm{m\,s^{-1}}$. Measurements in the wind tunnel on particles of sample Set II covered the range $8 \times 10^3 \leq Re \leq 6 \times 10^4$. The diverging design of the test section creates airflow with decreasing speed as the height of test section increases,

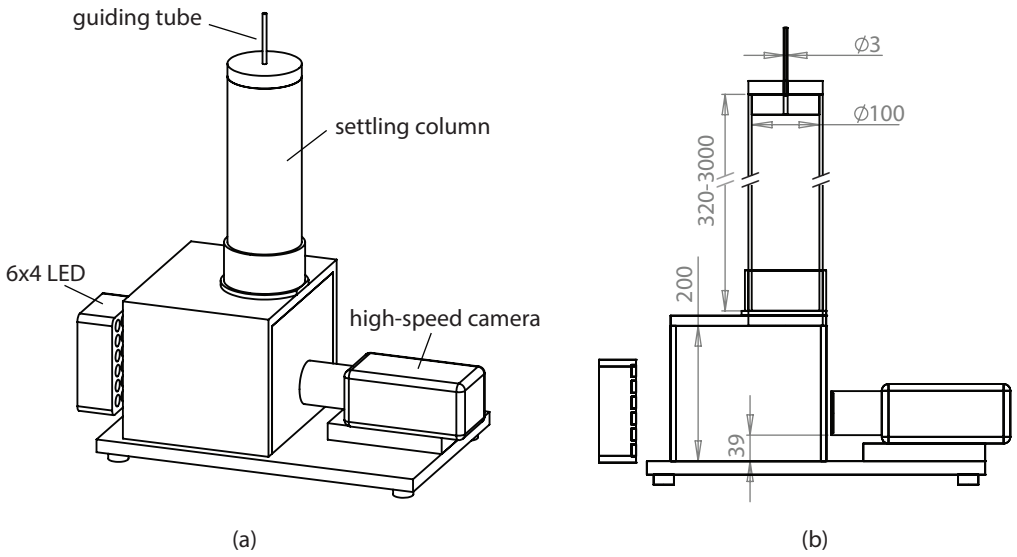

Figure 4.5: Schematic of the settling columns used in this study ($9 \leq Re \leq 900$). (a) the perspective view, (b) the cross section (dimensions are in mm).

which allows us to measure the variation of particle terminal velocity due to the change in their orientation. Particle motions in the test section were filmed with a high-speed camera and then were analyzed with the ImageJ software (Schneider et al., 2012) and a PTV code to obtain mean and variation of particle drag coefficient, terminal velocity and projected area normal to airflow. For each particle, at least three experiments were conducted in different airflow speeds to make sure that the variability of the particle terminal velocity due to change in the particle orientation is captured. The reader is referred to Chapter 2 for more details on the design of the wind tunnel, the PTV code, experimental setup and error analysis.

4.5 Results

We present a new model for the determination of the drag coefficient that is based on the Stokes and Newton drag corrections, i.e. k_S and k_N. In fact, k_S and k_N are derived following Ganser (1993) but accounting for shape descriptors that are more accurate and easier to determine than sphericity. First, we discuss the results for the Stokes' regime ($Re < 0.1$) in order to parameterize k_S and then the results for the Newton's regime ($10^3 \leq Re < 3 \times 10^5$) in order to parameterize k_N. Finally, we generalize the results for all Re, including the intermediate regime.

4.5.1 Stokes' regime

Average C_D of particle in random orientations in the Stokes' regime

First we investigated the possibility of estimating the average of particle crosswise sphericity $\overline{\psi}_\perp$ in random orientations with a particle shape descriptor since it is needed for benchmarking model of Leith (1987), Eq. (4.8). 1000 projections of 3D models of particles of different shapes in random orientations were created and their average projected area $\overline{A}_{projected}$ was measured (see Chapter 3 for more details). $\overline{\psi}_\perp$ was then calculated as the ratio of the projected area of an equivalent volume sphere ($\pi\, d_{eq}^2/4$) to $\overline{A}_{projected}$. The correlation between $\overline{\psi}_\perp$ and various shape descriptors of particles (e.g. sphericity, flatness, elongation) was investigated, and it was found that $\overline{\psi}_\perp$ is best correlated with $S^2/L\,I$(Fig. 4.6):

$$\overline{\psi}_\perp = 1.1\,\left(S^2/L\,I\right)^{0.177} - 0.1 \tag{4.23}$$

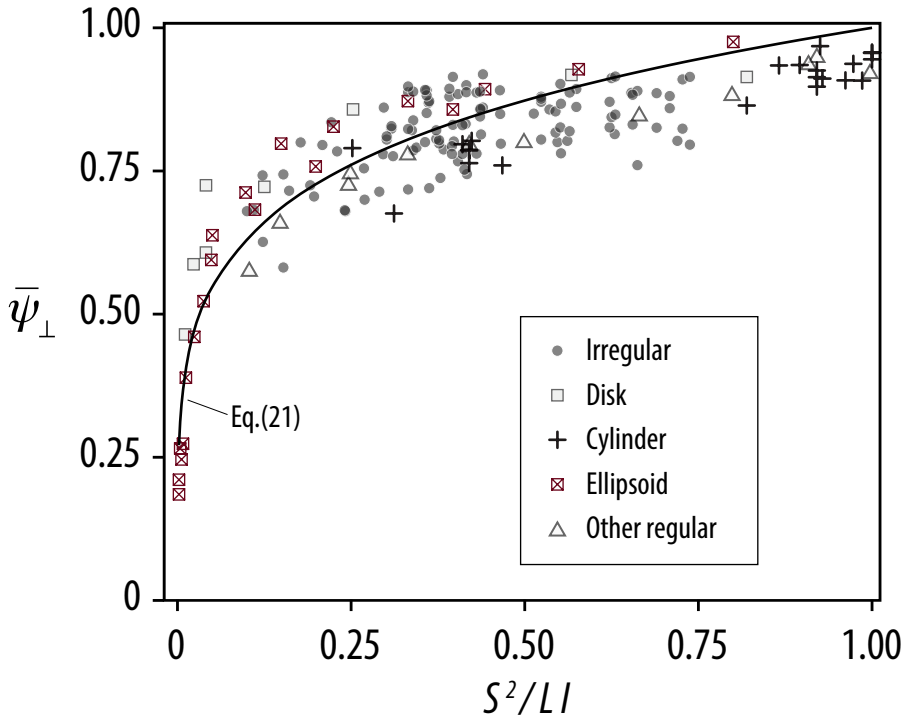

Figure 4.6: Dependency of the crosswise sphericity $\overline{\psi}_\perp$ averaged over random orientations for non-spherical particles of different shapes to the ratio of $S^2/L\,I$. $\overline{\psi}_\perp$ is calculated by image analysis of projections obtained from 3D models of particles in Sample Set I and II in random orientations. *Other regular* particles include cubes, pyramids, polyhedrons.

Eq. 4.23 is associated with an average error of 13% for ellipsoids and 7% for all particle shapes. As mentioned earlier, $S^2/L\,I$ is highly correlated with the particle flatness (Bagheri et al., 2015), which suggests that particle flatness is an important parameter for determining the particle projected area and $\overline{\psi}_{\perp}$.

The accuracy of Eqs. (4.6 – 4.9) and (4.12) (Table 4.4) for estimating k_S of particles calculated/measured in the Stokes' regime (see Table 4.3) is benchmarked. Fig. 4.7 shows that k_S increases with decreasing sphericity ψ. For particles with $\psi > 0.4$ the estimations of Ganser (1993) (Eq. 4.9) and Leith (1987) (Eqs. 4.8 and 4.23) are closer to the calculated k_S. In any case, from Fig. 4.7 it is evident that the sphericity ψ is not a good candidate for estimating drag coefficient of non-spherical particles in the Stokes' regime, given the large spread in the data.

The use of Eq. 4.23 for taking into account the particle orientation in the model of Leith (1987), Eq. (4.8), can fit the data better than the model of Ganser (1993). However, the improvement is not significant since these models assume that the contribution of form and friction drags are similar to those for sphere. In fact, the model of Leith (1987) is based on the fact that one third of the sphere drag in the Stokes' regime is due to the form drag that (affected by the particle orientation) and two thirds of it is the friction drag (related to the particle surface area). These ratios, however, can significantly vary for non-spherical particles of different shapes. As an example, the contribution ratios for ellipsoids can vary significantly from those of the sphere (Fig. 4.8).

A summary of error analyses for models shown in Table 4.2 is presented in Table 4.4. The calculated k_S based on the model of Haider and Levenspiel (1989) performs better for particles with $\psi < 0.25$ compare to other models, but is still associated with large deviations up to 57.5%.

Another shape descriptor suggested by Loth (2008) is a form factor defined as $L\,I\,S^2$ (Eq. 4.10 in Table 4.4). Fig. 4.9 shows that, similar to the sphericity, $L\,I/S^2$ is not correlated well with k_S. In particular, it cannot discriminate isometric shapes, such as cuboctahedron, octahedron and tetrahedron, from each other.

In the search for a better shape descriptor, we found that k_S is almost equally sensitive to both elongation and flatness, with slightly higher sensitivity to elonga-

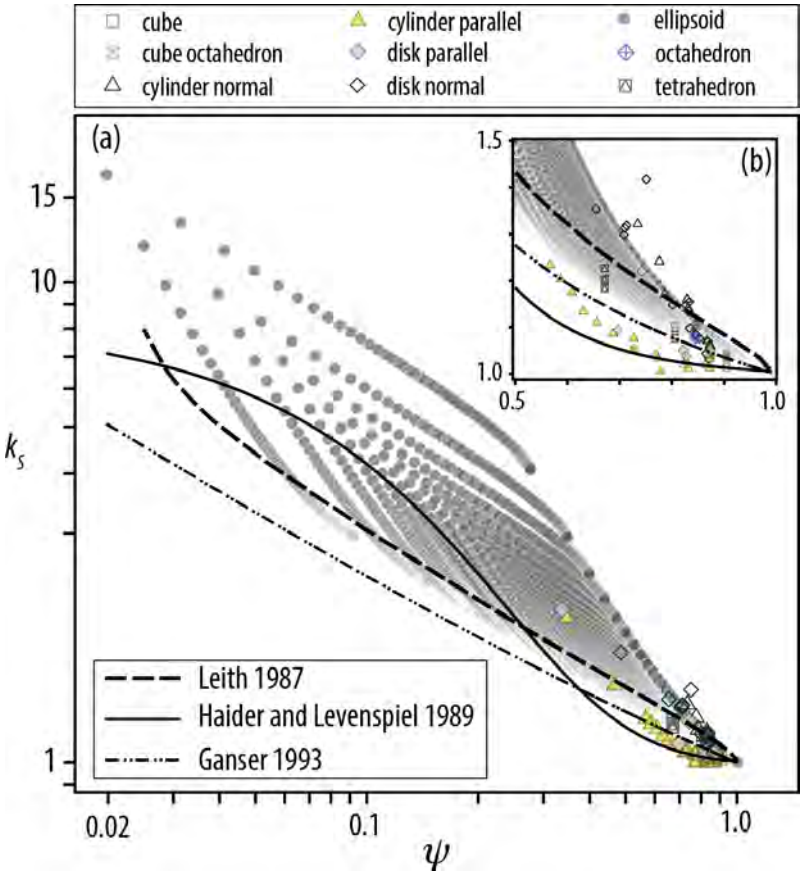

Figure 4.7: (a) Log plot showing the Stokes' drag correction k_S ($C_D/C_{D,\,sphere}$) against sphericity for particles of various shapes calculated/measured in the Stokes' regime, $Re < 0.1$ (see Table 4.3). (b) a zoom of plot (a) in linear scales. Cylinder and disks released with maximum projection area perpendicular to the falling direction called normal and those with minimum projection area normal to the falling direction called parallel. Data for non-ellipsoid shapes are from Pettyjohn and Christiansen (1948) and Clift et al. (2005).

tion, as it is shown in Fig. 4.10. Therefore, a simple form factor, such as $f\,e^{1.3}$ ($= S\,I^{0.3}/L^{1.3}$), can correlate well with k_S of ellipsoids. However, in order to avoid issues mentioned for the form factor of Loth (2008) (i.e. issues in discriminating isometric shapes), it is necessary to combine it with an additional parameter that is a function of characteristics of the particle other than form dimensions, such as d_{eq}. This parameter can be defined as $d_{eq}^3/L\,I\,S$ and if multiplied by the form factor found for ellipsoids, a new shape descriptors, which we define as Stokes form factor F_S, can be obtained:

$$F_S = f\,e^{1.3}\left(\frac{d_{eq}^3}{L\,I\,S}\right) = \frac{d_{eq}^3}{L^{2.3}\,I^{0.7}} \tag{4.24}$$

Eq. (4.24) indicates that F_S is comprised between 0 and 1; it is equal to 1 for a sphere and reduces as the particle shape becomes less spherical. It should be noted

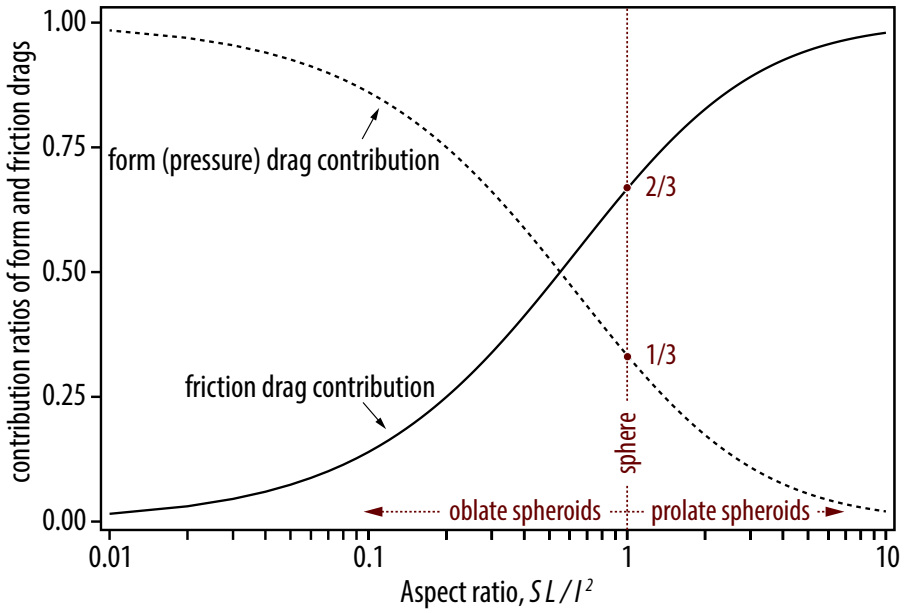

Figure 4.8: Contribution ratios of form and friction drags to the total drag exerted on oblate and prolate ellipsoids in the Stokes' regime versus ellipsoid aspect ratio. These ratios are calculated by analytical equations provided in Table 4.1 of Clift et al. (2005) for axisymmetric flow.

that for ellipsoids $d_{eq}^3 = L\,I\,S$ and therefore F_S reduces to $f\,e^{1.3}$. Fig. 4.11 shows that k_S correlates very well with F_S for ellipsoids and other regular particles and a correlation can be found for estimating k_S as a function of F_S:

$$k_S = \frac{1}{2}\left(F_S^{1/3} + \frac{1}{F_S^{1/3}}\right) \tag{4.25}$$

Eq. (4.25) is the most accurate and reliable equation with a mean error of 2.4% and maximum error of 33.9% (Table 4.4).

Effects of particle orientation on C_D in the Stokes' regime

As mentioned earlier, particle orientation is an important parameter that can significantly affect the drag. The effect of orientation of cylinders and disks on the drag coefficient can already be seen in Fig. 4.11, which shows how the cylinders and disks falling with the largest area perpendicular to the flow (i.e. cylinder and disk normal) have higher drag compare to when they fall with the smallest projected area (i.e. cylinder and disk parallel). The drag coefficient for ellipsoids that settle parallel to one of the semi-axis, i.e. $k_{S,x}$, $k_{S,y}$, $k_{S,z}$, are calculated through Eqs. (4.17 –

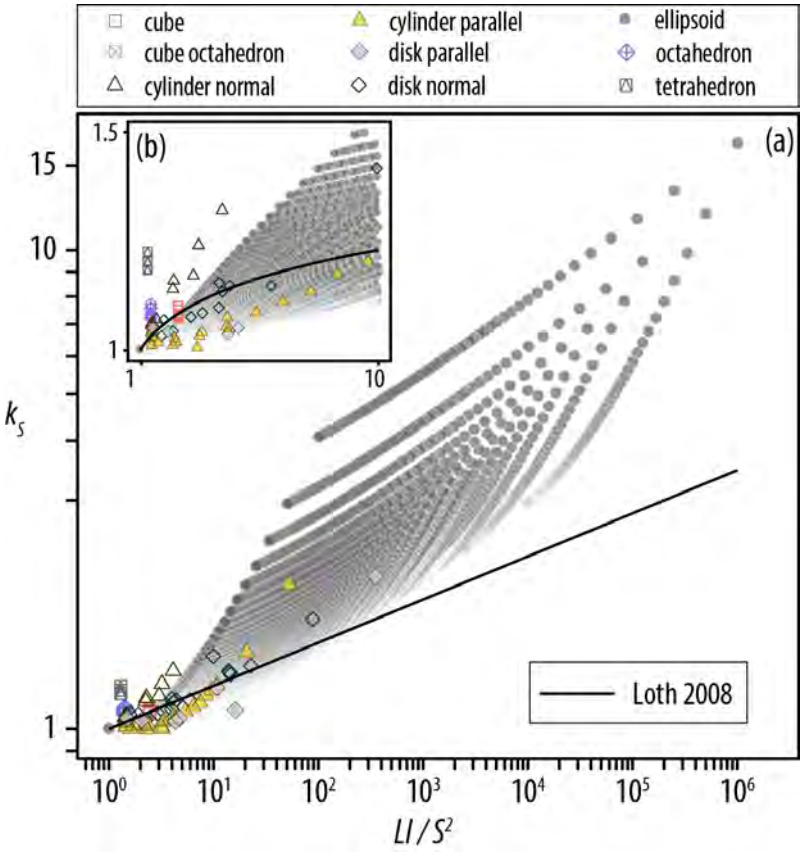

Figure 4.9: (a) Log plot showing the Stokes' drag correction k_S against the shape descriptor introduced by Loth (2008) for particles of various shapes moving in the Stokes' regime ($Re < 0.1$). (b) a zoom of plot (a) in linear scales. Data source is similar to Fig. 4.7.

4.20) and shown in Fig. 4.12. The trend for $k_{S,x}$, $k_{S,y}$ and $k_{S,z}$ is similar to that of k_S, except that in some orientations it is possible that the ellipsoid experiences a drag lower than the its volume-equivalent sphere (e.g. $k_{S,x} < 1$). The minimum values for $k_{S,x}$, $k_{S,y}$ and $k_{S,z}$ are respectively 0.955, 0.988 and 0.998 that occurs at F_S of 0.417, 0.700 and 0.457, respectively. However, the average drag coefficient of ellipsoids in random orientations is always larger than that of the volume-equivalent sphere, i.e. $k_S > 1$. The extremes of variation in the drag coefficient of an ellipsoid due to the change in its orientation can be predicted with a fit very similar to Eq. 4.25:

$$k_S = \frac{1}{2}\left(F_S^{\alpha_1} + \frac{1}{F_S^{\beta_1}}\right) \tag{4.26}$$

where $0.05 < \alpha_1 < 0.55$ and $0.29 < \beta_1 < 0.35$. The upper extreme curve $k_{S,max}$ occurs for $\alpha_1 = 0.55$ and $\beta_1 = 0.29$ in Eq. 4.26, and $k_{S,min}$ occurs when $\alpha_1 = 0.55$

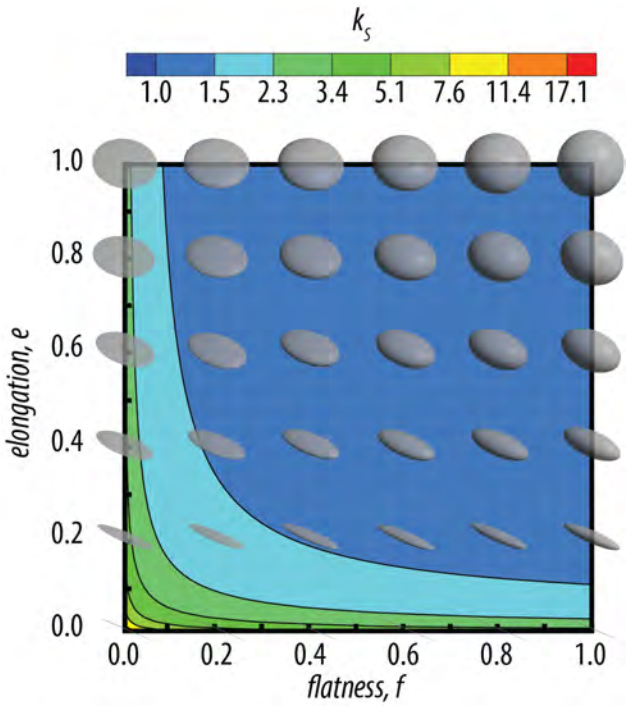

Figure 4.10: Impact of flatness f and elongation e on the particle Stokes' drag correction k_S.

and $\beta_1 = 0.29$ (Fig. 4.12). The average drag coefficient in random orientations, k_S, can be obtained simply by considering $\alpha_1 = \beta_1 = 1/3$.

It is also important to know how the effect of particle orientation on the drag coefficient depends on particle shape. As the particle shape becomes less spherical the effect of particle orientation becomes more significant due to the increase between the ratio of maximum and minimum projection areas (Fig. 4.13). It can also be noted that $k_{S,max}$ is on average 10% (maximum of 20%) higher than k_S, whereas $k_{S,min}$ is on average 13% (maximum of 37%) lower than k_S for the particles considered here (Fig. 4.13).

The accurate correlation for estimating k_S from F_S, which is based on particle form dimensions and spherical equivalent diameter, is a great simplification in comparison to surface area dependent parameters, such as sphericity, in particular for irregular particles. However, when the spherical equivalent diameter cannot be measured directly, correlations presented by Bagheri et al. (2015) can be used that are based on form dimensions. Finally, F_S can also be calculated by considering the term $d_{eq}^3/L\,I\,S$ equal to one, in which case the particle shape will be approximated

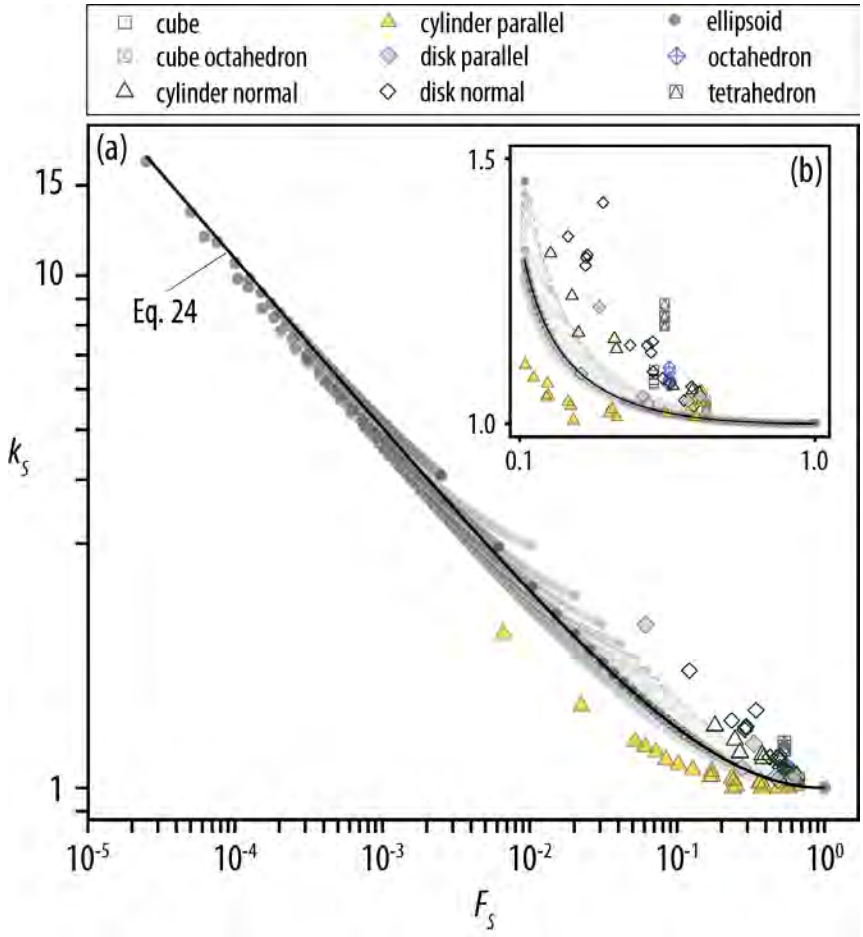

Figure 4.11: (a) Log plot showing the Stokes' drag correction k_S against the new Stokes shape descriptor F_S for particles of various shapes moving in the Stokes' regime ($Re < 0.1$). (b) a zoom of plot (a) in linear scales. Data source are similar to Fig. 4.7.

with an ellipsoid of a similar form (i.e. flatness and elongation).

Effects of surface roughness and vesicularity on C_D in the Stokes' regime

Another fundamental question is: how irregularities in the particle shape, e.g. surface roughness, small-scale vesicularity, that cannot be captured by F_S, can affect the particle drag? To answer this question, we performed a test study by applying the theorem of Hill and Power (Hill and Power, 1956) to find the drag coefficient of an irregular particle (Fig. 4.14). Assuming that the irregular particle shown in Fig. 4.14 is moving at $Re = 0.01$ with constant relative velocity, Re for inscribed and circumscribed ellipsoids will be 6.8×10^{-3} and 1.5×10^{-2}, respectively, since their diameters are different and they should move with the relative velocity. As a result, by calculating k_S of inscribed and circumscribed ellipsoids with Eq. 4.25,

Table 4.4: Mean and maximum error of models presented in Table 4.2 in estimating the average Stokes' drag correction, Eq. (4.21), of 10^4 ellipsoids. For models of Leith (1987) and Hölzer and Sommerfeld (2008), the average of crosswise sphericity in random orientations, Eq. (4.23), is used for estimating the crosswise sphericity.

Correlation	*error*%	
	mean	*max*
Haider and Levenspiel (1989), Eq. (4.6)	12.8	57.5
Leith (1987) & Hölzer and Sommerfeld (2008), Eqs. (4.8) and (4.12)	6.70	57.8
Ganser (1993), Eq. (4.9)	10.4	69.7
Loth (2008), Eq. (4.10)	10.3	79.3
Present, Eq. (4.25)	2.44	33.9

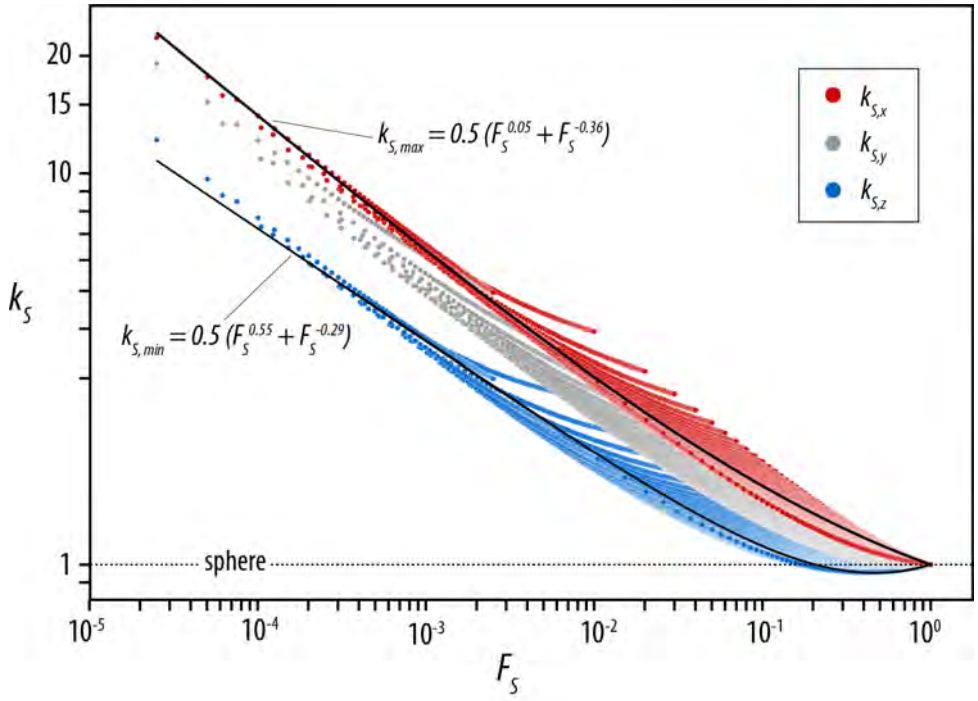

Figure 4.12: Calculated k_S of ellipsoids falling in different orientations against F_S. $k_{S,max}$ and $k_{S,min}$ are the Stokes' drag correction for ellipsoids that fall with their maximum and minimum projection areas normal to their falling paths, respectively.

it can be found that k_s for the irregular particle should be bounded between 0.97 and 1.64. However, we could improve the lower bound estimation furthermore by knowing that k_S is always ≥ 1. Thus, Hill and Power (Hill and Power, 1956) principle suggests that $k_S = 1.31$ for the irregular particle with a maximum uncertainty of 25%. On the other hand, if we use Eq. 4.25 directly, we would get $k_S = 1.34$, which is within 2.5% of deviation from the average of k_S found by the method of

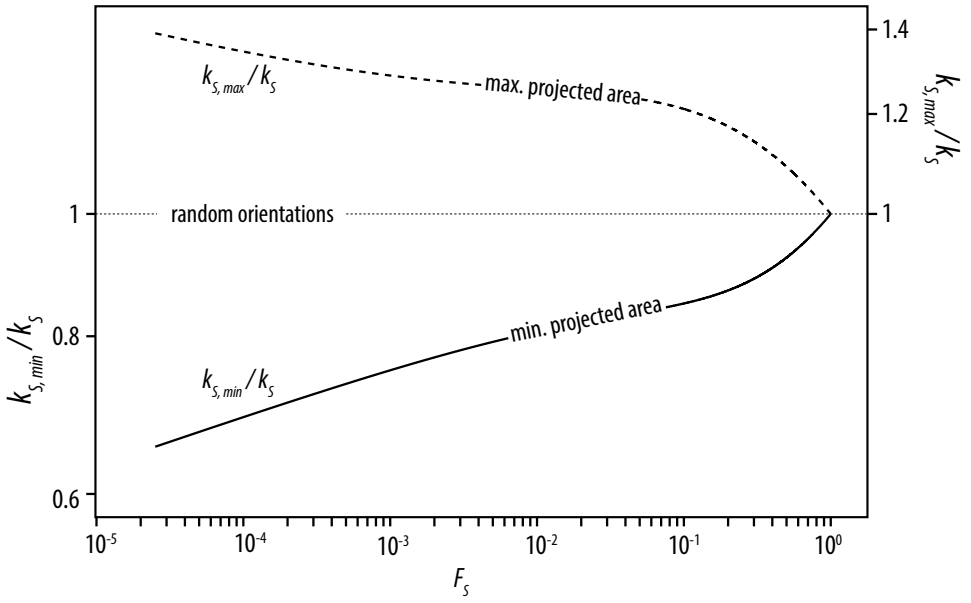

Figure 4.13: Effect of particle shape, F_S, on the sensitivity of ellipsoid drag to the change in orientation in the Stokes' regime. More the particle deviates from spherical shape (i.e. low F_S), more $k_{S,max}$ and $k_{S,min}$ deviate from k_S that is obtained for randomly orientated ellipsoids. This shows that the effect of the orientation on the drag coeffcient is more significant for highly non-spherical particles.

Hill and Power (Hill and Power, 1956). This indicates that small-scale irregularities and surface vesicularity do not significantly alter the drag coefficient.

Another point that can be understood with Hill and Power (Hill and Power, 1956) principle is that the sphericity is not an appropriate shape descriptor for estimating drag coefficient of irregular particles in the Stokes' regime. In fact, sphericity of the irregular particle is lower than sphericity of both inscribing and circumscribing ellipsoids. This means that any correlation based on sphericity would predict higher drag for the irregular particle than both the inscribed and circumscribed ellipsoids.

4.5.2 Newton's regime

Average of C_D for particles falling in the Newton's regime

Non-spherical particles experience Newton's regime at different range of Re depending on their shape. Here, the general range of $10^3 \leq Re\, k_N/k_S \leq 3 \times 10^5$ is used to define the Newton's regime of any particle shape. k_N for various non-spherical particles measured in the wind tunnel with $100 \leq \rho' \leq 2200$ are shown against sphericity in Fig. 4.15. Although the trend shows that by decreasing the sphericity

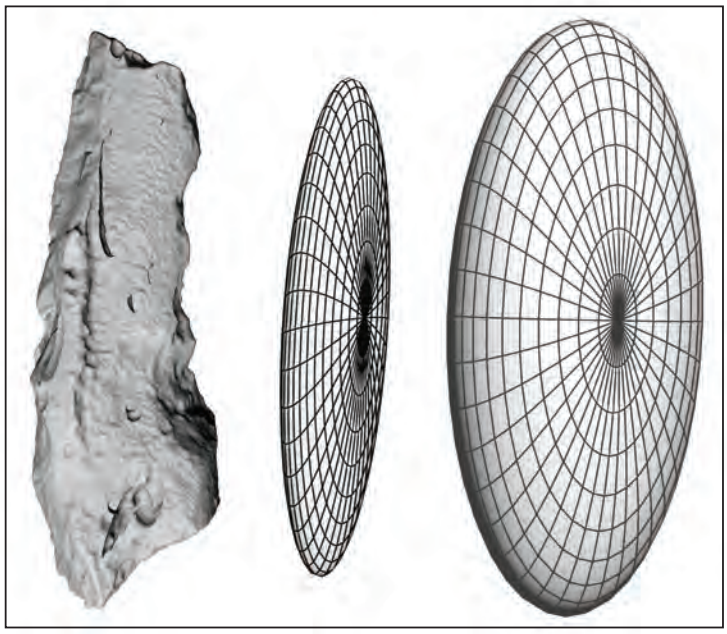

	irregular particle	inscribed ellipsoid	circumscribed ellipsoid
d_{eq} [µm]	225	154	335
e	0.33	0.23	0.45
f	0.64	0.49	0.72
ψ	0.56	0.62	0.86

Figure 4.14: Inscribed and circumscribed ellipsoids found manually for the 3D model of an irregular volcanic particle. f, e and ψ are particle flatness, elongation and sphericity, respectively.

the drag coefficient increases, there is a considerable scatter at $\psi > 0.5$ even for particles of regular shapes. For the sake of comparisons, estimations obtained from models of Haider and Levenspiel (1989), Ganser (1993) and Hölzer and Sommerfeld (2008)(Eqs. 4.6, 4.11 and 4.12) that are based on measurements at $1 < \rho' < 15$ are also shown in Fig. 4.15. For the model of Hölzer and Sommerfeld (2008) that accounts for particle orientation, the crosswise sphericity $\psi_\perp$ for each particle during the suspension in the wind tunnel is measured with computer vision algorithms (Bagheri et al., 2013).

In Table 4.5, it can be seen that models of Haider and Levenspiel (1989) and Ganser (1993) are very close together and overestimate the drag coefficient of all particles with an average error of 90% (max. error $\approx$ 240%). These large overestimations with respect to wind tunnel measurements is due to the fact that they are based on experiments at much lower density (low ρ'). On the other hand, the

model of Hölzer and Sommerfeld (2008) performs significantly better since it uses an additional variable to take into account the particle orientation, but it is still associated with a significant average error of 22% (max. error ≈ 66%). In particular, it underestimates k_N of regular particles and overestimates that of irregular particles.

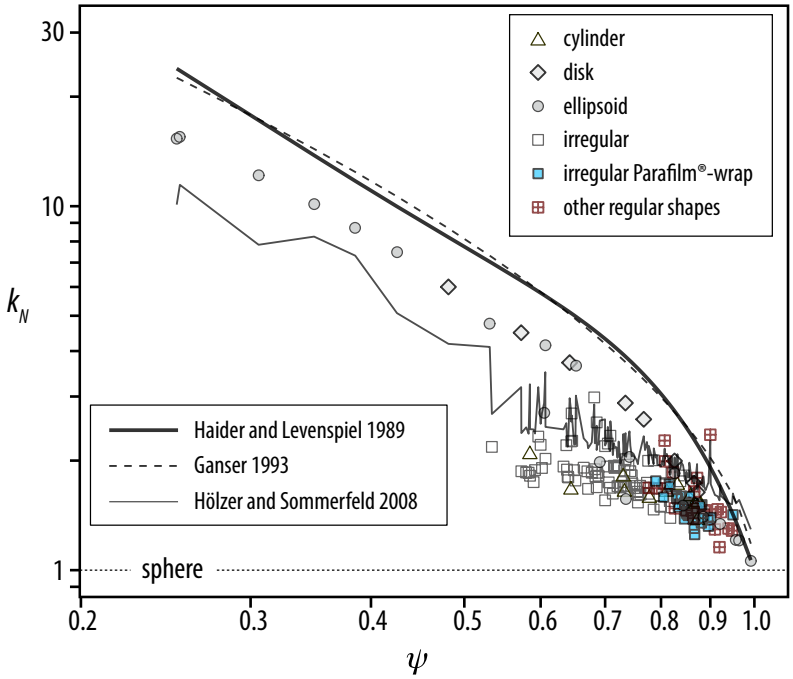

Figure 4.15: Newton's drag correction, k_N, of freely suspended non-spherical particles measured in the present study using the vertical wind tunnel against sphericity. Estimations of models presented in Table 4.2 are also plotted.

In order to find another shape descriptor that has a better correlation with k_N than sphericity, various shape descriptors including flatness, elongation and circularity measures were tested and it was found that k_N is more sensitive to flatness than to elongation (Fig. 4.16). As a result, the following shape descriptor, here defined as the Newton shape descriptor F_N, was found:

$$F_N = f^2\, e \left(\frac{d_{eq}^3}{L\, I\, S} \right) = \frac{S\, d_{eq}^3}{L^2\, I^2} \tag{4.27}$$

Note that $f^2\, e$ $(= S^2/L\, I)$ in Eq. (4.27) is the same as the shape descriptor used in Eq. (4.23) for estimating $\psi_\perp$ of particles in random orientations and as mentioned earlier is the square of the so called *Corey form factor* (Corey, 1963). Corey form factor is highly correlated with the particle flatness (Bagheri et al., 2015) and has been used in several studies for estimating drag coefficient of particles (Loth,

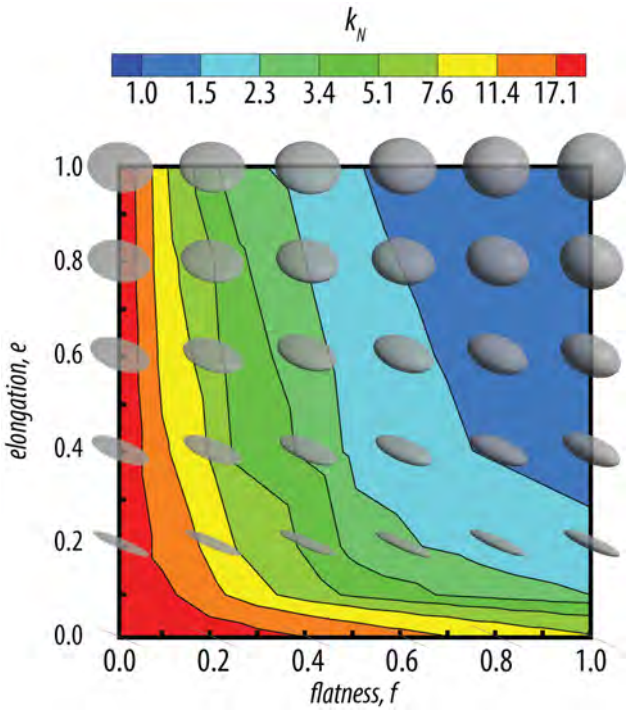

Figure 4.16: Impact of flatness f and elongation e on the Newton's drag correction k_N of non-spherical particles measured in the present study using the vertical wind tunnel.

2008). The term $d_{eq}^3/L\,I\,S$ in Eq. (4.27) is used to avoid issues mentioned earlier for distinguishing isometric particles and is equal to one for ellipsoids. It can be seen in Fig. 4.17 that k_N of particles measured in the wind tunnel is highly correlated with F_N and a fit can be found as:

$$\log(k_N) = 0.45\,[-\log(F_N)]^{0.99} \quad \text{for } 150 < \rho' < 2130 \tag{4.28}$$

As it is shown in Table 4.5, average error of Eq. (4.28) for estimating k_N is about 10.9% (max. error 43.6%), which is considerably lower than errors found for existing models.

Effects of surface roughness and vesicularity on C_D in the Newton's regime

An important point that can be mentioned regarding F_N is that it is not sensitive to the surface roughness and small-scale irregularities. However, as mentioned earlier, it is a known fact that for spheres and fixed cylinders in the Newton's regime, roughness can significantly decrease the drag force by shifting downwind the separation point

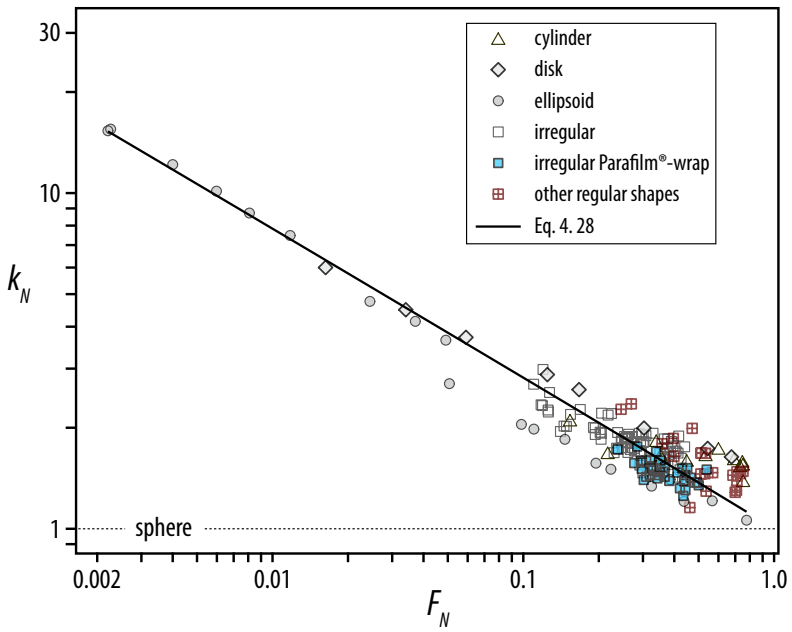

Figure 4.17: Newton's drag correction, k_N, of freely suspended non-spherical particles measured in the present study using the vertical wind tunnel versus the new Newton's shape descriptor F_N. Eq. (4.28) found in this study for estimating k_N is also shown on the plot.

of the boundary layer (Achenbach, 1974). To investigate the influence of roughness on the drag coefficient of irregular particles, 38 irregular particles were wrapped in Parafilm® to create smooth surfaces for particles (see Fig. 4.4b). Wrapping particles with Parafilm® increased both the particle mass, diameter, sphericity and F_N for about 9%, 6%, 21% and 19%, respectively.

Fig. 4.18 shows the terminal velocity for irregular particles with and without Parafilm® wrap measured in the wind tunnel. It can be seen that the terminal velocity of particles wrapped in Parafilm® increases by about 7%, which is a sign a of a reduction in the drag coefficient. In fact, by wrapping particles with Parafilm®, the drag coefficient decreases on average by about 19%. Based on Eq. (4.28), at least 8% of this reduction can be explained by the increase in F_N. The rest can be due to changes in shape characteristics that cannot be explained by F_N and Eq. (4.28).

In any case, this decrease cannot be due to the shift in the separation point for boundary layer, since, if this was the case, the reduction in the drag coefficient should have been much larger (e.g. $\sim$ 75% reduction for sphere). In conclusion,

Table 4.5: Mean and maximum error associated with the estimations of the drag coefficient of non-spherical particles (including particles of regular and irregular shapes) measured in the present study using the vertical wind tunnel ($150 \leq \rho' \leq 2130$) based on selected correlations. For a complete benchmark including all the particles studied in this work and literature see Table 4.6.

Correlation	$error\%$	
	$mean$	max
Haider and Levenspiel (1989), Eq. (4.6)	91.1	242
Ganser (1993), Eq. (4.11)	89.4	244
Hölzer and Sommerfeld (2008), Eq. (4.12)	21.6	66.3
Present, Eq. (4.28)	10.9	43.6

the effect of surface roughness and vesicularity on the drag coefficient of irregular particles, at least for those measured here and at $8 \times 10^3 \leq Re \leq 6 \times 10^4$, is about 10% that is negligible compare to the effect of main characteristics of the particle shape, such as F_N (i.e. $48\% - 77\%$).

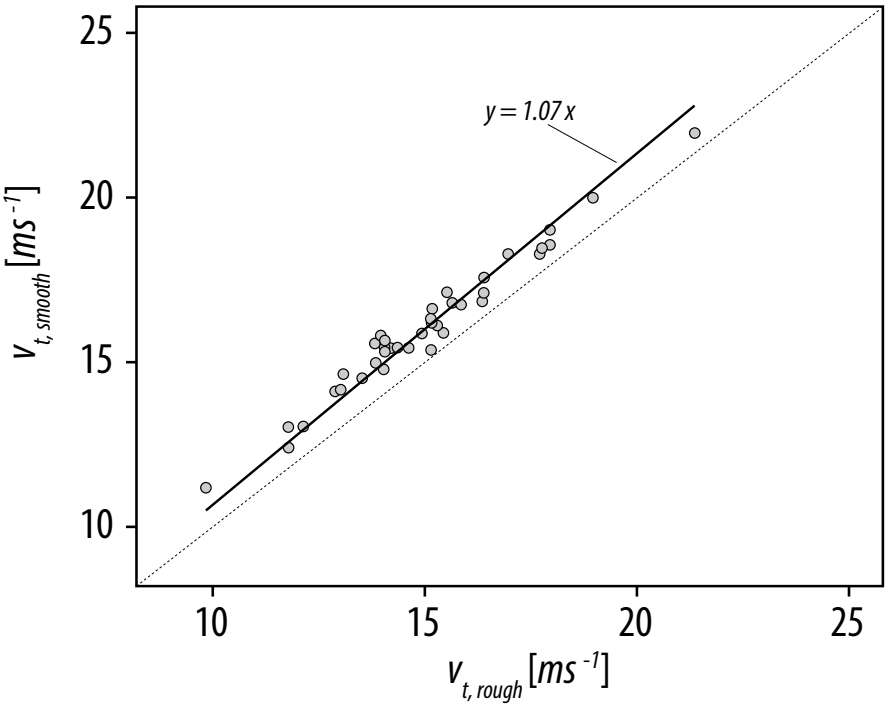

Figure 4.18: Comparison of terminal velocity, v_t, measured in the vertical wind tunnel for irregular particles without (rough) and with Parafilm® wrap (smooth).

Effects of particle orientation and density ratio on C_D in the Newton's regime

Fig. 4.19 shows the variability of the Newton's drag correction, k_N, of non-spherical particles measured in the vertical wind tunnel. The variability in the particle drag is due to the fact that orientation of non-spherical particles is not fixed during free suspension (or free fall). To capture this variability, results of at least three experiments conducted at different wind speeds are merged together for each particle. As it can be seen from Fig. 4.19, the drag coefficient (hence the terminal velocity) of non-spherical particles is not constant and it is better to explain it with a range of values. It is possible that the variability in the drag coefficient is broader than those we could measured in the vertical wind tunnel since highly flat/elongated particles could not be suspended in extreme orientations (i.e. maximum and minimum projection area) long enough to perform the measurements.

Additional data resulted from our wind tunnel study is the average of particle projection area normal to the airflow during suspension in the wind tunnel (Fig. 4.20). Interestingly, the average of particle projection area in the wind tunnel is very close to the average of projected areas of particles in random orientations, which is closer to their maximum projected area rather than to their minimum. This suggests that for a freely falling particle at high ρ', the *preferred orientation* is very close to the average of its random orientation.

In the Newton's regime, as mentioned before, orientation of freely falling particles is a function of particle-to-fluid density ratio, ρ'. The effect of particle orientation on the drag at high ρ' is already presented in Fig. 4.19. We also investigated the effect of ρ' for particles measured in the vertical wind tunnel only, but no correlation could be found between k_N and ρ'. This indicates that when $\rho' > 100$ the drag coefficient is not affected by ρ' anymore. However, in order to find a general correlation for estimating the drag coefficients of freely falling particles valid at any ρ', more data of particles with low ρ' should also be considered. This can be achieved by adding the available results in the literature for the drag of freely falling particles measured in liquids .

In Fig. 4.21, k_N for measurements made in both gases (i.e. present wind tunnel

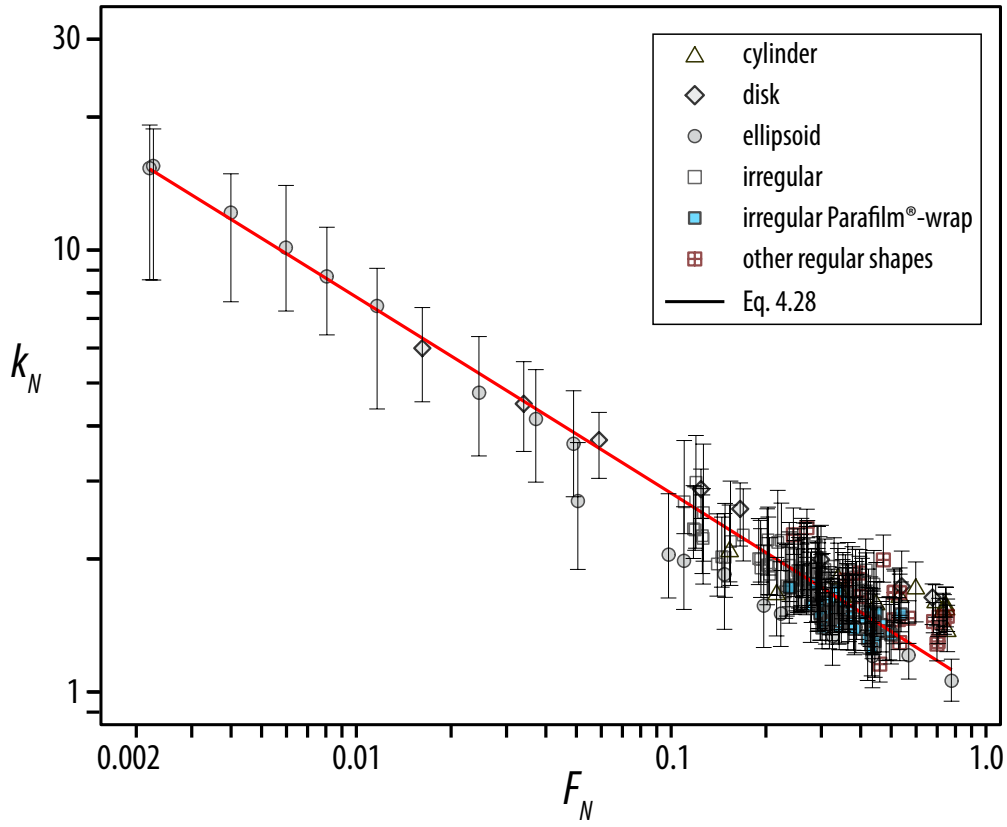

Figure 4.19: Variability of the Newton's drag correction, k_N, of non-spherical particles measured in the present study using the vertical wind tunnel. This variability is due to the change in the orientation of particles under free suspension conditions. Note that this plot is valid for particles falling in gases since it is based on the measurements at $150 \leq \rho' \leq 2130$.

data, same as in Fig. 4.17) and liquids (i.e. published, see figure caption and Table 4.3) is plotted against F_N. It is evident that at any given F_N, k_N of particles with higher ρ' is lower. Since particle shape is fixed, the only explanation is that by decreasing ρ', particles tend to have higher projection areas perpendicular to the falling direction and hence their drag coefficient increases. By taking ρ' into account and using non-linear regressions, a general correlation for obtaining k_N based on F_N and ρ' can be found that is valid for freely falling particles at any $\rho' > 1$:

$$\log(k_N) = \alpha_2 \left[-\log(F_N)\right]^{\beta_2} \quad \text{for } \rho' > 1 \tag{4.29}$$

where α_2 and β_2 are sigmoidal functions of ρ'

$$\alpha_2 = 0.45 + \frac{10}{\exp(2.5 \log \rho' + 30)} \tag{4.30}$$

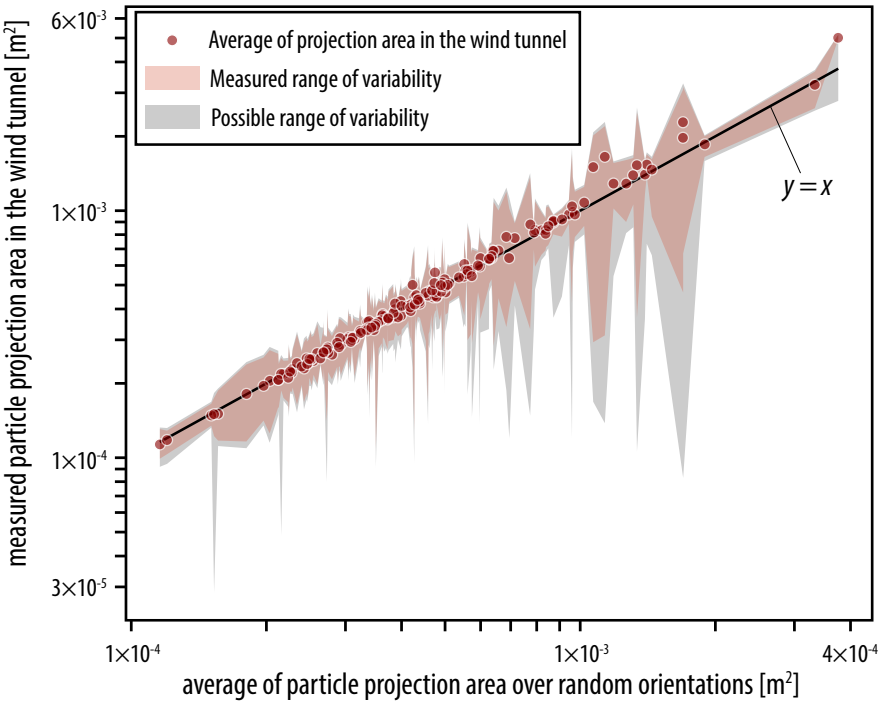

Figure 4.20: Average of particle projection area normal to the direction of flow measured in the wind tunnel versus average of particle projection area over 1000 random orientations. Variation of projection area is both measured based on wind tunnel experiments (red shading) and calculated from the particle 3D model (gray shading).

$$\beta_2 = 1 - \frac{37}{\exp\left(3\,\log\rho' + 100\right)} \tag{4.31}$$

A summary of error analyses of selected correlations on estimating k_N of all data points in the Newton's regime is presented in Table 4.6, which shows that Eqs.(4.29 – 4.31) are associated with a remarkable average error of 14.3% (max. error of 51.2%). Unfortunately, the model of Hölzer and Sommerfeld (2008) could not be benchmarked here, since particle orientation was not known for data points from the literature.

Eqs.(4.29 – 4.31) take into account the effects of preferred orientations of particles on the drag coefficient through ρ', however, not all possible orientations might happen when particles freely fall in a fluid. In fact, highly non-spherical particles (i.e. low F_N) might have very different drag coefficients in their extreme orientations. To explore this, the dependency of k_N on F_N for various non-spherical particles at fixed orientations is plotted in Fig. 4.22 (from published data, see Figure caption). Most particles are divided in two groups depending on their orientation relative to

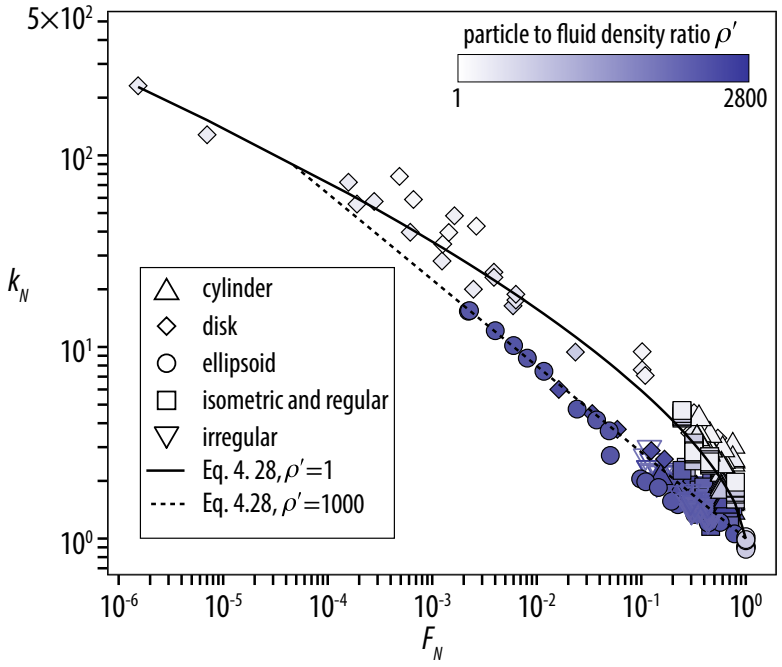

Figure 4.21: Newton's drag correction k_N for freely falling non-spherical particles versus F_N at different particle to fluid density ratios ρ' for our wind tunnel experiments (Fig. 4.17) and published data from Pettyjohn and Christiansen (1948), Willmarth et al. (1964), Christiansen and Barker (1965), Isaacs and Thodos (1967) and McKay et al. (1988) (see Table 4.3).

the flow: *normal* (maximum projection area perpendicular to the flow direction) and *parallel* (minimum projection area perpendicular to the flow direction). In general, drag coefficient of particles is always higher than that of the volume-equivalent sphere when they are fixed normal to the flow ($k_N > 1$) and is smaller than that of the sphere when they are fixed parallel to the flow ($k_N < 1$). The exception is cylindrical particles fixed parallel to the flow, where k_N is smaller than unity only when $F_N < 0.7$.

Table 4.6: Mean and maximum error associated with the estimations of the drag coefficient of non-spherical particles in the Newton's regime measured in various liquids (compiled from the literature) and air (present study), see Table 4.3.

Correlation	Error%	
	mean	*max*
Haider and Levenspiel (1989), Eq. (4.6)	54.9	242
Ganser (1993), Eq. (4.11)	53.9	244
This work, Eq. (4.29)	14.3	51.2

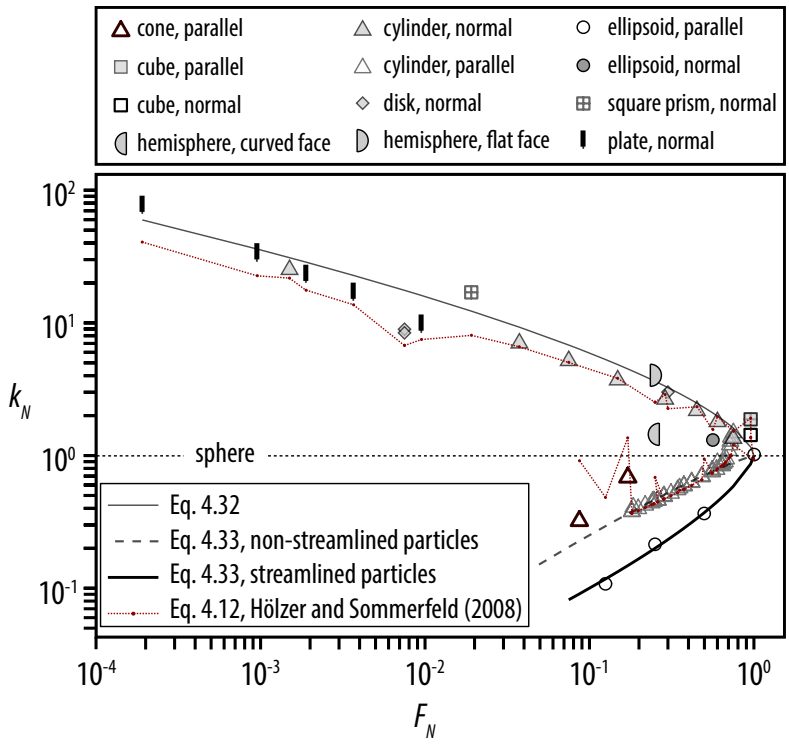

Figure 4.22: Newton's drag correction k_N for various non-spherical particles measured experimentally in fixed orientations against F_N from the data of Hoerner (1965), White (1998) and Higuchi et al. (2008).

In Fig. 4.22, it can be noted that the drag coefficient in a fixed orientation is dependent not only on the particle shape but also on the direction of the flow. As an example, for a hemisphere when the flow impinges the curved face, k_N is 1.4, which largely increases to 4.0 when the flat face is in the front. In this case, while particle projection area normal and parallel to flow is constant (i.e. constant $\psi_\perp$), the drag coefficient can change up to 185%. In addition, the differences between k_N for streamlined (e.g. ellipsoid) and flat-nose particles (e.g. cylinder) fixed parallel to the flow are significantly different, while their values of F_N and $\psi_\perp$ are very close together. Thus, no unique correlation as a function of F_N, ψ, $\psi_\perp$ or any other shape/orientation descriptor can be found for estimating k_N for all shapes. At most, general correlations can be found that can roughly constrain the extremes of variation in k_N at different orientations.

In Fig. 4.22 a curve based on Eq. (4.29) for $\rho' = 1$ is drawn (same as solid line in Fig. 4.21), which, interestingly, is very close to k_N for particles fixed normal to the flow. This indicates at the limit of $\rho' \approx 1$ particles fall with their maximum

projection area perpendicular to their falling direction. Therefore, the maximum drag, $k_{N,max}$, occurs for particles oriented normal to the flow and can be estimated by inserting $\rho' = 1$ in Eq. (4.29):

$$\log\left(k_{N,max}\right) = 0.77\ \left[-\log\left(F_N\right)\right]^{0.63} \tag{4.32}$$

For particles in the parallel orientation, for which the drag coefficient are the lowest at a given F_N, the simplest way for estimating $k_{N,min}$ is to define two separate correlations for non-streamline and streamline particles:

$$\log\left(k_{N,min}\right) = \begin{cases} -0.6\ \left[-\log\left(F_N\right)\right]^{1.17} & \text{non-streamline, } F_N > 0.1 \\ -\ \left[-\log\left(F_N\right)\right]^{0.48} & \text{streamline, } F_N > 0.1 \end{cases} \tag{4.33}$$

It should be noted that Eq. (4.33) results in $k_{N,min} < 1$ for all particles, which is not the case for cylinders with $F_N > 0.7$, but it is the only solution if we want to avoid complex correlations or using orientation-dependent parameters. In addition, Eq. (4.33) is valid only at $F_N > 0.1$ since no data at lower values of F_N were available to check its validity. Eq. (4.33) is associated with average error of 21% (max. error of 152%) for estimating drag coefficient end members of various particle shapes. Estimation of model of Hölzer and Sommerfeld (2008) is also plotted in Fig. 4.22, which shows that it is an accurate model with an average error of 17% (max. error of 184%) for all particles except for parallel ellipsoids. For parallel ellipsoids, however, it is associated with large errors up to 347% since it significantly overestimates the drag coefficient of parallel ellipsoids (even higher than the drag coefficient of parallel cylinders).

4.5.3 The general drag coefficient model

Based on the dimensional analysis of Ganser (1993), the drag coefficient of non-spherical particles for any subcritical Reynolds number can be predicted as a function of Stokes' k_S and Newton's k_N drag corrections. In particular, by normalizing the drag coefficient C_D and particle Reynolds number Re as C_D/k_N and $Re\,k_N/k_S$ (Ganser, 1993), repectively, all data points obtained for freely falling particles show

a similar trend as it is illustrated in Fig. 4.23. Finally, a general correlation for estimating the normalized drag coefficient based on normalized Reynolds number can be found that is valid for any particle shape:

$$\frac{C_D}{k_N} = \frac{24\,k_S}{Re\,k_N}\left(1 + 0.125\,(Re\,k_N/k_S)^{2/3}\right) + \frac{0.46}{1 + 5330/(Re\,k_N/k_S)} \tag{4.34}$$

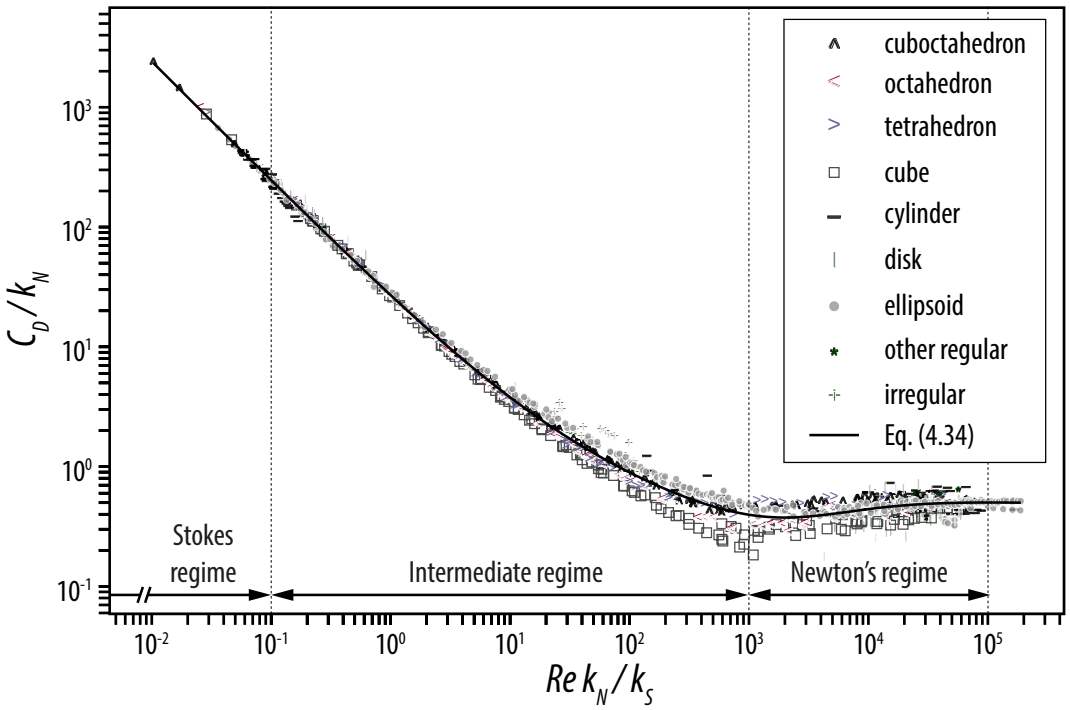

Figure 4.23: Dependency of normalized drag coefficient of freely falling particles on normalized Reynolds number. Data are from present study, Pettyjohn and Christiansen (1948), Willmarth et al. (1964), Christiansen and Barker (1965), Isaacs and Thodos (1967), Schlighting (1968), Roos and Willmarth (1971), Achenbach (1972), Clift Clift et al. (2005) and McKay et al. (1988) (see Table 4.3).

It is important to note that the fitting constants in Eq. (4.34) are different compare to those of Ganser (1993). In addition. k_S and k_N are based on different shape descriptors. Eq. (4.34) is associated with an average error of 5.3% for all data points (12.1% if 10^4 ellipsoids in the Stokes' regime are excluded). A detailed error analysis of Eq. (4.34) along with comparison with other models is shown in Table 4.7. It can be seen how Eq. (4.34) has the lowest mean of relative error for estimating drag coefficient of non-spherical particles that is half of that for the models of Haider and Levenspiel (1989) and Ganser (1993). If, for the sake of simplicity, we approximate non-spherical particles to ellipsoids by neglecting the

term $d_{eq}^3/L\,I\,S$ for calculating F_S and F_N (i.e. $F_S = f\,e^{1.3}$, $F_N = f^2\,e$), the average error of Eq. (4.34), for the particle considered in Table 4.7, slightly increases to 10.7% (maximum of 87.9%).

Table 4.7: Mean and maximum error associated with the estimations of the drag coefficient of all non-spherical particles freely falling at $Re < 3 \times 10^5$, including data points compiled from the literature and those obtained in the present study (see Table 4.3). It should be noted that the error analysis presented here was performed only for 500 of the 10^4 ellipsoids calculated in this study for the Stokes' regime in order to have a uniform distribution of data points at different Re.

Correlation	$error\%$	
	$mean$	max
Haider and Levenspiel (1989), Eq. (4.6)	19.4	244.0
Ganser (1993), Eqs. (4.7), (4.9) and (4.11)	20.0	247.6
This work, Eqs. (4.25), (4.29) and (4.34)	9.8	73.4

If we take a closer look at Fig. 4.23, a scatter in the data at intermediate Reynolds numbers can be observed. Loth (2008) suggested that this scatter in the intermediate regime is due to the effect of particle orientation, which for some specific shapes (e.g. sphere, broadside falling cylinder) results in circular cross sections in the direction of the flow while for other shapes (e.g. , broadside falling disk and cubes) results in sharp cross sections. He argued that this scatter can be explained considering that the separation point of the boundary layer for particles with circular cross sections is dependent on Re, whereas for the others the separation point remains almost fixed after initiation at low Re. A solution for this problem is to find separate fits for estimating the drag coefficient of particles of circular and non-circular sections (Loth, 2008). However, here we have decided not to present any correlation other than Eq. (4.34), since in any case the associated error is low (i.e. 5.9%) and the gain in the added accuracy probably is not worth the extra complications.

Results obtained in this study do not allow us to characterize secondary motion of irregular particles at intermediate range of Reynolds number systematically, simply because the field of view through our high-speed camera is too small ($24 \times 16\,mm$). Nevertheless, given that in contrast to previous studies our experiments are conducted in air-filled settling columns, some interesting aspects can be analysed by

inspecting the high-speed videos of falling particles. In Fig. 4.24, it can be seen that the falling orientation at $15 < Re < 30$ for irregular particles, is either steady (Fig. 4.24a), steady while rotating around a vertical axis (Fig. 4.24b) or associated with some oscillations (Fig. 4.24e – i). Additionally, particles shown in Fig. 4.24a – c and 4.24h – i fall with orientations close to their maximum projection area normal to their falling paths, whereas the projected area of the particle in Fig. 4.24d – g is variable (oscillation frequency $\approx 8\,Hz$). In any case, we did not observe any oscillation for particles with $Re < 18$, which is much lower compare to Re found for steady fall of cylinders (i.e. $Re < 80 - 300$) and disks (i.e. $Re < 100$) in liquids. This suggests that for irregular particles falling in quiescent gases when Brownian motion is not important and at $0.05 < Re < 18$, $k_{S,\,max}$ and $k_{N,\,max}$ can provide better estimations of the drag coefficient through Eq. (4.34) than k_S and k_N, given that particles fall with their maximum projected area normal to the flow.

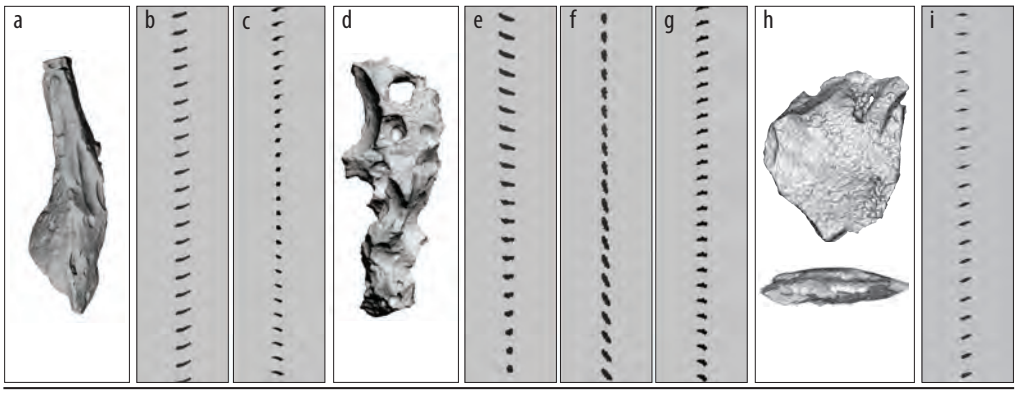

Re		15.9	16.3		19.8	20.2	20.4	28.8
ρ [kg m^{-3}]	*2320*			2268			2935	
d_{eq} [µm]	225			266			300	
e	0.33			0.31			0.75	
f	0.64			0.97			0.20	
ψ	0.56			0.44			0.59	

Figure 4.24: Falling pattern of irregular particles in settling columns. The 3D model of the falling particle is shown in the left side of high-speed image sequences. High-speed image sequences shown in b, e, f are from experiments carried out in the short settling column with the falling distance of $\approx 0.45\,m$, image height of $15.6\,mm$ and recording speed of $1600\,fps$; and in c, g and i are from experiments performed in the intermediate settling column with falling distance of $\approx 1.13\,m$, image height of $14.9\,mm$ and recording speed of $2000\,fps$.

At higher Re, the frequency of oscillation for irregular particles increases significantly and in some cases can lead to strong lateral deviations as it is shown in Fig. 4.25. However, even at high Re some particles have been observed to fall with a

steady orientation and, hence, a general conclusion cannot be made.

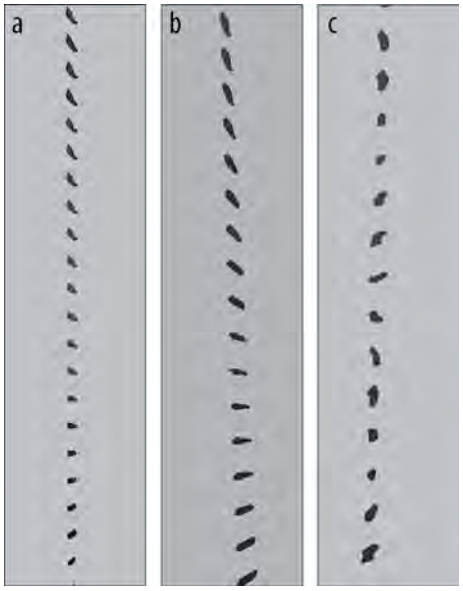

Figure 4.25: Irregular particles in settling columns falling at Reynolds number of (a) 120, (b) 190 and (c) 250. These experiments are conducted in the long settling column with falling distance of $\approx 3.6\,m$. Time interval between each snapshot of the particle is $0.625\,ms$ $(1600\,fps)$ and image height is $40.7\,mm$.

4.6 Caveats of the new model

Although a large number of data points in a wide range of Re are used to derive the general drag coefficient and other correlations in this study, it is important to discuss the assumptions and limitations behind the model. One of the crucial assumptions for obtaining the general drag coefficient model, Eq. (4.34), is that the drag coefficient of a particle with a given shape, density ratio and orientation is solely a function of Re, k_S and k_N. This, however, can be questionable in some particular cases (e.g. the observed spread in the data in Fig. 4.23 at intermediate Re). An example is shown in Fig. 4.26, which plots the drag coefficient of an ellipsoid with $f = e = 0.5$ and density of $2000\,kg\,m^{-3}$ falling in water and air predicted by Eq. (4.34) using Eqs. (4.25), (4.29). It can be seen that effect of the density ratio starts to be noticeable at $Re > 1$, while it was expected to be an influencing parameter at higher Re (at least not before Re of 18, see section 4.5.2).

This premature influence of density ratio at low Re can lead to an artificial

underestimation of the drag coefficient. In order to check this issue, falling velocities of particles measured in settling columns ($9 < Re < 900$) are compared to those predicted by Eq. (4.34). As it is shown in Fig. 4.27, the terminal velocity of particles in this range of Re seems to be slightly overestimated by Eq. (4.34). However, the average error for all particles is 12.5% and it is even lower for irregular particles that are better characterized by SEM micro-CT and regular particles (i.e. 7.5%). So, we can conclude that the overestimation of terminal velocity (i.e. the underestimation of the drag coefficient) does not affect the overall estimation error of Eq. (4.34). Finally, given that correlations derived in this work are empirical, it is important to apply them within the range of observation provided.

4.7 Discussion and conclusions

The drag coefficient of non-spherical particles of regular and irregular shapes at subcritical Re ($Re < 3 \times 10^5$) was investigated through analytical and experimental methods. Effects of particle shape, surface roughness, orientation and particle to fluid density ratio ρ' on the drag coefficient were discussed in detail. Two new shape descriptors, namely Stokes F_S and Newton shape descriptor F_N, were introduced that are based on particle flatness f, elongation e and spherical equivalent diameter d_{eq}. Compared to the sphericity that is the most used shape descriptor in the literature, the new shape descriptors are significantly easier to measure, are not a function of measurement scale and are better correlated with the drag coefficient. Based on our results the following conclusions can be drawn:

- A new general drag coefficient correlation is presented, Eq. 4.34 using Eqs. (4.25, 4.29, 4.30 and 4.31, summerized in Table 4.8 and Fig. 4.23, which can be used to predict the average drag coefficient of particles falling in fluids (gases and liquids). By using equations in Table 4.8, it is assumed that the particle orientation in the Stokes' regime is random and in the Newton regime is a function of particle to fluid density ratio ρ'. The average error of the new general drag coefficient correlation for predicting the drag coefficient of non-spherical particles presented in this study and literature is 9.7% (maximum of

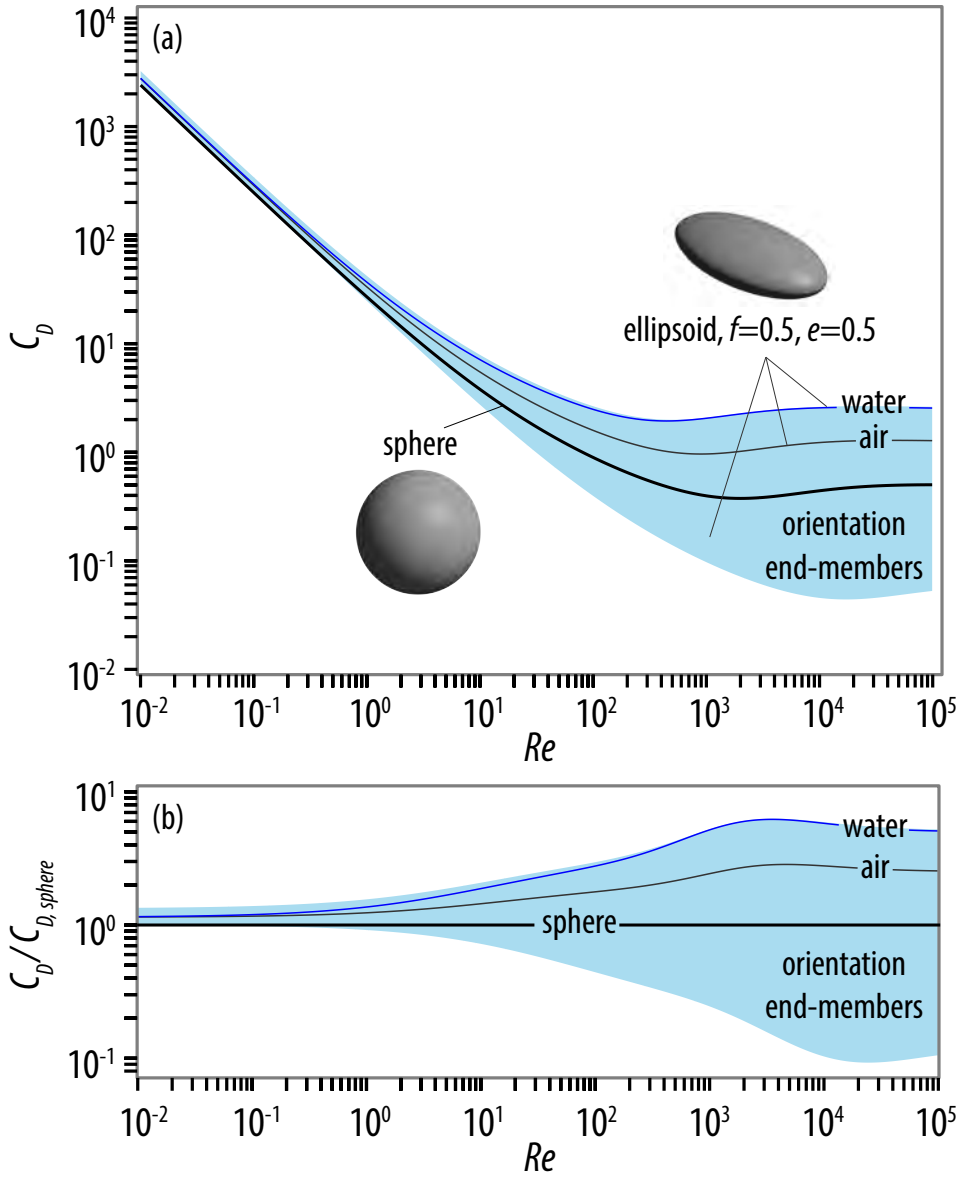

Figure 4.26: Effect of orientation on the drag coefficient of an ellipsoid with flatness and elongation of 0.5 and density of 2000 kg m^{-3} estimated by Eq. 4.34 using Eqs. (4.26, 4.33 and 4.32). (a) Ellipsoid drag coefficient against Reynolds number; (b) same as (a) with the ellipsoid drag coefficient normalized by the sphere drag coefficient. For the sake of comparison the average drag coefficient for free fall in water and air is also shown.

73.4%), see Table 4.7.

- If, we approximate non-spherical particles to ellipsoids by neglecting the term $d_{eq}^3/L\,I\,S$ for calculating F_S and F_N (i.e. $F_S = f\,e^{1.3}$, $F_N = f^2\,e$), the average error of Eq. (4.34), for the particle considered in Table 4.7, slightly increases to 10.7% (maximum of 87.9%).

- Effect of particle orientation on the drag coefficient, in particular at high Re,

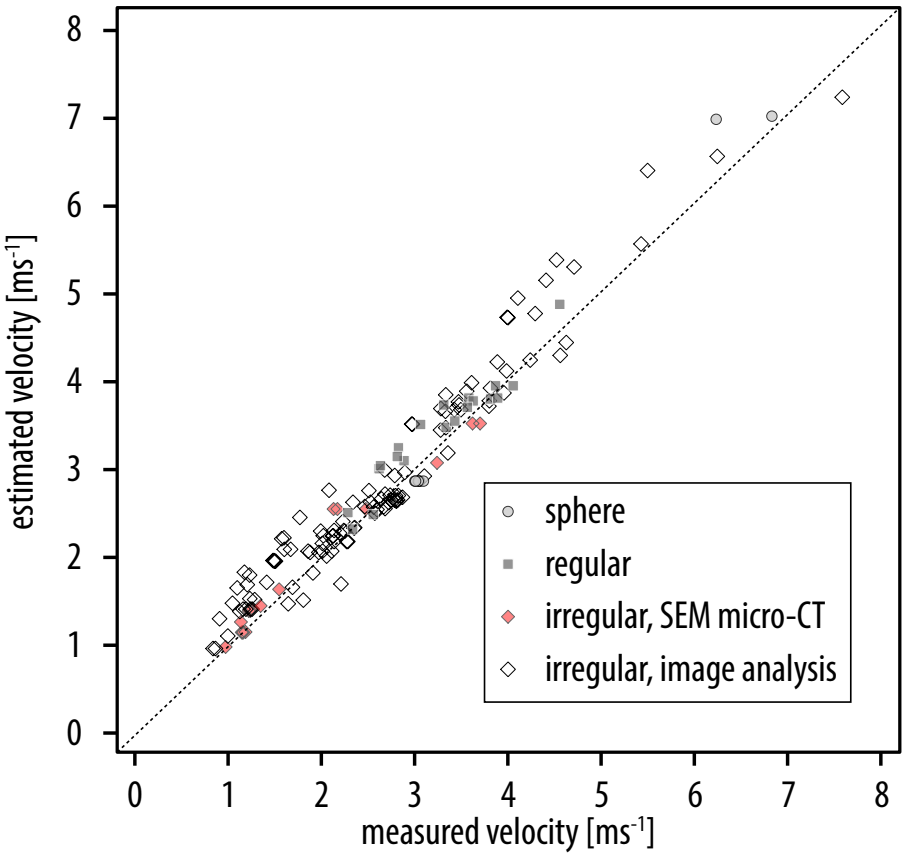

Figure 4.27: Falling velocity of particles measured in settling columns ($9 \leq Re \leq 300$) against velocity estimated through the general drag coefficient model, Eq. (4.34). Regular particles include cylinders and prisms (see Table 4.3). Characteristics of irregular particles (e.g. volume, form dimensions) are quantified either by SEM micro-CT or by performing image analyses on 2 – 3 projections of the particle.

is significant (Figs. 4.12 and 4.22). By using Eqs. (4.26), (4.32) and (4.33) within Eq. (4.34) end-members of the particle drag coefficient due to change in the orientation can be found (Fig. 4.26a). These end-members at high Re, however, are valid for specific orientations of particles that might occur rarely as the particle falls.

- Out of all parameters describing particle shape, it is the particle form that has the greatest impact on the drag coefficient and not the surface-related characteristics, such as sphericity.

- In the Stokes' regime ($Re < 0.1$), the drag coefficient is slightly more sensitive to changes in the elongation than in the flatness, i.e. $F_S \propto f\, e^{1.3}$, whereas in the Newton's regime ($1000 \leq Re \leq 3 \times 10^5$), the impact of the flatness on the

Table 4.8: The general correlation for estimating the average drag coefficient, C_D, of freely falling solid non-spherical particles in liquids or gases. f and e are particle flatness and elongation defined as the ratio of S/I and I/L, respectively; where L, I and S are particle form dimensions and defined as the longest, intermediate and shortest lengths of the particle, receptively. d_{eq} is the diameter of a volume-equivalent sphere, Re is the particle Reynolds number defined in Eq. (4.2) and ρ' is the particle to fluid density ratio. By neglecting the term $d_{eq}^3/L\,I\,S$ for calculating F_S and F_N, shape of non-spherical particles will be approximated to ellipsoids of similar flatness and elongation.

$$C_D = \frac{24\,k_S}{Re}\left(1 + 0.125\,(Re\,k_N/k_S)^{2/3}\right) + \frac{0.46\,k_N}{1 + 5330/(Re\,k_N/k_S)}$$

where

$$k_S = \left(F_S^{1/3} + F_S^{-1/3}\right)/2$$

$$k_N = 10^{\,\alpha_2}\,[-\log(F_N)]^{\beta_2}$$

$$\alpha_2 = 0.45 + 10/\exp(2.5\,\log\rho' + 30)$$

$$\beta_2 = 1 - 37/\exp(3\,\log\rho' + 100)$$

and

$$F_S = f\,e^{1.3}\left(\frac{d_{eq}^3}{L\,I\,S}\right)$$

$$F_N = f^2\,e\left(\frac{d_{eq}^3}{L\,I\,S}\right)$$

drag coefficient is much more significant than the impact of the elongation, i.e. $F_N \propto f^2\,e$.

- The average drag coefficient of a non-spherical particle falling in a gas or a liquid is always higher than the drag coefficient of its volume-equivalent spheres, i.e. k_S, $k_N > 1$ (Figs. 4.11 and 4.21). However, in some specific orientations, the particle drag can be even lower than its volume-equivalent sphere (e.g. minimum projected area normal to the motion path) (Fig. 4.26).

- The impact of both shape and orientation on the drag coefficient of non-spherical particles increases with Re (Fig. 4.26b).

- Effects of small-scale surface vesicularity and roughness on the drag coefficient of non-spherical particles are negligible at subcritical Re ($< 3 \times 10^5$).

- In the Newton's regime ($1000 \leq Re < 3 \times 10^5$), particle secondary motions and orientation are functions of the particle to fluid density ratio ρ' (Fig. 4.21). Particles falling in liquids (low ρ') have orientations close to their maximum projected area normal to their falling path, while those falling in gases (high

ρ') have random orientations and projection areas lower than their maximum. As a result, a solid particle of a given shape will experience higher drag when it falls in a liquid compared to when it falls in a gas.

4.8 Appendices

Analytical and experimental dataset obtained in this chapter is available on the accompanied CD-ROM.

Acknowledgments

This project was funded by the Swiss National Science Foundation (SNSF, Grant No. 200020-125024). Authors are grateful to I. Manzella for insightful discussions on the experimental set-ups, design of experiments and particle shape characterization, P. Pontelandolfo and P. Haas for their help and constructive discussions on the wind tunnel set-up and calibration, L. Dominguez for her help on particle image analysis, P. Vonlanthen for his support on particle SEM micro-CT, J. Phillips for brainstorming ideas at the design stage of the wind tunnel and F. Arlaud for his help to design and construct the settling columns.

4.9 Author's contributions

All authors were involved in the conceptual design of this study, and in the drafting and reviewing of this chapter. G. Bagheri conducted the experiments, analytical/numerical calculations and statistical analyses.

Chapter 5

Timing and Nature of Volcanic Particle Clusters Based on State-of-the-Art Field and Numerical Investigations[1]

5.1 Introduction

Dispersal and deposition of ash during volcanic explosive eruptions strongly affect the surrounding environment and distal atmosphere, with disruptive consequences on local communities and both land and aviation transport (Blong, 1984; Guffanti et al., 2010). Aggregation processes are well known to affect sedimentation of fine ash ($< 63\,\mu m$) by considerably reducing its residence time in the atmosphere (Lane et al., 1993; Rose and Durant, 2011; Brown et al., 2012). If particle aggregation is not considered, volcanic ash transport and dispersal models fail to accurately describe both particle deposition in proximal areas and atmospheric ash concentration in the far field, with important implications for both hazard assessment and real-time ash forecasting (Folch et al., 2009; Rose and Durant, 2011; Brown et al., 2012).

Volcanic particles mainly collide and cluster because of complex interactions of surface liquid layers, electrostatic forces, turbulence and/or differences in settling velocities. Depending on the water content, particle aggregation results in the formation of *particle clusters* and/or *accretionary pellets* (e.g. Sparks et al., 1997; Brown et al., 2012). Based on the classification introduced by Brown et al. (2012), the category of particle clusters (also known as *dry aggregates* in previous litera-

[1] To be submitted Bagheri G., Rossi E., Biass S., Bonadonna C. (2015)

ture) includes both *ash clusters*, noted as PC1, and *coated particles*, noted as PC2. Ash clusters are defined as fragile irregular shaped aggregates composed of particles $< 1 - 40\,\mu m$, whereas coated particles are defined as fragile aggregates comprised of a crystal, crystal fragment, pumice or lithic clast *partially* covered with fine ash particles. The category of accretionary pellets comprises poorly structured pellets noted as AP1, pellets with concentric structures (also known as *accretionary lapilli*), noted as AP2, and *liquid pellets* (also known as mud rain), noted as AP3 (Brown et al., 2012).

During the last two decades, experimental, numerical and field investigations have been attempted to describe aggregation processes in terms of grain-size distribution, terminal velocity, structure, density and porosity (Lane et al., 1993; Schumacher, 1994; Gilbert and Lane, 1994; Schumacher and Schmincke, 1995; James et al., 2002; Taddeucci et al., 2011; Bonadonna et al., 2011; Van Eaton and Wilson, 2013; Telling et al., 2013). However, due to the low preservation potential of particle clusters in deposits, most studies focused on characterization of the more resistant well-structured pellets (i.e. accretionary lapilli (Gilbert and Lane, 1994; Van Eaton and Wilson, 2013).

In this chapter we focus on particle clusters, in particular coated particles since they have poor preservation in the geological record. Field studies of particle clusters include the investigations of the 1980 eruption of Mount St. Helens, USA (Sorem, 1982), the 1990 – 1994 eruptions of Sakurajima volcano, Japan (Gilbert et al., 1991; Sparks et al., 1997), the 1997 eruption phase of Soufrire Hills volcano, Montserrat (Bonadonna et al., 2002b) and the 2010 eruption of Eyjafjallajökull volcano, Iceland (Taddeucci et al., 2011; Bonadonna et al., 2011). Sorem (1982) observed particle clusters with diameters between 250 µm to 500 µm about 390 km from the vent that were composed of ash $< 40\,\mu m$. He also reported that large ash particles (40 µm to 60 µm) deposited as clusters far beyond the distance at which they would have settled if traveling independently. Gilbert et al. (1991) and Sparks et al. (1997) reported ash clusters at Sakurajima volcano with diameters $< 3\,mm$, which consisted of particles $< 200\,\mu m$, whereas coated particles had diameters $> 200\,\mu m$ and were covered with particles $< 20\,\mu m$. Bonadonna et al. (2002a) observed both types

of particle clusters resulting from either dome collapse or Vulcanian explosions at Soufrire Hills volcano. Finally, Bonadonna et al. (2011) observed both types of particle clusters at distances between 10 km and 55 km from vent during the 2010 long-lasting eruption of Eyjafjallajökull volcano. Ash clusters had diameters up to 600 µm and consisted of particles < 90 µm, while coated particles were composed of large particles up to 760 µm that were coated with particles < 100 µm. For the same eruption, High-Speed (HS) videos recorded by Taddeucci et al. (2011) show how most particle clusters fell with terminal velocities between $1 - 4\ \mathrm{m\,s^{-1}}$.

The first laboratory experiment on the clustering of volcanic particles was conducted by Schumacher (1994), who found that electrically charged volcanic ash from the 1980 eruption of Mount St. Helens could cluster when they are transported within an electrostatic field. The results also indicated how the first particle clusters to sediment were coated particles that included a large particle > 63 µm and some accreted fines, whereas the last to sediment were ash clusters composed of particles < 45 µm and some incorporated larger particles up to 125 – 180 µm. The comparison with grain-size data from other volcanic eruptions suggested that the change in structures of proximal to distal particle clusters is not unique to Mount St. Helens. Almost a decade later, James et al. (2002) conducted a similar experiment to study the role of electrostatic charge on the aggregation of volcanic particles freely falling in dry conditions (relative humidity $\sim 25-30\%$). By charging pumices from the 1980 eruption of Mount St. Helens through fragmentation, they found that ash particles < 70 µm could cluster together to create particle clusters up to 800 µm with density of $\sim 100 - 200\ \mathrm{kg\,m^{-3}}$ and settling velocity of $< 1\ \mathrm{m\,s^{-1}}$. They also investigated the possibility of particle rafting through numerical methods. However, they concluded that the rafting of large particles (< 200 µm) due to aggregation is unlikely since the window of possibility are very narrow.

Despite numerous studies on volcanic particle clusters, fundamental questions remain unanswered, such as the structural and aerodynamic characteristics of particle clusters, the time required to form, their evolution in time and space, and the modification they impose on sedimentation patterns. The objective of this study is to answer these questions through a multi-technique approach applied to a specific

volcanic explosion of Sakurajima volcano (Japan), which includes field High-Speed-High-Resolution (HS-HR) imaging, analyses of in-situ collected particle clusters and numerical inversions combined with published data for additional volcanic eruptions.

5.2 Methods

5.2.1 Field investigations

Our experiment was designed to allow a comparison of pre- and post-depositional features and was conducted at Sakurajima volcano, Japan, which has been continuously active since 1955. The associated ash-rich Vulcanian plumes occurring on an almost daily basis show clear evidence of aggregation (Gilbert et al., 1991; Sparks et al., 1997). Detailed measurements were acquired for one particular explosion that occurred at 17 : 47 Japanese Standard Time (JST) on the 3rd of August 2013 (Figure 5.1A). The sky was almost clear with some clouds upwind of the vent. The explosion was recorded with a normal High-Definition (HD) camera, from which we inferred a maximum plume height of 2.8 km a.s.l. reached within 100 s after the onset. The rising plume was bent over by the wind and started spreading horizontally $\sim$ 900m away from the vent (i.e. plume corner) and spread toward south-east with a velocity of $\sim 5.5\,\mathrm{m\,s^{-1}}$. The plume base estimated to be at the constant height of 2.3 km a.s.l. from the HD movie.

Our ground-based observation site was located about 3.7 km downwind from the vent along the dispersal axis (see Figure 5.1). Tephra samples were collected in dedicated trays at two sequential time steps in order to monitor accumulation rates and time variations in grain-size distribution: Phase I) between 18:02 and 18:07 JST, associated with individual particles followed by sub-spherical particle clusters, and Phase II) between 18:07 and 18:12 JST mostly associated with sub-spherical particle clusters. Note that the fallout was continuous and the collection in separated trays was carried out only to study the evolution of deposition and aggregation processes in time (i.e. the choice of sampling intervals was arbitrary). The grain-size distributions of samples were analyzed using a laser-diffraction particle-size analyzer at the University of Geneva (CILAS 1180).

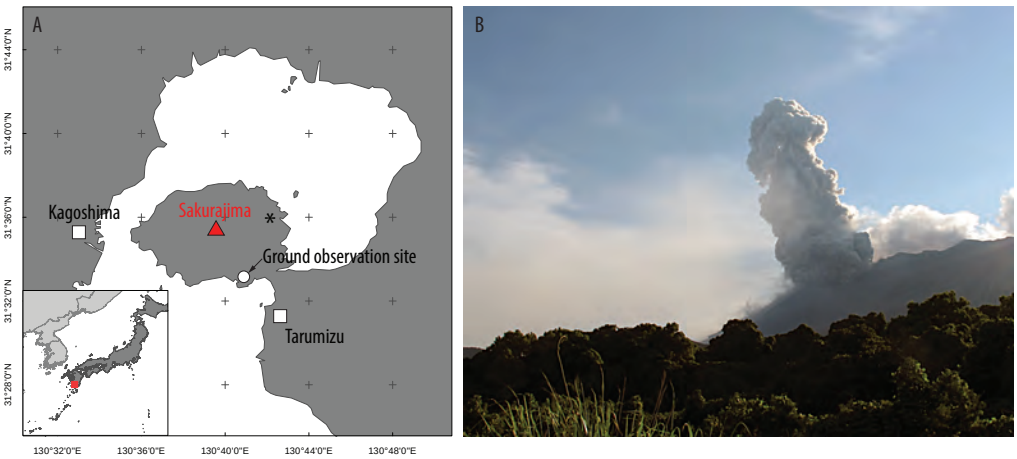

Figure 5.1: (A) Map of Sakurajima, Japan, showing the location of the vent and our ground-based observation site. (B) Photo of the Vulcanian explosions occurred at 17:47 Japanese Standard Time (JST) on the 3rd of August 2013. The * symbol on the map shows the location where the photo was taken.

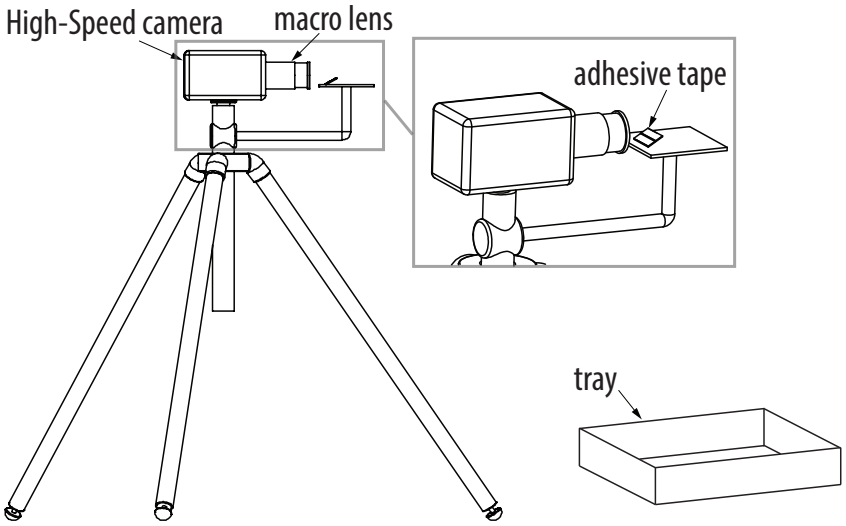

Figure 5.2: Sketch of the setup used in the field.

A schematic diagram of the Field setup is shown in Figure 5.2. The setup includes the HS camera on a tripod aimed at a thin-glass support covered with a specific double-sided tape allowing further analyses with a Scanning Electron Microscope (SEM). The thin-glass support for adhesive tapes was kept either horizontally or with an angle during the movie recording. A High-Speed (HS) camera with a resolution of 1200×800 pixels at 800 fps mounted with a Nikon 60 mm f/2.8D AF Micro-Nikkor lens was used at the ground-based observation site in order to capture HS-HR movies with a pixel size of 40 µm. Clusters were observed while impacting the thin-glass

support. HS-HR videos were taken at 18:05 and 18:09 JST and each lasted 10 s, since the camera memory was limited to 8 Gb of storage and videos had to be transferred before the next recording. The movies were then converted frame-by-frame to 8-bit Tiff format images and analysed by the ImageJ software to measure particle size, position and velocity. Aggregate density was calculated by solving particle equation of motion (considering gravity, drag and buoyancy forces) (Bagheri et al., 2013). Terminal velocity measurements are performed within the distance from the top of the videos to the plates, which is in the range of $\sim 10 - 45$ times the aggregates diameter.

Tephra collected in dedicated trays was manually sieved at half ϕ down to 500 µm and the fine fraction was analysed with the laser-diffraction CILAS 1180 instrument (http://www.cilas.com/). Particle density, measured by a water pycnometer (with an uncertainty of 3%), was found to vary linearly from 2330 $\mathrm{kg\,m^{-3}}$ for 1 – 2 mm particles (0 ϕ) to 2700 $\mathrm{kg\,m^{-3}}$ for 63 – 125 µm particles (4 ϕ) (Figure 5.3). Density of cores observed in HS-HR videos was assumed to be the same as the density of the particles measured with the water pycnometer. SEM images were processed with the ImageJ software, and particles were measured in the range 1 – 250 µm ($2 - 10\,\phi$). Areas of particles were reconverted to equivalent diameters (assuming spherical shapes) and then to volumes and ϕ values. To obtain the grainsize distribution of aggregates fro SEM images, particles in the SEM images were segmented manually or based on edge-detection algorithms.

Experimental errors and error analysis

The main error in measuring velocity of falling particles is due to the uncertainty in the particle centroid position. Considering the exposure time of videos (150 µs) and falling velocity of particles (1.2 – 2.9 $\mathrm{m\,s^{-1}}$), the uncertainty in the particle position δy is between 180 – 435 µm (i.e. exposure time multiplied by the falling velocity). Thus, given that the vertical displacement of particles in the image H is $\sim 400 \times 40$ µm (almost half of the image height), the error on the measured velocity is between 1.1 – 2.7% ($= 100 \times \delta y/H$).

The measured falling velocities of aggregates in the vertical direction were found

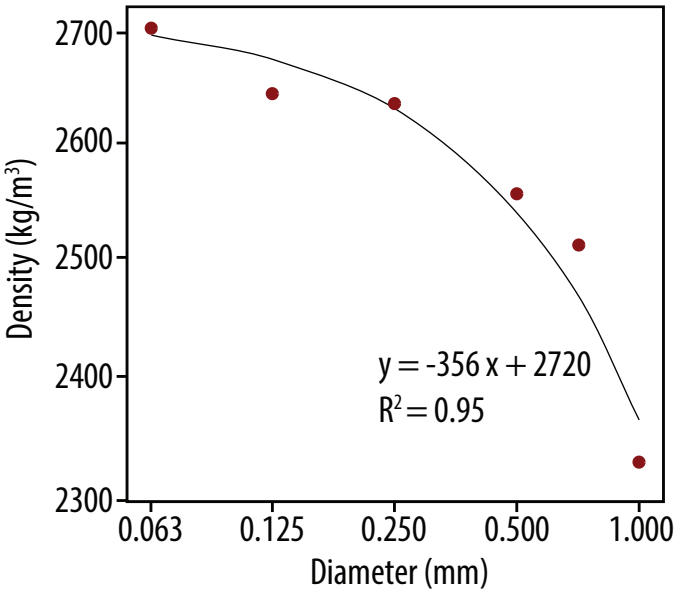

Figure 5.3: Logarithmic plot of particle diameter versus density measured with the water pycnometer for samples collected in the trays.

to be within $< 6\%$ of the average value. Thus, the effects of the thin-glass supports (end effects) on the terminal velocity of particles are negligible since the vertical distance is > 5 times the aggregate diameter (Chhabra, 2006) or at maximum is $2 - 9\%$ higher than measurements in unbounded conditions based on the Lorentz formulation (Hoper and Grant, 1948). We have neglected the end effects in our measurements.

The average error on the measurement of aggregate diameter from HS-HR movies is about 5% since in some frames they are not completely in focus. Converting 2D measurements from images to volume was done through correlations presented by Bagheri et al. (2015) that can be associated with an average error of 3% and uncertainty of $< 10\%$. This can result in $15 - 25\%$ error on the aggregate density. Uncertainty on the core diameters is higher since they are more irregular than aggregates. Assuming a shell density of $60 - 220$ kg m^{-3} (James et al., 2002; Brown et al., 2012), the diameter range of core particles is further constrained based on the calculated density of the whole aggregate and the mass conservation law. Through this procedure the uncertainty on the core diameter reduces to 10%. This uncertainty, however, can be higher if our assumption of the shell density is not valid.

Finally, some of the fine particles in the trays could be lost when we collected

samples into plastic bags. Although we did not observed strong winds, some re-suspended fine particles might be transported in the trays. In addition, grainsize distribution made by image analysis of SEM images can be biased by the overlapping of particles on each other.

5.2.2 Numerical investigations

Field observations were inverted using a two-dimensional Lagrangian particle tracking code to constrain the trajectory and the timing of clusters observed at the ground-based observation site and relies on the following assumptions. Numerical inversions were performed for the aggregates sedimented during both fallout phases (i.e. Phase I and Phase II). Forces considered in the particle equation of motion are the drag, buoyancy and gravity. Atmospheric properties were calculated based on atmospheric sounding measurements available from Wyoming University database (http://weather.uwyo.edu/upperair/sounding.html). First, we consider that aggregates formed in either the rising plume or the horizontal cloud due to high concentration of particles (Veitch and Woods, 2001; Costa et al., 2010). Thus, they do not grow/shrink due to aggregation/disaggregation after they are released from the rising plume or the horizontal cloud. Second, clusters were considered spherical since HS-HR videos indicate that aggregates have sub-spherical shapes. Thus, their drag coefficient was calculated with the standard drag coefficient model of Clift and Gauvin (1971).

Four different wind profiles were used since no direct measurement was available: i) a profile that linearly increases the wind speed from $0\,\mathrm{m\,s^{-1}}$ at the ground to 5.5 $5.5\,\mathrm{m\,s^{-1}}$ at the height of cloud base (2.3 km a.s.l.), ii) a two-segment linear profile based on experimental measurements of turbulent flow behind pyramids that linearly increases the wind speed from $0\,\mathrm{m\,s^{-1}}$ at the ground to $3.8\,\mathrm{m\,s^{-1}}$ at the vent height ($\sim$ 870 m asl) and then to $5.5\,\mathrm{m\,s^{-1}}$ at the height of the cloud base (Ikhwan, 2005), iii) interpolated data from ERA-Interim (ECMWF, European Center for Medium range Weather Forecasting) database, iv) interpolated data from atmospheric sounding measurements of Wyoming University.

In the simulations, fifty aggregates were released along the plume margins at

increasing heights with time and at 0.05 s intervals for a total duration of 10 minutes. As a result, a total of 10^4 particle clusters were tracked for each wind profile and fallout phase. Only particles matching the sampling location (i.e. 3.7 ± 0.25 km) and timing were considered. The range of ± 0.25 km is an arbitrary value, which we chose to increase the number of deposited particles during each phase for a reliable statistical analysis.

5.3 Results

5.3.1 Field Observations

Accumulation rate for Phase I (the first 5 minutes of fallout) was $2.9 \pm 0.3\,\mathrm{g\,m^{-2}\,min^{-1}}$, which decreased down to $2.2 \pm 0.2\,\mathrm{g\,m^{-2}\,min^{-1}}$ for Phase II (the second 5 minutes of fallout). Individual particles were recognized as non-vesiculated fragments with diameters between $\sim 300 - 1200\,\mu\mathrm{m}$ and density of $\sim 2500\,\mathrm{kg\,m^{-3}}$ (measured by water pycnometer). The variation of the density of particles between 63 – 1000 µm ($0 - 4\,\phi$) was found to be a linear function of the diameter (Figure 5.3).

HS-HR videos revealed that all clusters of both phases are composed of a single or multiple coarse ash particles acting as cores that rebounded upon impact with the adhesive tape. As a result of the impact, only an ensemble of ash $< 90\,\mu\mathrm{m}$ (i.e. shell particles) was preserved on the adhesive tape (Figure 5.4A, B). Classic SEM images of aggregates deposited on adhesive tape (e.g. Sparks et al., 1997; Bonadonna et al., 2011) can only show the occurrence of partially coated particles and broken ash clusters that appears to be separate objects (Fig. 5.5).

Sizes of core particles ($\sim 200 - 500\,\mu\mathrm{m}$) are comparable with the sizes of the entire aggregate before the impact ($\sim 400 - 800\,\mu\mathrm{m}$). Additionally, the size of core particles corresponds well to the mode of the coarse population of ground deposit (samples of trays) for both fallout phases (i.e. 500 µm and 250 µm, respectively; red arrows in Figure 5.4C,E). HS-HR movies were also used to derive size, terminal velocity and density of particle clusters that range between 1.2 – 2.9 $\mathrm{m\,s^{-1}}$ and 350 – 1000 $\mathrm{kg\,m^{-3}}$, respectively (see Table 5.1). Besides the videos described here in detail, we also recorded additional 19 videos of falling aggregates at Sakurajima

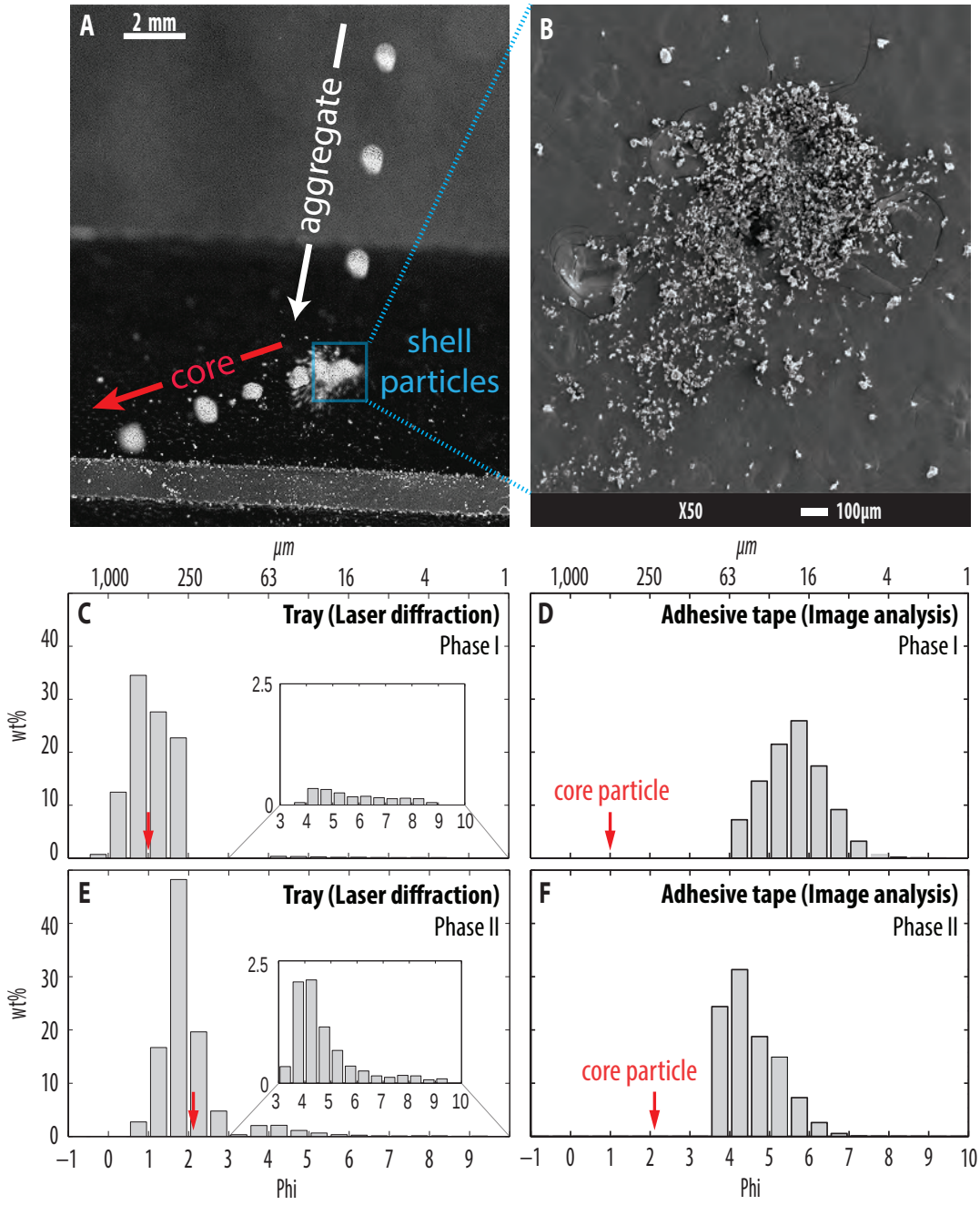

Figure 5.4: Selection of observed particle clusters. A: Image sequences of an HS-HR movie recorded for a Phase I particle cluster (time difference between each sequence is 2.5 ms). The HS-HR video shows that the particle cluster consists of a large core that rebounded the adhesive tape upon impact. B: SEM image of shell particles shown in Figure 5.4A (deposited at 18:05 JST). Particle size distributions in weight% obtained from C: laser diffraction measurements for the ash accumulated in the tray during Phase I fallout (18:00 – 18:07 JST). D: SEM analysis of Figure5.4B (Phase I particle cluster) E: laser diffraction measurements for the ash accumulated in the tray during Phase II fallout (18:07 – 18:12 JST). F: SEM analysis of a Phase II particle cluster deposited at 18:09 JST. Red arrows show the size of core particle derived from HS-HR videos.

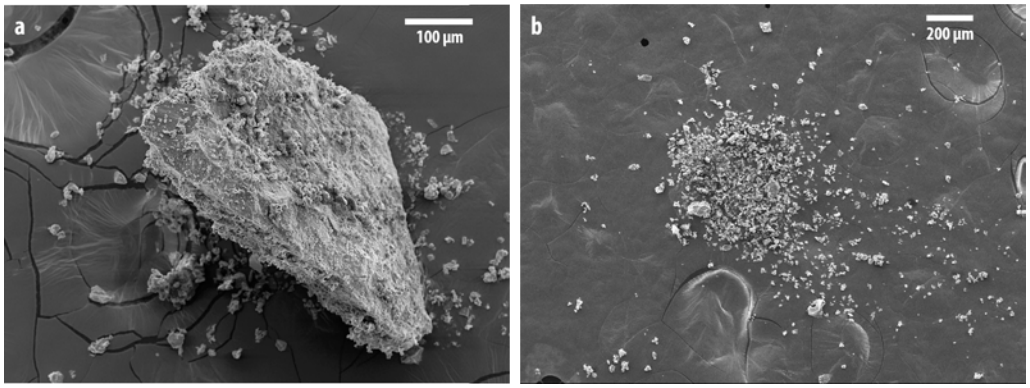

Figure 5.5: Sample SEM images of deposits collected on thin-glass supports during our field investigations in Sakurajima. (a) Core of a coated particle; (b) after-impact remaining of a coated particle on the adhesive tapes, which are particles within the aggregate shell. SEM images very similar to these images (e.g. Fig. 16.6 in Sparks et al. (1997); Fig. 7a – d in Bonadonna et al. (2011)) are considered as two different types of aggregates (i.e. a: coated particle, b: ash cluster), while our videos shows that these are, in fact, different aspects of coated particles.

Table 5.1: Characteristics of observed aggregates (i.e. coated particles) and core particles.

Fallout Phase[a]	Sed. Time	Aggregates				Core Particles	
		Diameter [µm]	Density [kg m^{-3}]	Velocity [m s^{-1}]	Porosity %	Diameter [µm]	Density [kg m^{-3}]
I	18:02 – 18:07	718 – 807	806 – 1009	2.7 – 2.9	60 – 68	500 – 525	2500 – 2700
II	18:07 – 18:12	440 – 630	357 – 864	1.2 – 1.8	67 – 83	200 – 330[b]	2500 – 2700

[a] Phase I and II indicate particle clusters sedimented during the first and second sampling interval, respectively.
[b] Special case of Phase II aggregates for which the core consisted of three particles with a minimum diameter of $\sim 200\,\mu m$

between 29th July-2nd August that show how 90% of aggregates were surly coated particles and the rest could also be ash clusters.

The mass fraction of particles $< 90\,\mu m$ in trays (which must have deposited as shell particles, since no individual fine ash was observed on adhesive tapes during SEM analysis) is about 4% and 12% for Phase I and Phase II, respectively. The mass fraction of shell particles (i.e. particles $< 90\,\mu m$) in each aggregate, f_{agg}, is quantified as follows:

$$f_{agg} = m_{shell}/(m_{shell} + m_{core}) \tag{5.1}$$

where m_{shell} and m_{core} are masses of shell particles and core particle, respectively. Based on Eq. (5.1), shell particles on average comprise 10% of the mass of Phase I

aggregates, which increases to 17% for Phase II aggregates. Finally, more aggregates fell during Phase II than Phase I. The aggregate fraction was quantified by first calculating the mass fraction of shell particles collected in trays (i.e. particles with diameter $< 90\,\mu m$), f_{tray}:

$$f_{tray} = m_{shell}/m_{total} = m_{shell}/(m_{shell} + m_{core} + m_{non-aggregated\,particles}) \tag{5.2}$$

where individual particles are non-aggregated particles. f_{tray} calculated by Eq. (5.2) is $\sim 4wt\%$ and $\sim 12wt\%$ for Phase I and Phase II aggregates, respectively (Figure 5.4C,E). Since $f_{tray} < f_{agg}$, we can conclude that a fraction of coarse-ash particles collected in trays sedimented as individual particles (i.e. $m_{non-aggregated\,particles} > 0$ in Eq. 5.2). It should be noted that by individual particles we mean particles that did not aggregate or were only coated with a negligible amount of fine ash. Assuming that all aggregates sedimented in trays were similar to those observed in HS-HR videos, we can conclude that the wt% of shell particles for each aggregate is the same as the wt% of shell particles in the trays:

$$\left.\frac{m_{shell}}{m_{shell} + m_{core}}\right|_{agg} = \left.\frac{m_{shell}}{m_{shell} + m_{core}}\right|_{tray} \tag{5.3}$$

As a result the total fraction of aggregates, F_{agg}, defined as the ratio of coarse-ash particles (i.e. ash$> 90\,\mu m$) that were involved in the aggregation process to the whole coarse-ash population can be derived by combining Eqs. (5.1 – 5.3):

$$F_{agg} \equiv \frac{m_{core}}{m_{core} + m_{non-aggregated\,particles}} = \frac{f_{tray} \times (1 - f_{agg})}{f_{agg} \times (1 - f_{tray})} \tag{5.4}$$

F_{agg} is 38 wt% and 67 wt% during Phase I and Phase II fallout, respectively. This means that both the rate of aggregation and the amount of shell particles increased from Phase I to Phase II.

5.3.2 Numerical investigations

The purpose of the numerical inversions is to have a rough estimation of the duration that aggregates spent in the plume, spreading cloud and atmosphere in order to be able to estimate an upper-bound for the time needed for particles to form aggregates. The size and density of clusters obtained from settling-velocity measurements at the ground-based observation site were used as an input to our Lagrangian code in order to resolve cluster trajectories.

Figure 5.6A shows all possible trajectories of Phase I clusters that could reach our sampling location within the observed deposition time. The resulting position in the plume at which particles were released for Phase I clusters ranges between 250 m and 2300 m from the vent depending on the wind profile. Thus, 95th percentile of Phase I clusters must have formed within 300 s seconds from eruption onset. In contrast, 95th percentile of Phase II particle clusters should have been formed within < 175 s (Figure 5.6B).

Based on our Lagrangian model, the maximum distances from the vent at which the observed Phase I and Phase II clusters were released are 2300 m and 1750 m, respectively. This is compatible with the sedimentation model of Bursik et al. (1992), which predicts that particle clusters of Phase I (terminal velocity of $\sim 3\,\mathrm{m\,s^{-1}}$) and Phase II (terminal velocity of $\sim 2\,\mathrm{m\,s^{-1}}$) represent $\sim 30\%$ and $\sim 60\%$ of the respective initial masses at the corner of the plume ($\sim$ 900m) at the distances of 2300 m and 1750 m from the vent (Figure 5.6).

5.3.3 Rafting effect

In addition to constraints and insights into timing and mechanisms of ash clustering, our data also confirm an important sedimentation process already speculated in the past, namely particle rafting (Sorem, 1982; Lane et al., 1993; James et al., 2002). Such a process bears fundamental implications on the sedimentation of relatively large particles. We observed how aggregation could simultaneously enhance the sedimentation of fine ash ($< 63\,\mu$m) and delay the deposition of large particles acting as cluster cores ($\sim 200 - 500\,\mu$m) (Fig. 5.7). In fact, while the terminal velocity of the observed fine ash increased up to several orders of magnitude due to

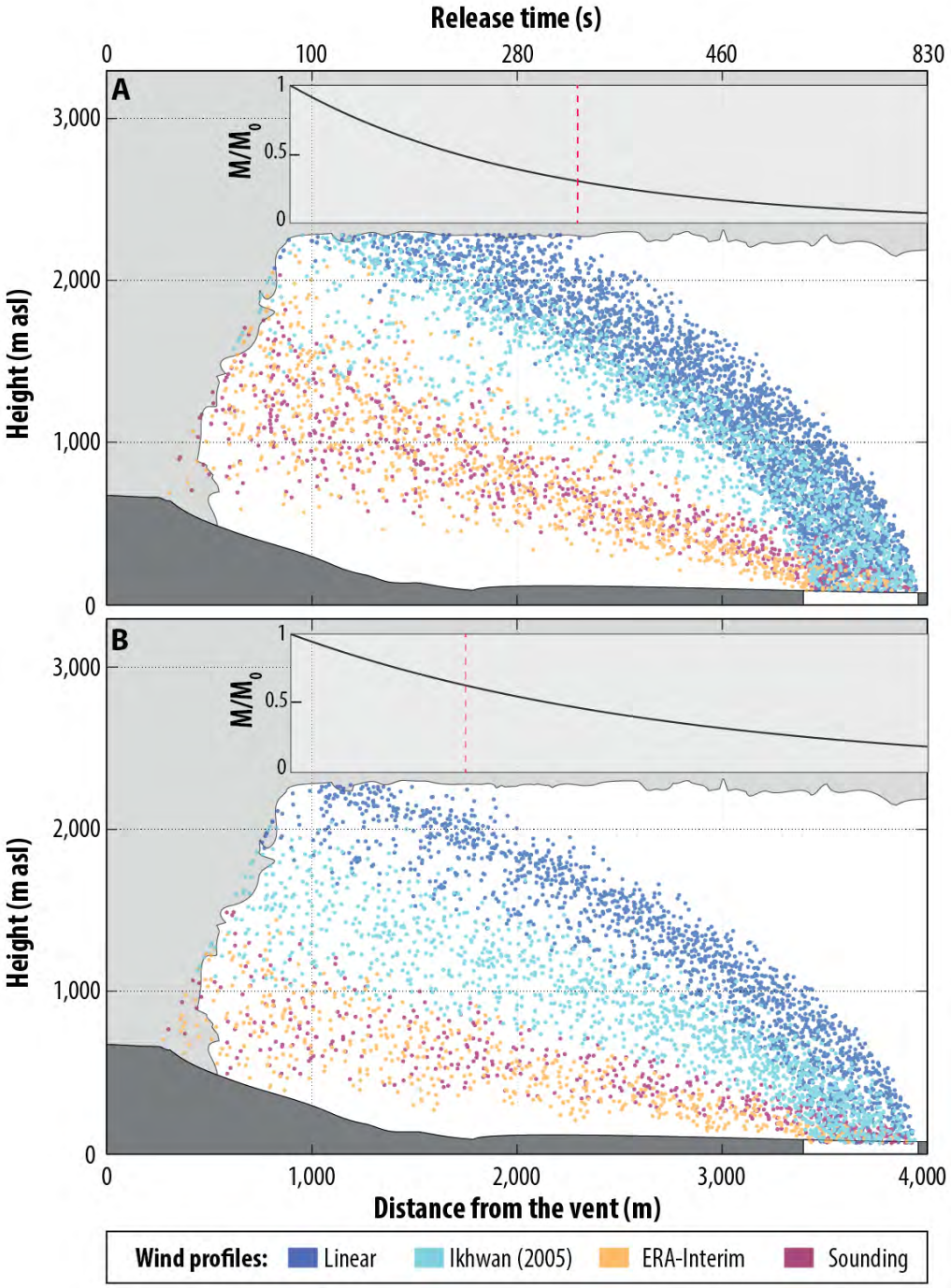

Figure 5.6: Lagrangian simulations of particle cluster trajectories based on four wind profiles. Particle clusters are released from the plume margins and cloud base, but only those that sedimented at our location (3.7 ± 0.25 km from vent) within the observed deposition time are considered. In order to account for the uncertainty in the wind, four different wind profiles are used based on various sources and assumptions (see Methods). A: Phase I particle clusters. B: Phase II particle clusters. Normalized mass concentration of particle clusters in the cloud ($M/M0$, with M the total mass for each particle cluster phase and M_0 the initial mass at plume corner for each particle cluster phase) are calculated for both fallout phases based on the sedimentation model (Bursik et al., 1992); particle cluster velocities are calculated based on atmospheric properties at the cloud height (3 and 2 $\mathrm{m\,s^{-1}}$ for Phase I and II, respectively). Red vertical dashed lines indicate the maximum distance of release.

particle aggregation, the terminal velocity of core particles decreased between 9% and 33% as a result of aggregation.

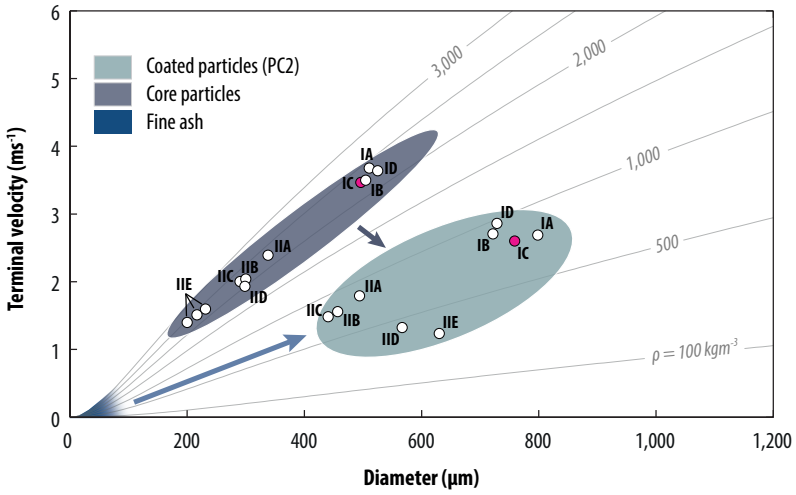

Figure 5.7: Terminal velocity versus diameter of coated particles and their constituent particles. The terminal velocity of coated particles are measured by analyzing videos, whereas the terminal velocity of fine ash and core particles are calculated numerically assuming spherical shapes for particles. Curves show the variation of terminal velocity for spheres with different densities; arrows indicate the direction of change in the terminal velocity of fine ash and core-particles as a result of aggregation. Note that particle cluster IIE is composed of three core-particles.

Given that the terminal velocity measured from HS-HR videos and the derived aggregate densities, size and shape of core particles extracted are all associated with some degrees of uncertainties, we also performed dedicated theoretical investigations to formulate a theoretical criteria for occurrence of rafting. Following James et al. (2002), the variations in terminal velocity of core particles are calculated as they get coated and grow in size James et al. (2002)(Fig. 5.8). Shape of core particles and aggregates are assumed to be spherical and effects of possible permeability of aggregates on the drag coefficient are neglected. Thus, the drag coefficient is calculated based on the empirical formulation suggested by Clift and Gauvin (1971) for spheres. The bulk density of ash shell around the core particle is considered to vary between $60\,\mathrm{kg\,m^{-3}}$ and $220\,\mathrm{kg\,m^{-3}}$, which are the lower- and upper-bounds of density for aggregates of typical dry ash clusters (James et al., 2002; Brown et al., 2012). The density of core particles is assumed to be constant and equal to $2500\,\mathrm{kg\,m^{-3}}$, which is the average density of individual particles measured by a water pycnometer (Figure 5.3).

As it is shown in Fig. 5.8, possible rafting of core particles depends on the size of core particles, the bulk density of the shell and final size of the aggregate. Rafting can reduce the terminal velocity of core particles up to 30 – 60% depending on both the shell density and the diameters of the core particle and aggregate. Impact of rafting is higher for larger core particles and lower shell densities. As an example, a core particle with a diameter of 64 µm can be rafted when it falls within an aggregate with a diameter less than ~ 7 times its diameter ($<\sim 450$ µm) and shell density of $60\,\mathrm{kg\,m^{-3}}$.

In Fig. 5.8, the Stokes limit corresponds to aggregates moving at very low Reynolds number ($<\sim 0.1$), where the drag coefficient is a linear function of particle Reynolds number based on the Stokes law (Happel and Brenner, 1983). Only very small particles and aggregates ($<\sim 30$ µm in diameter) fall at such low Reynolds numbers and, therefore, it does not represent a practical example for most volcanic clusters. However, the simple parameterization of drag coefficient-Reynolds number in the Stokes law allows for an analytical determination of the upper-bound limit for the variation of terminal velocity of aggregates as follows (Lane et al., 1993):

$$\frac{v_{agg}}{v_{core}} = \frac{(d_{agg}^3/d_{core}^3 - 1)(1-\varphi) + 1}{d_{agg}/d_{core}} \tag{5.5}$$

where φ is the porosity of the shell ($\equiv 1 - \rho_{shell}/\rho_{skeleton}$) and $\rho_{skeleton}$ is the skeleton density of particles without considering vesicles. An interesting point that can be extracted from Eq. (5.5) is that the rate of change in the terminal velocity ratio v_{agg}/v_{core} with respect to the diameter ratio d_{agg}/d_{core} is always negative for $\varphi > 2/3$ when $d_{agg}/d_{core} \to 1$. This indicates that a core particle of density of $2500\,\mathrm{kg\,m^{-3}}$ is always rafted upon aggregation with a shell density $< 833\,\mathrm{kg\,m^{-3}}$. Although the duration and impact of the rafting effect is dependent on various factors (e.g. Fig. 5.8) and can be very small for some core particles, it seems to be a wide-spread phenomena for particle clusters considering that the typical estimations of shell densities (i.e. 60 – 220 $\mathrm{kg\,m^{-3}}$) are much less than $833\,\mathrm{kg\,m^{-3}}$.

In any case, from Fig. 5.8 it is obvious that the possibility of rafting is extremely dependent on the shell density, which is still affected by large uncertainties. The extreme bounds for shell density that we have considered in this study are rough

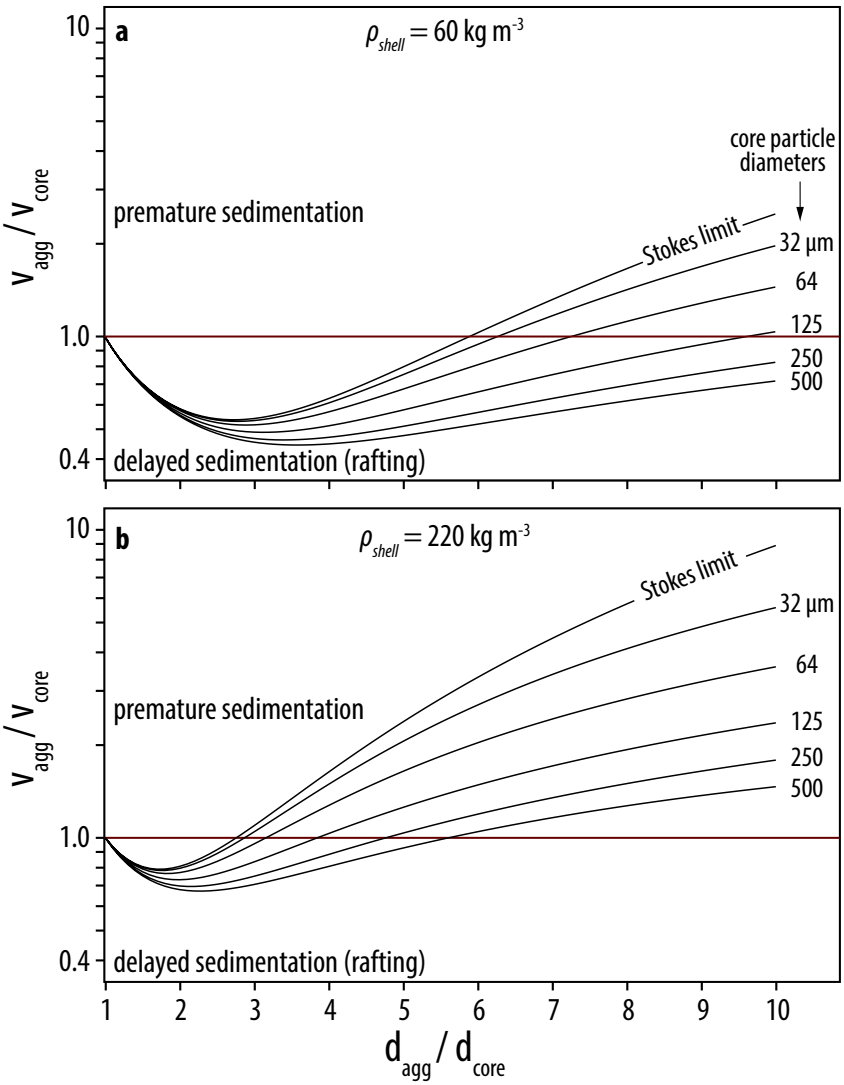

Figure 5.8: Impact of aggregate growth, d_{agg}/d_{core}, against the ratio of aggregate terminal velocity to that of the core particles, v_{agg}/v_{core}, for shell densities of (a) 60 kg m^{-3} and (b) 220 kg m^{-3}. Delayed sedimentation (rafting) of core particles due to aggregation occurs when $v_{agg}/v_{core} < 1$, whereas $v_{agg}/v_{core} > 1$ indicate enhanced sedimentation for core particles. Values on solid lines are diameters of core particles. The Stokes limit is valid for very small aggregates that are moving at Reynolds number < 0.1, and is given by Eq. 5.5.

estimations of the bulk density of *dry* ash clusters consisted of fine ashes. These bounds can be much higher if we take into account that what is considered a dry aggregate on the ground, might initially contain water when it leaves the volcanic cloud that eventually will be lost through evaporation/sublimation as the aggregate falls through the atmosphere (Durant and Rose, 2009).

In order to investigate the rafting effect in a more generalized manner, we have plotted the possibility of rafting against d_{agg}/d_{core} and aggregate porosity for various

types of aggregates (Fig. 5.9). Ranges of porosity and d_{agg}/d_{core} for each aggregate type is estimated based on our observation and those reported in the literature (Carey and Sigurdsson, 1982; James et al., 2002; Brown et al., 2012). The aggregate porosity is the porosity of aggregates including the core particle and shell ($\equiv 1 - \rho_{agg}/\rho_{skeleton}$). It should be noted that, based on the law of mass conservation, porosity of an aggregate cannot drop above the maximum porosity curve, which is the porosity when the shell density is zero (i.e. $m_{agg} = m_{core}$).

In Fig. 5.9 several curves, hereafter noted as constant velocity curves, are plotted for aggregates with core diameters in the range of Stokes regime, and of 40, 500 and 1000 µm. These curves are obtained numerically by assuming spherical shape for particles and indicate the aggregate porosity at which the terminal velocity of aggregate and core particle is equal. It is also assumed that the core particle has the highest mass in the particle and its density is $2500\,\mathrm{kg\,m^{-3}}$. If the aggregate porosity for a given d_{agg}/d_{core} falls above the constant velocity curve associated with its core diameter, the core is rafted due to aggregation ($v_{agg}/v_{core} < 1$). If, on the other hand, the aggregate porosity falls below the associated constant velocity curve, aggregation causes a premature sedimentation of the core ($v_{agg}/v_{core} > 1$).

Three examples are shown to better demonstrate the general effect of premature and delayed sedimentation as a result of particle aggregation. Aggregate 1 in Fig. 5.9 represents the aggregate of Fig. 5.4a that has a core diameter of $\sim 500\,\mu\mathrm{m}$ and since it lies above the corresponding constant velocity curves, its core is rafted (i.e. $v_{agg}/v_{core} \sim 0.68 - 0.77$). With $d_{agg}/d_{core} = 6$ and a $40\,\mu\mathrm{m}$ core particle, Aggregate 2 is an ash cluster similar to those deposited 390 km away from Mt St Helens during its 1980 eruption (Sorem 1982). If we assume an aggregate porosity of $\sim 97\%$, that Aggregate 2 lies on the constant velocity curve for d_{core} of $40\,\mu\mathrm{m}$, which indicates aggregation does not affect the sedimentation of the core particle. However, since the diameter ratio and aggregate porosity is not known for Aggregate 2, other scenarios (i.e. rafting or premature sedimentation) for the core particle are possible that are shown in the inset in Fig. 5.9. Finally, Aggregate 3 represents a well-structured accretionary pellet (also known as accretionary lapilli) similar to those observed for the 26 December 1997 dome collapse of Soufrire Hills volcano

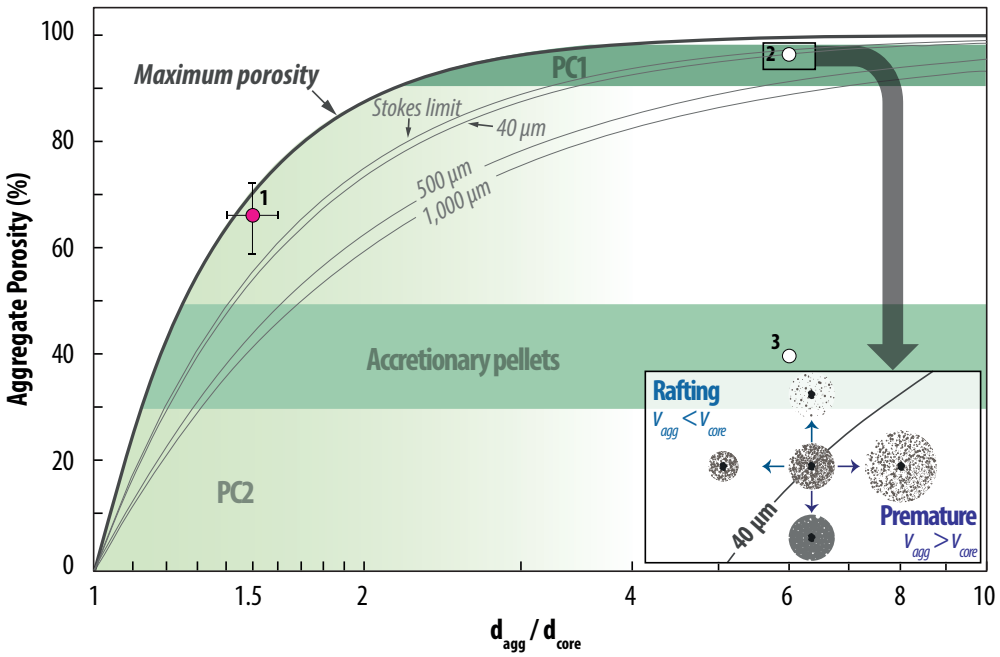

Figure 5.9: Generalized plot showing the potential of particle rafting for different types of aggregates. Values shown in the plots are diameters of core particles for associated curves. The constant velocity curves in this plot represent the line at which the terminal velocity of the aggregate is equal to the terminal velocity of the core particle $v_{agg}/v_{core} = 1$. If aggregate characteristics (i.e. porosity and d_{agg}/d_{core}) place the aggregate above its constant velocity curve, its core particle is rafted otherwise the core particle sedimentation is enhanced due to aggregation. The curve of the Stokes limit is valid for very small aggregates that are moving at Reynolds number < 0.1. Aggregates 1, 2 and 3 are discussed in main text and represent examples of aggregates of coated particle from Sakurajima database, ash cluster from the Mt St Helens 1980 eruption (Sorem, 1982) and structured accretionary pellet from a large dome collapse of Soufrire Hills volcano (Bonadonna et al., 2002b), respectively. The inset is a zoom around Aggregate 2 with $d_{core} = 40\,\mu m$ to show the influence of aggregate porosity and d_{agg}/d_{core} on the determination of premature or delayed particle sedimentation.

(Montserrat) (Bonadonna et al. 2002). The diameter ratio is similar to that of Aggregate 2 but with an aggregate porosity of 40%. As it can be seen in Fig. 5.9, Aggregate 3 falls below all constant velocity curves and, therefore, its terminal velocity is always greater than the that of the core particle. However, this was expected since shells of accretionary pellets are composed of compact fine ash with densities higher than the $833\,kg\,m^{-3}$ limit that we found earlier. The same applies to liquid pellets, which are liquid drops (with density of $\sim 1000\,kg\,m^{-3}$) containing ash particles. In summary, our analyses show that rafting is possible for ash clusters and coated particles, whereas for other aggregate types is unlikely to occur.

5.4 Discussion

5.4.1 Importance of coated particles in ash sedimentation

Coated particles have often been considered not to play an important role in particle aggregation because they have always been observed as only partially covered by fine ash (e.g. Sparks et al., 1997; Bonadonna et al., 2002b, 2011; James et al., 2002; Brown et al., 2012). As a result, fine ash has always been assumed to sediment prematurely mostly as ash clusters and accretionary lapilli. However, these new observations suggest that ash clusters observed previously are likely simply represent the shell particles of coated particles lost at impact with the sample collector. Thus, coated particles play an important role in the premature sedimentation of fine ash.

By reinterpreting the observations of Taddeucci et al. (2011) based on settling velocity measurements, we suggest that the proximal tephra fallout associated with the 2010 eruption of Eyjafjallajökull was similarly dominated by coated particles. In fact, they reported sedimentation of particle clusters with settling velocity mostly $> 1\,\mathrm{m\,s^{-1}}$, which is indicative of coated particle sedimentation based on our observations and experiments of (James et al., 2002) (also see "VIDEO DR2" in Taddeucci et al., 2011, in which the core particle can be clearly seen). We therefore suspect that most ash clusters described in literature at proximal and medial distances are deposited as coated particles and broke with impact with the ground. Thus, core particles that break away from the aggregate and fine ash in the shell result in bimodality of ground deposit, which is observed typically in proximal and medial distances in many volcanic deposits. This is supported with the fact that the mode of the grain size distribution for coarse ash particles deposited at our location is very close to the size of core particles measured from the videos (Fig. 5.4).

It should be noted that the formation of coated particles in volcanic fallout is dependent on the availability of coarse ash and decreases with distance from vent This indicates that strong bimodalities in tephra deposits are more likely caused by a dominance of coated particles than by a syn deposition of ash clusters and individual particles. Given that coarse ash concentration decreases with distance from vent, ash clusters become dominant and bimodality gradually disappears (e.g.

Bonadonna et al., 2011). Through this transition from dominant fallout of coated particles to ash clusters, the size of core particles in aggregates gradually decreases up to a point that all particles are comparable in size (i.e. sedimentation of ash clusters).

Besides their high efficiency in removing fine ash from volcanic clouds, the dominant role of coated particles in the volcanic deposits has also important implications for our understanding and modeling of particle aggregation (i.e. collision and sticking). First, at a given concentration and environmental conditions, coated particles can form faster and more easily than ash clusters. In fact, their collision mechanisms (i.e. ballistic and sedimentation) are several orders of magnitude more efficient than the collision mechanisms that typically control the formation of ash clusters (i.e. Brownian motion and turbulence) (Elimelech et al., 1998; Costa et al., 2010; Pruppacher and Klett, 2012). In addition, theoretical descriptions (Costa et al., 2010) show how the increase of sticking efficiency of fine ash is not sufficient to counterbalance the strong decrease in collision efficiency. As a result, whenever both fine and coarse ash are available, aggregation is more likely to result in coated particles than ash clusters.

Second, it has been suggested that grain-size of fallout deposits affected by particle aggregation are bimodal because of the simultaneous sedimentation of individual lapilli and/or coarse ash particles together with fine ash particles aggregated as ash clusters (e.g. Carey and Sigurdsson, 1982; Brazier et al., 1983). This theory can account for the deposition distance of individual particles, which in some cases matches the deposition distance of cluster core particles. However, it fails to explain the proximal deposition of clusters only composed of fine ash, since ash clusters typically have settling velocities $< 1\,\mathrm{m\,s^{-1}}$ (James et al., 2002). In fact, it is the high settling velocity of coated particles (here 1.2 – 2.9 $\mathrm{m\,s^{-1}}$, for 2010 eruption of Eyjafjallajökull mostly between ($\sim 1 - 4.0\,\mathrm{m\,s^{-1}}$ Taddeucci et al., 2011) that can explain alone the premature fallout of fine ash at proximal to medial distances.

5.4.2 Timing of aggregation

Given that Phase II clusters are characterized by thicker shells and most likely needed more time to form than Phase I clusters, we can conclude that particle clusters can be formed within 175 s seconds after the onset of the eruption. As a comparison, accretionary lapilli and frozen accretionary pellets were reported to be formed within 300 and 600 seconds after the onset of 1990 eruption of Sakurajima volcano (Japan) and the March 2009 eruption of Redoubt volcano (Alaska), respectively (Gilbert and Lane, 1994; Brown et al., 2012). We cannot exclude that in our case aggregation continued to occur beyond 175 s simply because our observation is just based on a single proximal location in the field. Nonetheless, we speculate that unexpected large particles observed in distal regions (e.g. Sorem, 1982) show that, in fact, volcanic clusters form in the vicinity of the vent, where the ash concentration is high and large particles are still present in the cloud. However, to be able to draw general and quantitative conclusions, this needs to be confirmed and investigated with further field studies on volcanic eruptions of different magnitudes and environmental conditions.

5.4.3 Temporal and spatial evolution of coated particles

Aggregation processes associated with the selected explosion evolved in time with significant differences in observed particle clusters. First, Phase I clusters have higher settling velocity compare to those of Phase II. Second, clusters of Phase I are characterized by larger core particles than those of Phase II (Figure 5.4 and Table 5.1). Third, shells of Phase I clusters are thinner than shells of Phase II compared to their core particle diameter. Finally, the wt% of coarse particles that sedimented individually (and not as core particles inside aggregates) decreased from Phase I to Phase II. Given that the terminal velocity of aggregates decreased with time at our location, we speculate that a similar variation is expected to occur also in space along the dispersal axis. As a result, the expected trends with distance from the vent are i) an increase of the ratio of the wt% of clusters to individual particles, ii) a decrease of the size of core particles and iii) an increase of the wt% of fine ash in clusters. The fine-ash population of fallout deposits is then expected to

increase with distance from vent with the associated grain-size distribution showing a weak bimodality in proximal region, a stronger bimodality in medial region and unimodality in distal region where sedimentation is expected to be characterized mostly by ash clusters (Schumacher, 1994; Bonadonna et al., 2011).

5.4.4 Importance of rafting on coarse ash sedimentation

We have provided the first field-based evidence for the rafting effect, which was previously only speculated in theory and its occurrence considered not to be likely. Our measurements indicated that terminal velocity of core particles is reduced up to 9 – 33% due to aggregation. Theoretical analyses showed that rafting can lead to 60% of reduction in the terminal velocity of core particles. Such a reduction becomes more significant the larger the core particles and the lower the shell densities. Thus, among all types of volcanic aggregates, coated particles are the most affected by the rafting effect. We have also found that core particles of any size will experience rafting effects upon aggregation when the shell porosity is $> 67\%$. This indicates that, regardless of its duration and impact, rafting is a common phenomenon since shell porosity of coated particles is typically higher than this limit.

As it is shown in Fig. 5.8 and 5.9, the possibility of rafting is higher for coated particles than ash clusters. The decrease in the settling velocity due to rafting effect allows for core particles to deposit at larger distances than expected. This contradicts the common idea that particle clusters results uniquely in higher terminal velocities than individual constituent particles and always induce a premature sedimentation of volcanic particles (Lane et al., 1993; Rose and Durant, 2011; Brown et al., 2012). As an example, rafting can potentially explain the sedimentation of 90 µm particles at about 1300 km from the vent during the 2010 Eyjafjallajökull eruption Stevenson et al. (2015), which is double the sedimentation distance expected for this particle size (Beckett et al., 2015).

5.5 Conclusions

Although our study is based on the field and numerical investigation of a simple Vulcanian explosion at Sakurajima volcano, important aspects of volcanic aggregates are revealed. Field observations showed the dominant presence of coated particles in proximal regions, which were composed of a core particle ($\sim 200-500$µm) enclosed in a thick shell of finer particles (< 90 µm). By reinterpreting published data, this was found to be also valid for the 2010 eruption of Eyjafjallajökull. These evidences suggest that in proximal and medial regions, where coarse and fine ash are both present, formed aggregates are most likely to be coated particles. Post processing of the field data showed that the shell of coated particles comprised $\sim 10-17wt\%$ of aggregates. This significant portion of shell particles is in contrast with previous description of coated particles, which considered them as particles only partially covered with fine ash and explains why they were considered not to play an important role in the aggregation processes. Coated particles with relatively thick shells can also explain the fine ash deposition observed in proximal region, which is not compatible with slowly falling ash clusters in this region. By conducting numerical inversions of field observations, it was also found that coated particles can be formed very rapidly and within order of seconds after the eruption onset. Finally, we presented the first field-based evidence for the rafting effect and it was shown that due to the rafting, particle clusters can promote premature fallout of fine ash and potentially explain the sedimentation of coarse ash hundreds of kilometers away from the volcano. Based on theoretical analyses it was also demonstrated that rafting is a widespread phenomenon that in extreme cases can reduce terminal velocity of core particles up to 60%.

5.6 Appendices

Selected High-Speed-High-Resolution videos used to obtain outcomes of this chapter are available on the accompanied CD-ROM.

5.7 Acknowledgments

The research leading to these results has received funding from the Swiss National Science Foundation (SNSF, Grant No. 200020-125024) and the People Programme (Marie Curie Actions) of the European Union's Seventh Framework Programme (FP7/2007-2013) under the project NEMOH, REA grant agreement n 289976. Authors are grateful to M. Ichiara, A. Kurokawa, L. Dominguez, L. Pioli, I. Manzella and F. Brogi for their enormous support in the field, to M. Pistolesi and R. Cioni for their insights into SEM analysis and to Mr. Frederic Arlaud for his help to design and construct the field setup.

5.8 Author's contributions

G. Bagheri processed and analyzed HS-HR and HD videos, developed the numerical inversion model and terminal velocity analysis. E. Rossi performed SEM image acquisition and related analysis, and applied the sedimentation model. S. Biass performed Laser Diffraction analysis, evaluated the accumulation rate and prepared the final version of figures. C. Bonadonna managed and led the project.All authors contributed to the experiment design, carrying out field experiments and ideas presented in the chapter. All authors were involved in the drafting and reviewing of this manuscript.

Chapter 6

Concluding remarks

In this thesis we explored various methods for measuring and characterizing size, shape and drag coefficient of irregular particles. In addition, new insights into the formation and structure of volcanic aggregates are presented. A vertical wind tunnel along with an experimental setup and particle tracking code for the measurement of the drag coefficient of non-spherical particles was presented. Measurements of the vertical wind tunnel was shown to be valid and reproducible.

In this chapter we summarize results of previous chapters, in particular Chapter 3 and 4, with a direct application to volcanic particles and their dispersal.

6.1 Characterization of size and shape of volcanic particles

The current state of methods for characterizing size, shape and aerodynamics of volcanic particles were investigated in detail in two chapters. Although volcanic particles are highly irregular and have random shapes, various aspects can be approximated by their dimension-equivalent ellipsoids (an ellipsoid with the same form dimensions as the particle) with an acceptable level of accuracy. As an example, surface area of dimension-equivalent ellipsoids of volcanic particles are within an average deviation of 6.4% from accurate laser scanning and SEM-micro CT measurements.

As a result, we can conclude that, at least for measuring particle volume and surface area, a highly detailed characterization of size and shape of volcanic particles,

Table 6.1: Variability range of flatness, f, elongation, e, and sphericity, ψ, of volcanic particles from deposits of various volcanic eruptions presented in Chapter 3 and published in Wilson and Huang (1979), Alfano et al. (2011) and Vonlanthen et al. (2015).

size category	f	e	ψ
Ash	0.07 – 1.00	0.24 – 1.00	0.21 – 1.00
Lapilli	0.42 – 1.00	0.51 – 1.00	0.53 – 1.00

such as 3D scanning, is not necessary as long as we can quantify their form dimensions (i.e. L: longest, I: intermediate and S: shortest lengths of the particle). This provides a great simplification for the shape characterization of volcanic particles. Nonetheless, a rapid method for measuring form dimensions of ash-size volcanic particles does not yet exists, with important implications on the accuracy of numerical descriptions of particle dispersal and the assessment of associated hazards and impact on our societies. As a result, when specific form dimensions are not available (e.g. during real-time dispersal forecasting), typical ranges of shape characteristics presented in Chapter 3 and published data in the literature are recommended to be used (e.g. Table 6.1).

Out of all parameters describing particle shape, the particle form has the greatest impact on the drag coefficient and not the surface-related characteristics, such as sphericity. Thus, the drag coefficient of irregular volcanic particles is also very similar to that of dimension-equivalent ellipsoids. In fact, if we approximate shape of irregular particles to ellipsoids, by neglecting the term $d_{eq}^3/L\,I\,S$ for calculating F_S and f_N, the average error of Eq. (4.34) increases for only $\sim 3\%$ compare to when the term $d_{eq}^3/L\,I\,S$ is not neglected. This indicates the deviation of the particle shape from its dimension-equivalent ellipsoid does not significantly affect their drag coefficient.

6.2 Evaluation of drag coefficient models in estimating drag of volcanic particles

A number of spherical (Eq. 4.4) and non-spherical models (e.g. Eq. 4.6 and 4.7) for estimating drag of particles are presented and discussed in Chapter 4. In vol-

canology, however, other non-spherical models can be found that are commonly used for modeling tephra dispersal. One of the first empirical correlation based on experiments on volcanic ash is presented by Wilson and Huang (1979):

$$C_D = \frac{24}{Re} F^{-0.828} + 2\sqrt{1.07 - F} \tag{6.1}$$

where F is a shape descriptor defined as a function of particle form dimensions:

$$F = \frac{S + I}{2L} \tag{6.2}$$

Later, by adding experimental data of Walker et al. (1971) for lapilli-size particles to the database of Wilson and Huang (1979), Suzuki (1983) presented a modified version of Eq. 6.1:

$$C_D = \frac{24}{Re} F^{-0.32} + 2\sqrt{1.07 - F} \tag{6.3}$$

Another model specifically derived for predicting terminal velocity of volcanic particles is that of Dellino et al. (2005), which can also be rearranged to derive the drag coefficient:

$$C_D = \frac{0.916\, g\, d_{eq}^3\, (\rho_p - \rho_f)}{\mu_f^2\, (g\, (\psi\sqrt{\phi_{Cox}})^{1.6}\, d_{eq}^3\, \rho_f\, (\rho_p - \rho_f)/\mu_f^2)^{1.0412}} \tag{6.4}$$

Unlike other models, the model of Dellino et al. (2005) is not a function of particle Reynolds number and, therefore, can provide an estimation of the drag coefficient directly without iteration processes. However, it is only valid roughly within the Newton's regime (i.e. $10^3 < Re < 3 \times 10^5$), where the drag coefficient is not a function of particle Reynolds number.

Lastly, the model we presented in Chapter 4 can be used to estimate the drag coefficient of volcanic particles:

$$\frac{C_D}{k_N} = \frac{24\, k_S}{Re\, k_N} \left(1 + 0.125\, (Re\, k_N/k_S)^{2/3}\right) + \frac{0.46}{1 + 5330/(Re\, k_N/k_S)} \tag{6.5}$$

where for particles falling with random orientations:

$$k_S = 0.5(F_S^{1/3} + F_S^{-1/3}) \tag{6.6}$$

and for volcanic particles falling in the atmosphere (i.e. gas):

$$k_N = 10^{0.45(-log(F_N))^{0.99}} \tag{6.7}$$

and, F_S and F_N are shape descriptors defined based on particle form dimensions and d_{eq}:

$$F_S = f\, e^{1.3}(\frac{d_{eq}^3}{L\, I\, S}) \tag{6.8}$$

$$F_N = f^2\, e(\frac{d_{eq}^3}{L\, I\, S}) \tag{6.9}$$

F_S and F_N are equal to 1 for sphere and decrease as the particle shape becomes less spherical. The term $d_{eq}^3/L\, I\, S$ is equal to 1 for ellipsoids, while for irregular particles is always < 1 (see d_G/d_{eq} in Fig. 3.9). If we neglect the term in Eqs. 6.8 and 6.9, the drag coefficient of the particle will be approximated by that of its dimension-equivalent ellipsoid (an ellipsoid with similar form dimensions and, therefore, flatness and elongation ratios as the particle):

$$F_S = f\, e^{1.3} \tag{6.10}$$

$$F_N = f^2\, e \tag{6.11}$$

In any case, as discussed in Chapter 4, F_S and F_N are dependent on the particle form, which shows that surface-related characteristics are not influencing factors for the drag of freely falling non-spherical particles. In the Stokes' regime ($Re < 0.1$), particle elongation and flatness have almost similar impacts on the drag coefficient since $F_S \propto f\, e^{1.3}$. Whereas in the Newtons regime ($10^3 < Re < 3 \times 10^5$), it is the particle flatness that has the dominant influence on the drag coefficient since $F_S \propto f^2\, e$.

To evaluate the accuracy of drag models on predicting drag coefficient of volcanic particles a subset of database shown in Table 4.3 is chosen. It includes the drag coefficient of 100 ellipsoids with flatness and elongation ratios according to Table 6.1 (i.e. $0.07 < f < 1.00$, $0.24 < e < 1.00$) obtained analytically at Stokes' regime, 30

Table 6.2: Average and maximum relative errors of various models for predicting drag coefficient of ellipsoids and volcanic particles. Spherical drag is calculated based on the model of Clift and Gauvin (1971) (Eq. 4.4). Relative error% is defined as $|observed - ref.| \times 100/ref.$.

size	**Average relative error%** (max. relative error%)					
category	Spherical	Wilson and Huang (1979)	Suzuki (1983)	Ganser (1993)	Dellino et al. (2005)	Present, Eq. (6.5 – 6.9)
Fine ash	**13** (55)	**81** (211)	**15** (33)	**3** (15)	–	**2** (10)
Coarse ash	**41** (69)	**22** (58)	**31** (62)	**32** (120)	**43** (131)	**23** (55)
Lapilli	**47** (70)	–	**54** (120)	**130** (248)	**16** (39)	**10** (33)
ALL	**30** (70)	**52** (211)	**32** (120)	**55** (248)	**24** (131)	**8** (55)

volcanic ash measured in air-filled settling columns with heights between $0.45-3.6\,m$ at $9 < Re < 900$, and 78 lapilli size particles measured in the vertical wind tunnel at $8 \times 10^3 < Re < 6 \times 10^4$. Ellipsoids at low Reynolds number are considered because no data for the drag coefficient of irregular particles can be found in the literature at this range of Reynolds number. In any case, it has been already shown in Chapter 4 that the drag coefficient of irregular particles is not affected by the surface roughness and small-scale surface vesicularity. Thus, ellipsoids can closely approximate the drag coefficient of irregular particles in the Stokes' regime.

In Table 6.2, evaluation of various drag models against our drag database of non-spherical particles are presnted. Surprisingly, the spherical model, performs better on average than some of the non-spherical models including the models of Wilson and Huang (1979), Suzuki (1983) and Ganser (1993). However, the accuracy of Suzuki (1983) and Ganser (1993) models increases as the particle size decreases. The model of Dellino et al. (2005) is better for lapilli-sized volcanic particles, which was expected since it is based on experiments of this particle size category. The model presented in this thesis, Eq.(6.5 – 6.9), performs significantly better than the other models with an average relative error of 8%. It is also associated with the lowest value of the maximum relative error. If, for the sake of simplicity, we approximate shape of irregular particles to ellipsoids, by using Eqs. (6.10 – 6.11) instead of (6.8 – 6.9), the average error of Eq. (6.5) slightly increases to 11% (max. 65%). This indicates that irregularity of volcanic particles (i.e. deviation of the particle shape from its dimension-equivalent ellipsoid) does not significantly affect their drag coefficient.

6.3 Terminal velocity of volcanic particles

The influence of particle shape on drag coefficient and terminal velocity has shown to increase with particle size (Fig. 4.25b). On the other hand, fine ash is less spherical than coarse ash and lapilli, since shape descriptors measured for fine ash are typically smaller (see Table 6.1). Thus, if we want to study the effect of shape on terminal velocity of volcanic particles, these two aspects should be considered together. We assessed the overall effect of shape and size on the terminal velocity of volcanic particles by applying the general equation presented, Eq. (6.5 – 6.7, 6.10, 6.11), to the particles of Table 6.1 (Figure 6.1). Particle shape descriptors (i.e. f, e) were varied logarithmically with size within the ranges shown in Table 6.1. It can be seen that the effect of shape of volcanic particles on the drag coefficient is almost independent of size. Terminal velocity of the most irregular volcanic particles of any given size is about 50% less than the terminal velocity of volume-equivalent spheres. As a result, their residence time in the atmosphere can be doubled at most due to their shape.

6.4 Aggregation of volcanic particles

By conducting field and numerical investigation of a Vulcanian explosion at Sakurajima volcano, important aspects of volcanic aggregates are revealed and the first field-based evidence for the rafting effect are presented. It is found that coated particles can play a significant role in the sedimentation of fine ash in volcanic eruptions. This was also found to be valid for the 2010 eruption of Eyjafjallajökull and, in general, for all ash deposits composed of both fine and coarse ash. In conclusion, coated particles can form rapidly after the onset of the eruption, rapidly remove fine ash from volcanic plumes, explain the fine ash deposition observed in proximal region and increase the possibility of particle rafting. We have also found that, regardless of its duration and impact, rafting is a common phenomenon that can reduce the terminal velocity of core particles up to 60%.

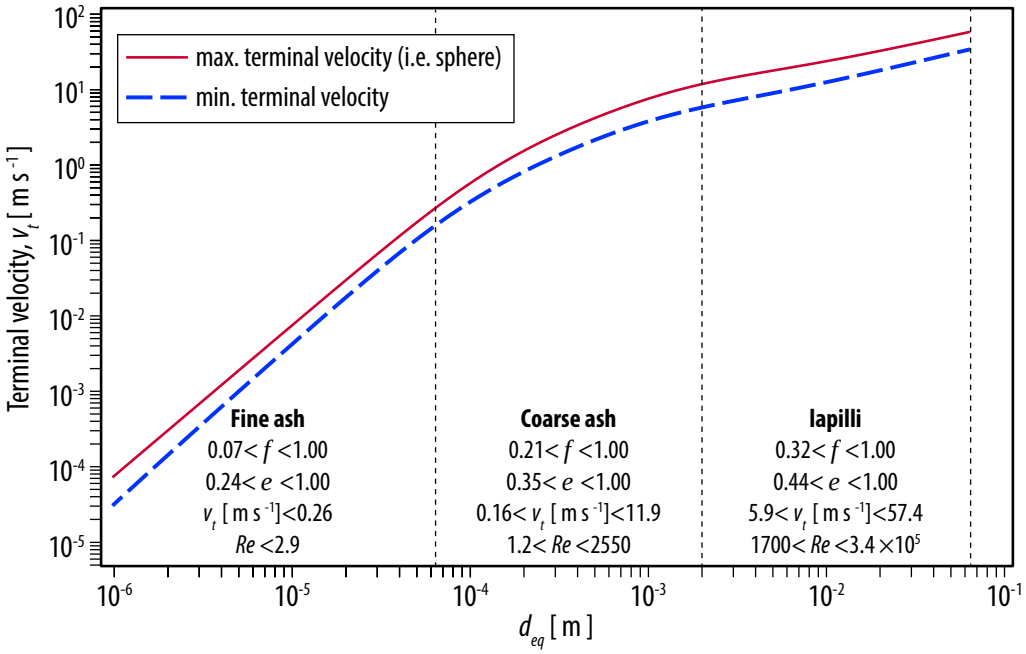

Figure 6.1: Dependency of the terminal velocity, v_t, of volcanic particles falling in the atmosphere at sea-level conditions against their diameter, d_{eq}. The particle density is assumed to be 2500 kg m^{-3}. Eq. (6.5 – 6.7, 6.10, 6.11) is used for estimating the drag coefficient of particles with flatness, f, and elongation, e, varied logarithmically as a function of d_{eq} within the ranges shown in Table 6.1 (ranges of f, e and terminal velocity for each size category are also written inside the figure). The maximum terminal velocity is for particles with $f = e = 1.00$ (i.e. sphere), whereas the minimum terminal velocity is for particles with the minimum values of f and e for each size category.

6.5 Future Perspectives

Even though we have described a range of strategies for the description of particle size, shape, drag coefficient and aggregation of volcanic particles, some open questions still remain that should be addressed in future studies. First, a new strategy for the rapid assessment of particle form dimensions (i.e. three axes of the particle) should be developed that could complement the numerical description of particle dispersal and sedimentation. DIA analysis methods, as an example, have a great potential for reliable and rapid retrieval of particle form dimensions due to their dynamic characterizations.

Second, it is important to study both the shape and drag coefficient of volcanic aggregates, especially particle clusters since they can be permeable and deformable. In fact, even though we have shown how the effect of particle shape on drag coefficient of small and large volcanic particles is very similar, most small particles (i.e.

the fine-ash fraction) do not fall individually and tend to cluster in larger aggregates characterized by larger terminal velocity (e.g. Brown et al. 2012). The aerodynamics features of particle aggregates are very complex and need to be studied in detail. However, if aggregates are not permeable and deformable, and their bulk density and form are known, models presented in Chapter 4 can be used to estimate their drag coefficient and terminal velocity.

Third, collision and sticking process of volcanic particles are still not well understood and should be thoroughly investigated. In addition, it is important to accurately measure the density of ash clusters and the bulk density of shell coating around coated particles with higher accuracy in future field studies. These are very important parameters influencing the settling rate of aggregates and possibility of particle rafting.

Fourth, particle shape, size and composition should also be investigated in relation to its effect on aggregation dynamics (e.g. efficiency of collision and sticking). As an example, sticking efficacy decreases with particle size and particle shape can affect the mechanical interlocking during clustering process (Brown et al., 2012). Moreover, composition is an important parameter indicating particle surface energy and the ability of electrical charging. Both of these parameters can affect the aggregation process of volcanic particles.

Finally, effects of *gravitational instabilities* on the aggregation processes should be investigated in more details. Recent studies suggest that some aggregation might occur within convective instabilities, in which fine particles are channeled and sediment faster (Carazzo and Jellinek, 2013; Manzella et al., 2015). Thus, convective instabilities can promote formation of ash clusters.

Bibliography

Achenbach, E., 1972. Experiments on the flow past spheres at very high Reynolds numbers. Journal of Fluid Mechanics 54, 565–575.

Achenbach, E., 1974. The effects of surface roughness and tunnel blockage on the flow past spheres. Journal of Fluid Mechanics 65, 113.

Albertson, M.L., 1953. Effect of Shape on the Fall Velocity of Gravel Particles, in: McNown, J.S., Boyer, M.C. (Eds.), Proceedings of the Fifth Hydraulics Conference, State University of Iowa, Iowa City. p. 308.

Alfano, F., Bonadonna, C., Delmelle, P., Costantini, L., 2011. Insights on tephra settling velocity from morphological observations. Journal of Volcanology and Geothermal Research 208, 86–98.

Arsenijević, Z., Grbavčić, v., Garić-Grulović, R., Bošković-Vragolović, N., 2010. Wall effects on the velocities of a single sphere settling in a stagnant and counter-current fluid and rising in a co-current fluid. Powder Technology 203, 237–242.

Asahina, D., Taylor, M., 2011. Geometry of irregular particles: Direct surface measurements by 3-D laser scanner. Powder Technology 213, 70–78.

Aschenbrenner, B., 1956. A new method of expressing particle sphericity. Journal of Sedimentary Research 26, 15.

Awbi, H., Tan, S., 1981. Effect of wind-tunnel walls on the drag of a sphere. Journal of Fluids Engineering 103, 461–465.

Baba, J., Komar, P., 1981. Measurements and analysis of setting velocities of natural quartz sand grains. Journal of Sedimentary Research 51, 631.

Bagheri, G., Bonadonna, C., Manzella, I., Vonlanthen, P., 2015. On the characterization of size and shape of irregular particles. Powder Technology 270, 141–153.

Bagheri, G.H., Bonadonna, C., Manzella, I., Pontelandolfo, P., Haas, P., 2013. Dedicated vertical wind tunnel for the study of sedimentation of non-spherical particles. Review of Scientific Instruments 84, 054501.

Bagheri, G.H., Salmanzadeh, M., Golkarfard, V., Ahmadi, G., 2012. Simulation of Solid Particles Behavior in a Heated Cavity at High Rayleigh Numbers. Aerosol Science and Technology 46, 1382–1391.

Banta, L., Cheng, K., Zaniewski, J., 2003. Estimation of limestone particle mass from 2D images. Powder Technology 132, 184–189.

Barberi, F., Coltelli, M., Frullani, A., Rosi, M., Almeida, E., 1995. Chronology and dispersal characteristics of recently (last 5000 years) erupted tephra of Cotopaxi (Ecuador): implications for long-term eruptive forecasting. Journal of Volcanology and Geothermal Research 69, 217–239.

Barlow, J.B., Rae, W.H., Pope, A., 1999. Low-Speed Wind Tunnel Testing. Wiley-Interscience.

Barrett, P.J., 1980. The shape of rock particles, a critical review. Sedimentology 27, 291–303.

Beard, K., Pruppacher, H., 1969. A Determination of the Terminal Velocity and Drag of Small Water Drops by Means of a Wind Tunnel. Journal of Atmospheric Sciences 26, 1066–1072.

Beckett, F.M., Witham, C., Hort, M., Stevenson, J., Bonadonna, C., Millington, S., 2015. Sensitivity of dispersion model forecasts of volcanic ash clouds to the physical characteristics of the particles. Journal of Geophysical Research submitted.

Biass, S., Bonadonna, C., 2011. A quantitative uncertainty assessment of eruptive parameters derived from tephra deposits: the example of two large eruptions of Cotopaxi volcano, Ecuador. Bulletin of Volcanology 73, 73–90.

von Blohn, N., Mitra, S.K., Diehl, K., Borrmann, S., Vonblohn, N., 2005. The ice nucleating ability of pollenPart III: New laboratory studies in immersion and contact freezing modes including more pollen types. Atmospheric Research 78, 182–189.

Blong, R., 1984. Volcanic hazards. A sourcebook on the effects of eruptions. Academic Press, Inc.,Orlando, FL.

Blott, S.J., Pye, K., 2007. Particle shape: a review and new methods of characterization and classification. Sedimentology 55, 070921092734002–???

Bonadonna, C., Cioni, R., Pistolesi, M., Connor, C., Scollo, S., Pioli, L., Rosi, M., 2013. Determination of the largest clast sizes of tephra deposits for the characterization of explosive eruptions: a study of the IAVCEI commission on tephra hazard modelling. Bulletin of Volcanology 75, 680.

Bonadonna, C., Costa, A., 2013. Modeling of tephra sedimentation from volcanic plumes, in: Fagents, S.A., Gregg, T.K.P., Lopes, R.M.C. (Eds.), Modeling volcanic processes: The physics and mathematics of volcanism. Cambridge University Press, pp. 173–202.

Bonadonna, C., Ernst, G., Sparks, R., 1998. Thickness variations and volume estimates of tephra fall deposits: the importance of particle Reynolds number. Journal of Volcanology and Geothermal Research 81, 173–187.

Bonadonna, C., Genco, R., Gouhier, M., Pistolesi, M., Cioni, R., Alfano, F., Hoskuldsson, A., Ripepe, M., 2011. Tephra sedimentation during the 2010 Eyjafjallajökull eruption (Iceland) from deposit, radar, and satellite observations. Journal of Geophysical Research 116, B12202.

Bonadonna, C., Macedonio, G., Sparks, R.S.J., 2002a. Numerical modelling of tephra fallout associated with dome collapses and Vulcanian explosions: application to hazard assessment on Montserrat. Geological Society, London, Memoirs 21, 517–537.

Bonadonna, C., Mayberry, G.C., Calder, E.S., Sparks, R.S.J., Choux, C., Jackson, P., Lejeune, A.M., Loughlin, S.C., Norton, G.E., Rose, W.I., Ryan, G., Young, S.R., 2002b. Tephra fallout in the eruption of Soufriere Hills Volcano, Montserrat. Geological Society, London, Memoirs 21, 483–516.

Bougas, A., Stamatoudis, M., 1993. Wall factor for acceleration and terminal velocity of falling spheres at high reynolds numbers. Chemical Engineering & Technology 16, 314–317.

Brazier, S., Sparks, R.S.J., Carey, S.N., Sigurdsson, H., Westgate, J.A., 1983. Bimodal grain size distribution and secondary thickening in air-fall ash layers. Nature 301, 115–119.

Briggs, L., 1962. The hydraulic shape of sand particles. Journal of Sedimentary Research 32, 645–656.

Brosse, N., Ern, P., 2013. The motion of an axisymmetric body falling in a tube at moderate Reynolds numbers. Journal of Fluid Mechanics 714, 238–257.

Brown, R., Bonadonna, C., Durant, A., 2012. A review of volcanic ash aggregation. Physics and Chemistry of the Earth, Parts A/B/C 45-46, 65–78.

Brunauer, S., Emmett, P.H., Teller, E., 1938. Adsorption of Gases in Multimolecular Layers. Journal of the American Chemical Society 60, 309–319.

Bursik, M.I., Sparks, R.S.J., Gilbert, J.S., Carey, S.N., 1992. Sedimentation of tephra by volcanic plumes: I. Theory and its comparison with a study of the Fogo A plinian deposit, Sao Miguel (Azores). Bulletin of Volcanology 54, 329–344.

Carazzo, G., Jellinek, a.M., 2013. Particle sedimentation and diffusive convection in volcanic ash-clouds. Journal of Geophysical Research: Solid Earth 118, 1420–1437.

Carey, S., Sigurdsson, H., 1982. Influence of particle aggregation on deposition of distal tephra from the May 18, 1980, eruption of Mount St. Helens volcano. Journal of geophysical research 87, 7061–7072.

Casadevall, T.J., 1994. Volcanic ash and aviation safety: proceedings of the first international symposium on volcanic ash and aviation safety. volume 2047. DIANE Publishing.

Cauchy, A.L., 1832. Mémoire sur la rectification des courbes et la quadrature des surfaces courbées.

Cheng, N., 1997. Simplified settling velocity formula for sediment particle. Journal of hydraulic engineering 123, 149.

Chhabra, R., 1996. Some further observations on the hindered settling velocity of spheres in the inertial flow regime. Chemical Engineering Science 51, 4531–4532.

Chhabra, R., Agarwal, L., Sinha, N., 1999. Drag on non-spherical particles: an evaluation of available methods. Powder Technology 101, 288–295.

Chhabra, R.P., 2006. Bubbles, drops, and particles in non-Newtonian fluids. CRC press.

Chow, A.C., Adams, E.E., 2011. Prediction of Drag Coefficient and Secondary Motion of Free-Falling Rigid Cylindrical Particles with and without Curvature at Moderate Reynolds Number. Journal of Hydraulic Engineering 137, 1406–1414.

Christiansen, E.B., Barker, D.H., 1965. The effect of shape and density on the free settling of particles at high Reynolds numbers. AIChE Journal 11, 145–151.

Clift, R., Gauvin, W.H., 1971. Motion of entrained particles in gas streams. The Canadian Journal of Chemical Engineering 49, 439–448.

Clift, R., Grace, J.R., Weber, M.E., 2005. Bubbles, Drops, and Particles. Dover Publications, Mineola, New York.

Coltelli, M., Miraglia, L., Scollo, S., 2008. Characterization of shape and terminal velocity of tephra particles erupted during the 2002 eruption of Etna volcano, Italy. Bulletin of Volcanology 70, 1103–1112.

Corey, A.T., 1963. Influence of shape on the fall velocity of sand grains. Audio Visual Service, Colorado State University.

Costa, A., Folch, A., Macedonio, G., 2010. A model for wet aggregation of ash particles in volcanic plumes and clouds: 1. Theoretical formulation. Journal of Geophysical Research 115, B09201.

Costantini, L., Houghton, B., Bonadonna, C., 2010. Constraints on eruption dynamics of basaltic explosive activity derived from chemical and microtextural study: The example of the Fontana Lapilli Plinian eruption, Nicaragua. Journal of Volcanology and Geothermal Research 189, 207–224.

Cox, E.P., 1927. A method of assigning numerical and percentage values to the degree of roundness of sand grains. Journal of Paleontology 1, 179–183.

Cox, R.G., 1965. The steady motion of a particle of arbitrary shape at small Reynolds numbers. Journal of Fluid Mechanics 23, 625–643.

Dellino, P., Mele, D., Bonasia, R., Braia, G., La Volpe, L., Sulpizio, R., 2005. The analysis of the influence of pumice shape on its terminal velocity. Geophysical Research Letters 32, L21306.

Delmelle, P., Villiras, F., Pelletier, M., 2005. Surface area, porosity and water adsorption properties of fine volcanic ash particles. Bulletin of Volcanology 67, 160–169.

Dubovik, O., Holben, B.N., Lapyonok, T., Sinyuk, A., Mishchenko, M.I., Yang, P., Slutsker, I., 2002. Non-spherical aerosol retrieval method employing light scattering by spheroids. Geophysical research letters 29, 3–6.

Durant, a.J., Bonadonna, C., Horwell, C.J., 2010. Atmospheric and Environmental Impacts of Volcanic Particulates. Elements 6, 235–240.

Durant, A.J., Rose, W.I., 2009. Sedimentological constraints on hydrometeor-enhanced particle deposition: 1992 Eruptions of Crater Peak, Alaska. Journal of Volcanology and Geothermal Research 186, 40–59.

Durant, a.J., Rose, W.I., Sarna-Wojcicki, a.M., Carey, S., Volentik, a.C.M., 2009. Hydrometeor-enhanced tephra sedimentation: Constraints from the 18 May 1980 eruption of Mount St. Helens. Journal of Geophysical Research 114, 1–21.

Elimelech, M., Gregory, J., Jia, X., Williams, R., 1998. Particle deposition and aggregation: measurement, modelling and simulation. Butterworth-Heinemann.

Ellis, P., 2000. The aerodynamic and combustion characteristics of eucalypt bark: a firebrand study. Phd thesis. Australian National University.

Ern, P., Risso, F., Fabre, D., Magnaudet, J., 2012. Wake-Induced Oscillatory Paths of Bodies Freely Rising or Falling in Fluids. Annual Review of Fluid Mechanics 44, 97–121.

Ersoy, O., 2010. Surface area and volume measurements of volcanic ash particles by SEM stereoscopic imaging. Journal of Volcanology and Geothermal Research 190, 290–296.

Ersoy, O., Aydar, E., Gourgaud, A., Bayhan, H., 2008. Quantitative analysis on volcanic ash surfaces: application of extended depth-of-field (focus) algorithm for light and scanning electron microscopy and 3D reconstruction. Micron (Oxford, England : 1993) 39, 128–36.

Ersoy, O., en, E., Aydar, E., Tatar, ., Çelik, H.H., 2010. Surface area and volume measurements of volcanic ash particles using micro-computed tomography (micro-CT): A comparison with scanning electron microscope (SEM) stereoscopic imaging and geometric considerations. Journal of Volcanology and Geothermal Research 196, 281–286.

Fage, A., Johansen, F., 1927. On the flow of air behind an inclined flat plate of infinite span. Proceedings of the Royal Society of London 116, 170–197.

Feng, Y., Goree, J., Liu, B., 2011. Errors in particle tracking velocimetry with high-speed cameras. The Review of Scientific Instruments 82, 053707.

Folch, A., 2012. A review of tephra transport and dispersal models: Evolution, current status, and future perspectives. Journal of Volcanology and Geothermal Research 235-236, 96–115.

Folch, a., Costa, A., Macedonio, G., 2009. FALL3D: A computational model for transport and deposition of volcanic ash. Computers & Geosciences 35, 1334–1342.

Ganser, G., 1993. A rational approach to drag prediction of spherical and nonspherical particles. Powder Technology 77, 143–152.

Garboczi, E., 2002. Three-dimensional mathematical analysis of particle shape using X-ray tomography and spherical harmonics: Application to aggregates used in concrete. Cement and Concrete Research 32, 1621–1638.

Garboczi, E., Liu, X., Taylor, M., 2012. The 3-D shape of blasted and crushed rocks: From 20μm to 38mm. Powder Technology 229, 84–89.

Gilbert, J., Lane, S., Sparks, R., Koyaguchi, T., 1991. Charge measurements on particle fallout from a volcanic plume. Nature 349, 598 – 600.

Gilbert, J.S., Lane, S.J., 1994. The origin of accretionary lapilli. Bulletin of Volcanology 56, 398–411.

Gögüs, M., pekçi, O., Kökpinar, M., 2001. Effect of particle shape on fall velocity of angular particles. Journal of Hydraulic Engineering 127, 860.

Guffanti, M., Casadevall, T.J., Budding, K., 2010. Encounters of Aircraft with Volcanic Ash Clouds: A Compilation of Known Incidents, 19532009. Technical Report.

Haider, A., Levenspiel, O., 1989. Drag coefficient and terminal velocity of spherical and nonspherical particles. Powder Technology 58, 63–70.

Happel, J., Brenner, H., 1983. Low Reynolds number hydrodynamics: with special applications to particulate media. volume 1. Springer Science & Business Media.

Higuchi, H., Sawada, H., Kato, H., 2008. Sting-free measurements on a magnetically supported right circular cylinder aligned with the free stream. Journal of Fluid Mechanics 596, 49–72.

Hill, R., Power, G., 1956. Extremum Principles For Slow Viscous Flow And The Approximate Calculation Of Drag. The Quarterly Journal of Mechanics and Applied Mathematics 9, 313–319.

Hilton, J., Mason, L., Cleary, P., 2010. Dynamics of gassolid fluidised beds with non-spherical particle geometry. Chemical Engineering Science 65, 1584–1596.

Hoerner, S., 1965. Fluid-dynamic drag: practical information on aerodynamic drag and hydrodynamic resistance. Hoerner Fluid Dynamics Midland Park, NJ.

Hölzer, A., Sommerfeld, M., 2008. New simple correlation formula for the drag coefficient of non-spherical particles. Powder Technology 184, 361–365.

Hoper, V., Grant, A., 1948. The Influence of a Horizontal Wall on the Motion of a Falling Oil Drop. Australian Journal of Chemistry 1, 28.

Horwell, C.J., Baxter, P.J., 2006. The respiratory health hazards of volcanic ash: a review for volcanic risk mitigation. Bulletin of Volcanology 69, 1–24.

Horwell, C.J., Fenoglio, I., Vala Ragnarsdottir, K., Sparks, R.J., Fubini, B., 2003. Surface reactivity of volcanic ash from the eruption of Soufrière Hills volcano, Montserrat, West Indies with implications for health hazards. Environmental Research 93, 202–215.

I.E. Idel'cik, 1986. Mémento des pertes de charges. 3rd editio ed., Eyrolles.

Ikhwan, M., 2005. Investigation of Flow and Pressure Characteristics around Pyramidal Buildings. Ph.D. thesis. Karlsruher Institut für Technologie.

Isaacs, J.L., Thodos, G., 1967. The free-settling of solid cylindrical particles in the turbulent regime. The Canadian Journal of Chemical Engineering 45, 150–155.

James, M.R., Gilbert, J.S., Lane, S.J., 2002. Experimental investigation of volcanic particle aggregation in the absence of a liquid phase. Journal of Geophysical Research 107, 2191.

Jayaweera, K.O.L.F., Mason, B.J., 1965. The behaviour of freely falling cylinders and cones in a viscous fluid. Journal of Fluid Mechanics 22, 709.

Joe D. Hoffman, Steven Frankel, 2001. Numerical Methods for Engineers and Scientists. 2 ed., CRC Press, New York.

Jongejans, E., Schippers, P., 1999. Modeling seed dispersal by wind in herbaceous species. Oikos 87, 362–372.

Kalashnikova, O., Sokolik, I., 2002. Importance of shapes and compositions of wind-blown dust particles for remote sensing at solar wavelengths. Geophysical research letters 29, 2–5.

Kamra, A.K., Bhalwankar, R.V., Sathe, A.B., 1985. A Simple Technique for Simultaneous Suspension of Multiple Drops in a Small Vertical Wind Tunnel. Journal of Atmospheric and Oceanic Technology 2, 408.

Kamra, a.K., Bhalwankar, R.V., Sathe, A.B., 1991. Spontaneous Breakup of Charged and Uncharged Water Drops Freely Suspended in a Wind Tunnel. Journal of Geophysical Research 96, 17159–17168.

Knight, I., 2001. The design and construction of a vertical wind tunnel for the study of untethered firebrands in flight. Fire Technology 37, 87–100.

Komar, P., Reimers, C., 1978. Grain shape effects on settling rates. The Journal of Geology 86, 193–209.

Korsawe, J., 2008. Minimal Bounding Box (http://www.mathworks.com/matlabcentral/fileexchange/18264-minimal-bounding-box).

Krotkov, N.A., Flittner, D.E., Krueger, A.J., Kostinski, A., Riley, C., Rose, W., Torres, O., 1999. Effect of particle non-sphericity on satellite monitoring of drifting volcanic ash clouds. Journal of Quantitative Spectroscopy and Radiative Transfer 63, 613–630.

Krumbein, W.C., 1941. Measurement and geological significance of shape and roundness of sedimentary particles. Journal of Sedimentary Research 11, 64–72.

Krumbein, W.C., Pettijohn, F., 1938. Manual of sedimentary petrology. Century and Crofts, New York.

Kunii, D., Levenspiel, O., 1968. Bubbling bed model. Model for flow of gas through a fluidized bed. volume 7. ACS Publications.

Kylling, A., Kahnert, M., Lindqvist, H., Nousiainen, T., 2014. Volcanic ash infrared signature: porous non-spherical ash particle shapes compared to homogeneous spherical ash particles. Atmospheric Measurement Techniques 7, 919–929.

Lane, S.J., Gilbert, J.S., Hilton, M., 1993. The aerodynamic behaviour of volcanic aggregates. Bulletin of Volcanology 55, 481–488.

Latto, B., Round, G., Anzenavs, R., 1973. Drag coefficients and pressure drops for hydrodynamically suspended spheres in a vertical tube with and without polymer addition. The Canadian Journal of Chemical Engineering 51, 536–541.

Laurentini, A., 1997. How many 2D silhouettes does it take to reconstruct a 3D object? Computer Vision and Image Understanding 67, 81–87.

Leith, D., 1987. Drag on Nonspherical Objects. Aerosol Science and Technology 6, 153–161.

Lin, C., Miller, J., 2005. 3D characterization and analysis of particle shape using X-ray microtomography (XMT). Powder Technology 154, 61–69.

Lindqvist, H., Nousiainen, T., Zubko, E., Muñoz, O., 2011. Optical modeling of vesicular volcanic ash particles. Journal of Quantitative Spectroscopy and Radiative Transfer 112, 1871–1880.

List, R., Schemenauer, R.S., 1971. Free-Fall Behavior of Planar Snow Crystals, Conical Graupel and Small Hail. Journal of the Atmospheric Sciences 28, 110–115.

Loth, E., 2008. Drag of non-spherical solid particles of regular and irregular shape. Powder Technology 182, 342–353.

LÜTHI, B., TSINOBER, A., KINZELBACH, W., 2005. Lagrangian measurement of vorticity dynamics in turbulent flow. Journal of Fluid Mechanics 528, 87–118.

Mandø, M., Rosendahl, L., 2010. On the motion of non-spherical particles at high Reynolds number. Powder Technology 202, 1–13.

Manzella, I., Bonadonna, C., Phillips, J.C., Monnard, H., 2015. The role of gravitational instabilities in deposition of volcanic ash. Geology 43, 211–214.

Marchildon, E., Gauvin, W., 1979. Effects of acceleration, deceleration and particle shape on single-particle drag coefficients in still air. AIChE Journal 25, 938–948.

Marchildon, E.K., Clamen, A., Gauvin, W.H., 1964. Drag and oscillatory motion of freely falling cylindrical particles. The Canadian Journal of Chemical Engineering 42, 178–182.

Marzano, F.S., Picciotti, E., Montopoli, M., Vulpiani, G., 2013. Inside Volcanic Clouds: Remote Sensing of Ash Plumes Using Microwave Weather Radars. Bulletin of the American Meteorological Society 94, 1567–1586.

Matzl, M., Schneebeli, M., 2010. Stereological measurement of the specific surface area of seasonal snow types: Comparison to other methods, and implications for mm-scale vertical profiling. Cold Regions Science and Technology 64, 1–8.

Maxey, M.R., Riley, J.J., 1983. Equation of motion for a small rigid sphere in a nonuniform flow. Physics of Fluids 26, 883.

McKay, G., Murphy, R.W., Hillis, M., 1988. Settling characteristics of discs and cylinders. Chemical Engineering Research and Design 16, 107–112.

McNown, J., Malaika, J., 1950. Effects of particle shape on settling velocity at low Reynolds numbers. Trans. Am. Geophys. Union 31, 74–82.

Mills, O.P., Rose, W.I., 2010. Shape and surface area measurements using scanning electron microscope stereo-pair images of volcanic ash particles. Geosphere 6, 805–811.

Mishchenko, M.I., Hovenier, J.W., Travis, L., 2000. Light Scattering by Nonspherical Particles: Theory, Measurements, and Applications. Academic press.

Mishchenko, M.I., Travis, L.D., Kahn, R.a., West, R.a., 1997. Modeling phase functions for dustlike tropospheric aerosols using a shape mixture of randomly oriented polydisperse spheroids. Journal of Geophysical Research 102, 16831.

Moore, J.G., Peck, D.L., 1962. Accretionary lapilli in volcanic rocks of the western continental united states. The Journal of Geology 70, pp. 182–193.

Mordant, N., Pinton, J., 2000. Velocity measurement of a settling sphere. The European Physical Journal B 18, 343–352.

Murrow, P.J., Rose, W.I., Self, S., 1980. Determination of the total grain size distribution in a Vulcanian eruption column, and its implications to stratospheric aerosol perturbation. Geophysical Research Letters 7, 893–896.

Nakamura, Y., Tomonari, Y., 1982. The effects of surface roughness on the flow past circular cylinders at high Reynolds numbers. Journal of Fluid Mechanics 123, 363–378.

Namkoong, K., Yoo, J.Y., Choi, H.G., 2008. Numerical analysis of two-dimensional motion of a freely falling circular cylinder in an infinite fluid. Journal of Fluid Mechanics 604, 33–53.

Nousiainen, T., Kahnert, M., Lindqvist, H., 2011. Can particle shape information be retrieved from light-scattering observations using spheroidal model particles? Journal of Quantitative Spectroscopy and Radiative Transfer 112, 2213–2225.

Nousiainen, T., Kahnert, M., Veihelmann, B., 2006. Light scattering modeling of small feldspar aerosol particles using polyhedral prisms and spheroids. Journal of Quantitative Spectroscopy and Radiative Transfer 101, 471–487.

Oberbeck, A., 1876. Ueber stationäre Flüssigkeitsbewegungen mit Berücksichtigung der inneren Reibung. Journal für die reine und angewandte Mathematik 81, 62–80.

Okuda, K., 1975. Pipe Wall Effects On Suspension Velocities of Single Freely-Suspended Spheres and on Terminal Velocities of Single Spheres in a Pipe. Bulletin of JSME 18, 1142–1150.

Pauwels, B., Liu, X., Sasov, A., 2010. X-ray nanotomography in a SEM, in: Proc. SPIE 7804, Developments in X-Ray Tomography VII, pp. 78040S–78040S–8.

Pettyjohn, E., Christiansen, E., 1948. Effect Of Particle Shape On Free- Settling Rates Of Isometric Particles. Chemical Engineering Progress 44, 157–172.

Pfeiffer, T., Costa, A., Macedonio, G., 2005. A model for the numerical simulation of tephra fall deposits. Journal of Volcanology and Geothermal Research 140, 273–294.

Pitter, R., Pruppacher, H., 1973. A wind tunnel investigation of freezing of small water drops falling at terminal velocity in air. Quarterly Journal of the Royal Meteorological Society 099, 540–550.

Pruppacher, H.R., Beard, K.V., 1970. A wind tunnel investigation of the internal circulation and shape of water drops falling at terminal velocity in air. Quarterly Journal of the Royal Meteorological Society 96, 247–256.

Pruppacher, H.R., Klett, J.D., 2012. Microphysics of Clouds and Precipitation: Reprinted 1980. Springer Science & Business Media.

RCT, 2014. R: A Language and Environment for Statistical Computing (http://www.r-project.org).

Ren, B., Zhong, W., Jin, B., Lu, Y., Chen, X., Xiao, R., 2011. Study on the Drag of a Cylinder-Shaped Particle in Steady Upward Gas Flow. Industrial & Engineering Chemistry Research 50, 7593–7600.

Riley, C.M., 2003. Quantitative shape measurements of distal volcanic ash. Journal of Geophysical Research 108, 2504.

Riley, N.A., 1941. Projection sphericity. Journal of Sedimentary Research 11, 94–95.

Roos, F.W., Willmarth, W.W., 1971. Some experimental results on sphere and disk drag. AIAA Journal 9, 285–291.

Rose, W., Durant, A., 2009. Fine ash content of explosive eruptions. Journal of Volcanology and Geothermal Research 186, 32–39.

Rose, W.I., Durant, A.J., 2008. El Chichón volcano, April 4, 1982: volcanic cloud history and fine ash fallout. Natural Hazards 51, 363–374.

Rose, W.I., Durant, a.J., 2011. Fate of volcanic ash: Aggregation and fallout. Geology 39, 895–896.

Rust, a.C., Cashman, K.V., 2011. Permeability controls on expansion and size distributions of pyroclasts. Journal of Geophysical Research 116, B11202.

Schlighting, H., 1968. Boundary-Layer Theory. volume 539. 6th editio ed., McGraw-Hill New York.

Schneider, C.A., Rasband, W.S., Eliceiri, K.W., 2012. NIH Image to ImageJ: 25 years of image analysis. Nat Meth 9, 671–675.

Schumacher, R., 1994. A reappraisal of Mount St. Helens' ash clusters-depositional model from experimental observation. Journal of volcanology and geothermal research 59, 253–260.

Schumacher, R., Schmincke, H.U., 1995. Models for the origin of accretionary lapilli. Bulletin of Volcanology 56, 626–639.

Scollo, S., 2005. Terminal settling velocity measurements of volcanic ash during the 20022003 Etna eruption by an X-band microwave rain gauge disdrometer. Geophysical Research Letters 32, L10302.

Sneed, E., Folk, R., 1958. Pebbles in the lower Colorado River, Texas a study in particle morphogenesis. The Journal of Geology 66, 114–150.

Sorem, R.K., 1982. Volcanic ash clusters: Tephra rafts and scavengers. Journal of Volcanology and Geothermal Research 13, 63–71.

Sparks, R.S.J., Burski, M.I., Carey, S.N., Gilbert, J.S., Glaze, L.S., Sigurdsson, H., Woods, A.W., 1997. Volcanic plumes. 1st editio ed., John Wiley & Sons.

Spengler, J., Gokhale, N., 1972. Freezing of Freely Suspended, Supercooled Water Drops in a Large Vertical Wind Tunnel. Journal of Applied Meteorology 11, 1101–1107.

Stevenson, J.a., Millington, S.C., Beckett, F.M., Swindles, G.T., Thordarson, T., 2015. Big grains go far: reconciling tephrochronology with atmospheric measurements of volcanic ash. Atmospheric Measurement Techniques Discussions 8, 65–120.

Stokes, G.G., 1851. On the Effect of the Internal Friction of Fluids on the Motion of Pendulums. volume 9.

Stow, C.D., Woodward, M.C., 1974. Evaluation of a Simple Open Circuit Wind Tunnel for Large Droplet Support. Journal of Geophysical Research 79, 4460–4466.

Stringham, G.E., Simons, D.B., Guy, H.P., 1969. The behavior of large particles falling in quiescent liquids. GEOL SURV PROF PAP 562-C, PP C 1-C 36, 1969. 36 P, 27 FIG, 7 TAB, 23 REF. , 1–36.

Sulpizio, R., Bonasia, R., Dellino, P., Di Vito, M.A., La Volpe, L., Mele, D., Zanchetta, G., Sadori, L., 2008. Discriminating the long distance dispersal of fine ash from sustained columns or near ground ash clouds: The example of the Pomici di Avellino eruption (Somma-Vesuvius, Italy). Journal of Volcanology and Geothermal Research 177, 263–276.

Suzuki, T., 1983. A theoretical model for dispersion of tephra, in: Shimozuru, D., Yokoyama, I. (Eds.), Arc Volcanism, Physics and Tectonics. Terra Scientific Pub. Co., pp. 95–113.

Tabak, S., Wolf, D., 1998. Aerodynamic Properties of Cottonseeds. Journal of Agricultural Engineering Research 70, 257–265.

Taddeucci, J., Scarlato, P., Montanaro, C., Cimarelli, C., Del Bello, E., Freda, C., Andronico, D., Gudmundsson, M.T., Dingwell, D.B., 2011. Aggregation-dominated ash settling from the Eyjafjallajokull volcanic cloud illuminated by field and laboratory high-speed imaging. Geology 39, 891–894.

Taylor, M., 2002. Quantitative measures for shape and size of particles. Powder Technology 124, 94–100.

Taylor, M., Garboczi, E., Erdogan, S., Fowler, D., 2006. Some properties of irregular 3-D particles. Powder Technology 162, 1–15.

Telling, J., Dufek, J., 2012. An experimental evaluation of ash aggregation in explosive volcanic eruptions. Journal of Volcanology and Geothermal Research 209-210, 1–8.

Telling, J., Dufek, J., Shaikh, A., 2013. Ash aggregation in explosive volcanic eruptions. Geophysical Research Letters 40, 2355–2360.

Tran-Cong, S., Gay, M., Michaelides, E.E., 2004. Drag coefficients of irregularly shaped particles. Powder Technology 139, 21–32.

Underwood, E.E., 1970. Quantitative stereology. Wesley Publishing Co, Reading, Mass.

Vallebuona, G., Arburo, K., Casali, A., 2003. A procedure to estimate weight particle distributions from area measurements. Minerals Engineering 16, 323–329.

Van Eaton, A.R., Muirhead, J.D., Wilson, C.J.N., Cimarelli, C., 2012. Growth of volcanic ash aggregates in the presence of liquid water and ice: An experimental approach. Bulletin of Volcanology 74, 1963–1984.

Van Eaton, A.R., Wilson, C.J., 2013. The nature, origins and distribution of ash aggregates in a large-scale wet eruption deposit: Oruanui, New Zealand. Journal of Volcanology and Geothermal Research 250, 129–154.

Veitch, G., Woods, A., 2001. Particle aggregation in volcanic eruption columns. Journal of Geophysical Research: Solid Earth 106, 26425–26441.

Veldhuis, C., Biesheuvel, A., 2007. An experimental study of the regimes of motion of spheres falling or ascending freely in a Newtonian fluid. International Journal of Multiphase Flow 33, 1074–1087.

Vonlanthen, P., Rausch, J., Ketcham, R.A., Putlitz, B., Baumgartner, L.P., Grobéty, B., 2015. High-resolution 3D analyses of the shape and internal constituents of small volcanic ash particles: The contribution of SEM micro-computed tomography (SEM micro-CT). Journal of Volcanology and Geothermal Research 293, 1–12.

Wadell, H., 1933. Sphericity and roundness of rock particles. The Journal of Geology 41, 310–331.

Walker, G.P.L., 1971. Grain-size characteristics of pyroclastic deposits. The Journal of Geology 79, 696–714.

Walker, G.P.L., 1973. Explosive volcanic eruptions - a new classification scheme. Geologische Rundschau 62, 431–446.

Walker, G.P.L., Wilson, L., Bowell, E.L.G., 1971. Explosive Volcanic Eruptions-I The Rate of Fall of Pyroclasts. Geophysical Journal International 22, 377–383.

Wang, C., 1970. Effects of Deceleration and Turbulence on the Drag Coefficients of Spheres Entrained in an Air Stream. Master thesis. McGill University.

White, F.M., 1998. Fluid Mechanics. Mcgraw-Hill College.

Wieselsberger, C., 1922. Further information on the laws of fluid resistance. Physikalische Zeitschrift 23, 219–244.

Willmarth, W.W., Hawk, N.E., Harvey, R.L., 1964. Steady and Unsteady Motions and Wakes of Freely Falling Disks. Physics of Fluids 7, 197.

Wilson, L., Huang, T., 1979. The influence of shape on the atmospheric settling velocity of volcanic ash particles. Earth and Planetary Science Letters 44, 311–324.

Zdravkovich, M.M., Brand, V.P., Mathew, G., Weston, A., 1989. Flow past short circular cylinders with two free ends. Journal of Fluid Mechanics 203, 557.

Zhang, Z., Yang, J., Ding, L., Zhao, Y., 2012. An improved estimation of coal particle mass using image analysis. Powder Technology 229, 178–184.

Zingg, T., 1935. Beitrag zur schotteranalyse.